

# **Functional characterization of ClC-K/barttin complexes of different stoichiometries**

Von der Naturwissenschaftlichen Fakultät der  
Gottfried Wilhelm Leibniz Universität Hannover

zur Erlangung des Grades  
Doktor der Naturwissenschaften (Dr. rer. nat.)

genehmigte Dissertation

von

Stefan Thiemann, M.Sc.

2021

Referent: Prof. Dr. Christian Wahl-Schott  
Korreferent: PD Dr. Martin Fischer  
Korreferent: Prof. Dr. Anaclet Ngezahayo  
Tag der Promotion: 14.07.2021

## Zusammenfassung

ClC-K Chloridkanäle tragen zur Salzurückresorption in der Niere und zur Kaliumsekretion in die Endolymphe im Innenohr bei. Sie bilden Homodimere, wobei jede  $\alpha$ -Untereinheit eine eigene leitende Protopore besitzt. Jede Protopore wird durch ein individuelles schnelles Tor (Fast Gate) reguliert, während ein gemeinsames langsames Tor (Slow Gate) beide Protoporen gemeinsam öffnet und schließt. Barttin ist die akzessorische  $\beta$ -Untereinheit der ClC-K Kanäle und beeinflusst deren Expression, subzelluläre Lokalisation und Schaltverhalten. Ko-Immunpräzipitationen zeigen eine Bindung von Barttin an die B- und J-Helices von ClC-K  $\alpha$ -Untereinheiten, was auf eine 1:2  $\alpha$ : $\beta$ -Stöchiometrie für eine Protopore hindeutet. Die funktionalen Konsequenzen von unterschiedlichen Stöchiometrien beider Untereinheiten sind jedoch noch unbekannt. Um deren Auswirkungen auf die Kanalfunktion zu untersuchen, wurden Barttin-Moleküle kovalent an hClC-Ka oder rClC-K1 Kanäle in einem 1:1, 1:2 und 2:1  $\alpha$ : $\beta$ -Verhältnis gebunden. Diese Konkamere wurden in HEK293T- und MDCKII-Zellen exprimiert, und ihr Einfluss auf Expression, subzelluläre Lokalisation und Kanal-Schaltverhalten wurde mit biochemischen Methoden, Konfokalmikroskopie und Patch-Clamp-Technik analysiert. Es zeigte sich, dass eine  $\beta$ - pro einer  $\alpha$ -Untereinheit für i) den korrekten Transport des Kanals zur Plasmamembran, ii) die Aktivierung des hClC-Ka Kanals und iii) die konstitutive Slow Gate Öffnung bei hClC-Ka und rClC-K1 ausreichend ist. Zwei  $\beta$ -Untereinheiten pro  $\alpha$ -Untereinheit öffnen zusätzlich das Fast Gate beider orthologen Kanäle konstitutiv. Daher ermöglicht eine 1:2  $\alpha$ : $\beta$ -Stöchiometrie pro Protopore eine vollständige, funktionelle Aktivierung von ClC-K Kanälen. Darüber hinaus wurden Palmitoylierungs-defiziente Barttin-Mutanten in Konkamere mit unterschiedlichen  $\alpha$ : $\beta$ -Stöchiometrien eingebaut, um den Einfluss der Barttin-Palmitoylierung auf die Kanaleigenschaften zu untersuchen. In dieser Studie wurde bestätigt, dass die Palmitoylierung von Barttin nicht für den Kanaltransport notwendig ist aber für die Öffnung des hClC-Ka Kanals. Die Koexpression von WT Barttin öffnet den Kanal, was auf einen dynamischen Austausch von Barttin-Molekülen an deren Bindungsstellen hinweist. Eine Palmitoylierung ist für Barttin nicht notwendig, um das rClC-K1 Slow Gate konstitutiv zu öffnen, jedoch essentiell für die konstitutive Öffnung des rClC-K1 Fast Gates. Weiterhin könnten solche Konkamere verwendet werden, um funktionale Stöchiometrien und Konsequenzen von krankheitsverursachenden Mutationen nicht nur für ClC-K/Barttin-Komplexe, sondern auch für andere Protein-Interaktionspartner aufzuklären.

Schlagwörter: ClC-K Chloridkanäle; Barttin; Stöchiometrie

## Abstract

ClC-K chloride channels contribute to salt reabsorption in the kidney and to potassium secretion into the endolymph in the inner ear. They build homodimers with each  $\alpha$ -subunit possessing its own conducting protopore. Each protopore is regulated by an individual fast gate, while a common slow gate opens and closes both protopores together. Barttin is the accessory  $\beta$ -subunit of ClC-K channels and affects their expression, subcellular localization and gating properties. Co-immunoprecipitations indicate binding of barttin to B- and J-helices of ClC-K  $\alpha$ -subunits assuming a 1:2  $\alpha$ : $\beta$ -subunit stoichiometry for one protopore. However, functional consequences of varying stoichiometry between both subunits are still unknown. To investigate effects of different subunit stoichiometries on channel function, barttin molecules were covalently linked to hClC-Ka or rClC-K1 in a 1:1, 1:2 and 2:1  $\alpha$ : $\beta$ -subunit ratio. These concatamers were expressed in HEK293T and MDCKII cells and the impact of these compositions on expression, trafficking and channel gating was analyzed using biochemical methods, confocal microscopy and patch clamp technique. We found that one  $\beta$ - per one  $\alpha$ -subunit is sufficient for i) proper transport of the channel to the plasma membrane, ii) hClC-Ka channel activation and iii) constitutive slow gate opening of hClC-Ka and rClC-K1. Two  $\beta$ -subunits per one  $\alpha$ -subunit additionally open the fast gate of both orthologous channels constitutively. Therefore, a 1:2  $\alpha$ : $\beta$ -subunit stoichiometry per protopore allows a complete, functional activation of ClC-K channels. Furthermore, palmitoylation-deficient barttin mutants were incorporated in concatamers with different  $\alpha$ : $\beta$ -subunit ratios to study the impact of barttin palmitoylation on channel properties. We here confirm that barttin palmitoylation is not necessary for channel trafficking but for hClC-Ka activation. Co-expression of WT barttin opens the channel, indicating a dynamic exchange of barttin molecules at their binding sites. Palmitoylation is not necessary for barttin to open the rClC-K1 slow gate constitutively but it is essential for constitutive opening of the rClC-K1 fast gate. In further approaches such concatamers might be used to elucidate functional stoichiometries and consequences of disease causing mutations not only for ClC-K/barttin complexes but also for other protein interaction partners.

Keywords: ClC-K chloride channels; Barttin; Stoichiometry



## Table of Content

<b>Zusammenfassung</b> .....	<b>I</b>
<b>Abstract</b> .....	<b>II</b>
<b>List of figures</b> .....	<b>VI</b>
<b>List of tables</b> .....	<b>VIII</b>
<b>List of abbreviations</b> .....	<b>IX</b>
<b>1 Introduction</b> .....	<b>1</b>
1.1 The ClC protein family .....	1
1.2 Role of ClC-K channels for physiological processes in the kidney and in the inner ear .....	3
1.3 The Bartter syndrome .....	5
1.4 The structure of ClC proteins and their selectivity filter .....	5
1.5 Molecules that influence the properties and functions of ClC proteins .....	9
1.6 The ClC-K $\beta$ -subunit barttin .....	10
1.7 Aim of this study.....	13
<b>2 Material and Methods</b> .....	<b>15</b>
2.1 Material .....	15
2.2 Methods .....	16
2.2.1 Molecular biology.....	16
2.2.1.1 Molecular biological vectors .....	16
2.2.1.2 Cloning strategies .....	16
2.2.1.3 Polymerase chain reaction (PCR) .....	17
2.2.1.4 Exchange of single amino acids using QuikChange® site directed mutagenesis kit.....	18
2.2.1.5 Transformation of vectors into competent bacteria.....	19
2.2.1.6 Enzymatic digestion of DNA and subcloning of DNA fragments into vector DNA .....	20
2.2.1.7 Agarose gel electrophoresis .....	20
2.2.1.8 Sanger sequencing.....	21
2.2.2 Cell culture and transfection .....	21
2.2.3 Freezing and thawing of cells .....	23
2.2.4 Protein biochemical methods .....	23
2.2.4.1 Determination of protein expression .....	23
2.2.4.2 Western Blot.....	25
2.2.4.3 Purification of plasma membrane proteins using biotinylation assay .....	26
2.2.5 Confocal microscopy .....	28
2.2.6 Fluorescence measurements of cells using the Cytation 5 imaging reader.....	28
2.2.7 Electrophysiology .....	29
2.2.7.1 Patch clamp setup and recording solutions .....	29
2.2.7.2 Analysis of electrophysiological data .....	31

2.2.7.3 Time constants .....	31
2.2.7.4 Determination of relative channel open probabilities .....	32
2.2.7.5 Determination of relative channel conductances from IV-plots.....	34
2.2.7.6 Determination of single pore parameters using stationary noise analysis.....	34
2.2.7.7 Single channel measurements .....	36
2.2.7.8 Inhibition of ClC-K channels by 1 mM niflumic acid .....	38
2.2.8 Statistics.....	38
<b>3 Results .....</b>	<b>39</b>
3.1 ClC-K/WT barttin concatamers of different stoichiometries .....	39
3.1.1 hClC-Ka and barttin expression in HEK293T and MDCKII cells.....	40
3.1.2 hClC-Ka/barttin concatamers are expressed in HEK293T and MDCKII cells and transported to the plasma membrane.....	41
3.1.3 Two $\beta$ -subunits per $\alpha$ -subunit are sufficient to increase hClC-Ka currents similar to barttin excess .....	45
3.1.4 hClC-Ka/barttin stoichiometry influences single pore properties.....	47
3.1.5 rClC-K1/barttin concatamers are expressed in HEK293T and MDCKII cells and transported to the plasma membrane .....	50
3.1.6 Two $\beta$ -subunits per $\alpha$ -subunit are sufficient to increase rClC-K1 currents similar to barttin excess .....	53
3.1.7 Two $\beta$ -subunits per $\alpha$ -subunit are sufficient to maximally induce hyperpolarization block	55
3.1.8 One $\beta$ -per $\alpha$ -subunit opens rClC-K1 slow gate and two $\beta$ -subunits open its fast gate .....	58
3.1.9 Effects of rClC-K1/barttin stoichiometry on slow channel gating .....	63
3.1.10 One barttin per two hClC-Ka $\alpha$ -subunits is not sufficient to facilitate surface membrane transport and channel function.....	65
3.1.11 The concatamer possessing one barttin per two rClC-K1 $\alpha$ -subunits is hardly expressed but generates robust currents .....	69
3.2 ClC-K/barttin concatamers of different stoichiometries containing non-palmitoylated barttin	73
3.2.1 Non-palmitoylated barttin does not influence relative expression and subcellular localization of hClC-Ka/barttin concatamers.....	74
3.2.2 Currents of hClC-Ka/barttin <sub>MUT</sub> concatamers recover by the co-expression of WT barttin.	75
3.2.3 Single pore parameters of hClC-Ka/barttin <sub>MUT</sub> concatamers recover by co-expression of WT barttin.....	76
3.2.4 Non-palmitoylated barttin does not influence relative expression and subcellular localization of rClC-K1/barttin concatamers .....	78
3.2.5 Non-palmitoylated barttin does not influence the macroscopic current amplitude of rClC-K1 channels.....	79
3.2.6 Non-palmitoylated barttin facilitates hyperpolarization-induced block for rClC-K1 less intense as palmitoylated barttin .....	81
3.2.7 Barttin palmitoylation is necessary for rClC-K1 fast gate modulation but not for slow gate modulation .....	82
3.2.8 Co-expression of WT barttin influences barttin <sub>MUT</sub> _rClC-K1_rClC-K1 .....	87

3.3 Single channel measurements of ClC-K/barttin concatamers.....	90
3.3.1 Niflumic acid blocks ClC-K channels in HEK293T cells .....	90
3.3.2 High availability of barttin molecules per hClC-Ka $\alpha$ -subunit stabilizes single pore opening and closing events .....	91
3.3.3 Barttin availability does not affect single pore conductance of rClC-K1 .....	98
<b>4 Discussion .....</b>	<b>101</b>
4.1 All ClC-K/barttin concatamers were successfully expressed in used cell lines .....	103
4.1.1 The concatamer barttin_rClC-K1_rClC-K1 represents an expressional and functional exception among tested concatamers .....	107
4.2 One barttin per one $\alpha$ -subunit is sufficient to promote plasma membrane insertion .....	110
4.3 One barttin per one ClC-K $\alpha$ -subunit opens the common slow gate .....	112
4.4 Two barttin molecules per one ClC-K $\alpha$ -subunit open the protopore fast gate .....	112
4.4.1 The fast gate as origin of time-dependent fast gating and hyperpolarization-induced block .....	114
4.5 Dwell times of single pore events affect the outcome of noise analyses .....	117
4.6 Barttin palmitoylation is responsible for rClC-K1 fast gate opening .....	119
4.7 Summary.....	122
4.8 Outlook.....	123
<b>5 References .....</b>	<b>127</b>
<b>6 Supplement.....</b>	<b>137</b>
<b>7 Acknowledgements .....</b>	<b>142</b>
<b>8 Curriculum vitae .....</b>	<b>144</b>
<b>9 List of publications.....</b>	<b>145</b>

## List of figures

<b>Fig. 1</b> Overview of the ClC protein family in mammals.....	1
<b>Fig. 2</b> Localization and function of ClC-K channels.....	4
<b>Fig. 3</b> Topology model and structure of ClC-K proteins .....	6
<b>Fig. 4</b> Model of the open and closed pore conformation of <i>EcClC</i> .....	8
<b>Fig. 5</b> Model of a double-barreled ClC channel with a rClC-K1 single channel measurement demonstrating fast and slow gating.....	9
<b>Fig. 6</b> Topology model of the $\beta$ -subunit barttin .....	11
<b>Fig. 7</b> Biotinylation assay procedure .....	28
<b>Fig. 8</b> Conduction and evaluation of stationary noise analysis.....	36
<b>Fig. 9</b> Binomial distribution of conductance states for a ClC-K channel with two independent pores.....	38
<b>Fig. 10</b> Design of ClC-K/barttin channels with diverse stoichiometries as investigated in this study.....	40
<b>Fig. 11</b> Fluorescence scan of SDS-PAGE gels with protein lysates from HEK293T and MDCKII cells expressing hClC-Ka_mYFP (red) alone or with barttin_mCFP (green) .....	41
<b>Fig. 12</b> Expression and plasma membrane insertion of hClC-Ka/barttin concatamers.....	42
<b>Fig. 13</b> Currents of hClC-Ka concatamers in absence and presence of additional barttin .....	47
<b>Fig. 14</b> Stationary noise analysis of hClC-Ka concatamers in absence and presence of additional barttin.....	49
<b>Fig. 15</b> Expression and plasma membrane insertion of rClC-K1/barttin concatamers.....	51
<b>Fig. 16</b> Currents of rClC-K1/barttin concatamers in absence and presence of additional barttin.....	54
<b>Fig. 17</b> Influence of barttin availability on hyperpolarization-induced block of rClC-K1.....	56
<b>Fig. 18</b> Stationary noise analysis of rClC-K1 with barttin co-expression.....	58
<b>Fig. 19</b> Determination of fast gate, slow gate and total rClC-K1 channel open probability in absence of barttin .....	59
<b>Fig. 20</b> Time-dependent fast gating of rClC-K1 under different $\alpha$ : $\beta$ -subunit stoichiometries .....	61/62
<b>Fig. 21</b> Impact of $\alpha$ : $\beta$ -subunit stoichiometry on slow gate kinetics of rClC-K1.....	65
<b>Fig. 22</b> Expression and plasma membrane insertion of barttin_hClC-Ka_hClC-Ka.....	67
<b>Fig. 23</b> Currents of barttin_hClC-Ka_hClC-Ka in absence and presence of additional barttin.....	68
<b>Fig. 24</b> Stationary noise analysis of barttin_hClC-Ka_hClC-Ka in absence and presence of additional barttin.....	69
<b>Fig. 25</b> Expression and plasma membrane insertion of barttin_rClC-K1_rClC-K1.....	70
<b>Fig. 26</b> Currents of barttin_rClC-K1_rClC-K1 in absence and presence of additional barttin.....	71
<b>Fig. 27</b> Influence of 2:1 $\alpha$ : $\beta$ -subunit stoichiometry on hyperpolarization-induced block of rClC-K1.....	72
<b>Fig. 28</b> Time-dependent fast gating of barttin_rClC-K1_rClC-K1 .....	73
<b>Fig. 29</b> Expression and plasma membrane insertion of hClC-Ka/barttin <sub>MUT</sub> concatamers.....	75
<b>Fig. 30</b> Currents of hClC-Ka concatamers, containing non-palmitoylated barttin, in absence and presence of additional WT barttin .....	76
<b>Fig. 31</b> Stationary noise analysis of hClC-Ka concatamers, containing non-palmitoylated barttin, in presence of additional WT barttin .....	77
<b>Fig. 32</b> Expression and plasma membrane insertion of rClC-K1/barttin <sub>MUT</sub> concatamers .....	78
<b>Fig. 33</b> Currents of rClC-K1 concatamers, containing non-palmitoylated barttin, in absence and presence of additional WT barttin .....	80

<b>Fig. 34</b>	Influence of barttin palmitoylation on hyperpolarization-induced block of rClC-K1...	82
<b>Fig. 35</b>	Time-dependent gating of rClC-K1 in co-expression of WT barttin or non-palmitoylated barttin .....	83
<b>Fig. 36</b>	Time-dependent fast gating of rClC-K1/barttin concatamers, containing non-palmitoylated barttin .....	85
<b>Fig. 37</b>	Impact of barttin palmitoylation under different $\alpha:\beta$ -subunit stoichiometries on rClC-K1 slow gate kinetics .....	86
<b>Fig. 38</b>	Currents of barttin <sub>MUT</sub> _rClC-K1_rClC-K1 in absence and presence of additional WT barttin.....	87
<b>Fig. 39</b>	Influence of barttin palmitoylation on hyperpolarization-induced block of barttin_rClC-K1_rClC-K1 .....	88
<b>Fig. 40</b>	Time-dependent fast gating of barttin <sub>MUT</sub> _rClC-K1_rClC-K1 .....	89
<b>Fig. 41</b>	Inhibition of ClC-K channels by 1 mM NFA in whole cell configuration .....	91
<b>Fig. 42</b>	Single channel recordings of hClC-Ka with barttin co-expression.....	92
<b>Fig. 43</b>	Single channel recordings of barttin_barttin_hClC-Ka .....	95
<b>Fig. 44</b>	Single channel recordings of barttin_hClC-Ka .....	97
<b>Fig. 45</b>	Single channel recordings of rClC-K1 under different $\alpha:\beta$ -subunit stoichiometries ....	99
<b>Fig. 46</b>	Overview about putative effects of palmitoylated and non-palmitoylated barttin on ClC-K channel gating.....	103
<b>Fig. 47</b>	Fluorescent expression products of rClC-K1/hClC-Ka concatamers in HEK293T cells	105
<b>Fig. 48</b>	Amount of rClC-K1 concatamer degradation product after one expression day correlates with concatamer expression level after two days .....	107
<b>Fig. 49</b>	Analysis of YFP fluorescence distribution between HEK293T cells expressing rClC-K1 or barttin_rClC-K1_rClC-K1.....	108
<b>Fig. 50</b>	Correlation between relative conductance at -255 mV and relative fast gate open probability at +105 mV for rClC-K1 under different $\alpha:\beta$ -subunit stoichiometries.....	116
<b>Fig. 51</b>	Influence of filter frequency on single pore current amplitudes in single channel recordings and on single pore conductance obtained by stationary noise analysis .....	118
<b>Suppl. Fig. 1</b>	Overview about representative current traces for each tested $\alpha:\beta_{WT}$ -subunit stoichiometry categorized into three classes of time-dependent fast gating .....	137/138
<b>Suppl. Fig. 2</b>	Overview about representative current traces for each tested $\alpha:\beta_{MUT}$ -subunit stoichiometry categorized into three classes of time-dependent fast gating .....	139
<b>Suppl. Fig. 3</b>	Representative current recording of rClC-K1 + barttin <sub>MUT</sub> used for determination of relative slow gate open probabilities.....	140
<b>Suppl. Fig. 4</b>	Comparison of slow gating time constants at -115 mV between rClC-K1/barttin <sub>WT</sub> and respective rClC-K1/barttin <sub>MUT</sub> concatamers .....	141

## List of tables

<b>Table 1:</b> Composition of PCR reaction mix.....	18
<b>Table 2:</b> PCR program for DNA amplification.....	18
<b>Table 3:</b> Compounds for QuikChange® PCR reaction mix.....	18
<b>Table 4:</b> PCR program for QuikChange® PCR .....	19
<b>Table 5:</b> Quikchange® primers for site directed mutagenesis of barttin.....	19
<b>Table 6:</b> Components of a SDS-PAGE gel, featuring a 10% acrylamide concentration in separating gel .....	24

## List of abbreviations

(n,p)A =	(nano-, pico-)ampere
al. =	alii, aliae (English: others)
ANOVA =	analysis of variance
(m)CFP =	(monomeric) cyan fluorescent protein
DMEM =	Dulbecco's modified eagle medium
(c)DNA =	(complementary) deoxyribonucleic acid
EDTA =	ethylenediaminetetraacetic acid
EGTA =	ethyleneglycol-bis(aminoethylether)-N,N,N',N'-tetra acetic acid
F =	Faraday constant (96485.3365 C mol <sup>-1</sup> )
FBS =	fetal bovine serum
Fig. =	figure
(μ,m)g =	(mikro-)gram
h =	hour
HEK =	human embryonic kidney
HEPES =	2-(4-(2-hydroxyethyl)-1-piperazinyl)-ethan sulfonic acid
(k)Hz =	(kilo-)Hertz
I =	current
kDa =	kilodalton
(μ, m)l =	(mikro-, milli-)liter
LB medium =	Luria Berani medium
(m)M =	(milli-)mol per liter
(μ, c, n)m =	(mikro-, centi-, nano-)meter
MDCK =	Madin-Darby canine kidney
MUT =	without palmitoylation sites
n =	number (of experiments)
NFA =	niflumic acid
n.s. =	not significant
(G, M)Ω =	(giga-, mega-)Ohm
PBS =	phosphate-buffered saline
PCR =	polymerase chain reaction
R =	universal gas constant (8.3144621 J K <sup>-1</sup> mol <sup>-1</sup> )
(n, p)S =	(nano-, pico-)Siemens
(m)s =	(milli-)second
S.E.M. =	standard error of the mean
SOC =	super optimal broth with catabolite repression
Suppl. =	supplement
SV =	simian virus
T =	absolute temperature
TAE =	tris-acetate-EDTA
TBS(-T)	tris-buffered saline (with Tween20)
U =	unit
(m)V =	(milli-)volt
V <sub>0.5</sub> =	voltage at the turning point of an activation curve at half maximum activation
V <sub>rev</sub> =	reversal potential
WT =	wildtype
(m)YFP =	(monomeric) yellow fluorescent protein

# 1 Introduction

## 1.1 The CIC protein family

Members of the heterogeneous CIC chloride channel/transporter family are phylogenetically widespread and can therefore be found in bacteria (Fujita et al., 1994), fungi (Huang et al., 1994), plants and animals (Jentsch et al., 1990). As the largest family of anion channels and transporters they fulfill numerous functions in various compartments of the cell. Some CIC proteins are localized in plasma membranes of cells, where they contribute to transepithelial transport of ions, homeostasis of ion distribution, regulation of cell volume and electrical excitability (Jentsch et al., 2002). Other CIC subtypes insert into membranes of cell organelles. These are essential for functionality of endosomes and lysosomes (Jentsch et al., 2002). So far, nine CIC isoforms have been identified in mammals. The phylogenetic tree of these nine isoforms, together with their localization and function are illustrated in figure 1. Due to sequence homologies they can be classified into two groups. CIC-1, CIC-2, hCIC-Ka and hCIC-Kb and the corresponding rat homologue rCIC-K1 and rCIC-K2 represent the first group. They exclusively form chloride channels and localize in the plasma membrane. CIC-1 is mainly expressed in skeletal muscles and is responsible for about 80% of the anion conductivity at resting membrane potential (Steinmeyer et al., 1991a,b). In turn, the expression of CIC-1 depends strongly on the electrical excitation and muscle innervation.

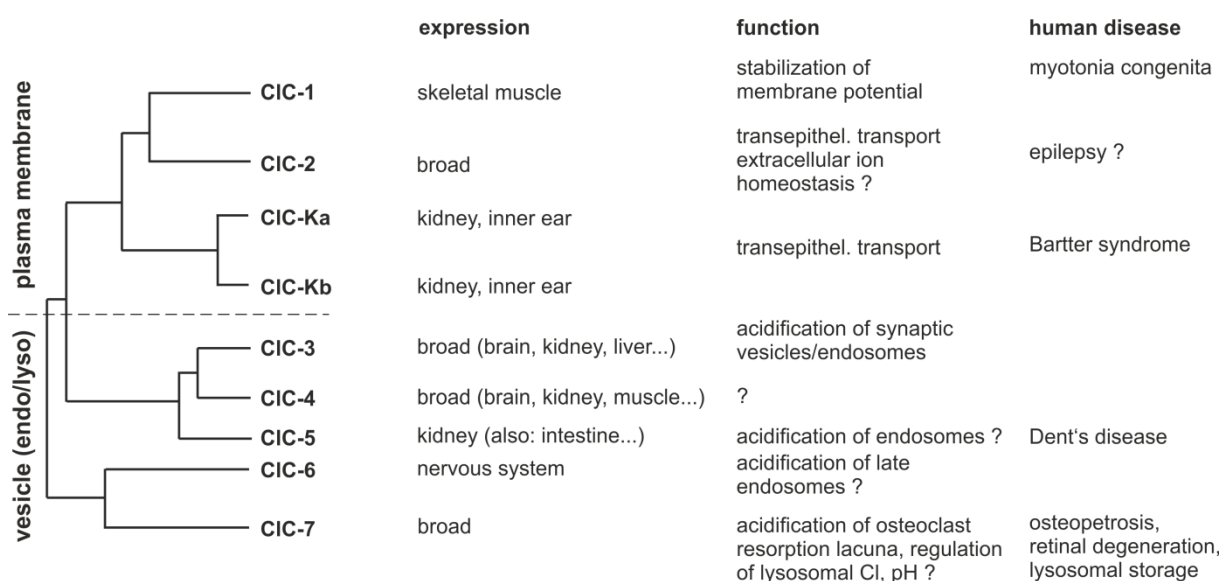


**Fig. 1 Overview of the CIC protein family in mammals**

Mammalian CIC proteins are shown in phylogenetic context (left). In addition, the corresponding sites of expression within the organism, the function of the CIC proteins and related human diseases are listed. CIC-1, CIC-2 as well as the CIC-K proteins are chloride ion channels, whereas the CIC-3 to CIC-7 proteins are chloride/proton antiporters. This figure was modified from Jentsch (2008).



If a muscle is less innervated or less electrically excited, the expression of ClC-1 decreases (Klocke et al., 1994). Mutations in the CLCN-1 gene coding for ClC-1 cause the muscle dysfunction myotonia congenita (George et al., 1993; Koch et al., 1992). ClC-2 is expressed in numerous tissues, where it fulfills various tasks (Jentsch, 2008). In the central nervous system ClC-2 performs excitatory tasks (Földy et al., 2010; Kleefuß-Lie et al., 2009; Rinke et al., 2010; Saint-Martin et al., 2009), contributes to wound healing processes in the retina (Cao et al., 2010) and to anion absorption in many tissues (Bösl et al., 2001; Catalán et al., 2004; Pena-Munzenmayer, 2005). ClC-2 is activated by hyperpolarization (Thiemann et al., 1992), by increase of cell volume (Gründer et al., 1992) and by extracellular acidification (Jordt & Jentsch, 1997). Recently, ClC-2 was found to be involved in aldosterone production in the adrenal gland (Fernandes-Rosa et al., 2018; Scholl et al., 2018). Dysfunction of this channel can trigger idiopathic epilepsy (Stölting et al., 2013). The channels hClC-Ka and hClC-Kb are mainly located in the kidney and inner ear and are involved in the transepithelial transport of chloride ions (Jentsch et al., 2002; Kieferle et al., 1994; Uchida et al., 1995).

The ClC proteins ClC-3 to ClC-7, expressed in many tissues, comprise the second group of the ClC family. They are located in membranes of endosomes and lysosomes and represent chloride/proton exchangers, which transport two chloride ions into vesicles and one proton into the cytosol per one transport cycle (Jentsch, 2008). This transport is driven secondary active by vesicular H<sup>+</sup>-ATPases, which pump protons into vesicles. By the transport of protons into vesicles, the inner milieu is acidified, which is important for the function of these cell organelles. As positive charges would accumulate in the intravesicular compartment during this process, a further acidification would consequently be inhibited after a short time due to electrostatic repulsion. The electrogenic transport of two negatively charged chloride ions into the vesicles by ClC transporters ensures effective and ongoing acidification of endo- and lysosomes (Jentsch, 2008, 2015; Weinert et al., 2014). The absence of ClC-3 in ClC-3 knock-out mice results in a degeneration of certain areas of the hippocampus and potentially to a pathological lysosomal storage (Farmer et al., 2013; Stobrawa et al., 2001; Wang et al., 2006; Yoshikawa et al., 2002). ClC-4 is expressed in brain, muscles and liver and is supposed to be important for the above mentioned endosomal acidification (Mohammad-Panah et al., 2003). Furthermore, it was found that ClC-4 can be influenced by extracellular anions like thiocyanate in a way that it is functionally converted to an anion channel (Alekov & Fahlke, 2009). Loss of ClC-4 function leads to neurological disorders (Hu et al., 2016; Meindl et al., 1993; Veeramah

et al., 2013). Dysfunctions of ClC-5 can cause the Dent's disease, where the endocytosis in the proximal renal tubule is impaired (Friedrich et al., 1999; Gunther et al., 1998). This disease is associated with proteinuria, and nephrocalcinosis (Piwon et al., 2000; Wang et al., 2000). ClC-5 is located in apical epithelial cells of the kidney but also of the small intestine and colon (Gunther et al., 1998; Vandewalle et al., 2001). ClC-6 was found in the central and peripheral nervous system. Knockout of this transporter seems to be involved in lysosomal storage disorders (Poët et al., 2006). The transporter ClC-7 is the only ClC protein, which has been shown to localize in lysosomes until now (Poët et al., 2006). Furthermore, together with H<sup>+</sup>-ATPases it is localized in the resorption lacunas of osteoclasts and seems to be involved in dissolution of bone material (Kornak et al., 2001). Therefore, loss of ClC-7 function is associated with osteopetrosis but also with retinal degradation, neurodegeneration and lysosomal storage disorders (Kasper et al., 2005; Kornak et al., 2001).

## **1.2 Role of ClC-K channels for physiological processes in the kidney and in the inner ear**

In this study, the focus was on ClC-K channels. hClC-Ka and hClC-Kb are the human isoforms of rClC-K1 and rClC-K2 in the rat. For the human isoforms there is a sequence homology of 83%, for the rat isoforms 91% and for the two orthologous channels about 80% (Fahlke & Fischer, 2010; Kieferle et al., 1994; Kobayashi, 2002; Krämer et al., 2008). hClC-Ka/rClC-K1 are located within the kidney mainly in the thin ascending limb of Henle's loop, where they apically conduct the chloride influx from the tubulus lumen into the epithelial cells and, basolaterally, the chloride efflux from the epithelial cells into the interstitium (Fig.2A). Here, the transport of the chloride ions is passive and only mediated by the chemical gradient. In the thick ascending limb of Henle's loop mainly hClC-Kb/rClC-K2 are expressed. These channels support the transepithelial reabsorption of sodium and chloride from the lumen into the interstitium. The basolateral Na/K-ATPase actively transports three Na<sup>+</sup> ions into the interstitium in exchange for two K<sup>+</sup> ions. On the apical side, the secondary active co-transporter NKCC2 conveys one Na<sup>+</sup>, two Cl<sup>-</sup> and one K<sup>+</sup> into the cytosol. Subsequently, chloride ions are passively carried from the cell into the interstitium by basolateral hClC-Kb/rClC-K2 channels. Potassium ions, which would accumulate in the cell, are passively transported *via* ROMK1 channels into the lumen of the nephron and thus recirculate at the apical membrane.

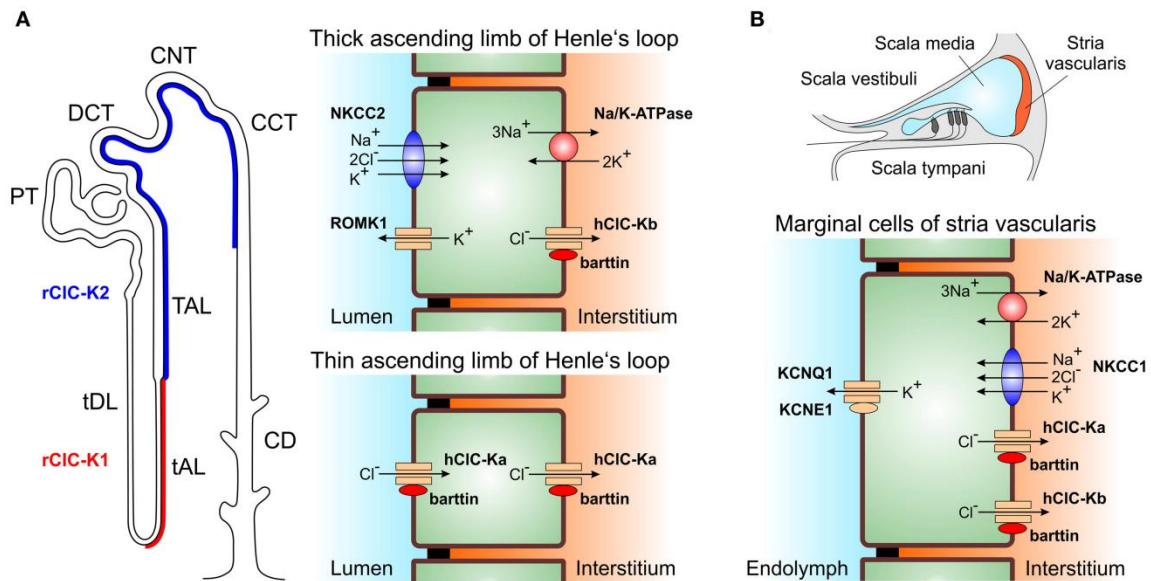


**Fig. 2 Localization and function of ClC-K channels**

(A) Left: Site of ClC-K channel expression in rats. The rClC-K1 channel (red) is expressed in the thin ascending limb of Henle's loop in the kidney. The rClC-K2 channel (blue) is expressed in the thick ascending limb of Henle's loop. Right: the hClC-Ka/rClC-K1 channel allows passive transport of chloride ions from the lumen of the thin ascending limb into the interstitium. The hClC-Kb/rClC-K2 is required for secondary active transport of sodium chloride from the lumen of the thick ascending limb to the outer medulla and to the cortical region of the kidney (PT, proximal tubule; tDL, thin descending limb of Henle's loop; tAL, thin ascending limb of Henle's loop; TAL, thick ascending limb of Henle's loop; DCT, distal convoluted tubule; CNT, connecting tubule; CCT, cortical collecting tube; CD, collecting duct). (B) Both hClC-Ka/rClC-K1 and hClC-Kb/rClC-K2 are expressed in the marginal cells of the stria vascularis in the inner ear. They contribute to the transport of potassium ions into the endolymph. This is necessary for signal transduction of the inner hair cells. The figure was taken from Fahlke and Fischer (2010).

Due to the transport of Cl<sup>-</sup> ions *via* hClC-Ka/rClC-K1 and hClC-Kb/rClC-K2 as well as Na<sup>+</sup> ions *via* the Na/K-ATPase into the interstitium of the Henle's loop an osmotic gradient is built up, which is used for ADH-(anti-diuretic hormone)-mediated reabsorption of water from the lumen of the collecting duct.

Both hClC-Ka/rClC-K1 and hClC-Kb/rClC-K2 are also co-expressed in the marginal cells of the stria vascularis in the inner ear (Estévez et al., 2001). In the marginal cells KCNQ1/KCNE1 channels transport K<sup>+</sup> ions from the cytosol into the endolymph (Fig.2B). A high K<sup>+</sup>-concentration in the endolymph is important for the signal transduction of the inner hair cells and thus for hearing. One K<sup>+</sup> will be transferred together with two Cl<sup>-</sup> and one Na<sup>+</sup> *via* a NKCC1 co-transporter from the interstitium into the marginal cells. Driving force is a Na<sup>+</sup> gradient, which is built up by the basolaterally localized Na/K-ATPase. It transports Na<sup>+</sup> from the cytosol into the interstitium and at the same time contributes to an accumulation of K<sup>+</sup> in the cytosol. Due to the NKCC1 activity, chloride ions would accumulate in the cytosol, which would finally lead to cessation of NKCC1 turnover. However, passive diffusion of chloride ions back to the interstitium *via* hClC-Ka/rClC-K1 and hClC-Kb/rClC-K2 channels counteracts this undesired effect.

### 1.3 The Bartter syndrome

Disorders of these physiological processes lead to kidney failure accompanied with increased renal salt loss, polyuria, polydipsia, hyperaldosteronism and hypokalemic alkalosis (Bartter et al., 1962). Following the first discovery by Frederic Bartter in 1962 the characteristic disease pattern was called Bartter syndrome. Up to now five types of Bartter syndrome are identified according to their mutated protein component. Type I is associated with mutations in the gene coding for the NKCC2 co-transporter and type II with mutations in the gene for the ROMK1 potassium channel. Mutations in the *CNCLC-Kb* gene coding for the hClC-Kb channel induce Bartter syndrome type III. ClC-K channels need an accessory  $\beta$ -subunit to be functional. Also named after Frederic Bartter, this subunit is called barttin. Mutations in the *BSND* gene, coding for barttin can cause the Bartter syndrome type IV. Barttin is the  $\beta$ -subunit for both hClC-Ka and hClC-Kb. Thus, an additional hearing loss occurs next to the renal dysfunction because in this case the two channels cannot recycle  $\text{Cl}^-$  ions in the stria vascularis of the inner ear any more, which would be necessary for the transport of  $\text{K}^+$  ions into the endolymph (Birkenhäger et al., 2001; Hebert, 2003; Janssen et al., 2009; Riazuddin et al., 2009). While Bartter syndrome types I-IV are autosomal recessive diseases, type V is an autosomal dominant mutation of the gene coding for the  $\text{Ca}^{2+}$  sensing receptor (CaR). This receptor impacts the NKCC2 transporter and the ROMK1 channel (Hebert, 2003; Seyberth, 2008).

### 1.4 The structure of ClC proteins and their selectivity filter

For a long time only structures were available for ClC transporters, from which structural features were transferred to ClC channels. By X-ray crystallography of prokaryotic *EcClC* from *Escherichia coli* and *StClC* from *Salmonella enterica* serotype *typhimurium* the structure of ClC proteins could be described at first (Dutzler et al., 2002). Later, the structure of a eukaryotic ClC transporter from the red alga *Cyanidioschyzon merolae* has been resolved (Feng et al., 2010). These ClC proteins form homodimers, with one pore for each monomer/subunit (also called protopore), through which chloride ions can migrate (Ludewig et al., 1996). Each monomer consists of 18  $\alpha$ -helices, named A to R, while the first and second nine  $\alpha$ -helices are similarly composed and arranged antiparallel within the membrane. Moreover, eukaryotic ClC proteins possess a long intracellularly located C-terminus with two cysteine  $\beta$ -synthase

(CBS) domains (Fig.3A). Adenosine nucleotides can bind to CBS domains of some ClC proteins (ClC-1 to ClC-5) but not to ClC-K channels, which contribute to channel gating and dimerization (Bennetts et al., 2005; Grieschat et al., 2020; Hebeisen et al., 2004; Hebeisen & Fahlke, 2005; Meyer et al., 2007; Stölting et al., 2013). Due to the high similarity of amino acid sequence between pro- and eukaryotes, one can assume that this three-dimensional structure applies to all ClC proteins.

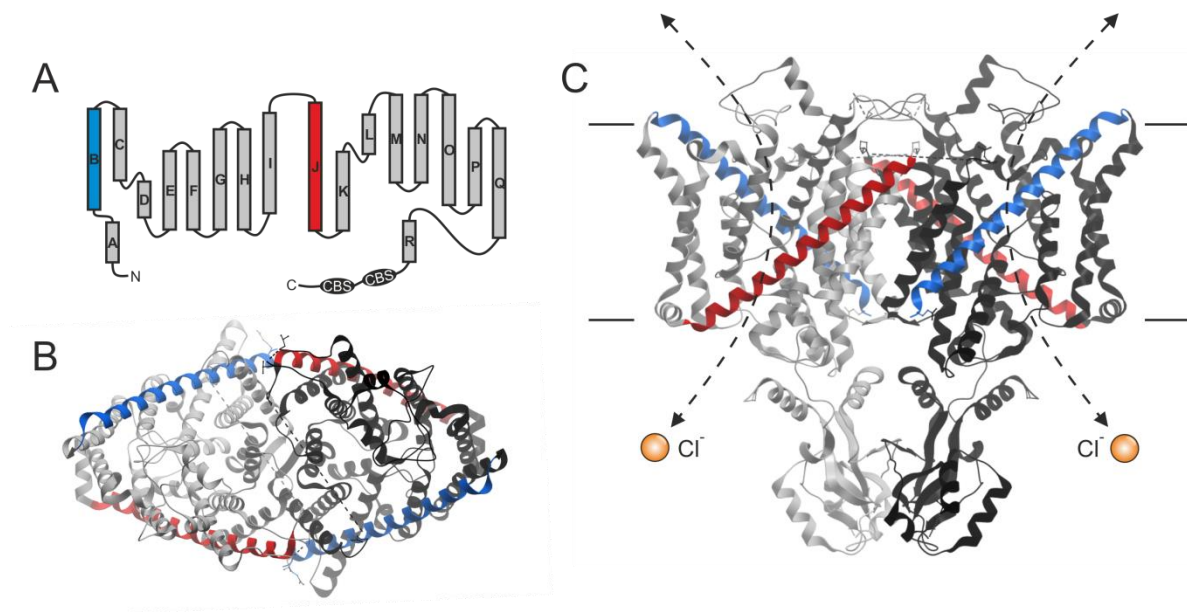


**Fig. 3 Topology model and structure of ClC-K proteins**

(A) Topology model of one subunit of the bovine ClC-K channel.  $\alpha$ -helices are shown as cylinders labeled from A to R. Helices A to I and J to R arrange antiparallel within plasma membrane to form one pore. C-terminally two CBS domains are located at the intracellular side. (B) Crystal structure of a bovine ClC-K homodimer in top view (PDB Code: 5TQQ, Park et al. (2017)). (C) Crystal structure of a bovine ClC-K homodimer in side view. Arrows with dashed lines indicate chloride ion conduction pathway and orange dots chloride ions. Black lines indicate the plasma membrane. In (A)-(C) B-helix is depicted in blue and J-helix in red, which cover the outer lateral surface of the protein and represent one potential binding sites per helix for ClC-K's  $\beta$ -subunit barttin. In (B) and (C) single monomers (the two  $\alpha$ -subunits) are highlighted in grey and black.

The ion specificity is guaranteed by a selectivity filter. It comprises three binding sites for chloride ions within *EcClC* and is composed both of the N-terminal regions of the  $\alpha$ -helices D, F, N and R and of adjacent amino acid side chains. Their sequences are highly conserved within the ClC family and form an electrostatic environment that is optimal for chloride ions (Dutzler et al., 2002, 2003). From the intracellular aqueous pore environment, chloride ions are introduced to the selectivity filter of *EcClC* by the binding site  $S_{int}$  (Dutzler et al., 2003) (Fig.4A). This is achieved by dipole interactions between the chloride ion and nitrogen atoms at the end of the  $\alpha$ -helix D. At the second binding site  $S_{cen}$ , chloride ions are coordinated by nitrogen atoms at the end of the  $\alpha$ -helix F and by the hydroxyl residues of the amino acids serine 107 and tyrosine 445. The third binding site  $S_{ext}$ , which gives the chloride ions access to the extracellular space, is created by the ends of the  $\alpha$ -helices N and F (Dutzler, 2004). This binding

site can be occluded by the carboxyl group of a glutamate to block the passage of chloride ions. Due to the negative charge of the carboxyl group dipole interactions with the  $\alpha$ -helices N and F can be built up causing the pore to close. By neutralizing the glutamate using protonation (Niemeyer et al., 2003) or by changing the transmembrane voltage the occlusion of the external chloride binding site can be abolished. In this case the carboxyl group of glutamate moves out of the pore potentially accompanied by changes of further parts of the channel and selectivity filter (Accardi & Pusch, 2003; Dutzler et al., 2003). This enables chloride ions to pass the pore. The glutamate at this position is therefore seen as a gate, which opens and closes voltage dependently (Fahlke, Yu, et al., 1997). Since both pores own this glutamate, it is called a 'protopore gate' (Middleton et al., 1996). It is also named 'fast gate', which is due to the fast reaction to voltage changes (Fischer et al., 2010). This 'gating glutamate' is conserved in almost all representatives of the CIC family.

Recently, even the structures of the human CIC-1 and of a bovine CIC-K channel have been determined using cryo electron microscopy (Park et al., 2017; Park & MacKinnon, 2018; Wang et al., 2019) (Fig.3B,C). Indeed, these structures are in high accordance with structures from pro- and eukaryotic CIC-transporters, confirming the hypothesis that CIC channels developed from CIC-transporters (Lísal & Maduke, 2008, 2009). Since chloride binding sites and the selectivity filter are highly conserved for both transporters and channels, the anion selectivity from  $\text{Cl}^- > \text{Br}^- > \text{NO}_3^- > \text{F}^- > \text{I}^-$  arises for almost all CIC proteins. For CIC transporters the  $\alpha$ C-D loop containing a serine, which is orientated directly into the pore, is meant to establish a kinetic barrier for chloride ions, essential for transporter function (Park et al., 2017). A displacement of this  $\alpha$ C-D loop out of the pore towards the cytosol, which is characteristic for CIC channels, seems to enlarge the pore radius to let chloride ions flow freely through the pore.

One further structural difference between CIC-K channels, transporters but also other CIC channels is, that CIC-K channels possess a valine or leucine instead of the 'gating glutamate' (Fig.4B). Despite the absence of the 'gating glutamate', CIC-K channels still exhibit fast gating (Fischer et al., 2010), which demonstrates that fast gating has not been fully understood, yet. The loss of the 'gating glutamate' could possibly be an evolutionary adaptation to the  $\beta$ -subunit barttin, causing channel opening not only to be voltage dependent, but also barttin dependent.

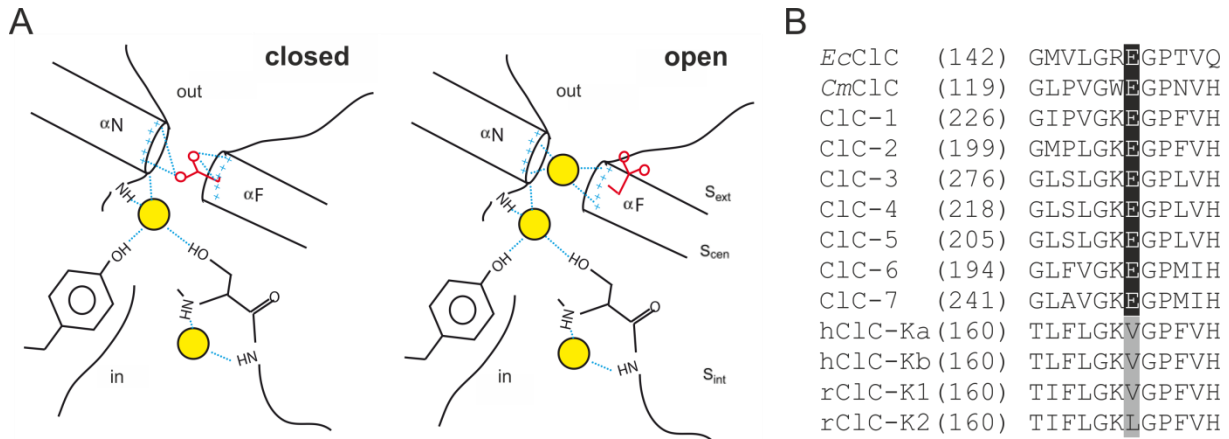


**Fig. 4 Model of the open and closed pore conformation of *EcClC***

(A) In the closed state, the chloride-binding sites  $S_{int}$  and  $S_{cen}$  are occupied by chloride ions, while  $S_{ext}$  is occupied by the side chain of a conserved glutamate. In the open conformation, the glutamate swings out of  $S_{ext}$  into the extracellular space, so that another chloride ion can take its place. Chloride ions are shown in yellow and the glutamate side chain in red. Hydrogen bonds and charges are shown in blue. This figure was modified from Dutzler et al. (2003). (B) Amino acid alignments of different ClC-proteins. Gating glutamate (E) is conserved in almost all ClC-proteins (black). In ClC-K channels this glutamate is replaced by valine (V) or leucine (L) (grey).

Structurally less well characterized is the second gate of ClC proteins (Miller et al., 1982; Saviane et al., 1999). Like the ‘fast gate’, this gate is voltage dependent, but acts much slower. This is the reason why it is called ‘slow gate’. In addition, it regulates both protopores commonly and, thus, also carries the name ‘common gate’ (Fischer et al., 2010). The C-termini of the homodimer together with the CBS domains might be involved in slow gating, since it was shown that the C-termini conduct movements according to slow current kinetics (Bykova et al., 2006). For the ion permeability of ClC pores, it is essential that both the fast and the slow gates are open because both gates are meant to be connected in series. Thus, the product of fast (protopore) gate ( $P_p$ ) and slow (common) gate open probability ( $P_c$ ) equals the total channel open probability ( $P_{total}$ ).

$$P_{total} = P_p \cdot P_c \quad (\text{equation 1})$$

Already in 1982 single channel recordings of the ClC-0 channel from *Torpedo electroplax* exhibited three different but equidistant conductance levels with one closed state and two open states indicating a double-barreled channel (Miller et al., 1982). If the channel was active, the probability of taking in one of the three conductance levels was binomially distributed and dwell times in one state were around several milliseconds. This gating was attributed to the action of the fast gate, which performed individually per each of both pores (Fig.5A, yellow gates). Besides channel activity, there were phases, in which both pores were closed for several seconds. This was interpreted as closure of slow gate, which commonly closes both pores (Fig.5A blue gate). A representative single channel measurement of rClC-K1 demonstrating gating of both fast and slow gates is shown in figure 5B.

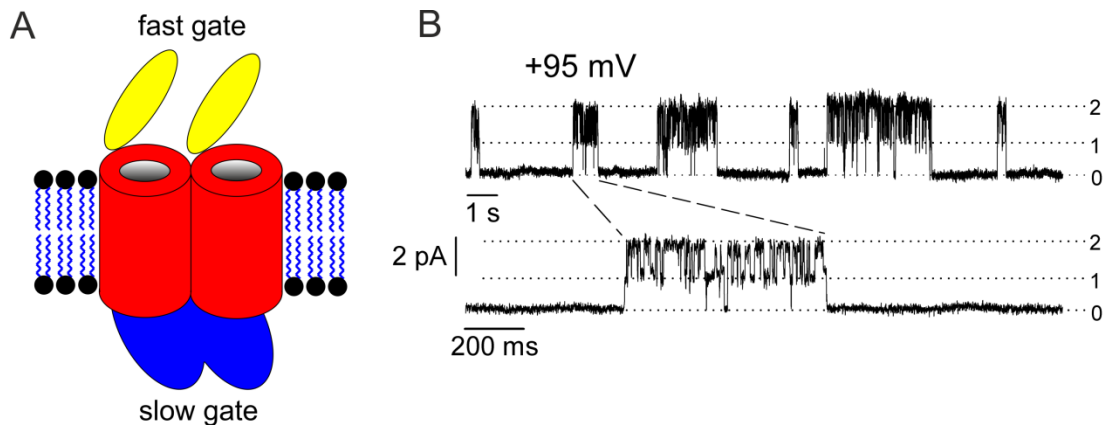


**Fig. 5 Model of a double-barreled ClC channel with a rClC-K1 single channel measurement demonstrating fast and slow gating**  
**(A)** A ClC channel consists of two protopores that can pass chloride ions. The protopores are regulated by two independent gates. One gate is the slow gate (blue), which opens and closes slowly, and the other is the fast gate (yellow), which opens and closes quickly. The slow gate regulates both protopores together, while each protopore has a fast gate. Only when both gates are open chloride ions can pass through the channel. **(B)** Two different conductivities in the open state of a mutant (V166E) rClC-K1 channel illustrate the existence of two pores. Lower current trace represents an enlarged section of the upper current trace. Periods, in which both pores are closed, are assigned to a closed slow gate. In the period, which is marked by dashed lines in the enlarged section of the lower trace, the slow gate is meant to be open, while conducting states switch rapidly due to the action of the fast gate. Measurement in (B) is taken from Fischer et al. (2010).

### 1.5 Molecules that influence the properties and functions of ClC proteins

In addition to the two pore-forming  $\alpha$ -subunits of ClC channels, other ligands, adapter molecules and subunits are known to contribute to the functionality and to the intracellular transport of ClC proteins.

Function of ClC proteins is known to be influenced by ion availability. For example, the extra- and intracellular  $\text{Cl}^-$  ion concentration can influence the gating of ClC proteins (Niemeyer et al., 2003; Pusch et al., 1995, 1999). In addition, ClC-K channels are influenced by extracellular  $\text{Ca}^{2+}$  concentration and pH (Gradogna et al., 2010, 2012; Waldegger & Jentsch, 2000). High  $\text{Ca}^{2+}$  concentration and pH cause an opening of ClC-K channels. Two amino acids in the loop between the I- and J-helices are identified as binding sites for  $\text{Ca}^{2+}$  ions. One histidine at the beginning of the Q-helix seems to be involved in sensing of  $\text{H}^+$  ions, which induces channel closing.

Furthermore, function of ClC proteins can be modified by temporary interaction with other cellular proteins or by posttranslational modifications. Transport sequences of the ClC channel like dileucine or tyrosine-based motifs are recognized by adapter molecules such as AP1-4, GGA (Golgi-localized,  $\gamma$ -ear containing, Arf-binding protein) or GOPC (Golgi-associated PDZ and coiled-coil motif-containing protein), which in turn recruit additional molecules such as clathrin or influence further transport of the ClC proteins (Bonifacino, 2004; Bonifacino & Traub, 2003; Braulke & Bonifacino, 2009; Gentzsch et al., 2003). ClC-3 activity can be enhanced



by phosphorylation and direct interaction with the Ca<sup>2+</sup>/calmodulin-dependent protein kinase II (CaMKII), critically involved in movement of malignant glioma cells (Cuddapah & Sontheimer, 2010). On the contrary, it was found recently that hClC-Ka channels can be inhibited by activation of protein kinase C (PKC) (Gerbino et al., 2020).

Besides molecules and proteins modulating ClC proteins but not being necessary for general function there are three  $\beta$ -subunits identified, whose permanent interaction with the  $\alpha$ -subunit is essential for basic function of several ClC proteins. Firstly, for ClC-2 the IgG-like cell adhesion molecule GlialCAM has been reported as an additional subunit, which interacts with ClC-2 to localize the channel complex at cell-cell contacts in neurons and to modify ClC-2 gating behavior (Jeworutzki et al., 2012, 2014). Also the protein MLC1 seems to be involved in ClC-2 modulation at least indirectly through GlialCAM interaction (Hoegg-Beiler et al., 2014). Secondly, the protein Ostm1 exists as further  $\beta$ -subunit for the ClC-7 transporter, which influences trafficking and transporter function by increasing protein stability (Lange et al., 2006; Zhang et al., 2020). Thirdly, the  $\beta$ -subunit barttin exists for ClC-K channels and potentially also for ClC-5 (Birkenhäger et al., 2001; Estévez et al., 2001; Wojciechowski et al., 2018a). Over several years heterologous expression of almost all ClC-K channels without barttin did not lead to measurable currents. Only by co-expression of barttin, an essential ClC-K activator, these channels become conductive (Estévez et al., 2001).

### **1.6 The ClC-K $\beta$ -subunit barttin**

Barttin comprises 320 amino acids with a short, eight amino acids long, intracellular N-terminus, two transmembrane helices and a 260 amino acids long, intracellularly located C-terminus (Fig.6). Since until now a crystal structure of barttin could not be established, the described topology model of barttin is based on hydrophobicity studies (Birkenhäger et al., 2001). With respect to ClC-K channels barttin influences their stability and intracellular transport to plasma membrane (Janssen et al., 2009; Scholl et al., 2006; Waldegger et al., 2002). Furthermore, barttin influences gating behavior of ClC-K channels by opening the slow gate (Fischer et al., 2010). In the absence of barttin, ClC-K channels are not conductive. The exception is rClC-K1, which conducts chloride ions even without barttin. Recently, even for the human ClC-5 antiporter it was demonstrated that barttin modulates subcellular localization and posttranslational modification (Wojciechowski et al., 2018a).

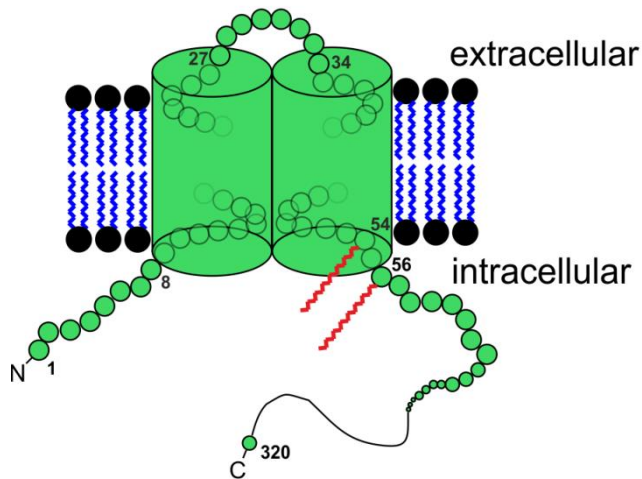


**Fig. 6 Topology model of the  $\beta$ -subunit barttin**

The hypothetical secondary structure of barttin possesses two transmembrane helices, a short N-terminus of eight amino acids and a long C-terminus. Both N- and C-termini are located intracellularly. Cysteines 54 and 56 are linked to palmitoyl groups (red). Model was created after studies of barttin's hydrophobicity (Birkenhäger et al., 2001).

Several studies were performed to identify molecular determinants within the barttin molecule, which are important for the functional interaction with the  $\alpha$ -subunit. It was shown that a barttin truncation at the glutamate at position 88 is still sufficient to promote hCIC-Kb to the plasma membrane and to functionally activate the channel (Janssen et al., 2009). Even truncated barttin at position 72 is able to activate hCIC-Kb and rCIC-K1 (Scholl et al., 2006). Further truncation below position 61 reduces current amplitudes of hCIC-Kb and below position 32 even abolishes transport and insertion of hCIC-Kb into the surface membrane. This indicates that trafficking and function of CIC-K channels are mediated by separate sections within the barttin molecule. The transmembrane core of barttin is sufficient for the transport to the plasma membrane whereas an additional short sequence of 15-17 amino acids from the C-terminus is necessary to functionally activate the channel. Replacement of single amino acids by tryptophan within the transmembrane core revealed that the transport function of barttin was rather less affected by the mutations (Wojciechowski et al., 2015). Instead, mutations severely impaired CIC-K gating, especially when mutations were inserted within a cluster of hydrophobic residues in transmembrane domain 1. Presuming the first transmembrane domain as major responsible for a tight interaction between barttin and CIC-K channels, a reduced binding of barttin to the  $\alpha$ -subunit seems to be sufficient for proper intracellular transport of the whole channel complex whereas functional channel modification is only conveyed through a tight interaction. Besides the transmembrane core and parts of the C-terminus, it was also demonstrated that the integrity of barttin's N-terminus is essential for trafficking and functional CIC-K activation (Wojciechowski, et al., 2018b). While complete deletion of the N-terminus as well as deletion of the N-terminus together with the first transmembrane domain abolish surface membrane transport and conductivity of hCIC-

Ka/barttin complexes, partial deletions, point mutations or amino acid replacements by alanines lead to decreased current amplitudes caused by a reduced number of conductive channels in the plasma membrane. Due to the close proximity to the first transmembrane domain it can be assumed that barttin's N-terminus is critically involved in the interaction between barttin and ClC-K channels. The importance of barttin's N-terminus under physiological conditions is even more emphasized by the two missense mutations R8L and R8W that have been reported to cause Bartter syndrome (Birkenhäger et al., 2001). Proper modulation of ClC-K channels by barttin is not exclusively guaranteed by barttin's amino acid sequence but also by post-translational modifications. Barttin's cysteines at positions 54 and 56 have been identified as target sites for the covalent linkage with palmitate (Steinke et al., 2015). DHHC7, a palmitoyl acyltransferase, was found to conduct the linkage of palmitate to the thiol side chains of those cysteines (Gorinski et al., 2020). The naturally occurring barttin mutations R8W, R8L and G47R, which are known to cause Bartter syndrome (Birkenhäger et al., 2001; Miyamura et al., 2003), have been reported to lead to a reduced barttin palmitoylation compared to WT barttin, highlighting the physiological importance of this post-translational modification. Preventing barttin palmitoylation by replacing both cysteines with serines or by knockdown of DHHC7 using shRNA caused a complete abolishment or a remarkable reduction of hClC-Ka and hClC-Kb currents, respectively. Whereas non-palmitoylated barttin supports the expression of ClC-K/barttin channels and its transport to the surface membrane in a similar manner compared to palmitoylated barttin, current reduction in ClC-K channels expressing non-palmitoylated barttin is exclusively explained by the disability of non-palmitoylated barttin to transfer ClC-K channels into an active state (Gorinski et al., 2020; Steinke et al., 2015). Potentially, palmitoyl groups facilitate the correct orientation and binding of barttin towards the ClC-K channel by hydrophobic interaction with other plasma membrane lipids. Moreover, palmitoylation might cause a change in the lipid membrane environment of the protein complex, which in turn influences channel function. For the  $\alpha$ -subunit only little is known about the binding interface to barttin and about the involved channel domains. In one study it was postulated that the individual B and the J helices of rClC-K2 are sufficient to bind to barttin, which was proved by co-immunoprecipitation and by immunofluorescence microscopy (Tajima et al., 2007). The presence of several leucines and other hydrophobic side chains in both helices of the  $\alpha$ -subunit in combination with many hydrophobic amino acids in barttin's first transmembrane helix imply that barttin and ClC-K  $\alpha$ -

subunits may interact by leucine zipper motifs (Wojciechowski et al., 2015). Both helices are located at the outer lateral surface of the ClC-K channel and within the lipid bilayer of the membrane (visualized in Fig.3B,C). As ClC-K channels form an internal antiparallel structure with B and J helices situating at opposite sides of the channel, this might suggest that two barttin molecules can bind to one  $\alpha$ -subunit. However, up to now structural and functional stoichiometry between barttin and ClC-K channels is a matter of speculation.

### **1.7 Aim of this study**

During this study it should be clarified how a different  $\alpha$ : $\beta$ -stoichiometry has an impact on already known functions of ClC-K channels, for example if one or two barttins are available per  $\alpha$ -subunit of one channel or if one barttin is available per channel homodimer. Hereby the focus is on the investigation of the conditions that define the correct plasma membrane trafficking of the whole channel complex and how the proper gating is coordinated. Additionally, it should be addressed how the gating of the fast and slow gate is modified by different barttin availabilities. All these questions could be unraveled by defined stoichiometries between  $\alpha$ - and  $\beta$ -subunits. Simple co-expression of both subunits would be not sufficient to answer these questions because real stoichiometry between both subunits could not be controlled precisely by this approach. Instead, the functional stoichiometry of both subunits was investigated in this study by generation of concatamers with defined composition of covalently linked  $\alpha$ - and  $\beta$ -subunits. We tested the conditions in which one or two  $\beta$ -subunits were available per one  $\alpha$ -subunit. Furthermore, concatamers which harbored one  $\beta$ -subunit per two covalently linked  $\alpha$ -subunits were characterized. All concatamers were tested with and without additional barttin overexpression to obtain the condition at which channel should be fully occupied by barttin. Two orthologous ClC-K channels were used for this study – the human hClC-Ka and the rodent rClC-K1 channel.

Indeed, we found a modification of channel function in dependence of the  $\alpha$ : $\beta$ -subunit stoichiometry. However, the fully activated and functional channel is most likely comprised of a 1:2  $\alpha$ : $\beta$ -subunit stoichiometry. Other compositions might be relevant for correct trafficking and gating regulation.

Based on this knowledge we used this tool in another approach to investigate effects on trafficking and functional channel modulation evoked by potential disease causing alterations within barttin such as palmitoylation deficiency. The purpose was to get more insights into the

regulation of the fast and slow gate by barttin palmitoylation. A palmitoylation deficiency was achieved by exchange of cysteines by serines at two positions as described above. It became apparent that barttin palmitoylation is not necessary for channel trafficking but for distinct gating processes of ClC-K channels.

## 2 Material and Methods

### 2.1 Material

Chemicals and other material were obtained from Agilent (Waldbronn), BD (Heidelberg), Bio-Rad (Munich), Colgate-Palmolive (Hamburg), GE Healthcare (Solingen), Gibco (Eggenstein), Goodfellow (Bad Nauheim), Greiner Bio-One (Frickenhausen), Harvard Apparatus (March-Hugstetten), Ibidi GmbH (Martinsried), Invitrogen (Karlsruhe), Kisker (Steinfurt), Life Technologies (Darmstadt), Lonza (Cologne), Machery-Nagel (Düren), Merck (Darmstadt), Millipore (Eschborn), Qiagen (Hilden), Roche (Mannheim), Roth (Karlsruhe), Santa Cruz (Heidelberg), Sarstedt (Nümbrecht), Schott Glaswerke (Mainz), Serva (Heidelberg), Sigma-Aldrich (Munich), Thermo Fisher Scientific (Bremen), Thomas Oertel Dental (Calden).

Following devices were used during this study: Axon 200B amplifier (Molecular Devices Corporation, Biberach an der Riss), micromanipulator (Luigs & Neumann, Ratingen), vibration damped table (TMC, Meerbusch), Puller P-97 (Sutter Instrument, Novato), Microforge MF-830 (Narishige, Japan), Victor<sup>3</sup> Plate reader 1420 Multilabel Counter (Perkin Elmer, Rodgau), table centrifuges (Eppendorf, Hamburg; Thermo Fisher Scientific), Heraeus cooled centrifuge (Thermo Fisher Scientific), Coulter Avanti J-25 (Beckman Coulter, Krefeld), Nanodrop photometer (Thermo Fisher Scientific), Gel-Doc (Bio-Rad), Fusion SL/FX Spectra (Vilber Lourmat, Eberhardzell), thermocycler (Eppendorf; Biometra, Göttingen), thermoblock (Eppendorf), Enviro-Genie incubator (Scientific Industries Inc., Bohemia, U.S.), confocal laser scanning microscope Zeiss 780 (Zeiss, Oberkochen), Cytation 5 imaging reader (BioTek, Bad Friedrichshall), inverted light microscope (Leica, Wetzlar), pH-meter (WTW, Weilheim; Knick, Berlin), Mini-Protean<sup>®</sup> SDS-PAGE electrophoresis chamber and power supply (Bio-Rad), Shaker Multitron Eco (Infors HT, Einsbach).

## 2.2 Methods

### 2.2.1 Molecular biology

#### *2.2.1.1 Molecular biological vectors*

To express a desired protein within a mammalian cell system, molecular biological vectors constituted as plasmids, which encode the DNA sequence of this protein, were introduced into the cells. In this study two types of expression vectors were used:

*pSVL*: This vector was used to express  $\alpha$ -subunits of CIC-K channels/concatamers. Since CIC-K channels were formerly known to generate enormous current amplitudes when patch clamp experiments in HEK293T cells were performed in whole cell mode, the pSVL vector was chosen due to its rather low expression efficiency. For protein expression in eukaryotic cells it carries the SV40 (Simian virus 40) promoter and an ampicillin resistance gene for prokaryotic selection.

*pcDNA3.1(+/-)*: This vector was used to express the  $\beta$ -subunit barttin. It harbors the CMV promoter for protein expression in eukaryotic cells and reaches higher expression levels than the pSVL vector. Thus, it was ensured that barttin was always expressed in excess compared to  $\alpha$ -subunits of the CIC-K channel, which were expressed by the co-transfected pSVL vector. Furthermore,  $\alpha$ -subunits of the CIC-K channel itself were also expressed by pcDNA3.1, when MDCKII cells served as eukaryotic expression system that have a lower expression efficiency compared to HEK293T cells. In this case the amount of transfected barttin-coding plasmid was doubled to ensure a barttin excess. The multiple cloning site of pcDNA3.1 can be oriented in forward (+) or reverse (-) direction; both constructs have been used in this study. For prokaryotic DNA amplification of these constructs, ampicillin was used for selection.

#### *2.2.1.2 Cloning strategies*

In this study concatenated channel proteins were constructed, which were composed of different numbers of  $\alpha$ - and  $\beta$ -subunits as well as fluorophores. Within these concatamers  $\beta$ -subunits were always located N-terminally, the  $\alpha$ -subunits in the middle of the protein and the fluorophore tag YFP or CFP tag C-terminally. N-terminal localization of  $\beta$ -subunits was essential for barttin because it has been shown that integrity of barttin's N-terminus has a major influence on expression, subcellular localization and function on barttin itself but also on CIC-K channels (Wojciechowski et al., 2018b). Two identical subunits within a concatamer

were located directly one after the other. Two  $\beta$ -subunits were connected by a linker sequence built of twelve amino acids (RDPPVSIPRAAA),  $\beta$ - to  $\alpha$ -subunits by a linker of 14 amino acids (WDVCAPSRWSGAAA) and  $\alpha$ -subunits to YFP by 14 amino acids (LKGSGSGSGGPVAT), too. Two  $\alpha$ -subunits were linked by 22 amino acids (LKLKHPGLYPYDVPDYAISLK). The  $\beta$ -subunit was connected to CFP by seven amino acids (RDPPVAT), when barttin was separately co-expressed. Throughout this study the human variant of barttin was always used. It was expressed within concatamers or in co-expression with rCIC-K1 or with hCIC-Ka.

The cDNA of  $\alpha$ - and  $\beta$ -subunits within the above mentioned expression vectors has been already available in the institute for further use. The above mentioned linkers between subunits and fluorophores have been proved for functionality in terms of other concatamers (Fahlke et al., 1997; Liman et al., 1992; Stölting et al., 2014). However, concatamers with different stoichiometry of  $\alpha$ - and  $\beta$ -subunits were new constructs that have to be built during this study. This was done exclusively by subcloning the cDNA fragments of the appropriate  $\alpha$ -/ $\beta$ -subunit in an existing expression vector. Accordingly, cDNA fragments were extended by linker sequences or restriction sites using polymerase chain reaction (PCR). Another part of this thesis was the analysis of CIC-K concatamers with barttin molecules, which lack palmitoylation of cysteines at positions 54 and 56. For this, both cysteines were replaced by serines using site directed mutagenesis PCR. Cloning procedure of all constructs was done with great support of Birgit Begemann and Toni Becher.

#### *2.2.1.3 Polymerase chain reaction (PCR)*

For the amplification of DNA sequences, sense and antisense primers were designed, which bind to the flanking nucleotides of the cDNA sequence (see online tool: [www.eurofinsgenomics.eu](http://www.eurofinsgenomics.eu)). Primers were ordered (Sigma-Aldrich) and diluted to a concentration of 100  $\mu$ M in Tris-EDTA (TE)-buffer (Qiagen) for storage. Using the High Fidelity PCR Kit (Roche) PCR reaction mix was constituted as indicated in table 1. Amplification of DNA fragments was done by a thermocycler (Biometra/Eppendorf) upon application of different temperatures for several cycles: Initially, template DNA was denatured at 94°C, following annealing of primers to the target sequence at 45-65°C and a final step at 68°C where the polymerase optimally elongated primers at their 3'-tail according to the template sequence. The temperature of annealing usually depends on the length and G/C-content of primers,



while the duration of elongation depends on the product length (1 min/1.5 kilobases (kb)). Table 2 summarizes the program for DNA amplification.

**Table 1:** Composition of PCR reaction mix

PCR reaction	Volume ( $\mu$ l)
High Fidelity Premix	25
Template DNA (100 ng)	1
Primer sense (300 nM)	1
Primer antisense (300 nM)	1
H <sub>2</sub> O	ad. 50

**Table 2:** PCR program for DNA amplification

PCR program	Temperature	Duration	Cycles
1 denaturation	94°C	2 min	1
2 denaturation	94°C	10 sec	
3 annealing	45-65°C	1 min 10 sec	10
4 elongation	68°C	1 min/1.5 kb	
5 denaturation	94°C	15 sec	
6 annealing	45-65°C	30 sec	20
7 elongation	68°C	1 min/1.5 kb + 5 sec per cycle	
8 final elongation	68°C	7 min	1
9 end	10°C	$\infty$	1

#### 2.2.1.4 Exchange of single amino acids using QuikChange® site directed mutagenesis kit

To introduce point mutations into vectors sense and antisense primers were designed that both bind exactly to the region, where the mutation should be inserted. Within the center of the primer the related nucleotides contained the mutation, which was to be introduced into the vector. As the overhanging nucleotides exactly matched to the template, primer binding was still ensured. Here the QuikChange® Primer Design Tool from Agilent was used (<https://www.agilent.com/store/primerDesignProgram.jsp>). PCR reaction was established as shown in table 3 and performed as recommended by the manufacturer (Agilent Technologies) shown in table 4.

**Table 3:** Compounds for QuikChange® PCR reaction mix

QuikChange® PCR reaction	Volume ( $\mu$ l)
Template DNA (50 ng/ $\mu$ l)	1
Primer sense (125 ng/ $\mu$ l)	1
Primer antisense (125 ng/ $\mu$ l)	1
10x reaction buffer	5
dNTP mix	1
Pfu Turbo polymerase	1
H <sub>2</sub> O	ad. 50

**Table 4:** PCR program for QuikChange® PCR

PCR program	Temperature	Duration	Cycles
1 denaturation	95°C	1 min	1
2 denaturation	95°C	1 min	
3 annealing	55°C	1 min	18
4 elongation	68°C	1 min/1.5 kb	
5 final elongation	68°C	10 min	1
6 end	10°C	∞	1

In this study cysteines of barttin at positions 54 and 56 were replaced by serines. The sense and antisense Quikchange® primers used for this mutagenesis are shown in table 5.

**Table 5:** Quikchange® primers for site directed mutagenesis of barttin

Mutation	s/as	Primer sequence (5'-3')
Barttin C54S C56S	s	CGGGGGCATCATCTGGAGCATGAGCCAGAGCTACCCCAAGATCACCTTCG
	as	CGAAGGTGATCTTGGGGTAGCTCTGGCTCATGCTCCAGATGATGCCCCCG

As a product of the Quikchange® reaction the whole vector was amplified harboring both mutations. However, the original vector without mutations remained within the reaction mix, which might lead to transformation of unchanged vectors in downstream steps. To remove this contamination, the reaction mix was incubated for 30 min at 37°C with 1 µl *DpnI* restriction enzyme (Thermo Fisher Scientific). The characteristic of this enzyme is to cut only methylated DNA, which is the case for vector DNA produced by bacteria but not for DNA generated by PCR reactions. The PCR product was controlled for correct size by agarose gel electrophoresis and subsequently transformed into competent bacteria. Reconstituted vectors were checked for correct mutagenesis by Sanger sequencing, and the DNA segment with introduced mutation was subcloned into the original vector.

#### 2.2.1.5 Transformation of vectors into competent bacteria

40 µl of competent *Escherichia coli* bacteria (strain DH5-α) were thawed on ice and 10-50 ng of vector cDNA was added. Bacteria suspension was incubated for 20 min on ice following a heat shock of 42°C for 1 min. The heat shock may enhance transformation efficiency by induction of little fissures within the bacterial membrane, though which plasmids may be taken up more easily. Subsequently, SOC-medium (2% bacto-tryptone, 0.5% bacto yeast extract, 10 mM NaCl, 2.5 mM KCl, 20 mM MgCl<sub>2</sub>, 20 mM glucose, pH 7.0, sterile filtered) was added and cells were shaken for 45 min at 37°C. Then, cells were centrifuged for 30 sec at

3500 x g and the supernatant was discarded. After resuspending the cell pelett within the remaining liquid, bacteria were plated on LB-agar plates (5 g/l Bacto-yeast extract, 10 g/l Bacto-tryptone, 20 g/L Bacto-Agar) including the selection antibiotic ampicillin (100 µg/ml). Only bacteria transformed with vectors and thus containing the resistance gene against ampicillin were able to grow on these plates and form colonies. Plates were incubated for around 16 hours at 37°C. Afterwards colonies were isolated and transferred to LB-medium with ampicillin for further growing. Amplified DNA constructs were extracted by NucleoSpin plasmid Mini kits for plasmid DNA or by NucleoBond Xtra Midi kits (Machery-Nagel) as recommended by the manufacturer. The final DNA concentration was determined using a NanoDrop™ photometer (Thermo Fisher Scientific).

#### *2.2.1.6 Enzymatic digestion of DNA and subcloning of DNA fragments into vector DNA*

DNA had to be restricted by enzymes, when recovered plasmids were checked for correct size or when DNA fragments were subcloned into a vector. For simple control restriction around 1 µg DNA was used. For subcloning 7 µg of insert DNA and 1 µg of vector DNA were adopted. Together with 10x Fast digest buffer and appropriate Fast digest enzymes (0.5 µl per 1 µl DNA, all from Thermo Fisher Scientific) DNAs were individually restricted at 37°C for 45 min. Subsequently, vector DNA was dephosphorylated by alkaline phosphatase (Thermo Fisher Scientific) at 37°C to avoid vector re-ligation in further steps. Reaction was stopped by stepping to 75°C for 5 min. Restricted DNA was separated using agarose gel electrophoresis and desired bands were isolated and cleaned up by Machery-Nagel NucleoSpin Gel and PCR Clean-up Kit. After determination of DNA concentration insert and vector were ligated in a molar ratio of 3:1. Using 10x ligase buffer and 1 µl T4 ligase (Thermo Fisher Scientific) ligation was carried out at 22°C for 1 hour. The reaction was stopped by heating up to 65°C for 10 min. Ligated plasmids were transformed into competent bacteria, amplified and recovered as described above.

#### *2.2.1.7 Agarose gel electrophoresis*

Agarose was dissolved in 1x TAE buffer (400 mM Tris-Base, 200 mM acetic acid, 10 mM EDTA) to a 1% concentration by heating and supplied with 0.01% SYBR Safe (Thermo Fisher Scientific), which stains DNA by intercalation. Gel was casted and cooled down for about 20 min in darkness. The cured gel was run in 1x TAE buffer for 30 min at 125 V. As size marker

the GeneRuler 1 kb plus DNA ladder (Thermo Fisher Scientific) was used. The stained DNA bands were visualized by UV-light using a Gel-Doc imaging system (Bio-Rad).

#### *2.2.1.8 Sanger sequencing*

Sequencing of DNA was performed by Eurofins Genomics (Ebersberg). Before sequencing the DNA was diluted with TE-buffer to a concentration of 50-100 ng/ $\mu$ l.

#### 2.2.2 Cell culture and transfection

HEK293T and MDCKII cells were used for this study. They were cultivated in the DMEM (Dulbecco's modified eagle medium) cell culture medium (Ref.: 41965-047, Gibco). It was supplemented with 10% fetal bovine serum, 2 mM L-glutamine, penicillin (50 U/ml) and streptomycin (50  $\mu$ g/ml). Transfection of HEK293T cells was performed using calcium phosphate precipitation method. For expression analysis and patch clamp measurements 4  $\mu$ g of pSVL-plasmids encoding  $\alpha$ -subunit monomers or concatamers were mixed with 10  $\mu$ l UltraPure™ salmon sperm DNA solution (Thermo Fisher Scientific, 1:10 dilution in TE-buffer). To co-express  $\beta$ -subunits in excess 1  $\mu$ g barttin-coding pcDNA3.1 cDNA was added.

For biotinylation assays 2  $\mu$ g barttin-coding and 4  $\mu$ g channel-coding plasmids were used. Here, pcDNA3.1 vectors were used for expression of both protein components. Barttin excess was ensured as barttin\_mCFP fluorescence after expression time was still far more intense than the YFP fluorescence of the  $\alpha$ -subunits under both transfection ratios. This was tested by fluorescence microscopy of living cells and by fluorescence measurements of cell lysates after SDS-PAGEs. As the molecular weight of  $\beta$ -subunits is lower than of  $\alpha$ -subunits, barttin molecules might have been synthesized faster than  $\alpha$ -subunits.

For transfection the DNA mix was mixed with 500  $\mu$ l 0.25 molar  $\text{CaCl}_2$  solution and then added dropwise in 500  $\mu$ l 2x HEBS buffer (274 mM NaCl, 40 mM HEPES, 12 mM D-glucose, 10 mM KCl, 1.4 mM  $\text{Na}_2\text{HPO}_4$ , pH 7.05). After further mixing of  $\text{CaCl}_2$  and DNA/HEBS solution an incubation period of 20 minutes followed. During this time calcium phosphate built crystals which bound the DNA. After incubation, the transfection solution including the calcium phosphate crystals was transferred dropwise to the HEK293T cells that were grown up to about 80% confluence in a 10 cm cell culture dish. Calcium phosphate crystals together with the DNA generally precipitate onto the surface of the cells and are incorporated by endocytosis into the cells (Graham & Eb, 1973). After 24 hours at 37°C the transfected cells

were used for electrophysiological investigations and biotinylation assays. For expression analyses transfected cells were incubated for 48 hours at 37°C.

To perform electrophysiological measurements on HEK293T cells, the cells were split to single cell level. For this purpose, the cell culture medium was first removed and the cells were washed with 5 ml PBS (Lonza). Afterwards, 3 ml trypsin-EDTA 0.25% (Gibco) was added to the cells to detach them from the ground. After incubation of about 3-5 minutes at 37°C, the cells were separated by harsh resuspending. The addition of 7 ml DMEM stopped the activity of trypsin-EDTA by the including fetal bovine serum (FBS). In addition, DMEM was used to dilute the cell suspension. 0.3-1.5 ml of this cell suspension was transferred into a 6 cm cell culture dish (BD). The cells were cultivated in 3 ml DMEM for at least 3 hours at 37°C before starting electrophysiological measurements. After this time the cells had attached tightly to the bottom of the cell culture dish.

MDCKII cells were used for confocal microscopy and biotinylation assay. They were cultivated at 37°C in 10 cm cell culture dishes up to a confluence of 80%. When cells were used for confocal imaging, they were detached from the ground with 3 ml trypsin-EDTA and split in the same way mentioned above (HEK293T cells). After addition of 7 ml DMEM, 0.3 ml of the cell suspension was transferred to a 35 mm cell culture  $\mu$ -Dish (Ibidi GmbH) and subsequently incubated with 2 ml DMEM for 24 hours at 37°C. The bottom of this cell culture dish is made of a synthetic polymer, which is suitable for confocal microscopy with water immersion lenses due to its refractive index. On the next day, the MDCKII cells were transfected using Lipofectamin 2000<sup>®</sup> (Invitrogen). The transfection was performed according to the manufacturer's specifications. The cell culture dishes were 70% to 90% confluent. 1  $\mu$ g barttin-encoding plasmid and 2  $\mu$ g channel-encoding plasmids were used for subsequent confocal microscopy. For biotinylation assay, 80% confluent cells were transfected with 2  $\mu$ g barttin-encoding plasmids and 4  $\mu$ g channel-encoding plasmids in a 10 cm dish. The plasmids were diluted in OptiMEM (Gibco) with a dilution factor of 1:25 up to 1:100. Lipofectamine 2000<sup>®</sup> was also pipetted into OptiMEM with a dilution factor of 1:50. Both solutions were mixed and, after an incubation time of 5 minutes at room temperature, transferred to MDCKII cells together with 1 ml DMEM (in Ibidi dish) or 3 ml (in 10 cm dish). While liposomes can only introduce DNA into cells within 6 hours, the medium was removed after this time and replaced by 2 ml (Ibidi) or 10 ml (10 cm dish) DMEM. Following 24-48 hours of incubation at 37°C the cells were subjected to further experiments.

### 2.2.3 Freezing and thawing of cells

HEK293T and MDCKII cells can be typically stored for a long time at -150°C. To prepare appropriate storing conditions, cells that have been grown nearly confluent in a 10 cm dish were washed with PBS in a first step. Subsequently, cells were detached from the ground by incubation with 3 ml trypsin-EDTA at 37°C. Enzymatic reaction was stopped by applying 10 ml standard DMEM medium following thorough resuspension. Cells in suspension were centrifuged for 3 min at 193 x g and the supernatant was discarded. 3 ml 'Freeze 1' medium (40% FBS, 60% DMEM without FBS/penicillin/streptomycin, sterile filtered) was added and the cell pellet was resuspended. The suspension was briefly mixed with 3 ml 'Freeze 2' medium (40% FBS, 40% DMEM without FBS/penicillin/streptomycin, 20% DMSO (dimethylsulfoxid), sterile filtered) and filled into reaction tubes in aliquots of 1 ml. Aliquots cooled down at -80°C for at least 6 hours in a Nunc-box filled with isopropanol. Afterwards, cells were stored at -150°C. On the following days one aliquot was thawed to prove cell vitality. Thawing was carried out fast at room temperature, possibly under running water. DMSO was removed by centrifuging the cells for 5 min at 86 x g. After resuspension in standard DMEM medium cells were transferred to a new 10 cm culture dish.

### 2.2.4 Protein biochemical methods

#### *2.2.4.1 Determination of protein expression*

Transiently transfected HEK293T and MDCKII cells were lysed for analyses of protein expression of ClC-K/barttin concatamers.

The cells were washed three times with 3 ml PBS (Lonza) and lysed with 700-1000 µl lysis buffer. For expression analysis the lysis buffer contained 150 mM NaCl, 10 mM HEPES, 1% Triton X-100 and 1% protease inhibitor (Roche complete). For biotinylation assays radioimmune precipitation assay (RIPA) buffer was applied containing 100 mM NaCl, 20 mM HEPES, 1 mM sodium orthovanadate, 1 mM NaF, 1 mM EDTA, 1% SDS, 1% deoxycholate, 8 U/ml benzonase and 1% protease inhibitor mix. Both buffers were adjusted to a pH of 7.4. By using non-ionic detergents like Triton X-100 only plasma membranes were disrupted. Ionic detergents as SDS and deoxycholate were also able to lyse nuclear membranes. Proteases were inhibited by the protease inhibitor mix. Lysis was performed at 4°C for 30 minutes. Afterwards, cell remnants were removed from the bottom of the culture dish with a cell

scraper (Sarstedt). The lysate was transferred to a 1.5 ml reaction tube (Kisker) and stored on ice. The lysate was mixed mechanically every 5 minutes to break the last intact membrane compartments. A subsequent centrifugation step at 16200 x g at 4°C for 15 minutes separated insoluble cell debris from the soluble cell fraction. The supernatant was transferred to a new 1.5 ml reaction vessel and stored at -20°C.

Sodium dodecyl sulfate polyacrylamide gel electrophoresis (SDS-PAGE) allows separating proteins according to their molecular weight. SDS-PAGE gels with a 10% concentration of acrylamide in the separating gel were casted between two glass plates (Bio-Rad) according to the components of table 6.

10% ammonium persulfate (APS) was generally prepared just before pouring the gel. It is a radical former and crosslinks acrylamide monomers. Tetramethylethylenediamine (TEMED) was added directly before pouring the gel, as it starts the polymerization of acrylamide. The separating gel was casted at first and served for the actual separation of proteins. After polymerization of the separating gel, the stacking gel was poured, which collects the proteins at the upper edge of the separating gel, so that the separation of proteins started from one point.

**Table 6:** Components of a SDS-PAGE gel, featuring a 10% acrylamide concentration in separating gel

10% SDS-PAGE gel	Separating gel (5 ml) 10%	Stacking gel (2,5 ml) 4%
H <sub>2</sub> O (ml)	2	1,525
Separating gel buffer 1,5 M Tris pH 8,8 (ml)	1,25	
Stacking gel buffer 1,5 M Tris pH 6,8 (ml)		0,625
Acrylamide/bis-solution (ml)	1,65	0,325
10% SDS (μl)	50	25
10% APS (μl)	50	12,5
TEMED (μl)	5	2,5

The protein concentration of the previously obtained cell lysates was determined by BCA assay (Roth). The determination was performed according to the information of the manufacturer. For this purpose, we here utilized the property of amino acids (cysteine, tryptophan and tyrosine) that are able to reduce Cu<sup>2+</sup> to Cu<sup>1+</sup> in an alkaline environment. The reduced copper forms a purple complex with two bicinchoninic acid (BCA) molecules, with an absorption maximum at 562 nm wavelength. The absorption is directly proportional to the protein

concentration of the solution, which can be precisely determined using a standard curve from bovine serum albumin (BSA) solutions (Sigma-Aldrich) with known concentrations. All samples of one gel always contained the same amount of total protein (usually 50-100 µg per sample). The samples were treated with 5x Lämmli buffer (250 mM Tris/HCl pH 6.8; 10% SDS; 10% Glycerol; 100 mM DTT; 0.05% bromophenol blue) and incubated for 30 minutes at room temperature. Samples were not heated up to prevent quenching of fluorophores. The Lämmli buffer contained DTT (dithiothreitol), which was used for reduction of the disulfide bonds within proteins. It also contained sodium dodecyl sulfate (SDS), which usually breaks down tertiary structures of proteins and shielded their intrinsic charge. As SDS is itself negatively charged and the bound SDS amount was equal to the length of the peptide chain, the proteins were separated towards the anode according to their molecular weight. The glycerol within the Lämmli buffer has a higher density than water and causes the samples to sink into the pockets. As molecular weight markers 4 µl Spectra™ Multicolor Broad Range Protein Ladder (Thermo Fisher Scientific) or Precision Plus Protein™ Dual Color Standards (Bio-Rad) were used. Before loading the SDS-PAGE gel, the gel was placed in a Mini-PROTEAN® electrophoresis chamber (Bio-Rad). The tank was filled with 1x electrophoresis buffer (25 mM Tris; 192 mM glycine; 3.5 mM SDS) and samples were loaded. For one hour a constant voltage of 180 V was applied.

Since all proteins investigated in this work were fused to fluorescent proteins, the protein expression was determined by the fluorescence intensity of the bands in the SDS-PAGE gel. Using a fluorescence detector (Fusion SL/FX Spetra, Vilber) the mYFP of the CIC-K channels/concatamers was excited by wavelengths of 505-550 nm and the mCFP of barttin with wavelengths of 360-480 nm. The emitted light of mYFP was detected with an emission filter at 565 nm with a bandpass of 30 nm and mCFP with an emission filter at 535 nm with a bandpass of 20 nm. Marker bands were visualized by white light. To quantify the expression levels of the CIC-K channel components the programs ImageJ and Excel (Microsoft, Unterschleissheim) were used. Relative expression was quantified by normalizing the expression of the CIC-K concatamers to the expression quantity of the CIC-K monomers.

#### *2.2.4.2 Western Blot*

For the biotinylation assay it was essential to exclude the contamination of surface membrane fraction by cytosolic proteins. This was done by Western blots detecting GAPDH (glycerol-



aldehyde-3-phosphate dehydrogenase). Since it is a cytosolic housekeeping protein, it should exclusively be present in total cell lysates but not in the surface membrane fraction. For GAPDH detection, the electrophoretically separated proteins were transferred to a nitrocellulose membrane. The transfer of the proteins took place in a tank (Bio-Rad) filled with 1x transfer buffer (25 mM Tris-Base, 192 mM glycine, 10% ethanol, pH 8.3) for one hour with a constant current of 300 mA and at 4°C. During this process the proteins were pulled towards the anode onto the nitrocellulose membrane (GE Healthcare). Nitrocellulose is protein affine. After protein transfer to the nitrocellulose membrane the membrane was incubated for one hour at room temperature with 3% BSA in 1x TBS-T (10 mM Tris, 15 mM NaCl, 0.1% Triton X-100) to block unspecific binding sites for antibodies. Subsequently, the membrane was washed in TBS-T for 5 minutes. The primary antibody 'GAPDH (mouse monoclonal  $\alpha$ -GAPDH) antibody' (Santa Cruz, sc-137179) was diluted 1:2000 in TBS-T with 1% BSA and shaken together with the nitrocellulose membrane overnight at 4°C. By washing the nitrocellulose membrane three times with TBS-T an excess of antibodies was removed. The secondary antibody (goat anti-mouse IgG secondary antibody-HRP, Thermo Fisher Scientific) was diluted 1:20000 in TBS-T with 1% BSA and incubated together with the nitrocellulose membrane for one hour at room temperature. The secondary antibody bound to the heavy chain of the primary antibody. It also possessed the enzyme domain of horseradish peroxidase (HRP). This enzyme converts luminol and H<sub>2</sub>O<sub>2</sub> into light. This chemiluminescence can be detected. After incubation with the secondary antibody, the membrane was washed four times with TBS-T. Afterwards the chemiluminescence reaction was initiated by the ECL Kit Pico Western Signal (Thermo Fisher Scientific). Using a luminescence detector, the luminescent GAPDH bands were displayed.

#### *2.2.4.3 Purification of plasma membrane proteins using biotinylation assay*

To isolate plasma membrane proteins from cytosolic proteins cells expressing the desired proteins were incubated with 0.375 mg EZ-link Sulfo-NHS-SS-biotin (Thermo Fisher Scientific) dissolved in PBS, for 30 min at 4°C. This modified biotin was able to bind covalently to primary amino groups, which are side chain components of several amino acids like arginine, asparagine, glutamine and lysine. Usually, plasma membrane proteins expose at least some of these amino acids to the extracellular space, which offers the possibility to label these proteins. After labelling, the biotin solution was removed and the reaction was stopped by

washing the cells three times with 10 mM glycine, while the last washing step was done for 20 min at 4°C.

Free glycine molecules exhibit primary amino groups, which abreacted with remaining biotin molecules and prevented further protein labelling during the subsequent procedure. Afterwards, cells were washed again twice with PBS and lysed with RIPA buffer. Lysis and consecutive BCA assay were performed as described above to take comparable protein amounts for further steps. Around 1-3 mg protein were loaded on High Capacity NeutrAvidin Agarose (Thermo Fisher Scientific), which had previously been equilibrated with RIPA buffer. Protein lysate and resin were incubated at least two hours at 4°C within a rotary shaker (Enviro-Genie incubator, Scientific Industries Inc.) During this time biotin, linked to plasma membrane proteins, bound strongly to avidin molecules on the resin surface in a non-covalent way. After this period protein/resin mixture was loaded on Pierce™ Centrifuge Columns (Thermo Fisher Scientific) separating the liquid from the solid components. Solid components were washed once with RIPA buffer and additional five times with washing buffer (500 mM NaCl, 5 mM EDTA, 50 mM Tris, 0.1% Triton X-100, pH 7.4) applying short and smooth centrifugation steps. By washing remaining cytosolic proteins, which were not labeled by biotin and thus not bound to the resin, should be completely removed. To check the success of washing, the last washing fraction was always subjected to SDS-PAGE. If no fluorescence signal of heterologously expressed proteins was detectable within the SDS-PAGE gel, surface membrane fraction was meant to be pure. This fraction was eluted from agarose resin by adding 2x concentrated Lämmli buffer for at least 40 min at 4°C. The DTT within the buffer reduces and cleaves the disulfide bond within the EZ-link Sulfo-NHS-SS-biotin leading to a release of surface membrane proteins from the matrix when centrifugation occurred. Together with samples of whole cell lysate fraction the surface membrane fractions were subjected to SDS-PAGE. YFP signals of  $\alpha$ -subunits for surface membrane fraction normalized to the respective signals for the whole cell fraction revealed the relative surface membrane expression of the  $\alpha$ -subunits. In addition, relative surface membrane expression of all tested conditions was normalized to the condition when the ClC-K monomer was co-expressed with barttin. Western blot analysis detecting GAPDH was used to exclude the labelling of cytosolic proteins by biotin. If there was no exposition of cytosolic proteins to biotin, there would be no GAPDH signal within surface membrane fractions. An illustration of biotinylation assay is given in figure 7.

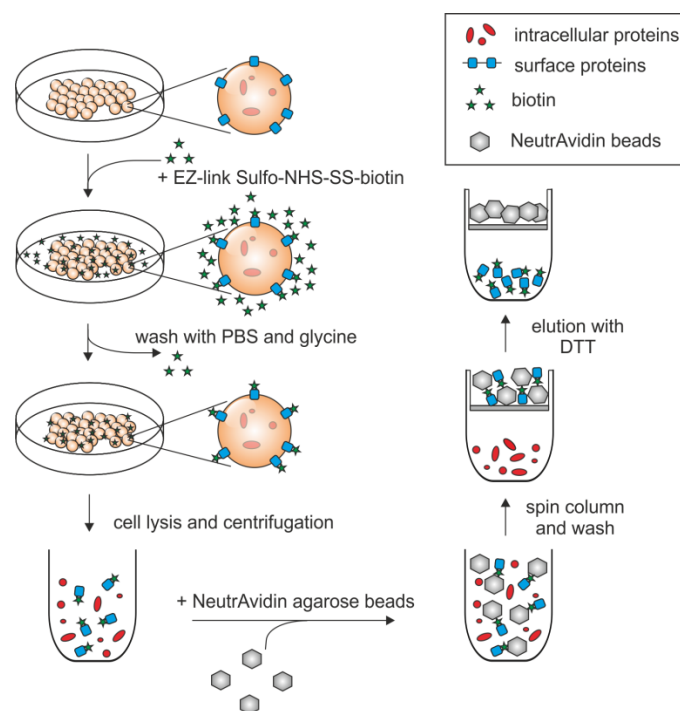


**Fig. 7 Biotinylation assay procedure**

Cell surface proteins were labeled at their primary amino acid side chains, exposed to the extracellular side, by a modified form of biotin. After washing and cell lysis, biotinylated proteins were bound and purified *via* NeutrAvidin agarose resin.

Detailed explanations of workings steps required for biotinylation assay like cell lysis, BCA assay, Western blot and determination of fluorescence intensity are described above.

### 2.2.5 Confocal microscopy

Transfected MDCKII cells were analyzed 48 hours after transfection using a confocal laser scanning microscope Zeiss 780 (Zeiss) at a 40x magnification (objective) regarding the subcellular distribution of CIC-K/barttin concatamers. The mYFP of  $\alpha$ -subunits was excited at a wavelength of 514 nm and the emitted light with a wavelength of 520 to 620 nm was detected. For the  $\beta$ -subunit's mCFP the excitation wavelength was 440 nm and the detection wavelength 454 to 520 nm. Spectral unmixing of YFP- and CFP-fluorescence was performed with support of Dr. Andre Zeug to avoid a crosstalk of YFP fluorescence in the CFP channel and *vice versa*. ZEN 3 software (Zeiss) was used to linearly adjust brightness and contrast in representative images.

### 2.2.6 Fluorescence measurements of cells using the Cytation 5 imaging reader

HEK293T cells were seeded in a 6 well plate (Greiner Bio-One) and cultured one day in 3 ml standard medium. Subsequently, cells were transfected with 0.7  $\mu$ g plasmid DNA, which coded for the tested  $\alpha$ -subunits, using calcium phosphate precipitation method. After additional two

days cells were washed once with 1 ml PBS per well before application of 0.5 ml of trypsin-EDTA 0.25%, which detached the adherent cells within a few minutes at 37°C. By adding 2 ml standard medium per well, cells were separated from each other by thorough resuspending. 0.5 ml of the cell suspension of one well was transferred to a new well of a 6 well plate together with 1.5 ml standard medium. After 4 hours the nuclei of individualized cells were stained for 15 minutes at 37°C with Hoechst 33342 (Thermo Fisher Scientific), diluted 1:2000 in standard medium. Then cells were washed twice with 3 ml DMEM without phenol red (Ref.: 31053-028, Gibco) including 10% fetal bovine serum, 2 mM L-glutamine, penicillin (50 U/ml) and streptomycin (50 µg/ml). The presence of phenol red was avoided to exclude that this dye influences registration of YFP signal from expressed proteins. Cells were kept in this medium until imaging. Fluorescence detection and analysis were performed with the Cytation 5 imaging reader (BioTek) at 20x magnification (objective). A mask was applied onto the Hoechst-positive nuclei and the YFP signal within was measured. The YFP of  $\alpha$ -subunits was excited at a wavelength of 505 nm and the emitted light with a wavelength of 530 to 560 nm was detected. For the Hoechst staining the excitation wavelength was 365 nm and the detection wavelength 420 to 480 nm. Mean YFP fluorescence values and standard deviation for all measured cells of one respective condition were calculated by the Gen5™ Software (BioTek).

### 2.2.7 Electrophysiology

#### *2.2.7.1 Patch clamp setup and recording solutions*

For the electrophysiological investigation of ClC-K channels the patch clamp technique in the whole-cell and single channel configuration was applied. Under an inverted fluorescence microscope (Leica Microsystems) transfected HEK293T cells were selected. The microscope was located on a vibration-damped table (TMC) and shielded by a Faraday cage. For measurements in whole cell configuration HEK293T cells were bathed in a solution containing 140 mM NaCl, 4 mM KCl, 2 mM CaCl<sub>2</sub>, 1 mM MgCl<sub>2</sub> and 5 mM HEPES (SERVA, Sigma-Aldrich). The intracellular solution of the micropipettes contained 120 mM NaCl, 2 mM MgCl<sub>2</sub>, 5 mM EGTA in NaOH and 10 mM HEPES. For single channel measurements bath and pipette solution were identical and contained 130 mM N-methyl-D-glucamine (NMDG), 2 mM CaCl<sub>2</sub>, 5 mM MgCl<sub>2</sub> and 10 mM HEPES. All solutions were adjusted to a pH value of 7.4 (pH meter: WTW,

Knick). The micropipettes were made of borosilicate glass (Harvard Apparatus). Capillaries with a wall thickness of 0.13 mm were used to produce micropipettes for measurements in the whole-cell configuration. For single channel measurements, capillaries with 0.42 mm thickness were preferred. Capillaries were pulled using a Flaming/Brown Micropipette Puller P-97 (Sutter Instrument). Thereupon the tips of the pipettes were heat polished (Micro Forge MF-830). The micropipettes for whole cell measurements should have, together with the corresponding solutions, a resistance of 1.0 to 2.0 M $\Omega$ , which correlated to an aperture diameter of about 5  $\mu\text{m}$  for the pipette. For measurements of current noise the micropipettes were immersed with hot wax (Thomas Oertel Dental) before filling with the pipette solution. The thin layer that was formed around the pipette by the wax reduced the capacitance of the pipette and thus reduced some of the background noise. Micropipettes for single channel measurements in combination with their solution should have a resistance in the range of 10-30 M $\Omega$ . For hydrophobic coating of these micropipettes they were briefly submerged in Sigmacote<sup>®</sup> (Sigma-Aldrich), which had a similar effect as wax. Silver wires were used as measuring electrodes (Goodfellow), which were treated with a sodium hypochlorite solution (Danklorix, Colgate-Palmolive) for about 10 minutes so that a thin layer of silver chloride was deposited onto the wire. With these electrodes potentials and currents between pipette solution (= intracellular space) and bath solution (= extracellular space) were measured.

To locate the micropipette exactly over a cell, a micromanipulator (Luigs & Neumann) was used. The pipette aperture was placed on the plasma membrane and a slight negative pressure was applied. When the plasma membrane completely sealed the pipette aperture, this condition was called 'gigaseal', because the resistance between bath and pipette electrode reached values in the G $\Omega$  area. With a continuous test pulse of 5 mV applied by the pipette, the quality of the gigaseal was checked and the current between bath and pipette electrode was measured. At the beginning and end of the test pulse current peaks occur, which were caused by capacitive charging and discharging of the pipette wall. These capacitive current peaks were compensated by a feedback amplifier (Axopatch 200B, Molecular Devices Corporation). Thereby later current measurements were cleaned from such artifacts. To achieve the whole cell configuration, the plasma membrane of the cell was opened by a short, jerky negative pressure. As result, the cell interior and the pipette solution formed a continuum. Similar to the pipette wall also the cell membrane owned capacitive properties and could be charged and discharged by voltage steps. Therefore, capacitive currents occur

again at the beginning and at the end of voltage steps. The plasma membrane capacitance was analogously compensated by regulating the applied voltage during the voltage steps at the feedback amplifier, so that also these current peaks were eliminated. In addition, the pipette aperture represents a resistor which lies in series to the membrane resistance. Thus, a fraction of voltages would decline at the pipette aperture and reduce the voltage that influenced the ion channels within the plasma membrane. Therefore, these voltage errors were corrected by increasing the applied potentials. This compensation was, however, only possible up to about 90%. The remaining, uncompensated voltage error at the series resistance falsified the results, because the voltage applied to the channels was less than the specified (command) voltage. Therefore, currents exceeding 20 nA and with series resistances of 2-5 M $\Omega$  contained after compensation a voltage error of 4-10 mV already after compensation. For this reason, current measurements above 20 nA were excluded from analysis. For single channel measurements the compensation of membrane capacity and serial resistance was not necessary because membrane patch simply plugs pipette aperture. The currents were measured using the Clampex software (Molecular Devices Corporation) after they had been digitalized using an analog-digital converter (Digidata 1440, Molecular Devices Corporation). The sampling rate was 50 kHz for whole cell measurements and 20 kHz for single channel measurements.

#### *2.2.7.2 Analysis of electrophysiological data*

The current measurements were performed using the software pCLAMP (Molecular Devices Corporation) and Excel (Microsoft, Unterschleißheim). Graphics were developed with the software Sigmaplot (Systat Software Inc., Erkrath), GraphPad Prism (GraphPad Software, San Diego, CA) and CorelDRAW (Corel Corporation, Ottawa).

#### *2.2.7.3 Time constants*

In this study voltage-dependent currents were measured by applying voltage steps. When changing from one voltage to another, current amplitudes may change in a time-dependent manner as the open probability of the channels changes. Such changes often show an exponential time course, which is the reason why mono- or bi-exponential functions can be fitted to current traces. The time constants of these functions are a degree of the rate at which a channel changes from one voltage-dependent state to another. The time constant ( $\tau$ ) represents the time that a current requires to reach 63.2% of the final current amplitude ( $C$ )

at a certain voltage. To obtain time constants in this study, voltages were applied, which usually step from +65 mV to negative voltages in a range from -155 mV to -5 mV. Mono-exponential functions were fitted into defined sections of current traces. In equation 2,  $I(t)$  represents the time course of activation or deactivation,  $(A)$  the current amplitude factor and  $(t)$  the time.

$$I(t) = A e^{\frac{-t}{\tau}} + C \quad (\text{equation 2})$$

#### 2.2.7.4 Determination of relative channel open probabilities

To determine relative open probabilities of the total rClC-K1 channel, which exhibits, in contrast to hClC-Ka, a time- and voltage-dependence for both gates, voltage steps were used. Starting from 0 mV, forward pulses of -155 mV to +145 mV for 300 ms were applied. A test pulse of +105 mV was then set for 100 ms. The current amplitude ( $I$ ) depended on the number of active membrane channels ( $N$ ), the single channel current amplitude ( $i$ ) and the open probability of channels ( $P_o$ ) (Alvarez et al., 2002).

$$I = N \cdot i \cdot P_o \quad (\text{equation 3})$$

Since the number of membrane channels remained the same during measurement and the single channel amplitude was also constant at a constant voltage, a change of current amplitude at a defined voltage could be exclusively attributed to a change of channel open probability. In contrast to the single pore amplitude, the open probability of the ClC-K1 channels is not only voltage- but also time-dependent. This means that the open probability required a certain time to adjust to a new voltage after a voltage step.

Thus, the current amplitude at the beginning of the test pulse was still dependent on the open probability of the channel under the conditions of the pre-pulse. When different voltages were set during the pre-pulse, current amplitudes differed at the beginning of the test pulse. However, after a certain time they reached the same value, since the open probabilities adjusted to the test pulse voltage, accordingly. If the different current amplitudes at the beginning of the test pulse were divided by the maximum current, relative open probabilities resulted.

ClC-K channels possess two independent gates (Accardi & Pusch, 2000). The first gate is the fast gate, the second one is the slow gate. The channel is only conductive for chloride ions, if both the fast and slow gates are open because fast and slow gates are meant to be connected in series. If independence of fast and slow gate is assumed, the open probability of the (total)

channel is calculated as the product of the fast (protopore) gate and slow (common) gate open probability (see equation 1).

$$P_{total} = P_p \cdot P_c$$

To determine the relative slow gate open probabilities of rClC-K1 in presence of barttin an intermediate pulse of -180 mV was set for 20 ms between the pre-pulse and the test pulse (Suppl. Fig.3). This pulse caused the fast gate to open ( $P_p \approx 1$ ), while the slow gate did not change its open probability due to the shortness of the pulse (Fischer et al., 2010). The current amplitudes at the beginning of the test pulse were therefore only dependent on the relative slow gate open probabilities.

For rClC-K1 in absence of barttin we took advantage of the differences between fast and slow gate kinetics, visible in the clearly bi-phasic current progression. After the early kinetic of fast gating at the beginning of the test pulse, the kinetic of the slow gating followed. Only this second component of the current relaxation was fitted by mono-exponential functions, which were continued up to the voltage step between the pre- and test pulse. The current values at the voltage step were directly proportional to the relative open probabilities of the slow gate. Based on equation 1, the relative open probabilities of the fast gate can be calculated by the ratio of the relative total channel and slow gate open probability. When these open probabilities were plotted against the voltages of the pre-pulses, activation curves were obtained for the individual gates.

Voltage-dependence of relative open probabilities was analyzed by fitting a Boltzmann function to the data.

$$P(V) = P_{min} + \frac{P_{max} - P_{min}}{1 + e^{\frac{Z_d F (V - V_{0.5})}{RT}}} \quad (\text{equation 4})$$

In this equation,  $V$  corresponds to the applied voltage,  $Z_d$  to the charge, which moves through the membrane by channel gating,  $F$  to the Faraday constant,  $R$  to the gas constant and  $T$  to absolute temperature.  $V_{0.5}$  is the voltage of half maximum activation.  $P_{min}$  and  $P_{max}$  are the minimum and maximum relative open probabilities. The maximum relative open probability was normalized to 1.

Determination of relative open probabilities by the here described method was feasible only for rClC-K1 because gating kinetics are slow enough to obtain relevant values at the beginning of test pulses. For hClC-Ka gating processes are different from rClC-K1, and gates adapt much faster to applied voltages than the orthologous channel, making it impossible to obtain



relative open probabilities by current amplitudes after voltage steps. Thus, open probabilities of hClC-Ka were determined using stationary noise analysis.

#### 2.2.7.5 Determination of relative channel conductances from IV-plots

To characterize hyperpolarization-induced block for rClC-K1 relative channel conductances were shown for negative voltages in this study. In a first step IV-plots were established for voltages from -255 mV to +195 mV. Around the reversal potential of -4.8 mV the IV-relationship of rClC-K is linear. Thus, linear regression was performed for currents between -55 mV and +55 mV. At voltages which were more negative than -100 mV currents decreased and deviated from linear regression. The fraction of measured current from the corresponding value of linear regression represents the relative conductance at a certain voltage. Voltage-dependence of obtained conductance curves could be fitted by Boltzmann functions analogously as for relative open probabilities.

$$G(V) = G_{min} + \frac{G_{max}-G_{min}}{1+e^{\frac{z_d F(V-V_{0.5})}{RT}}} \quad (\text{equation 5})$$

#### 2.2.7.6 Determination of single pore parameters using stationary noise analysis

Stationary noise analysis of macroscopic currents allows the determination of single channel conductance, absolute channel open probability and the number of active channels in the plasma membrane (Alvarez et al., 2002).

The macroscopic current amplitude is the product of the number of membrane channels ( $N$ ), the single channel current amplitude ( $i$ ) and the single channel open probability ( $P_o$ ) (see equation 3).

$$I = N \cdot i \cdot P_o$$

When macroscopic current amplitude ( $I$ ) changes, usually ( $N$ ) and ( $i$ ) do not change during measurement. Only the open probability of a channel ( $P_o$ ) changes. In turn, the current variance of macroscopic currents ( $\sigma^2$ ) depends on the open probability of the involved channels. It is smallest, if the channel is closed and open probability zero. If open probability increases, also current variance increases. The current variance is greatest at an open probability of 50% because in this case most channels change between a closed and an open state and variability of macroscopic current ( $I$ ) is highest. If the open probability is further reduced, the noise is reduced, too, because more and more channels remain in the closed

state. In addition, the intensity of the current noise depends on the number of membrane channels ( $N$ ) and also on the single channel current amplitude ( $i$ ), which depends on the membrane voltage. The larger the number of membrane channels ( $N$ ), the larger the amplitude deviations from the mean macroscopic current amplitude ( $I$ ) can be.

Accordingly, the variance of the current amplitude is related to the single channel current amplitude, the macroscopic current amplitude and the number of membrane channels like a square function (Alvarez et al., 2002):

$$\sigma^2 = i \cdot I - \frac{I^2}{N} \quad (\text{equation 6})$$

There is a linear distribution, if the variance ( $\sigma^2$ ), divided by the product of the mean current amplitude ( $I$ ) and the electric driving force ( $V-V_{rev}$ ), was plotted against the macroscopic conductance ( $\frac{I}{(V-V_{rev})}$ ) (Sesti & Goldstein, 1998):

$$\frac{\sigma^2}{I \times (V-V_{rev})} = -\frac{1}{N} \cdot \frac{I}{(V-V_{rev})} + \frac{i}{(V-V_{rev})} \quad (\text{equation 7})$$

The electrical driving force ( $V-V_{rev}$ ) for an ion flux through chloride channels is given by the difference between the applied voltage and the reversal potential for chloride ions. From equation 7 it follows that the negative reciprocal of the slope from the regression line ( $-\frac{1}{N}$ ) corresponds to the number of active plasma membrane pores (Fig.8B). It has to be emphasized that in this study the ( $N$ )-number corresponds to the number of membrane pores and not to channels as the here investigated CIC-K channels own two individually gated pores per one channel. The y-axis intercept ( $\frac{i}{(V-V_{rev})}$ ) corresponds to the single pore conductance and the x-axis intercept to the maximum possible macroscopic conductance of the cell when all ion channels are open. The quotients of the conductances at the applied voltages and the maximum conductance represent the absolute open probabilities. The smallest measured variance is near the reversal potential. It has to be subtracted from all other variances because it includes the background noise of the system (not included in equation 7). At the reversal potential no currents flow, therefore the noise cannot be caused by channel action. For noise analyses the current traces were digitized with a sampling rate of 50 kHz. A low-pass filter with an upper cut-off frequency of 10 kHz was used.

To investigate the voltage-dependence, a protocol was used that applied voltages from -5 mV to -255 mV to the cell for 100 ms in voltage steps of +10 mV (Fig.8A). This was followed by a depolarization of +75 mV for 60 ms. This depolarization caused chloride ions to flow into the

cell again, since the strong hyperpolarization could previously have led to a depletion of chloride ions in the intracellular space. The reversal potential for the chloride ion concentration of the here used bath and pipette solution calculated from the Nernst equation was -4.8 mV. Therefore, the current noise at -5 mV, which includes the background noise, was always subtracted from current noise at other voltages.

This noise analysis was applied in this study on ClC-K/barttin concatamers with different  $\alpha:\beta$ -subunit stoichiometries. When cells expressing ClC-K/barttin channels were hyperpolarized, the current traces started to increase their noise. According to the description above, this noise was caused by the fact that the channels reduced their open probability.

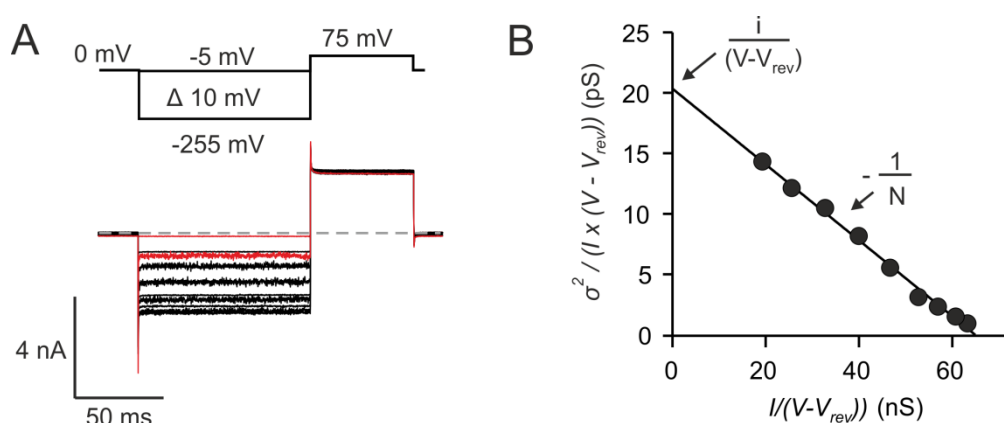


**Fig. 8 Conduction and evaluation of stationary noise analysis**

(A) After a holding potential of 0 mV negative voltages from -5 mV to -255 mV in 10 mV steps were applied. Subsequently, a depolarization of 75 mV occurred (upper image). Below an exemplary current recording of hClC-Ka plus barttin is visualized. Dashed line represents 0 nA. Red colored current traces represent currents at voltages of -255 mV and -5 mV. (B) Exemplary stationary noise analysis of hClC-Ka plus barttin according to equation 7. The y-axis intercept of linear regression embodies the single pore conductance in pS, the negative reciprocal of the slope the number of active membrane pores and the x-axis intercept the maximum macroscopic conductance in nS.  $i$  = single pore current amplitude,  $V$  = applied voltage,  $V_{rev}$  = reversal potential,  $N$  = number of active membrane pores.

### 2.2.7.7 Single channel measurements

Single channel measurements were used in this study to investigate single pore conductance, pore open probabilities and properties of fast and slow gating. They were performed in the cell attached or excised inside-out patch configuration. For cell attached configuration a piece of the plasma membrane, which was still connected to the whole cell membrane, was sealed to the tip of the micropipette. To obtain the excised patch mode the micropipette was then jerkily moved back so that the intracellular side of the membrane was directed to the bath solution and the extracellular side of the membrane to the pipette solution. For single channel

measurements a low pass filter with an upper cut-off frequency of 1 kHz was used. During the analysis of single channel measurements an additional digital low pass filter of 300 Hz was used. The software pCLAMP was used to comprise the statistical distribution of data over a defined time section and to create histograms from it. The class width for histogram generation was 0.01 pA. Gaussian functions (equation 8) were adapted to the histograms so that single pore current amplitudes could be determined through the differences between Gaussian peaks.

$$f(x) = A \frac{e^{-\frac{(x-\mu)^2}{2\sigma^2}}}{\sigma\sqrt{2\pi}} \quad (\text{equation 8})$$

Within the Gaussian function ( $A$ ) represents the amplitude of the function, ( $\mu$ ) the expectancy value or the position on the x-axis where the Gaussian function reaches its maximum and ( $\sigma$ ) the standard deviation of the expectancy value or the width of the distribution, respectively. Histograms as well as fitted Gaussian functions were transmitted to the software Excel. On their basis single pore current amplitudes were determined. For calculation of single pore conductances, the current amplitude of a pore was divided by the applied voltage.

During single channel measurements a CIC-K channel with two individual pores can take in three different conducting states: closed ( $C$ ), one open pore ( $O1$ ) and two open pores ( $O2$ ). The probabilities that one pore is closed ( $p_c$ ) or open ( $p_o$ ) are binomially distributed and equal as sum 1.

$$p_c + p_o = 1 \quad (\text{equation 9})$$

$$p_c^2 + 2p_cp_o + p_o^2 = 1 \quad (\text{equation 10})$$

Within equation 10  $p_c^2$  represents the probability that both pores are closed ( $C$ ),  $2p_cp_o$  that only one pore is open ( $O1$ ) and  $p_o^2$  that both pores are open ( $O2$ ). Gaussian functions, which were fitted to histograms of data distribution, represent the conditions ( $C$ ), ( $O1$ ) and ( $O2$ ) (Fig.9). Using equation 10, the relative areas of the individual Gaussian curves in relation to the area of all Gaussian curves, which corresponds to probabilities of individual states ( $C$ ), ( $O1$ ) and ( $O2$ ), could be used to determine the open probability of one pore within single channel recordings.

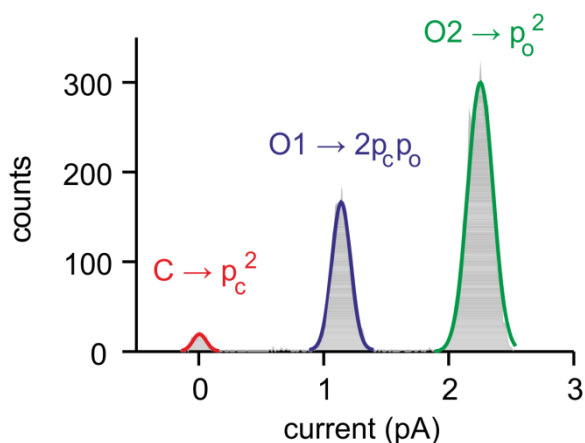


**Fig. 9 Binomial distribution of conductance states for a ClC-K channel with two independent pores**

Representative single channel current amplitude histogram of hClC-Ka + barttin at +50 mV and fits with the sum of three equidistant Gaussian distributions. Each conformation, a channel with two pores can take in, was fitted by one Gaussian function. The area of each Gaussian distribution represents the relative probability of occurrence, calculable by individual summands of the binomial equation 10. C = both pores are closed (red), O1 = only one pore is open (blue), O2 = both pores are open (green),  $p_c$  = probability that one pore is closed,  $p_o$  = probability that one pore is open.

#### 2.2.7.8 Inhibition of ClC-K channels by 1 mM niflumic acid

Niflumic acid (NFA, Sigma-Aldrich) was dissolved in DMSO to a concentration of 50 mg/ml. From this stock solution a respective volume was transferred to bath solutions for whole cell or single channel measurements to obtain a final concentration of 1 mM NFA. Using a self-made gravity-driven perfusion system NFA solution was directly applied to the cell. Accordingly, a bath solution without NFA, which was applied by the same perfusion system, served as washing solution to displace NFA from near cell environment.

#### 2.2.8 Statistics

In this thesis bar graphs and scatter plots show mean values  $\pm$  standard error of the mean (S.E.M.), if not otherwise indicated. Statistical analysis was performed using the software Sigmaplot (Systat Software Inc., San Jose, CA). One-sample Student's t-test was used to test two groups for significant difference. One-way analysis of variance (ANOVA) was applied to test the statistical significance in multiple-group comparisons. If groups were indicated to be significantly different, a subsequent Holm-Sidak post hoc test was applied to determine, which distinct groups differ from each other. Levels of significance are indicated as follows: \*,  $p < 0.05$ ; \*\*,  $p < 0.01$ ; \*\*\*,  $p < 0.001$ .

## 3 Results

### 3.1 ClC-K/WT barttin concatamers of different stoichiometries

Figure 10 schematically illustrates the different composition of constructs harboring ClC-K pore forming  $\alpha$ -subunits and barttin  $\beta$ -subunits that were investigated in this study. As a reference, an  $\alpha$ -subunit was expressed as monomer, which spontaneously builds the physiologically active ClC-K homodimer (Fig.10A). Such channels were characterized in absence of barttin or in presence of the co-expressed  $\beta$ -subunit. A great excess of barttin should guarantee the occupation of all relevant barttin binding sites of the channel, which finally forms the homodimer surrounded by the necessary number of  $\beta$ -subunits. All tested concatamers were fused to YFP at the C-terminus of the channel subunit. The first concatamer with fixed stoichiometry was composed of one barttin covalently linked by an amino acid linker to one ClC-K channel  $\alpha$ -subunit (barttin\_ClC-K; Fig.10B). Here, the C-terminus of the  $\beta$ -subunit was fused to the N-terminus of the  $\alpha$ -subunit. This orientation is recommended, because it has previously been shown that proper activation of the ClC-K channels depends on a free barttin N-terminus (Wojciechowski et al., 2018b). The  $\alpha$ -subunits formed homodimers with an  $\alpha$ : $\beta$ -subunit ratio of 1:1 for one protopore or 2:2 for a ClC-K dimer. Moreover, the condition was tested when further  $\beta$ -subunits were co-expressed to occupy all binding sites of the pore forming subunit. The next concatamer contained two barttin molecules that were covalently linked to the N-terminus of ClC-K (barttin\_barttin\_ClC-K; Fig.10C). Within this protein one barttin molecule was linked by its C-terminus to the N-terminus of the second barttin. Functionally, this concatamer forms homodimers with an  $\alpha$ : $\beta$ -subunit ratio of 1:2 for one protopore or 2:4 for a ClC-K dimer. This condition was also tested in presence of additionally co-expressed barttin. Finally, we covalently linked one barttin with two  $\alpha$ -subunits (barttin\_ClC-K\_ClC-K; Fig.10D). The  $\beta$ -subunit was covalently linked by its C-terminus to the N-terminus of an  $\alpha$ -subunit, which was itself connected to a further  $\alpha$ -subunit by an amino acid linker. This construct was supposed to build no dimers because it contained already two  $\alpha$ -subunits in an  $\alpha$ : $\beta$ -subunit ratio of 2:1. As for the other concatamers, this protein was characterized under additional barttin overexpression, too.

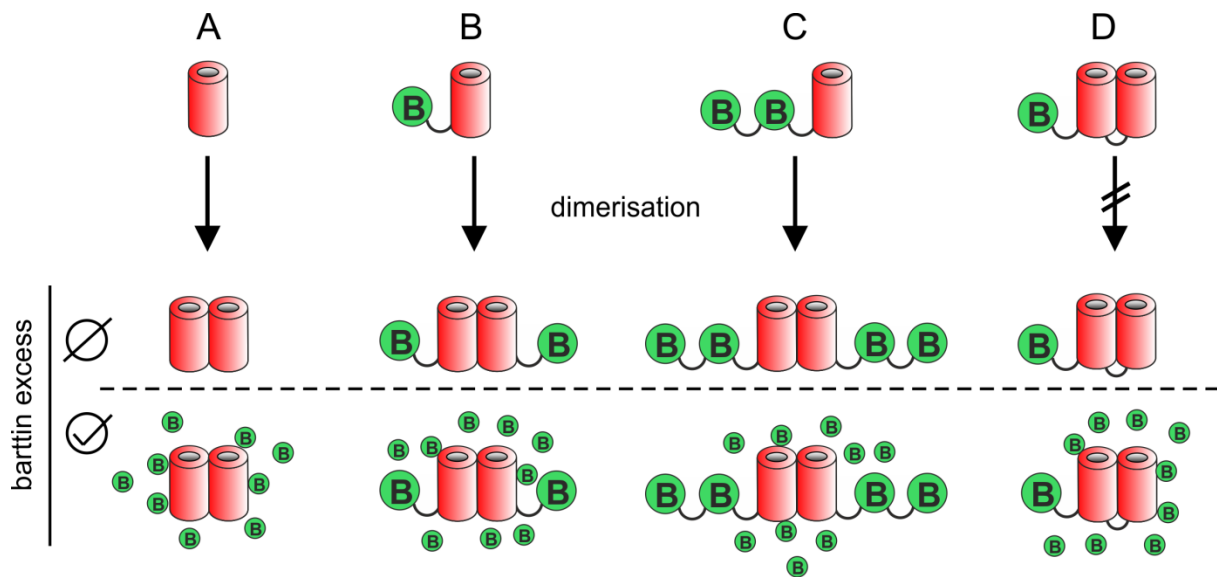


**Fig. 10 Design of ClC-K/barttin channels with diverse stoichiometries as investigated in this study**

ClC-K channels were either expressed as  $\alpha$ -subunit monomers (A) or as  $\alpha$ -subunit monomers covalently linked to one (B) or two  $\beta$ -subunits (C) or as two linked  $\alpha$ -subunits connected to one  $\beta$ -subunit (D). All constructs were C-terminally fused to a YFP-tag (not shown). Proteins from (A) to (C) are expected to build channel homodimers after expression. As concatamers in (D) were already designed as  $\alpha$ -subunit homodimer, multimerization is not assumed (crossed arrow). All conditions were analyzed both without and with excessive additional barttin co-expression. Barttin = green circle; ClC-K  $\alpha$ -subunit (monomer) = red cylinder.

### 3.1.1 hClC-K $\alpha$ and barttin expression in HEK293T and MDCKII cells

We first investigated proper expression of ClC-K/barttin constructs. Here, plasmids encoding the DNA of the investigated proteins were transiently transfected into HEK293T or MDCKII cells. HEK293T cells were used for biochemical analyses and especially for patch clamp experiments. This cell line harbors the SV40 large T antigen, which causes a robust expression even of proteins with potentially lower rates of biosynthesis like disease-causing mutant proteins or large concatamers (Pear et al., 1993). The MDCKII cells offer a lower expression efficiency of heterologous proteins than HEK293T cells and are therefore more suitable for the characterization of subcellular localization and trafficking. They, moreover, grow as monolayer with tight cell to cell contacts resembling epithelial tissue. In a first step, hClC-K $\alpha$  monomers tagged with the mYFP at their C-terminus were expressed in HEK293T or MDCKII cells in absence or presence of barttin tagged with mCFP at its C-terminus. Subsequently, cells were lysed and equal amounts of protein lysates were subjected to SDS-PAGE. Figure 11 depicts representative fluorescence images of gels containing separated  $\alpha$ - and  $\beta$ -subunits, expressed from both cell lines. hClC-K $\alpha$ \_mYFP is visible in each lane of both gels (red color). Between 75 and 100 kDa there are three bands for the  $\alpha$ -subunit, which were caused by different glycosylation-states of the channel protein. The lowest one is the non-glycosylated

(open circle), the middle one the core-glycosylated (filled circle) and the highest band the complex-glycosylated state of the channel (hashtag; Wojciechowski et al., 2018b, Janssen et al., 2009). Core-glycosylation is performed in the endoplasmic reticulum (ER) during channel maturation, whereas binding of more sugar residues to the asparagines at positions 364 and 373 (Kieferle et al., 1994) results in larger, complex-glycosylated channels during trafficking through the Golgi apparatus. Both HEK293T and MDCKII cells show all three hCIC-Ka glycosylation patterns in whole cell lysates. For MDCKII cells the relative fraction of non-glycosylated channel seems to be reduced in comparison to HEK293T cells. Potentially, the amount of non-glycosylated channel is higher in HEK293T as this cell line exhibits stronger overexpression of heterologously expressed proteins, which lag behind glycosylation. Bands below the non-glycosylated channel are probably caused by protein degradation. Due to full disruption of quaternary protein structures by SDS, fluorescent bands exclusively represent monomeric  $\alpha$ -subunits. When barttin\_mCFP was co-expressed, as shown in the right lanes of both gels (green color), it migrated according to a molecular weight of around 60 kDa. In presence of the  $\beta$ -subunit total expression of the channel protein was reduced in both cell lines, which is likely caused by competitive usage of cellular pathways for protein biosynthesis.

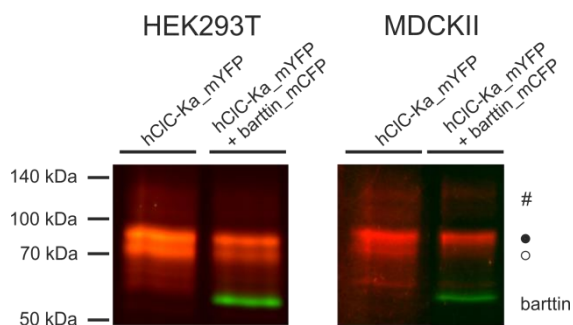


**Fig. 11** Fluorescence scan of SDS-PAGE gels with protein lysates from HEK293T and MDCKII cells expressing hCIC-Ka\_mYFP (red) alone or with barttin\_mCFP (green)

CIC-K channels typically feature three distinctive bands in SDS-PAGEs: Non-glycosylated (○), core-glycosylated (●) and complex-glycosylated channel monomers (#). Core-glycosylation is performed in the endoplasmic reticulum and complex-glycosylation in the Golgi apparatus. Barttin forms only one distinctive band.

### 3.1.2 hCIC-Ka/barttin concatamers are expressed in HEK293T and MDCKII cells and transported to the plasma membrane

An essential prerequisite of this study was the robust expression of concatamers with diverse stoichiometries of  $\alpha$ - and  $\beta$ -subunits. Especially, their expression in HEK293T cells was necessary for functional characterization using the patch clamp technique. For this, HEK293T cells expressing hCIC-Ka and concatamers in absence or presence of additional barttin were lysed and whole cell lysates were separated by SDS-PAGE. Figure 12A shows an



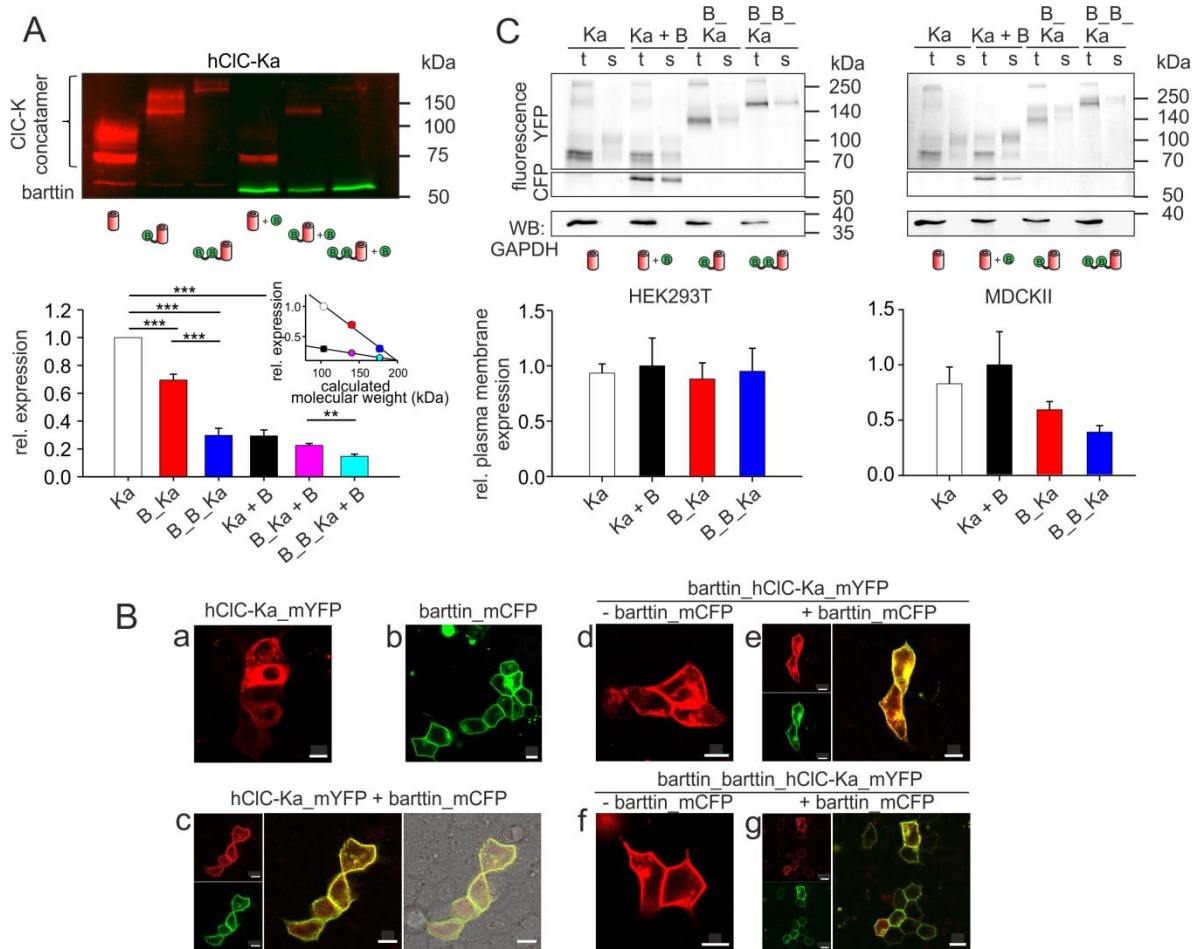


**Fig. 12 Expression and plasma membrane insertion of hClC-Ka/barttin concatamers**

(A) Fluorescence scan of a SDS-PAGE gel with protein lysates from HEK293T cells expressing hClC-Ka/barttin\_mYFP concatamers (red) without or with barttin\_mCFP (green). The faint red bands below the Ka monomer and the concatamers at around 60 kDa are degradation products of the channel and not barttin molecules. The quantitative expression analysis is shown in a bar chart below. Relative expression levels were normalized to the expression of the hClC-Ka monomer (white bar). All data show mean values  $\pm$  S.E.M.. Student's t-test was performed to test for significance ( $n \geq 3$ , \*\*  $p < 0.01$ ; \*\*\*  $p < 0.001$ ). Inset shows linear correlation between the relative protein expression level and the calculated molecular weight. Dot colors correlate to colors of the bar chart. (B) Confocal microscopy images of MDCKII cells, expressing hClC-Ka\_mYFP monomers or concatamers in absence or presence of additional barttin\_mCFP. YFP is visualized in red and CFP in green. Co-localization of  $\alpha$ - and  $\beta$ -subunits is visualized in yellow. - barttin = without barttin co-expression, + barttin = with barttin co-expression. Scale bars = 10  $\mu$ m. (C) Fluorescence scan of SDS-PAGE gels with protein lysates from HEK293T (left) and MDCKII cells (right) expressing hClC-Ka monomers in absence or presence of barttin as well as hClC-Ka/barttin concatamers. YFP-tagged  $\alpha$ -subunits were visualized in the YFP- and barttin in the CFP-channel. Total cell lysates (t) and surface membrane fractions (s), obtained from biotinylation assay, were loaded pairwise onto the gel. Relative plasma membrane expression of CiC-K proteins was determined by dividing surface membrane fluorescence intensity by intensity of total cell lysate and normalizing this to the condition hClC-Ka + barttin (black bar). All data show mean values  $\pm$  S.E.M. ( $n=4$  (HEK293T),  $n \geq 3$  (MDCKII)). Statistical difference was tested by one-way ANOVA. Western blot (WB) detecting GAPDH was used to exclude contamination of surface membrane fractions by cytosolic proteins. Ka (+ B) = hClC-Ka (+ barttin), B\_Ka (+ B) = barttin\_hClC-Ka (+ barttin), B\_B\_Ka (+ B) = barttin\_barttin\_hClC-Ka (+ barttin).

image of a representative SDS-PAGE gel together with densitometric expression analysis ( $n=3$ ; hClC-Ka\_mYFP in red, barttin\_mCFP in green). hClC-Ka monomers in absence of barttin migrated between 75 and 100 kDa and exhibited the highest expression level. They served as reference for all other conditions. The concatamer barttin\_hClC-Ka without further co-expression of barttin migrated - as expected - around 100 to 150 kDa and was significantly lower expressed than the  $\alpha$ -subunit monomer. The concatamer barttin\_barttin\_hClC-Ka

migrated at around 170 to 180 kDa and was even lower expressed than the barttin\_hClC-Ka concatamer. In presence of additional barttin the expression level for hClC-Ka monomers as well as for the concatamers was reduced. Interestingly, in presence of barttin\_mCFP the complex-glycosylated protein fraction almost vanished. Between barttin\_hClC-Ka and barttin\_barttin\_hClC-Ka there was still a significant difference when additional  $\beta$ -subunits were present in excess. The insert in figure 12A visualizes a linear relationship between the molecular weight of proteins and their relative expression. The longer the concatamer sequence the lower was the fluorescence intensity and therefore also the expression. Excessive barttin co-expression decreased channel biosynthesis and the slope of linear regression.

Besides robust expression a successful transport of all investigated concatamers to the plasma membrane was also indispensable for whole cell current recording in patch clamp experiments. Moreover, checking the surface membrane presence of all concatamers gave information about the number of  $\beta$ - per  $\alpha$ -subunits that is necessary for proper trafficking of the channel complex. We performed confocal microscopy to evaluate the effect of  $\alpha$ : $\beta$ -subunit stoichiometry on subcellular localization and plasma membrane trafficking. 48 h after transfection of MDCKII cells with plasmids encoding hClC-Ka\_mYFP, barttin\_mCFP or combinations of both cells were subjected to live cell confocal imaging. YFP fluorescence is shown in red and CFP fluorescence in green (Fig.12B). In absence of barttin a great fraction of hClC-Ka stayed in intracellular compartments (a). Barttin, solely expressed, was well transported to the plasma membrane even without the  $\alpha$ -subunit (b). Furthermore, subcellular localization was tested under co-expression of both subunits (c). The individual fluorescence signals (mYFP in red, mCFP in green) are shown on the left side. An overlay of both signals in the middle panel should indicate co-localization of hClC-Ka and barttin by a yellow color. On the right side of this merged image the same section of the cell layer is presented together with transmitted light, demonstrating that evaluated signals are not generated by auto-fluorescence of cells but by specific fluorophore expression within individual cells of a confluent layer. In presence of barttin  $\alpha$ - and  $\beta$ -subunit co-localized well in the plasma membrane as visualized by the yellow color in the merged image. This finding agrees very well with previously published observations (Scholl et al., 2006). Barttin\_hClC-Ka in absence of further  $\beta$ -subunits also localized at the plasma membrane, indicating that one barttin per  $\alpha$ -subunit is sufficient for proper transport of the whole channel complex (d).

Excess of barttin by co-expression of further  $\beta$ -subunits did not lead to an apparent change of concatamer distribution (e). Both barttin\_hClC-Ka and unlinked  $\beta$ -subunit co-localized well at the plasma membrane. Same holds true for the concatamer barttin\_barttin\_hClC-Ka in absence and presence of additional  $\beta$ -subunits (f,g). In both cases concatamers were well transported to the plasma membrane.

Although confocal images show both barttin\_hClC-Ka and barttin\_barttin\_hClC-Ka localized at the plasma membrane they did not prove the integration of proteins into this surface membrane. Instead, it could be possible that they stayed in intracellular compartments in closest proximity to the cell surface. To exclude this possibility, biotinylation experiments were performed. During this approach only proteins incorporated in the plasma membrane were labeled with biotin from the extracellular side, which gave the opportunity to separate them from all other intracellular proteins. Therefore, HEK293T or MDCKII cells expressing the investigated proteins were exposed to biotin and subsequently lysed. Biotinylated proteins were isolated by NeutrAvidin beads and both whole cell lysate and purified surface membrane fractions were subjected to SDS-PAGE (see 'methods' chapter for details). Fluorescence scans of SDS-PAGE gels revealed the relative surface membrane fraction of YFP- and CFP-labeled proteins compared to the whole cell fraction of such proteins. Figure 12C represents fluorescence scans of electrophoresed proteins obtained from lysates of HEK293T (left) and MDCKII cells (right). The upper lane depicts the YFP fluorescence of the hClC-Ka  $\alpha$ -subunit unlinked or linked to  $\beta$ -subunits. Fluorescence of additionally co-expressed barttin\_mCFP is shown in the middle line and GAPDH, which was detected by Western Blot, in the lowest line. For HEK293T cells hClC-Ka channels were integrated into the plasma membrane even in absence of barttin. The relative fraction of complex-glycosylated channels was larger than in the whole cell lysate. The same holds true for the same condition in MDCKII cells. Plasma membrane insertion of hClC-Ka in HEK2932T cells in presence of unlinked barttin was comparable but with a higher fraction of non-/core-glycosylated channel protein. Also in MDCKII cells hClC-Ka was inserted into the plasma membrane to similar extend but exhibited a greater portion of complex-glycosylated channel protein than in HEK293T cells. With regard to the surface membrane expression of hClC-Ka/barttin concatamers, which is presented on the right side of both gels, biotinylation experiments confirmed results from confocal microscopy. Both concatamers with one or two barttins bound to one  $\alpha$ -subunit were able to reach the surface membrane in HEK293T and MDCKII cells. Still, surface membrane expression

depended on total channel/concatamer expression (see also Fig.12A). Therefore, surface membrane expression decreased proportionally the longer the concatamer was. To compare the relative plasma membrane fraction of all tested conditions, the surface membrane fractions of the  $\alpha$ -subunits were normalized to the fractions of the total cell lysate. By further normalization to the maximum mean value - in this case hClC-Ka plus extra barttin - this condition was set, as reference, to 1. This quantification is shown in bar graphs, resulting from three gels, below the gel images (see Fig.12C). There was no significant difference in relative surface membrane expression for all tested constructs. Despite the remarkable trend of expression decrease compared to the two other conditions - especially in MDCKII cells - this finding is in accordance with confocal imaging for both concatamers and prove the successful insertion of concatamers into the surface membrane. Notably, there was also no difference between the two conditions when the  $\alpha$ -subunit is expressed without and with  $\beta$ -subunit co-expression. This is at a first glance in contradiction to confocal microscopy and previous results that demonstrate an enhancement of ClC-K channel insertion into the plasma membrane by barttin (Scholl et al., 2006). In the 'discussion' chapter this finding will be debated in more detail. Western blots detecting GAPDH were performed as control for contamination of surface membrane fractions by cytosolic proteins. In case of cytosolic contamination, GAPDH would be present also in the surface membrane fraction. As shown in the lowest panel of images in figure 12C, GAPDH is only detectable in the whole cell lysate but not in the surface membrane fraction.

### 3.1.3 Two $\beta$ -subunits per $\alpha$ -subunit are sufficient to increase hClC-Ka currents similar to barttin excess

One major aspect of this thesis was the electrophysiological characterization of concatamers with different ClC-K/barttin stoichiometries. Up to now, it is unknown whether one or more barttin molecules per channel subunit are sufficient to bestow full electrophysiological functionality on the ClC-K channel complex. Therefore, the use of ClC-K/barttin concatamers should illuminate the effects of different  $\alpha$ : $\beta$ -subunit stoichiometries on channel function.

Currents of hClC-Ka/barttin concatamers, which were expressed in HEK293T cells, were analyzed electrophysiologically using the whole cell patch clamp technique. Figure 13A shows representative current traces of hClC-Ka under different  $\alpha$ : $\beta$ -subunit stoichiometries for

voltages between -255 and +195 mV. hClC-Ka without any  $\beta$ -subunit was not conducting and generated no currents. If the  $\beta$ -subunit was co-expressed or included in a concatamer, the channel complex became conductive. The reduction of current amplitudes at negative voltages below -150 mV is characteristic for hClC-Ka currents and interpreted as a hyperpolarization-induced 'block' (Fischer et al., 2010; Riazuddin et al., 2009; Steinke et al., 2015; Wojciechowski et al., 2015). For the sake of clarity, current traces at -255 and +195 mV are colored in red in figure 13A. Mean IV-plots of tested conditions are visualized in figure 13B. The current/voltage (I/V) relationship at positive potentials is linear, giving a hook-like shape for the IV-plot. In presence of barttin abundance hClC-Ka channels produced mean whole cell current amplitudes of around 9 nA at +105 mV (Fig.13B,C). If one barttin is linked to one channel subunit, the channels were active, too, but with strongly decreased current amplitudes of about 1 nA at +105 mV. The co-expression of additional barttin raised current amplitudes to around 7 nA. This observation differs from the condition with two barttin molecules bound to one channel subunit. Here, the current of the concatamer in absence of additional barttin exceeded with around 6 nA the concatamer current in presence of additional barttin with about 4 nA. At a first glance, this is surprising because a greater excess of barttin is known to increase ClC-K currents. However, it is important to consider the different cellular expression of concatamers with varying composition and molecular weight. As described above the expression of channels and concatamers strongly depend on their protein size and whether there is a co-expression of additional barttin. Thus, mean currents at +105 mV were normalized to the relative expression level of pore forming  $\alpha$ -subunits to obtain valuable information about effects of the here tested  $\alpha$ : $\beta$ -subunit stoichiometry (Fig.13D). After normalization, it became obvious that addition of extra barttin resulted in an enormous increase in current amplitude, if no or one barttin was linked to one channel subunit. If two barttins were linked to one channel subunit, there is no significant difference between presence and absence of co-expressed barttin. These results indicate that two barttin molecules per hClC-Ka channel subunit are necessary and sufficient to reach full channel activity. Nevertheless, one barttin per channel subunit is able to activate hClC-Ka at least to a small extend.

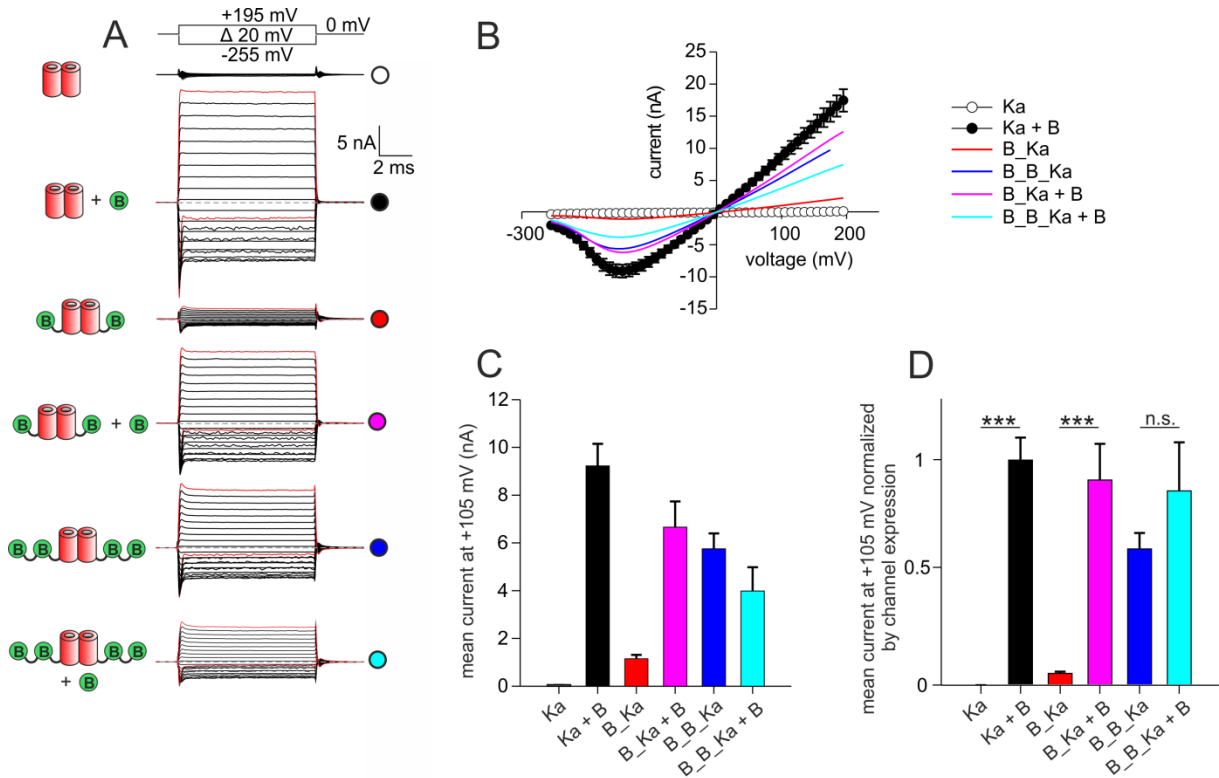


**Fig. 13 Currents of hClC-Ka concatamers in absence and presence of additional barttin**  
 (A) Representative current traces of hClC-Ka concatamers in absence and presence of additional barttin after application of voltages between -255 mV and +195 mV. Red colored current traces represent currents at voltages of -255 mV and +195 mV. Dashed line represents 0 nA. (B) IV-plot of hClC-Ka concatamers, showing a hook-shaped IV-relationship at negative voltages. All data are mean values ( $\pm$  S.E.M. for Ka and Ka + B). (C) Mean current at +105 mV. All data are mean values  $\pm$  S.E.M.. (D) Mean current at +105 mV normalized to channel expression as shown in Fig.12A. All data are mean values  $\pm$  S.E.M.. Statistical significance was tested using Student's t-test. B-D: Ka: n=9, Ka + B: n=21, B\_Ka: n= 18, B\_Ka + B: n=15, B\_B\_Ka: n= 35, B\_B\_Ka + B: n=13, \*\*\*  $p < 0.001$ , n.s. = not significant. Ka (+ B) = hClC-Ka (+ barttin), B\_Ka (+ B) = barttin\_hClC-Ka (+ barttin), B\_B\_Ka (+ B) = barttin\_barttin\_hClC-Ka (+ barttin).

### 3.1.4 hClC-Ka/barttin stoichiometry influences single pore properties

In the next step, the great difference between the currents of one and two barttins bound to a channel subunit will be elucidated in more detail. The whole cell current amplitude ( $I$ ) of hClC-Ka is not only dependent on the expression of ClC-K channel complexes but additionally on the single pore current amplitude ( $i$ ) and the open probability of the channel ( $P_o$ ) (see equation 3).

$$I = N \cdot i \cdot P_o$$

As only active membrane pores, which are inserted into the plasma membrane, contribute to the whole cell current ( $I$ ), the parameter ( $N$ ) is not only dependent on the whole cell expression but also on proper trafficking of the channel complex. It was shown by confocal microscopy and biotinylation assay that proper channel trafficking is f by one or two barttins available per one  $\alpha$ -subunit. To investigate the influence of different  $\alpha$ : $\beta$ -subunit stoichiometries on single pore current amplitude ( $i$ ) and channel open probability ( $P_o$ ) of hClC-

Ka either single channel measurements are required or a special method, the noise analysis of whole cell currents. In the following part the stationary noise analysis was applied in a first instance to elucidate how the stoichiometry between both subunits affects single pore parameters.

For this, negative voltages from -5 to -255 mV for 100 ms were applied and current amplitude and current variance were measured. As shown in figure 14A the current amplitude decreased and current variance increased for voltages below -150 mV. A voltage step to +75 mV (50 ms) was subsequently applied to avoid depletion of chloride ions from the intracellular solution by successive hyperpolarization, which presents strong outward driving forces for negative charges. Figure 14B shows representative noise analyses for the tested channels/concatamers in presence and absence of additional barttin. The macroscopic current variance (noise), normalized to the product of the mean current amplitude and the electrical driving force was plotted against the macroscopic conductance. A linear regression line yields the unitary channel conductance as y-axis-intercept. The number of active channel pores in the plasma membrane is given by the negative reciprocal of the slope from linear regression. A more detailed description of noise analysis including mathematical derivation can be found in the chapter 'methods'. Co-expressed barttin led to a single pore conductance of approximately 24 pS for hClC-Ka (black dots/bars, Fig.14B,D). When only one barttin was linked to a channel subunit, the single pore conductance was significantly decreased to around 13 pS (red dots/bars). Accordingly, the macroscopic conductance was also decreased for the same concatamer, since the number of active membrane pores was smaller than for other conditions. Reduced pore numbers led to a steeper slope in the representative plot of figure 14B because the pore number is given by the negative reciprocal of the slope ( $-\frac{1}{N}$ ). In conclusion, the small macroscopic current amplitude generated by  $\alpha:\beta$ -subunits with a 1:1 stoichiometry (see Fig.13A) is not only explained by lower protein expression but also by lower conductance of the single pore. Availability of more than one barttin per subunit raised the conductance to about 20 pS. However, for the concatamer, which owned two barttins per channel subunit, the single pore conductance was not affected by co-expressed barttin. But for both conditions, in presence and absence of additional barttin (dark and light blue dots/bars), the conductances were still significantly lower than those of hClC-Ka with co-expression of barttin.

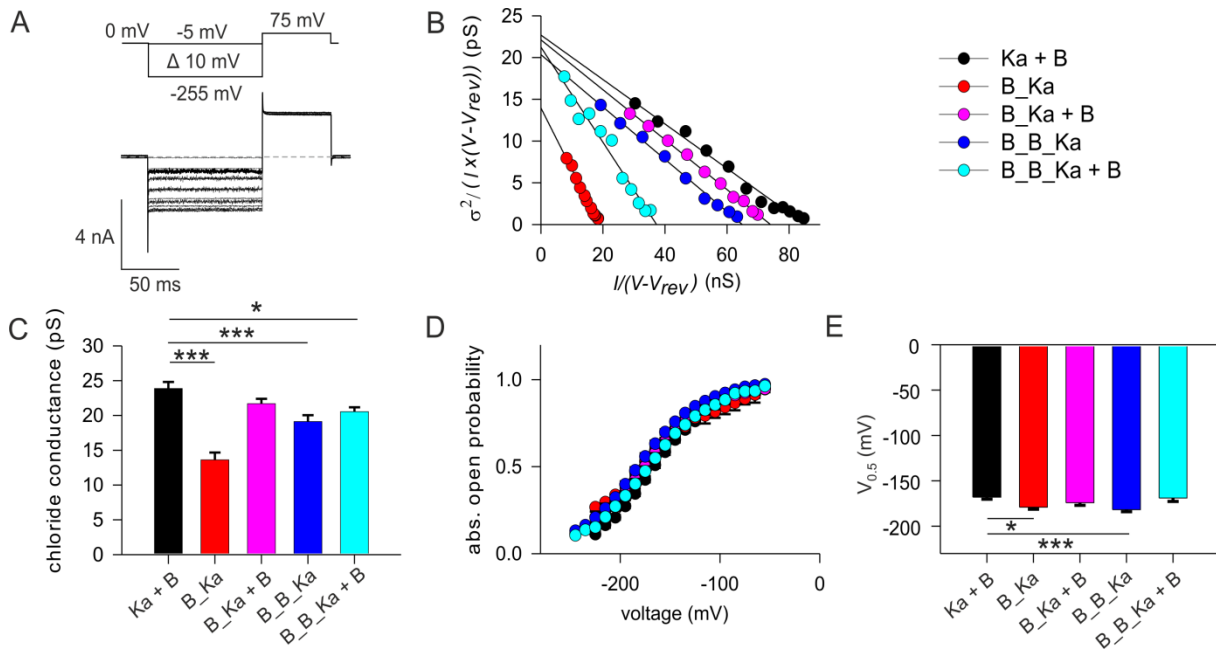


**Fig. 14 Stationary noise analysis of hClC-Ka concatamers in absence and presence of additional barttin**

(A) Representative current trace of hClC-Ka + barttin used for stationary noise analysis. Voltages from -5 mV to -255 mV were applied for 100 ms followed by +75 mV for 50 ms. For more negative voltages current decreases with increasing noise. Dashed line represents 0 nA. (B) Representative stationary noise analyses for hClC-Ka and concatamers in absence and presence of barttin. Data points were fitted by linear regression. (C) Mean chloride conductance of tested hClC-Ka/barttin stoichiometries, obtained by y-axis intercepts of linear regressions as in (B). All data are mean values  $\pm$  S.E.M. Statistical significance was tested by one-way ANOVA and Holm-Sidak post hoc test versus Ka + B:  $F_{(6, 65)} = 20.2$  and  $p < 0.001$ , Ka + B: n=12, B\_Ka: n= 9, B\_Ka + B: n=9, B\_B\_Ka: n=19, B\_B\_Ka + B: n=7. (D) Absolute open probabilities of tested hClC-Ka/barttin stoichiometries at negative voltages, determined from (B). (E) Voltage of half maximum activation ( $V_{0.5}$ ) obtained from fits of activation curves from (D). All data in (D) and (E) are shown as mean  $\pm$  S.E.M.. Statistical significance was tested using one-way ANOVA and Holm-Sidak post hoc test versus Ka + B:  $F_{(6, 55)} = 9.3$  and  $p < 0.001$ , Ka + B: n=11, B\_Ka: n= 6, B\_Ka + B: n=10, B\_B\_Ka: n=17, B\_B\_Ka + B: n=6. Ka (+ B) = hClC-Ka (+ barttin), B\_Ka (+ B) = barttin\_hClC-Ka (+ barttin), B\_B\_Ka (+ B) = barttin\_barttin\_hClC-Ka (+ barttin).

Since whole cell currents represent mean conditions for thousands of channels, slightly reduced mean conductance could be interpreted as mixture of different channel states with full and reduced conduction depending on the number of barttin molecules bound to a single pore. Then, binding of  $\beta$ -subunits to the  $\alpha$ -subunit within a concatamer is supposed to be reduced compared to the hClC-Ka homodimer. Furthermore, this could explain the small number of active membrane pores for the concatamer with a 1:1 stoichiometry despite proper expression levels. For this condition many pores, which do not bind barttin in correct manner, would stay completely inactive and do not contribute to current and noise, as if these pores do not exist. Therefore, the conductance value of 12 pS for a 1:1 stoichiometry cannot result by a mixture of full and no conduction but by a reduced conduction of active pores featuring one correctly bound  $\beta$ -subunit. To evaluate results for single pore conductance obtained by stationary noise analysis hClC-Ka/barttin concatamers were subjected to single channel measurements. The outcome of these experiments is presented below in chapter 3.3.2.

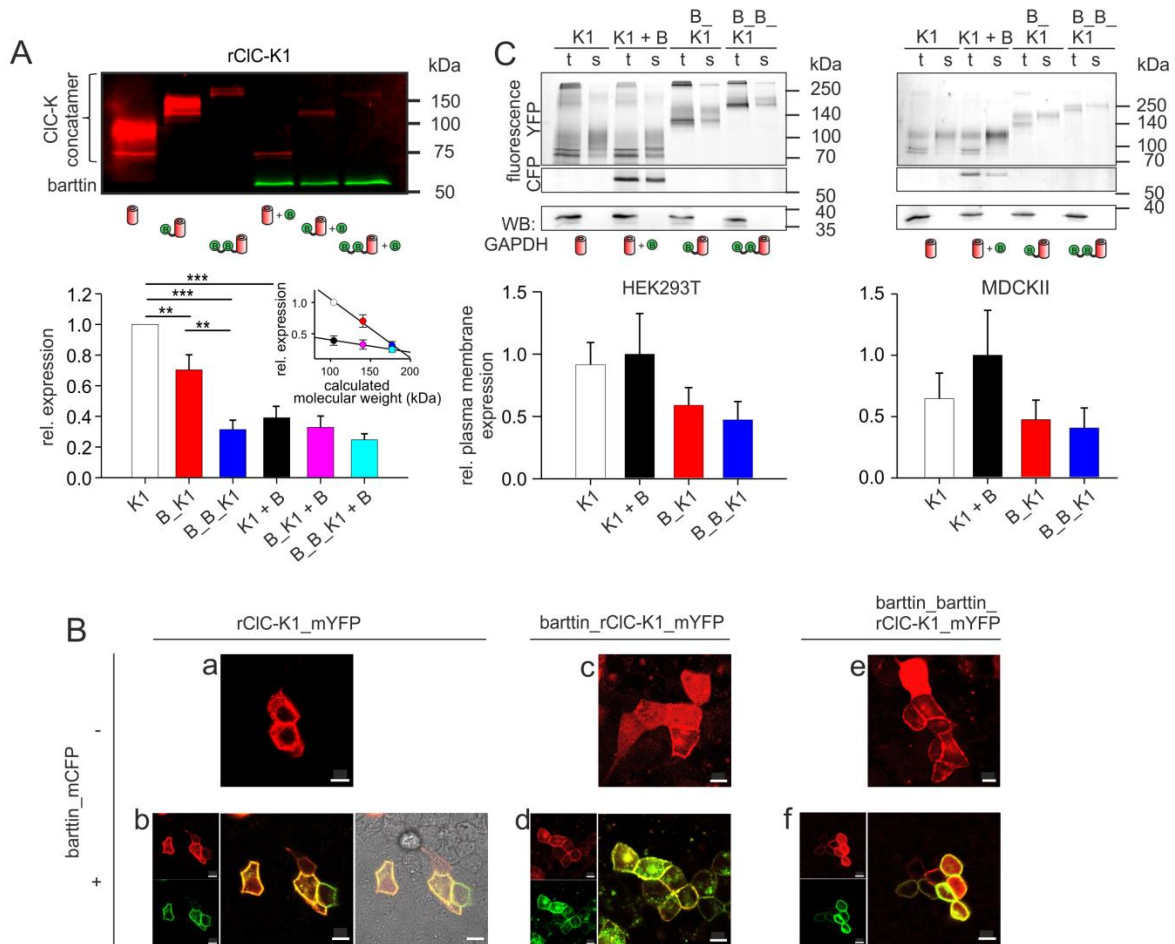


Figure 14D illustrates the voltage-dependence of absolute open channel probabilities, which were determined as the quotient of the conductance at certain voltages and the maximum absolute macroscopic conductance represented as x-axis intercept. Activation curves are presented as mean values from measurements of various cells. For each cell, the activation curve was fitted separately by a Boltzmann function. Parameters of these fits were consulted to evaluate potential differences between tested conditions. Considering the voltage at half maximum activation ( $V_{0.5}$ ), there is no difference between almost all stoichiometries (Fig.14E). Very low scatter within approaches results in few cases of significance between constructs without substantial shifts of activation curves.

### 3.1.5 rCIC-K1/barttin concatamers are expressed in HEK293T and MDCKII cells and transported to the plasma membrane

Generally, two different gates regulate CIC-K channels. The protopore gate opens and closes the individual pore of each subunit and a distinct common gate regulates both pores of the dimer together. With hCIC-Ka, however, such gating processes are not visible in whole cell recordings, because the common gate is constitutively opened by barttin and the channel is not conductive in absence of barttin (Fischer et al., 2010; Riazuddin et al., 2009; Steinke et al., 2015; Wojciechowski et al., 2015). Therefore, we also studied effects of  $\alpha$ : $\beta$ -subunit stoichiometry on the rodent rCIC-K1 channel. In contrast to hCIC-Ka, rCIC-K1 shows time-dependent gating of the fast protopore and slow common gate, which offers the possibility to analyze stoichiometry effects on channel kinetics. In addition, rCIC-K1 is the only CIC-K channel that is conductive even in absence of barttin, displaying inverse voltage dependencies for fast and slow gating processes (Fischer et al., 2010). Therefore, rCIC-K1 channels with the same  $\alpha$ : $\beta$ -subunit stoichiometries as for hCIC-Ka were constructed.

As for hCIC-Ka, successful concatamer expression in HEK293T cells was tested in a first step. Figure 15A shows a representative fluorescence SDS-PAGE gel with YFP fluorescence of  $\alpha$ -subunit monomers/concatamers in red and CFP fluorescence of barttin in green, together with expression analysis obtained from three gels. The rCIC-K1 monomer in absence of barttin exhibited the highest expression level and, therefore, served as reference for all other conditions. The concatamer barttin\_rCIC-K1 in absence of barttin excess migrated at



**Fig. 15 Expression and plasma membrane insertion of rCIC-K1/barttin concatamers**

(A) Fluorescence scan of a SDS-PAGE gel with protein lysates from HEK293T cells expressing rCIC-K1/barttin\_mYFP concatamers (red) without or with barttin\_mCFP (green) together with quantitative expression analysis shown in a bar chart below. Relative expression levels were normalized to the expression of the rCIC-K1 monomer (white bar). All data show mean values  $\pm$  S.E.M. ( $n \geq 3$ , \*\*  $p < 0.01$ ; \*\*\*  $p < 0.001$ ). Student's t-test was performed to test for significance. Inset shows linear correlation between the relative protein expression level and the calculated molecular weight. Dot colors correlate to colors of the bar chart. (B) Confocal microscopy images of MDCKII cells, expressing rCIC-K1\_mYFP monomers (a,b) or barttin\_rCIC-K1\_mYFP (c,d) and barttin\_barttin\_rCIC-K1\_mYFP (e,f) in absence or presence of additional barttin\_mCFP. YFP is visualized in red and CFP in green. Co-localization of  $\alpha$ - and  $\beta$ -subunits is visualized in yellow. - barttin = without barttin co-expression, + barttin = with barttin co-expression. Scale bars = 10  $\mu$ m. (C) Fluorescence scan of SDS-PAGE gels with protein lysates from HEK293T (left) and MDCKII cells (right) expressing rCIC-K1 monomers in absence or presence of barttin as well as rCIC-K1/barttin concatamers. YFP-tagged  $\alpha$ -subunits were visualized in the YFP- and barttin in the CFP-channel. Total cell lysates (t) and surface membrane fractions (s), obtained from biotinylation assay, were loaded pairwise onto the gel. Relative plasma membrane expression of CIC-K proteins was determined by dividing of surface membrane fluorescence intensity by intensity of total cell lysate and normalizing this to the condition hCIC-Ka + barttin. All data show mean values  $\pm$  S.E.M. ( $n=3$  (HEK293T),  $n=3$  (MDCKII)). Statistical difference was tested by one-way ANOVA. Western blot (WB) detecting GAPDH was used to exclude contamination of surface membrane fractions by cytosolic proteins. K1 (+ B) = rCIC-K1 (+ barttin), B\_K1 (+ B) = barttin\_rCIC-K1 (+ barttin), B\_B\_K1 (+ B) = barttin\_barttin\_rCIC-K1 (+ barttin).

an expected molecular weight of 110 to 150 kDa and was lower expressed than the  $\alpha$ -subunit monomer. The concatamer barttin\_barttin\_rCIC-K1 in absence of barttin excess migrated at around 170 to 180 kDa and was lower expressed than the rCIC-K1 monomer and barttin\_rCIC-K1. In presence of additional barttin the expression level for rCIC-K1 monomers as well as for the concatamers was reduced. Moreover, in presence of barttin the complex-glycosylated monomer/concatamer fraction almost vanished. These results are in complete accordance with the hCIC-Ka/barttin concatamers. However, the difference between barttin\_rCIC-K1 and

barttin\_barttin\_rClC-K1 under barttin excess was not significant as for hClC-Ka. The insert in figure 15A visualizes a linear relationship between the molecular weight and the relative protein expression comparable to figure 12A. The longer the concatamer sequence the lower is the fluorescence intensity and therefore also the expression. A further barttin excess decreased the slope of linear regression.

To test the subcellular distribution of rClC-K1 concatamers, confocal microscopy was performed. MDCKII cells were imaged 48 h after transfection with plasmids encoding the desired proteins. YFP fluorescence of  $\alpha$ -subunits/concatamers is depicted in red and CFP fluorescence of  $\beta$ -subunits in green (Fig.15B). rClC-K1 in absence of barttin stayed intracellularly in major parts but also entered the plasma membrane (a). In presence of barttin  $\alpha$ - and  $\beta$ -subunits channel complexes were well transported to the surface membrane (b). The single fluorescence channels are shown on the left side of this merged picture. On the right side the same recording together with transmitted light demonstrates that successfully transfected cells belonged to a confluent monolayer showing specific fluorophore expression without any auto-fluorescence of non-transfected cells. Barttin\_rClC-K1 in absence of further  $\beta$ -subunits also localized at the plasma membrane, demonstrating that one  $\beta$ - per  $\alpha$ -subunit is sufficient for proper rClC-K1 transport (c). In contrast to approaches with hClC-Ka concatamers, cytosol of some transfected MDCKII cells displayed uniform YFP staining, which is not expected for fluorescent tags fused to membrane-associated proteins. It was probably caused by some degradation of rClC-K1 concatamers leading to freely floating YFP molecules within the cytosol. The excess of  $\beta$ -subunits led again to a clear surface membrane localization of this concatamer and barttin (d). Same holds true for barttin\_barttin\_rClC-K1 in absence (e) and presence (f) of additional  $\beta$ -subunits. In both cases this concatamer was well transported to the plasma membrane. Also barttin\_barttin\_rClC-K1 exhibited a pronounced degradation leading to free YFP in the cytosol. Therefore, it seems to be a special and characteristic finding for rClC-K1 constructs.

To substantiate the insertion of rClC-K1 concatamers into surface membrane and to confirm confocal microscopy, biotinylation experiments were performed analogously to hClC-Ka concatamers as described above. Figure 15C represents fluorescence scans of electrophoresed protein lysates from HEK293T (left) and MDCKII cells (right), revealing the relative surface membrane fraction of YFP- and CFP-labeled proteins compared to the whole cell fraction. The upper lane depicts the YFP fluorescence of the  $\alpha$ -subunit unlinked or linked

to  $\beta$ -subunits. CFP fluorescence of additional barttin expression is shown in the middle line and GAPDH, which was detected by Western Blot, in the lowest line. rClC-K1 in absence and presence of barttin was integrated into plasma membrane for HEK293T and MDCKII cells. Also both concatamers with one or two barttins bound to one  $\alpha$ -subunit were able to reach the surface membrane. For all conditions plasma membrane fraction comprised a higher fraction of complex-glycosylated channels compared to the total cell fraction. In HEK293T cells barttin predominantly promoted the plasma membrane insertion of non-/core-glycosylated channels, while in MDCKII cells mainly complex-glycosylated channels were incorporated into the surface membrane. As for hClC-Ka concatamers, surface membrane expression depends on total  $\alpha$ -subunit/concatamer expression, which decreased for proteins with higher molecular weight (see also Fig.15A). To compare the relative plasma membrane fraction of all tested conditions, the surface membrane fractions of the  $\alpha$ -subunits were normalized to the fractions of the total cell lysate. This quantification is shown in bar graphs, which include results from three gels. There was no significant difference in relative surface membrane expression for all tested constructs. This finding is in accordance with confocal imaging for both concatamers and proves the insertion of concatamers into the surface membrane. Noteworthy, the presence or absence of barttin did not alter the relative plasma membrane expression of rClC-K1. This seems in contradiction to confocal microscopy and literature results that demonstrated an enhancement of ClC-K channel insertion into the plasma membrane by barttin (Scholl et al., 2006). As for hClC-Ka concatamers this finding is commented in the 'discussion' chapter. Western blots detecting GAPDH showed that there is no contamination of plasma membrane fractions by cytosolic compounds because GAPDH was only visible in whole cell lysate fraction (Fig.15C, lowest panels).

### 3.1.6 Two $\beta$ -subunits per $\alpha$ -subunit are sufficient to increase rClC-K1 currents similar to barttin excess

For hClC-Ka we found that  $\alpha$ : $\beta$ -subunit stoichiometry has a remarkable influence on whole cell current amplitudes by modulation of single pore parameters. In a next step, it was tested how the  $\alpha$ : $\beta$ -subunit stoichiometry affects the rClC-K1 channel properties. Figure 16A demonstrates representative patch clamp recordings of rClC-K1 as well as rClC-K1/barttin concatamers in absence and presence of co-expressed barttin. Corresponding IV-plots, which were measured immediately after initial capacitive peak, are shown in figure 16B. Without barttin rClC-K1 currents revealed a time-dependent current decrease upon depolarization and

an increase upon hyperpolarization. IV-plot shows a rather linear relationship especially under negative voltages and a mean current amplitude of 2.4 nA at +105 mV (Fig.16B,C, white dots/bars). rClC-K1 currents changed their kinetics under co-expression of excessive amounts of barttin. Here, current traces lost time-dependence. Instead, IV-plots revealed a hyperpolarization-induced reduction of current amplitudes (Fig.16B, black dots). Both missing time-dependent gating and the hook-shaped IV-plot have been reported to be characteristic features of the human hClC-Ka. The here obtained results, however, indicate that these features are also characteristic for rClC-K1. The barttin-dependent current increase results in a mean current amplitude of 6.4 nA at +105 mV (Fig.16C, black bars).

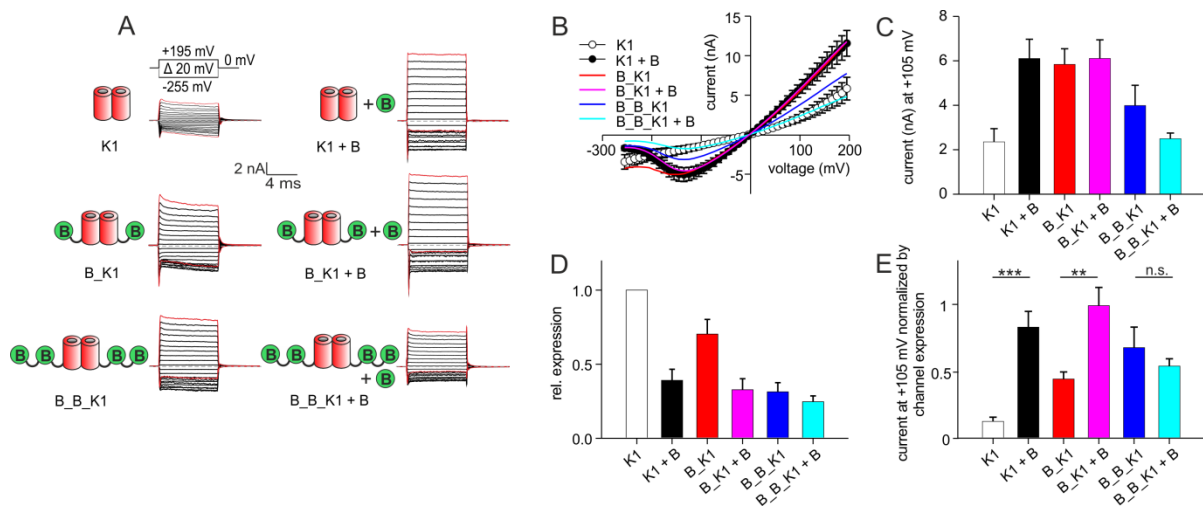


**Fig. 16 Currents of rClC-K1/barttin concatamers in absence and presence of additional barttin**

(A) Representative current traces of rClC-K1 concatamers in absence and presence of additional barttin after application of voltages between -255 mV and +195 mV. Red colored current traces represent currents at voltages at -255 mV and +195 mV. Dashed line represents 0 nA. (B) IV-plots of all tested rClC-K1 stoichiometries, measured immediately after initial capacitive peak. All values are shown as mean  $\pm$  S.E.M. for K1 and K1 + B. (C) Mean current at +105 mV. All data are shown as mean  $\pm$  S.E.M.. (D) Relative expression levels of rClC-K1 monomers/concatamers in absence and presence of additional barttin as shown in Fig.15A (E) Mean current at +105 mV normalized to channel expression as shown in (D). All data are shown as mean  $\pm$  S.E.M.. Statistical significance was tested using Student's t-test. B,C,E: K1: n=11, K1 + B: n=13, B\_K1: n= 21, B\_K1 + B: n=14, B\_B\_K1: n= 10, B\_B\_Ka + B: n=9, \*\* p < 0.01, \*\*\* p < 0.001, n.s. = not significant. K1 (+ B) = rClC-K1 (+ barttin), B\_K1 (+ B) = barttin\_rClC-K1 (+ barttin), B\_B\_K1 (+ B) = barttin\_barttin\_rClC-K1 (+ barttin).

For the concatamer barttin\_rClC-K1 instantaneous currents decreased under positive and increased under negative potentials similar to the condition in absence of barttin (Fig.16A). However, now a hyperpolarization-induced current reduction became apparent, being one hint for interaction of the linked barttin with the channel protein (Fig.16B, red line). Furthermore, current amplitudes were increased to 5.8 nA at +105 mV (Fig.16C, red bar). A barttin excess by co-expression led to a diminished time-dependent gating and a pronounced hook-shaped IV-plot as observed for rClC-K1 in co-expression of barttin (Fig.16A,B, pink line). Mean current amplitude was 6.1 nA at +105 mV (Fig.16C, pink bar).

Currents of barttin\_barttin\_rClC-K1 showed a slight time-dependent gating but a more apparent hyperpolarization-induced block demonstrating an even stronger barttin influence as compared to barttin\_rClC-K1 (Fig.16A,B, blue line). The mean current amplitude was 4 nA at +105 mV (Fig.16C, blue bar) and thus lower than for barttin\_rClC-K1. The presence of more  $\beta$ -subunits led to a further current reduction to 2.5 nA at +105 mV but also to a reduced time-dependent gating, which was observable for all the other channel constructs, too (Fig.16A,B,C). However, as for hClC-Ka, it was necessary to normalize currents to expression levels shown in figure 16D. Normalization unraveled that currents could be boosted by additional barttin expression for channel subunits with no or only one linked barttin (Fig.16E). Only if two barttins were linked to one channel subunit, additional barttin expression did not lead to a further current increase. This is conform to results of hClC-Ka, which indicate that two barttins per channel subunit are necessary for full activation of ClC-K in both subtypes of channel.

### 3.1.7 Two $\beta$ -subunits per $\alpha$ -subunit are sufficient to maximally induce hyperpolarization block

Because the reduction of current amplitudes at negative voltages seemed to be one possible criterion to quantify the effect of rClC-K1/barttin stoichiometry on channel function, we analyzed this hyperpolarization-induced current reduction for the different  $\alpha$ : $\beta$ -subunit compositions more precisely. As similar current reduction at negative voltages was also observed for hClC-Ka, the current reduction for rClC-K1 is, consistently, also called 'block' in the following parts even though the exact mechanism is not known so far. Figure 17A collects IV-plots of instantaneous current amplitudes from concatamers in presence and absence of barttin excess. IV-plots were normalized to the current at +105 mV to compare their shape. We calculated relative conductances for rClC-K1/barttin concatamers by fitting a linear regression line to the IV-data between -55 mV and +55 mV, where open probability was high and voltage independent. Here maximum relative channel conductance was set to 1 ( $G_{max}$ ), revealing lower relative conductances for currents obtained at hyperpolarized membrane potentials (G).

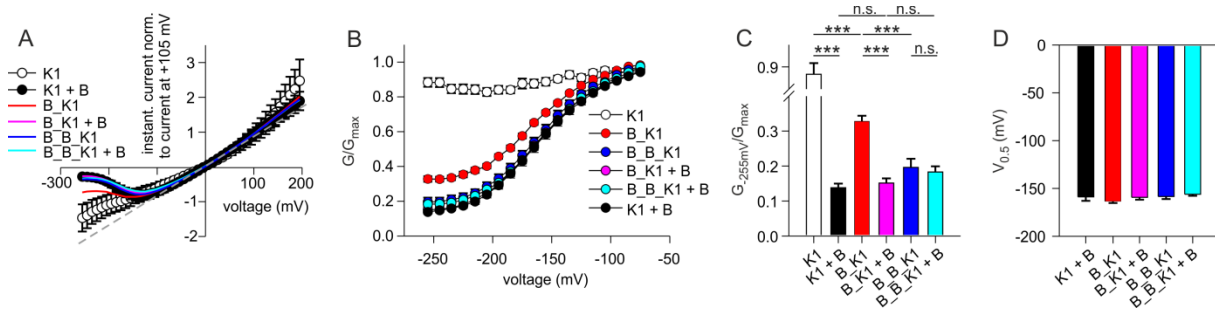


**Fig. 17 Influence of barttin availability on hyperpolarization-induced block of rClC-K1**

(A) IV-plot of instantaneous rClC-K1 currents, obtained from currents as shown in Fig.16A. All data are shown as mean values ( $\pm$  S.E.M. for K1 and K1 + B). Dashed line represents linear regression of currents between -55 mV and +55 mV. (B) Relative conductances at negative voltages of all tested stoichiometries, obtained from current deviations from linear regression in (A). (C) Relative conductances at -255 mV for all tested stoichiometries. (D) Voltage of half maximum conductance ( $V_{0.5}$ ) obtained from fits of conductance curves from (B). (B)-(C): all values are shown as mean  $\pm$  S.E.M.. K1: n=11, K1 + B: n=13, B\_K1: n=21, B\_K1 + B: n=14, B\_B\_K1: n=10, B\_B\_K1 + B: n=9. For (C) and (D) statistical significance was tested by one-way ANOVA with in (C) subsequent Holm-Sidak post hoc test:  $F_{(7, 93)} = 137.4$  and  $p < 0.001$ . K1 (+ B) = rClC-K1 (+ barttin), B\_K1 (+ B) = barttin\_rClC-K1 (+ barttin), B\_B\_K1 (+ B) = barttin\_barttin\_rClC-K1 (+ barttin).

Voltage-dependence of mean relative conductances ( $G/G_{max}$ ) is summarized in figure 17B for all tested conditions. Since deviation from linear regression appeared small for rClC-K1 in absence of barttin, relative conductances above 80% were obtained for the whole range of negative voltages (white dots). The presence of one barttin per channel subunit intensely promoted deviation from linear dependency. Minimum relative conductances declined to 0.33 at -255 mV (Fig.17A,B,C, red dots/bar). Moreover, when two barttins were linked to one channel subunit relative conductances decreased even to 0.2 at -255 mV (Fig.17A,B,C, blue dots/bar). Further barttin excess did not cause any significant change (Fig.17A,B,C, pink, cyan, black dots/bar). This confirms the hypothesis that two barttin molecules per channel subunit are necessary and sufficient to obtain full effect on ClC-K channels. Boltzmann functions could be fitted to relative conductance curves for all conditions with the exception of rClC-K1 without barttin. Voltage of half maximum channel conductance ( $V_{0.5}$ ) was determined, resulting in comparable values for all constructs (Fig.17D).

So far, hyperpolarization-induced current ‘block’ has been reported for hClC-Ka but not for rClC-K1. Thus, the underlying mechanism for this block of rClC-K1 has not been investigated, yet. As described before, macroscopic currents depend on the number of active membrane pores, the single pore current and the pore’s open probability. Because number of active membrane pores was not supposed to change during measurements, it was rational to consider only open probability and single pore current amplitude. For hClC-Ka it has been shown above that stationary noise analyses revealed plots with linear dependence of current variance divided by  $(I \cdot (V - V_{rev}))$  versus macroscopic conductance  $(I / (V - V_{rev}))$  (see Fig.14). We now took advantage of the rClC-K1 characteristic in presence of barttin excess, which is similar

to hClC-Ka, to perform stationary noise analysis for this type of channel as well. As described above, voltages between -5 to -255 mV were applied (Fig.18A). The more negative the applied voltage was the higher was the current noise. Parameters for current and current noise were obtained at negative voltages and plotted like in figure 14B. A representative noise analysis for rClC-K1 together with barttin excess is visualized in figure 18B. Obviously, data points resembled a linear regression, proving that single pore conductance did not change for the voltage range, where hyperpolarization block occurred. If single pore current amplitude would have decreased upon hyperpolarization, regression would be non-linear with lowered slope at lower conductances (Fig.18C). Therefore, hyperpolarization-induced block was presumably caused by changes in open probability and not by reduction of single pore currents. A chloride conductance of around 17 pS was obtained as represented by the y-axis intercept of linear regression (Fig.18D). Based on single channel measurements, Fischer et al. (2010) published a chloride conductance of around 33 pS for rClC-K1. However, it has been unclear whether this value reflected single or double pore conductance. High open probabilities for both protopore gates, which were permanently open, in combination with a lowered open probability for the common gate, which showed opening and closing events, might have masked double pore as single pore events. Results of the here shown noise analysis demonstrate that the previously determined 33 pS reflects double pore conductance and the here obtained 17 pS single pore conductance for rClC-K1 in presence of barttin. Decreasing channel open probabilities were responsible for hyperpolarization-induced block. The voltage-dependence of this 'block' is visible in figure 18E, where we plotted the mean absolute open properties of the channel, given by the conductance at different voltages normalized to the maximum absolute macroscopic conductance, which is represented by the x-axis intercept of the regression line in Fig.18B. By stationary noise analysis absolute conductances and open probabilities could be obtained, which decreased at negative voltages ( $V_{0.5} = -158.4 \pm 6.4$  mV;  $P_{\min} = 0.16$ ). As absolute open probabilities from noise analysis, which were near 100% at 0 mV, are in very good agreement with the voltage-dependence of relative conductances as obtained from IV-plots (compare Fig.17B) it can be assumed that maximum relative conductance ( $G_{\max}$ ) corresponds to a condition where all channels are open and maximally conducting.



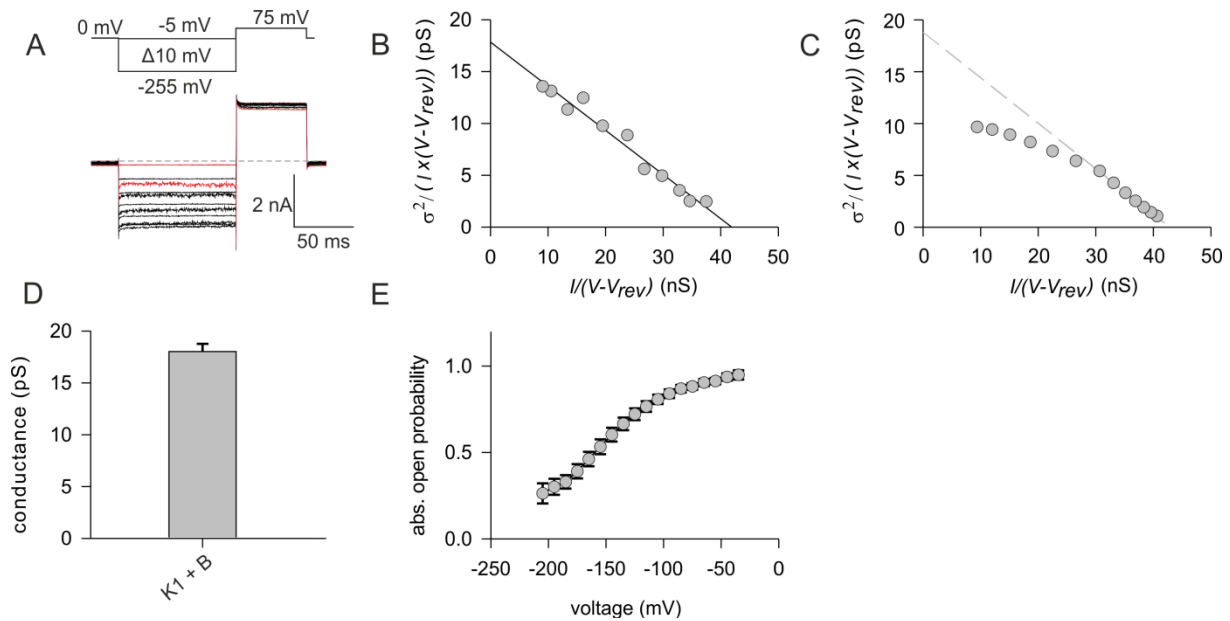


**Fig. 18 Stationary noise analysis of rClC-K1 with barttin co-expression**

(A) Representative current trace of rClC-K1 + barttin used for stationary noise analysis. Voltages from -5 mV to -255 mV were applied for 100 ms followed by +75 mV for 50 ms. For more negative voltages current decreases with increasing noise. Red colored current traces represent current at -255 mV and -5 mV. Dashed line represents 0 nA. (B) Representative stationary noise analysis for rClC-K1 in presence of barttin. Data points were fitted by linear regression. (C) Simulation of stationary noise analysis for a ClC-K channel, whose single pore conductance decreases successively from 19 pS to 10 pS at voltages lower than -135 mV. Simulation was conducted using equations 3, 6 and 7. Dashed line represents linear regression, if single pore conductance would not decrease for more negative voltages. (D) Mean chloride conductance of rClC-K1 plus barttin, obtained by y-axis intercepts of linear regressions as in (B). Data are shown as mean  $\pm$  S.E.M.. (E) Absolute open probabilities of rClC-K1 plus barttin at negative voltages, determined from (B). All data in (D) and (E) are shown as mean  $\pm$  S.E.M. (n=11 in (D) and n=10 in (E)).

### 3.1.8 One $\beta$ -per $\alpha$ -subunit opens rClC-K1 slow gate and two $\beta$ -subunits open its fast gate

Besides the induction of hyperpolarization-induced block, barttin excess seems to alter time-dependent gating of rClC-K1. This finding motivated us to focus on the influence of ClC-K/barttin stoichiometry on gating processes, mediated by the fast action of two individual protopore gates, and one common slow gate that regulates both protopores of the dimer simultaneously. For this, we applied voltage steps between -155 and +145 mV over a longer period of time (300 ms) followed by a shorter test pulse (100 ms). Figure 19A demonstrates a representative measurement of rClC-K1 with a comparable voltage protocol as used by Fischer et al. (2010). In absence of barttin rClC-K1 current quickly increased upon hyperpolarization, which was referred to the opening of the fast protopore gates. Subsequently, current slowly decreased, which was attributed to the closing of the slow common gate exhibiting an inverse voltage-dependence as compared to the fast gates. Under depolarization, respectively, fast gates tended to close and the slow gate opened. This characteristic time-dependent gating behavior, which was observed here, accords very well to that one, described previously for rClC-K1 in absence of barttin (Fischer et al., 2010).

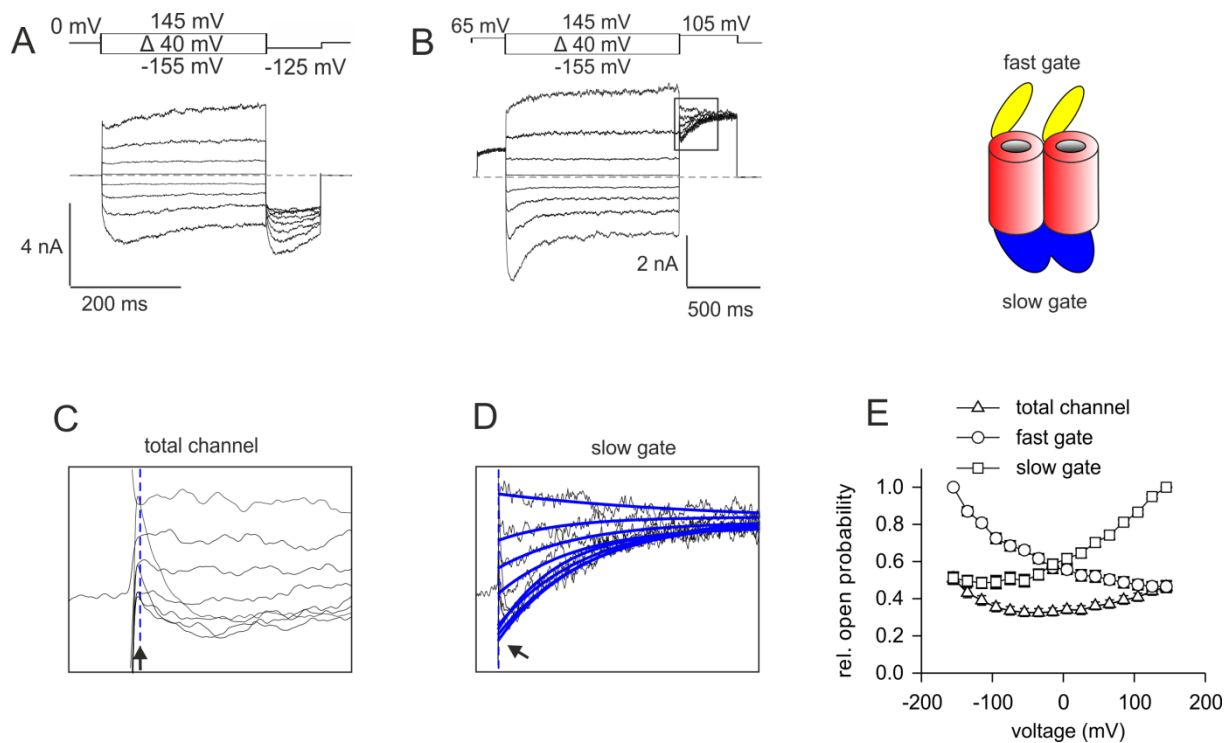


**Fig. 19 Determination of fast gate, slow gate and total rClC-K1 channel open probability in absence of barttin**

(A) Representative current traces of rClC-K1 in absence of barttin at voltages between -155 mV and +145 mV for 300 ms. Currents show clear fast and slow gating components. Dashed line represents 0 nA. (B) Representative current traces of rClC-K1 in absence of barttin at voltages from -155 mV to +145 mV for 1.2 s. Dashed line represents 0 nA. Black frame surrounds instantaneous current of the test pulse at +105 mV, magnified in (C) and (D) and used for determination of relative total channel and slow gate open probabilities. (C) Determination of relative total channel open probabilities by plotting the current amplitudes at the beginning of the test pulse (blue dashed line + arrow) against respective voltages of the pre-pulse. (D) Determination of relative slow gate open probabilities by fitting mono-exponential functions into slow current relaxation during test pulses at +105 mV. Mono-exponential functions were fitted back to the previous voltage step (blue dashed line + arrow). Current amplitudes at this time point correspond to relative slow gate open probabilities. (E) Combination of slow gate (rectangle), fast gate (triangle) and total channel (circle) activation curves of rClC-K1. Relative fast gate open probabilities were re-calculated as the quotient of total channel and slow gate open probabilities (see equation 1). Data are shown as mean values  $\pm$  S.E.M. ( $n \geq 6$ ). Channel model at the top right illustrates protopore fast gates (yellow) and common slow gate (blue).

To determine the relative open probabilities of fast gate, slow gate and of the total channel under different voltages, similar voltage protocols were used as in figure 19A leading to voltage and time-dependent adaption of gating processes (Fig.19B). For a better visualization of gating processes longer voltage pulses as in figure 19A were shown. After reaching a steady state open probability, a test step to +105 mV was applied and instantaneous tail current amplitudes were used to calculate the relative open probabilities of the total channel ( $rel. P_o = I/I_{max}$ ). Voltage-dependence of such open probabilities is plotted in figure 19E (triangles). Lowest open probabilities were observed around -35 mV with higher values upon hyper- and depolarization. Tail current traces at the applied test pulse showed a clear bi-phasic shape. After an early and very fast current decrease a slow current increase was observed, which could be exclusively attributed to slow gating. Notably, changes of slow gate open probability must have started directly after the voltage step although masked by fast gating processes. To extract pure slow gate open probabilities the slow current relaxations were fitted back to the

voltage step by mono-exponential functions (blue lines) and the instantaneous current amplitudes from such fits were used (arrow and blue dashed line) to calculate relative slow gate open probabilities (Fig.19D). They were lowest for negative voltages and increased at positive voltages (Fig.19E, rectangle). Since the total channel open probability is the product of fast and slow gate open probability, relative fast (protopore) gate open probabilities were calculated as the quotient of total channel and slow (common) gate open probability as described in methods chapter 2.2.7.4 (according to equation 1).

$$P_p = P_{total} / P_c$$

Relative fast gate open probabilities were inversely voltage-dependent compared to slow gate open probabilities. Their highest value was found at -155 mV, while open probabilities decreased for more positive potentials (Fig.19E, circles).

The presence of barttin – either linked to the pore subunit or added in co-expression – changed the shape of current traces. In contrast to rClC-K in absence of barttin, slow current relaxations vanished and only fast gating processes remained. This finding agrees with previous publications, that report a constitutively opened slow gate in presence of barttin (Fischer et al., 2010; Wojciechowski et al., 2015; Wojciechowski et al., 2018b). Notably, the amount of fast time-dependent gating varied considerably between cells. Typical examples are shown in figure 20A. We sorted cells into three groups with more or less time-dependent gating. For this, we took advantage of voltage steps from -155 mV to +105 mV and analyzed the current relaxation at +105 mV. A quotient between the steady state current ( $I_{ss}$ ) and the instantaneous current ( $I_{inst}$ ) was calculated. If steady state tail currents at +105 mV were below 60% of the maximum tail current amplitude ( $I_{ss}/I_{inst} < 0.6$ ), cells were classified as phenotype with + (strong) time-dependent fast gating. These current responses were very similar to previously published measurements of rClC-K1 in presence of co-expressed barttin, which exhibited an open slow gate under the here used pulse lengths and a fast gate with voltage-dependent open probabilities (Fischer et al., 2010).

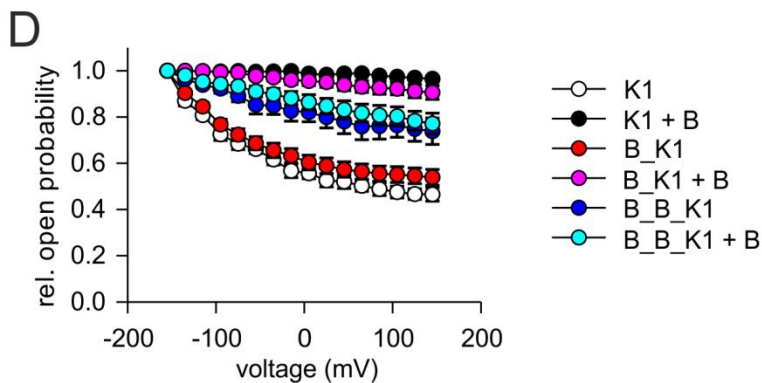
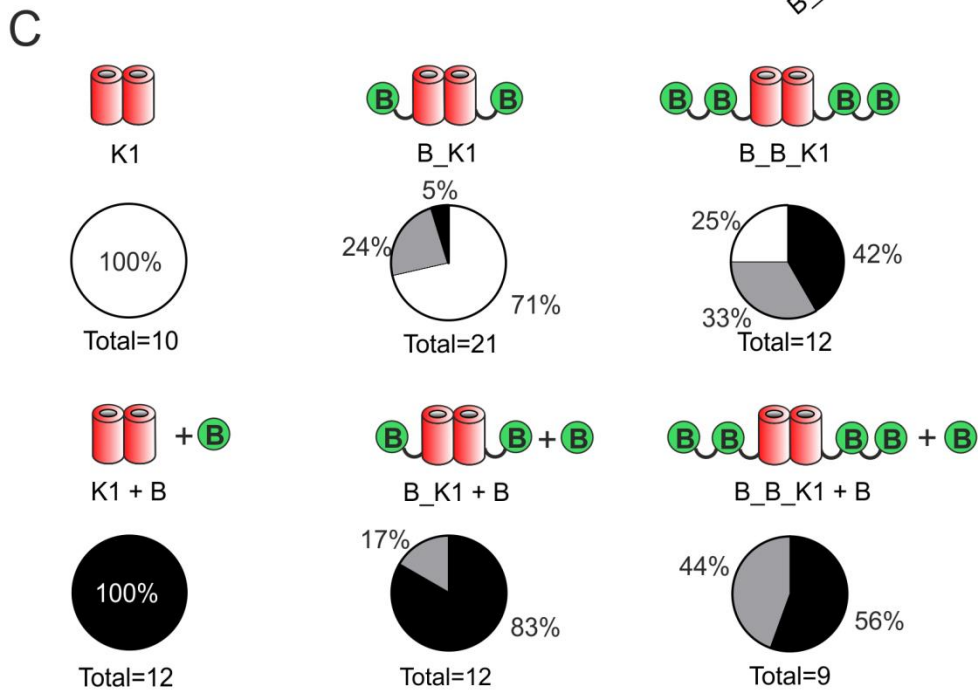
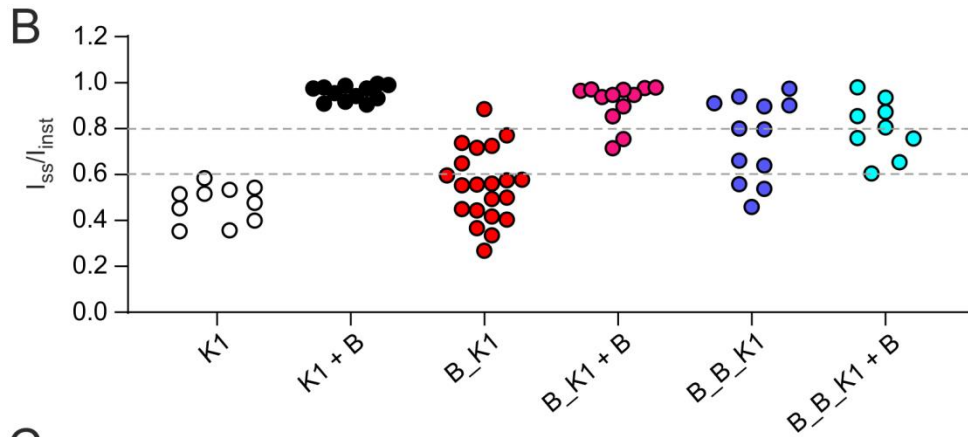
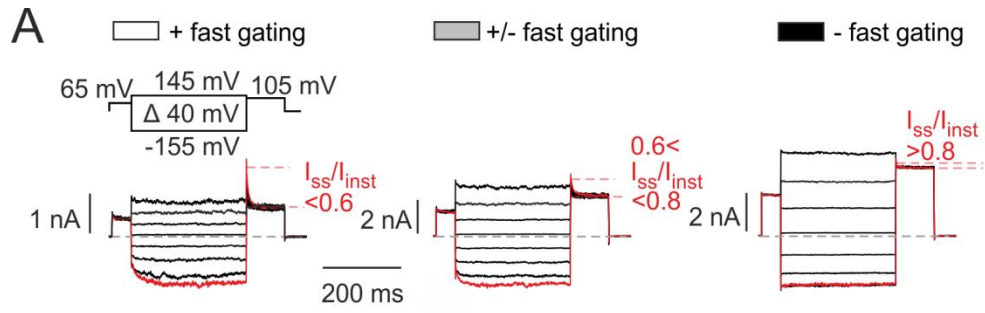


**Fig. 20 Time-dependent fast gating of rClC-K1 under different  $\alpha:\beta$ -subunit stoichiometries**

(A) Categorization of time-dependent fast gating of rClC-K1 currents for different barttin availabilities. Cells were sorted as strong time-dependent (white color), when after the voltage step from -155 mV to +105 mV the steady state current amplitude ( $I_{ss}$ ) was lower than 60% of instantaneous current amplitude ( $I_{inst}$ ), as medium time-dependent (grey color), when  $I_{ss}/I_{inst}$  was between 60% and 80% and as weak time-dependent (black color), when  $I_{ss}/I_{inst}$  was higher than 80%. Red colored current traces represent relevant traces for categorization and dashed grey line 0 nA. (B) Scatter plot of cells measured under different  $\alpha:\beta$ -subunit stoichiometries according to their  $I_{ss}/I_{inst}$  values. Each dot is one measured cell. Dashed lines represent thresholds for categorization as in (A). (C) Distribution of cells under different barttin availabilities after categorization into the three classes as in (A) visualized as pie charts. Colors accord to color code as in (A). (D) Relative fast gate open probabilities under different barttin availabilities, determined by plotting instantaneous current amplitudes during test pulse *versus* voltages of the pre-pulse. For rClC-K1 fast gate open probabilities were taken from Fig.19E. Data in (D) are shown as mean values  $\pm$  S.E.M.. K1: n=10, K1 + B: n=12, B\_K1: n=21, B\_K1 + B: n=12, B\_B\_K1: n=12, B\_B\_K1 + B: n=9. K1 (+ B) = rClC-K1 (+ barttin), B\_K1 (+ B) = barttin\_rClC-K1 (+ barttin), B\_B\_K1 (+ B) = barttin\_barttin\_rClC-K1 (+ barttin).

Cells with  $I_{ss}/I_{inst}$  between 60% and 80% were sorted into a group with +/- (medium) time-dependent fast gating and cells with  $I_{ss}/I_{inst}$  higher than 80% were defined as subtype with - (weak) time-dependent fast gating. Using these criteria for categorization, HEK293T cells expressing the diverse constructs of rClC-K1/barttin channels were sorted according to their fast gate relaxation mode in figure 20B. Cells expressing rClC-K1 in absence of barttin were also included in this graph. In this case, however, fast gate current relaxations were difficult to extract from bi-phasic tail current traces. We therefore took fast gate open probabilities from figure 19E (circles) and divided steady state open probabilities at +105 mV by steady state open probabilities at -155 mV which would closely resemble the current relaxation by fast gate closure, if slow gating was absent. As shown in the scatter plots of figure 20B and pie charts of figure 20C, rClC-K1 in absence of barttin (white dots) showed strong time-dependent fast gating for all cells. When barttin was co-expressed additionally to the  $\alpha$ -subunit, rClC-K1 generated only weak time-dependent fast gating (Fig.20B, black dots, C). For the concatamer barttin\_rClC-K1 the majority of cells (68%) showed strong time-dependent fast gating (Fig.20B, red dots, C). Barttin\_rClC-K1 in co-expression of extra barttin led to a great portion of cells exhibiting weak time-dependent fast gating (83%, Fig.20B, pink dots, C). However, 17% of cells showed medium time-dependent fast gating. Connecting two barttins to one rClC-K1, data points were shifted towards weak time-dependent gating compared to barttin\_rClC-K1 (Fig.20B, blue dots). Even 42% of cells had weak time-dependent gating, 33% medium and 25% strong time-dependent gating (Fig.20C). So, the more barttin molecules were covalently linked to rClC-K1 the weaker was the time-dependent fast gating. Cells expressing barttin\_barttin\_rClC-K1 in presence of extra barttin were classified at 44% as medium and at 56% as weak time-dependent fast gating (Fig.20B, light blue dots, C). This indicates that the effect of additional expressed barttin to attenuate time-dependent fast gating lessens the more  $\beta$ -subunits are linked to one  $\alpha$ -subunit. In total, pie charts in figure 20C demonstrate that the prevalence of weak time-dependent gating raised the more barttin molecules were

connected to one  $\alpha$ -subunit (black area enlarges). Moreover, the co-expression of barttin induced a further shift towards weak time-dependent fast gating. If two barttins were linked to one  $\alpha$ -subunit, values for with and without barttin co-expression converged.

Representative current recordings for all tested conditions and categories are given in supplemental figure 1.

Since current relaxations represent time-dependent changes in open probabilities, the voltage-dependence of fast gate open probabilities is summarized for all conditions in figure 20D. Values were obtained from instantaneous tail current amplitudes at the +105 mV test step and normalized to the maximum tail current amplitude as observed for a pre-potential of -155 mV. In case of rClC-K1 in absence of barttin the relative fast gate open probabilities were taken from figure 19E. All conditions had highest fast gate open probabilities at -155 mV and lowest at +145 mV. Data demonstrate, as already indicated by figures 20B and C, that a higher barttin presence increased fast gate open probabilities. Notably, already two barttin molecules, which were connected to one rClC-K1 subunit, were able to considerably higher minimum fast gate open probabilities. This conveys the presumption that two barttin molecules are necessary to obtain constitutive fast gate opening. Barttin co-expression in addition to concatamers increased minimum fast gate open probabilities but not as strong as for the rClC-K1 monomer. Values were lower the more barttin subunits were bound to the  $\alpha$ -subunit (pink, light blue dots). For the here applied pulse lengths the slow gate seemed to open constitutively, if at least one barttin molecule was connected at one  $\alpha$ -subunit. Results of figure 20 indicate that in contrast to previous studies barttin is supposed not only to constitutively open the slow gate but also fast gates of both pores, if all barttin binding sites are occupied.

However, not every cell showed a maximum barttin effect despite two barttin molecules per channel subunit. In general, there is a variation in time-dependent fast gating even for individual conditions. Potential explanations for this remarkable finding are given in the 'discussion' chapter.

### 3.1.9 Effects of rClC-K1/barttin stoichiometry on slow channel gating

In a next step, we reconsidered the effects of barttin on slow gating. So far, it is known that barttin in general opens the slow gate of rClC-K1 constitutively and independent of voltage. Recordings with voltage protocols as shown in figure 20 supported this accepted view by the vanished slow current relaxations. However, a closer look disclosed a residual slow gating

process, especially, if only one barttin is linked to one rClC-K1 subunit (Suppl. Fig.1). To investigate this process in more detail, we applied voltage steps with extended duration, i.e. four times longer than previous protocols (Fig.21), and indeed found slow gating processes with prolonged time constants. In absence of barttin the voltage step from +65 mV to negative voltages led to an initial fast current increase followed by a well-known slow decrease (Fig.21A). This slow process was fitted by mono-exponential functions (blue lines) and we obtained voltage-independent time constants ( $\tau$ ) around 100 ms (Fig.21E, white dots). If one barttin was linked to one rClC-K1 subunit, time constants increased to around 300-400 ms (Fig.21B,E, red dots). Two barttins per channel subunit decelerated slow gating even more, resulting in time constants of around 1 s (Fig.21C,E, blue dots). Notably, this value closely approximates to time constants, when  $\alpha$ -subunits/concatamers were co-expressed with large excess of barttin ( $\sim 1.5$  s) (Fig.21D,E, black dots). These findings indicate that barttin does not totally abolish but decelerates the slow gating process of rClC-K1 channels. Furthermore, deceleration was promoted by the increasing number of available barttins per channel subunit. Presumably, two barttins per rClC-K1 subunit corresponded to the state at which all available binding sites were occupied. Otherwise this was only achieved by excessive barttin co-expression. Due to the less pronounced gating processes at positive voltages, we only focused on time constants at negative voltages.

However, a possible pitfall comes into consideration, when cells are clamped using long-lasting negative potentials. Intracellular depletion of chloride ions could reduce current amplitudes due to limited charge carriers and thus mimic slow gating processes. To rule out this possibility, we tested cells with a specific envelope protocol. We applied negative voltage steps to -135 mV with increasing duration ( $\Delta = 50$  ms) and stepped afterwards to +105 mV for 200 ms (Fig.21F). If the current reduction at negative pre-pulses were caused by depletion of chloride ions and not by gating, instantaneous currents at +105 mV test pulses would stay at constant amplitude, since extracellular solution provides an unlimited number of charge carriers for chloride influx at positive voltages. If the current decrease at -135 mV is caused by reduction of slow gate open probability, instantaneous currents at +105 mV would decrease likewise according to reduced permeability of the cell membrane for chloride ions.

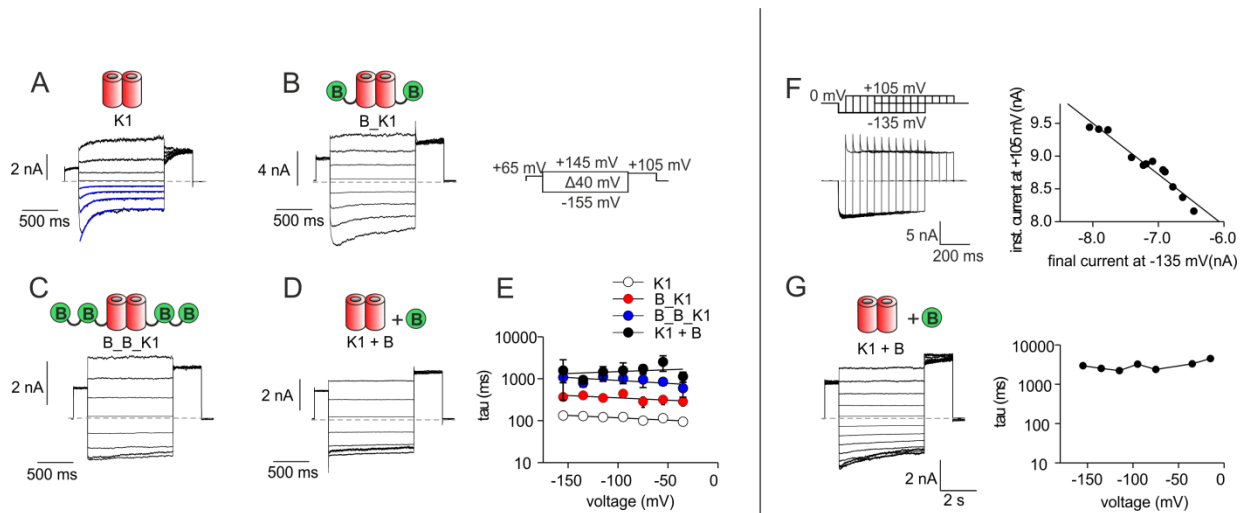


**Fig. 21 Impact of  $\alpha$ : $\beta$ -subunit stoichiometry on slow gate kinetics of rClC-K1**

(A) Representative current traces of K1 used for determination of slow gating time constants. Blue lines demonstrate mono-exponential functions, fitted in slow current relaxations at negative voltages. Voltages steps, used for determination of time constants were 1.2 s long. (B) Representative current traces of B\_K1. (C) Representative current traces of B\_B\_K1. (D) Representative current traces of K1 + B. (A)-(D) dashed lines indicate 0 nA. (E) Slow time constants ( $\tau$ ) obtained from mono-exponential fits of currents as shown in (A)-(D) at negative voltages. Values are given as mean  $\pm$  S.E.M.. K1: n=8, B\_K1: n=7, B\_B\_K1: n=9, K1 + B: n=5. Values were fitted by linear regressions. (F) Protocol and representative current trace used to evaluate potential intracellular chloride ion depletion by long negative voltages. Right panel: Instantaneous currents at +105 mV plotted versus final currents at pre-pulses of -135 mV for different pre-pulse lengths. Values were fitted by linear regression. (G) Representative current trace of K1 + B for voltage steps, which were 4.8 s long. On the right, time constants ( $\tau$ ) of slow current relaxation were plotted against the applied voltages for this shown example registration. K1 = rClC-K1, B\_K1 = barttin\_rClC-K1, B\_B\_K1 = barttin\_barttin\_rClC-K1, K1 + B = rClC-K1 + barttin.

Plotting instantaneous current amplitudes at +105 mV against final current amplitudes at -135 mV revealed a clear, linear correlation between currents under negative and positive potentials. Therefore, intracellular chloride ion depletion could be excluded as reason for current reduction at negative voltages. Time constants of slow gating were very large for rClC-K1 with two barttins bound and therefore possibly underestimated using protocols with step durations of one second. Unfortunately, only very few cells were stable enough to endure voltage pulses for several seconds. Figure 21G shows one example measurement of rClC-K1 in co-expression of barttin excess with voltages applied for 4.8 s. On the right side time constants of slow gating for the same recording were plotted against their respective voltages. They ranged from 2 to 4 s and were higher compared to mean values for the same condition in figure 21E.

### 3.1.10 One barttin per two hClC-Ka $\alpha$ -subunits is not sufficient to facilitate surface membrane transport and channel function

So far, we have seen that one barttin per pore is sufficient to promote surface membrane integration of the channel complex and to open the slow gate of rClC-K1, while hClC-Ka currents remained small. With two barttins per pore, fast gate open probability of rClC-K1



increases and hClC-Ka displays robust currents. We next asked how a single barttin molecule linked to two pores of the dimer would affect the channel conductance. Is one barttin sufficient to open the common slow gate? So, we built two concatamers, i.e. barttin\_hClC-Ka\_hClC-Ka with the human isoform and barttin\_rClC-K1\_rClC-K1 with the rodent isoform. At first, proper expression of barttin\_hClC-Ka\_hClC-Ka was checked in HEK293T cells, which were used for electrophysiological characterization. For this, cells expressing this concatamer were lysed and whole cell lysates were subjected to SDS-PAGE. Figure 22A shows a representative SDS-PAGE gel and expression analysis for hClC-Ka monomers and barttin\_hClC-Ka\_hClC-Ka concatamers in absence and presence of additional barttin. YFP was fused to hClC-Ka monomers and concatamers, and CFP to barttin. The concatamer was expressed with an expected molecular weight of 219 kDa. However, expression level was only around 30% as compared to hClC-Ka monomer expression. The presence of additional barttin caused an even lower expression, which has been shown also for other constructs (compare Figs.12,15). Subcellular localization of barttin\_hClC-Ka\_hClC-Ka was investigated by confocal microscopy (Fig.22B). Here, MDCKII cells were transfected and imaged after expression periods of 48h. In general, expression efficiency of concatamer was very poor and YFP fluorescence mainly localized intracellularly (left image). Co-expression of barttin\_mCFP resulted in partial co-localization of pore-forming subunits (red) and barttin (green) at the plasma membrane (right image). Though, a considerable fraction of pore-forming subunits remained in intracellular compartments. We next aimed to verify observation of confocal microscopy by biotinylation assay. For this, surface membrane proteins were exposed to biotin and subsequently separated from other cytosolic proteins by avidin affinity chromatography. Figure 22C shows a fluorescence scan of whole cell and surface membrane fractions of MDCKII (left) and HEK293T (right) cells, expressing either hClC-Ka monomers or barttin\_hClC-Ka\_hClC-Ka. While hClC-Ka monomers were detected in the surface membrane for both cell lines, fluorescence of barttin\_hClC-Ka\_hClC-Ka was found almost exclusively in the cytosolic fraction. Western blots, detecting GAPDH, demonstrated that plasma membrane fractions were free of cytosolic remnants. This result gives evidence that a linkage of one  $\beta$ -subunit to two  $\alpha$ -subunits is insufficient for proper trafficking to the plasma membrane.

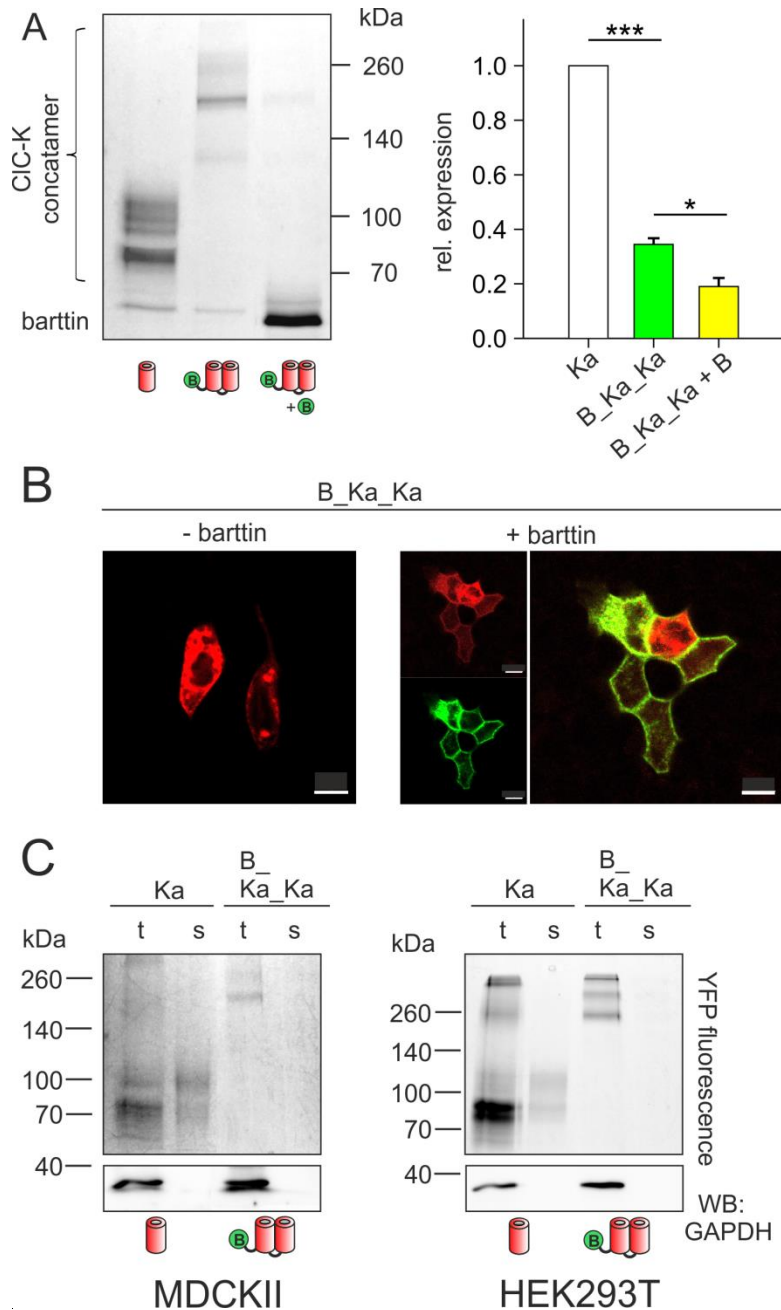


**Fig. 22 Expression and plasma membrane insertion of barttin\_hClC-Ka\_hClC-Ka**

(A) Fluorescence scan of a SDS-PAGE gel with protein lysates from HEK293T cells expressing the Ka monomer or B\_Ka\_Ka in presence or absence of additional barttin. YFP fluorescence of  $\alpha$ -subunits was merged with CFP fluorescence of co-expressed  $\beta$ -subunits (right lane). The faint bands below the Ka monomer and the B\_Ka\_Ka concatamer at around 60 kDa are degradation products of the channel and not barttin molecules. On the right a quantitative expression analysis is shown as bar chart. Relative expression levels were normalized to the expression of the hClC-Ka monomer (white bar). All data show mean values  $\pm$  S.E.M.. Student's t-test was performed to test for significance ( $n=3$ , \*  $p < 0.05$ ; \*\*\*  $p < 0.001$ ). (B) Confocal microscopy images of MDCKII cells, expressing B\_Ka\_Ka\_mYFP in absence (left) or presence (right) of additional barttin\_mCFP. YFP is visualized in red and CFP in green. Colocalization of  $\alpha$ - and  $\beta$ -subunits is visualized in yellow. - barttin = without barttin co-expression, + barttin = with barttin co-expression. Scale bars = 10  $\mu$ m. (C) Fluorescence scan of SDS-PAGE gels with protein lysates from MDCKII (left) and HEK293T cells (right) expressing Ka monomers as well as B\_Ka\_Ka concatamers. YFP-tag of  $\alpha$ -subunits was visualized. Total cell lysates (t) and surface membrane fractions (s), obtained from biotinylation assay, were loaded pairwise onto the gels. Western blot (WB) detecting GAPDH was used to exclude contamination of surface membrane fractions by cytosolic proteins. Ka = hClC-Ka, B\_Ka\_Ka (+ B) = barttin\_hClC-Ka\_hClC-Ka (+ barttin).

Still, we tried to perform patch clamp measurements and obtained small but valid chloride currents for barttin\_hClC-Ka\_hClC-Ka. Figure 23A opposes representative current recordings of barttin\_hClC-Ka\_hClC-Ka in absence (green symbols) and presence of barttin (yellow symbols) as well as the representative currents of hClC-Ka plus barttin (black symbols). Mean concatamer currents were smaller than currents of hClC-Ka plus barttin but also featured the typical hooked-shaped IV-relationship (Fig.23A,B). The presence of further barttin excess increased current amplitudes. Figure 23C compares the mean values at +105 mV (1.7 nA in presence and 1.0 nA in absence of additional barttin). After normalization to protein expression the difference in current amplitudes became significant (Fig.23D).

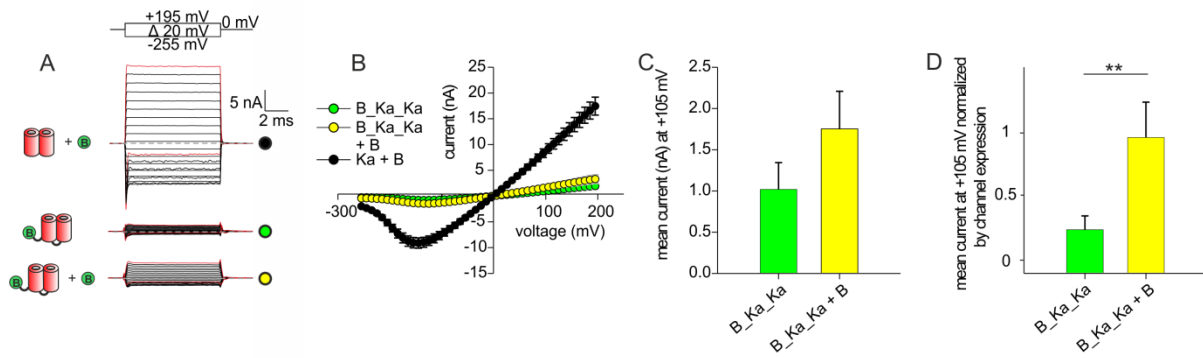


**Fig. 23 Currents of barttin\_hClC-Ka\_hClC-Ka in absence and presence of additional barttin**

(A) Representative current traces of Ka in presence of barttin and B\_Ka\_Ka in absence or presence of co-expressed barttin under application of voltages between -255 mV and +195 mV. Red colored current traces represent currents at voltages of -255 mV and +195 mV. Dashed line represents 0 nA. (B) IV-plot of hClC-Ka dimers/concatamers, showing a hook-shaped IV-relationship at negative voltages. All values are shown as mean  $\pm$  S.E.M.. (C) Mean current at +105 mV. All data are shown as mean  $\pm$  S.E.M.. (D) Mean current at +105 mV normalized to channel expression as shown in Fig.22A. Current traces and mean current values for Ka + B in (A) and (B) are taken from Fig.13. All data are shown as mean  $\pm$  S.E.M.. Statistical significance was tested using Student's t-test. (B)-(D): Ka + B: n=21, B\_Ka\_Ka: n=12 (+9 not included cells without current), B\_Ka\_Ka + B: n=6 (+10 not included cells without current), \*\* p < 0.01. Ka + B = hClC-Ka + barttin, B\_Ka\_Ka (+ B) = barttin\_hClC-Ka\_hClC-Ka (+ barttin).

Stationary noise analysis was performed to obtain single pore parameters as described above for other hClC-Ka/barttin concatamers. As shown by the example in figure 24A, noise increase at negative voltages could be resolved successfully despite relatively small current amplitudes. Representative noise analyses for barttin\_hClC-Ka\_hClC-Ka in absence and presence of barttin excess are visualized in figure 24B. Y-axis intercept of linear regression revealed single pore conductance for the concatamer of around 12 pS, which is in great accordance with the value for a 1:1 stoichiometry (compare Fig.14). Thus, the concatamer presented a reduced single pore conductance, when compared to hClC-Ka plus barttin (Fig.24C, green/black bars). Remarkably, the concatamer's single pore conductance was hardly increased by barttin excess (Fig.24C, yellow bar), which on trend was also noticed for barttin\_barttin\_hClC-Ka (see Fig.14C). Possible explanations for this finding are given in the 'discussion' chapter. Figure 24D shows the voltage-dependence of absolute channel open probabilities, which were determined as described above for other hClC-Ka concatamers. Activation curve of this concatamer was not altered compared to hClC-Ka with barttin excess and  $V_{0.5}$  was not significantly shifted (Fig.24D-E).

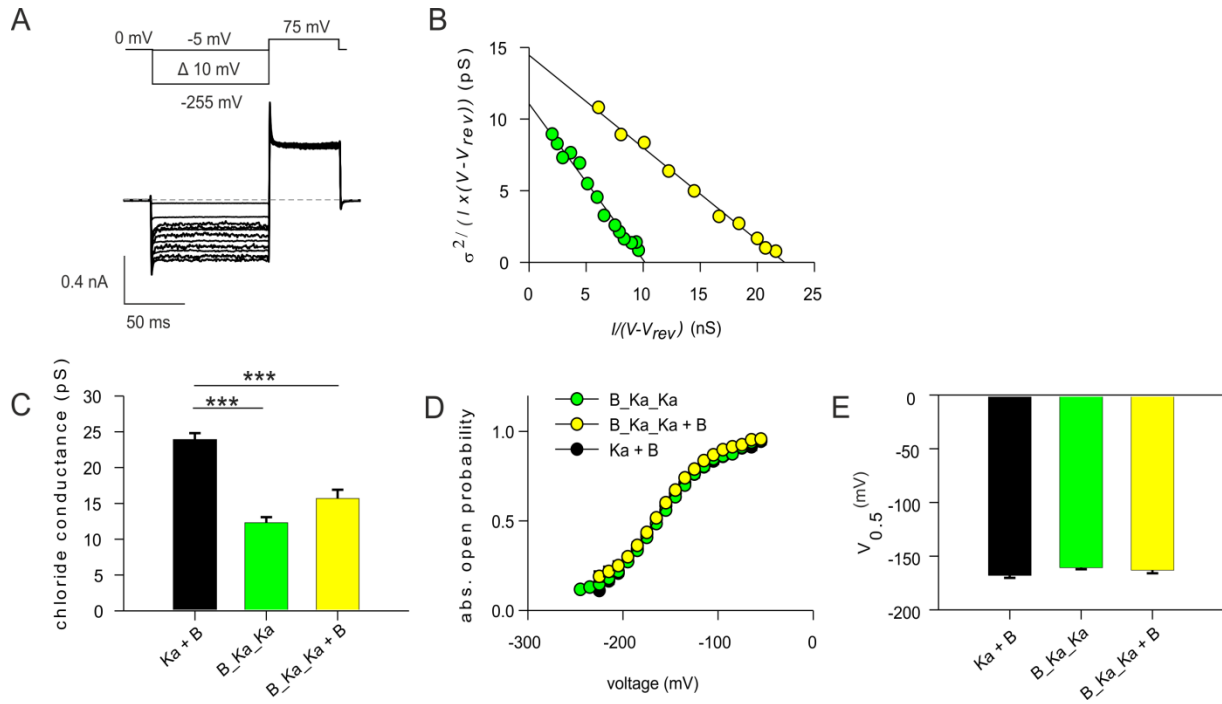


**Fig. 24 Stationary noise analysis of barttin\_hClC-Ka\_hClC-Ka in absence and presence of additional barttin**

(A) Representative current trace of B\_Ka\_Ka used for stationary noise analysis. Voltages from -5 mV to -255 mV were applied for 100 ms followed by +75 mV for 50 ms. For more negative voltages current decreases with increasing noise. Dashed line represents 0 nA. (B) Representative stationary noise analyses for B\_Ka\_Ka in absence and presence of barttin. Data points were fitted by linear regression. (C) Mean chloride conductance of tested hClC-Ka/barttin stoichiometries, obtained by y-axis intercepts of linear regressions as in (B). All data are shown as mean values  $\pm$  S.E.M.. Statistical significance was tested by one-way ANOVA and Holm-Sidak post hoc test versus Ka + B:  $F_{(6, 65)} = 20.2$  and  $p < 0.001$ , Ka + B: n=12, B\_Ka\_Ka: n=10, B\_Ka\_Ka + B: n=6. (D) Absolute open probabilities of tested hClC-Ka/barttin stoichiometries at negative voltages, determined from (B). (E) Voltage of half maximum activation ( $V_{0.5}$ ) obtained from fits of activation curves from (D). Data for Ka + B are taken from Fig.14. All data in (D) and (E) are shown as mean values  $\pm$  S.E.M.. Statistical significance was tested using one-way ANOVA. Ka + B: n=11, B\_Ka\_Ka: n=7, B\_Ka\_Ka + B: n=5. Ka + B = hClC-Ka + barttin, B\_Ka\_Ka (+ B) = barttin\_hClC-Ka\_hClC-Ka (+ barttin).

### 3.1.11 The concatamer possessing one barttin per two rClC-K1 $\alpha$ -subunits is hardly expressed but generates robust currents

The concatamer barttin\_rClC-K1\_rClC-K1 gave the opportunity to investigate the behavior of fast and slow gate, if an rClC-K1 homodimer was supplied with only one barttin molecule. Figure 25A left panel shows a representative SDS-PAGE gel of lysates from HEK293T cells, expressing rClC-K1 monomers or barttin\_rClC-K1\_rClC-K1 in absence and presence of barttin excess. On the right there is a densitometric quantification of respective channel protein expression. The concatamer reached only 16% of monomer expression. The presence of further barttin molecules left expression levels unchanged (15% of the monomer expression). The concatamer migrated at a molecular weight of 219 kDa, which was expected. Next, subcellular localization of barttin\_rClC-K1\_rClC-K1 was determined by confocal microscopy of transfected MDCKII cells (Fig.25B). YFP fluorescence of the concatamer (red) in absence of barttin localized intracellularly with a quite even distribution (left picture). This suggests a concatamer degradation leading to free YFP molecules within the cytosol. Fluorescence scans

of SDS-PAGEs for rClC-K1 concatamers confirmed this presumption by the presence of a distinct degradation product for rClC-K1 concatamers (discussion Fig.47). The excess of CFP-tagged barttin (green) led to a similar channel distribution within the cells (right picture). A faint YFP staining near the plasma membrane for some cells with rather no cytosolic YFP might indicate that the concatamer was transported to the cell surface. Biotinylation assay would help to prove plasma membrane insertion. However, expression levels were so low that this assay failed to give reliable results. We therefore subcloned the construct into a pcDNA3.1 vector with higher transcription rate. But in contrast to any other tested constructs, this vector did not lead to any detectable expression of expected molecular weight for this concatamer in HEK293T or MDCKII cells. Instead, only an intense band of degraded protein was detected (data not shown).

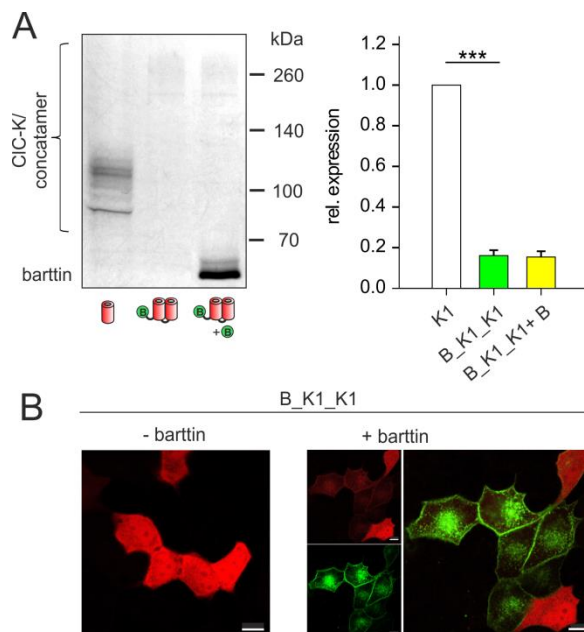


**Fig. 25 Expression and plasma membrane insertion of barttin\_rClC-K1\_rClC-K1**

(A) Fluorescence scan of a SDS-PAGE gel with protein lysates from HEK293T cells expressing the K1 monomer or B\_K1\_K1 in absence or presence of additional barttin. YFP fluorescence of  $\alpha$ -subunits was merged with CFP fluorescence of co-expressed  $\beta$ -subunit (right lane). On the right quantitative expression analysis is shown in a bar chart. Relative expression levels were normalized to the expression of the rClC-K1 monomer (white bar). All data are shown as mean values  $\pm$  S.E.M.. Student's t-test was performed to test for significance ( $n=3$ , \*\*\*  $p < 0.001$ ). (B) Confocal microscopy images of MDCKII cells, expressing B\_K1\_K1 in absence or presence of additional barttin\_mCFP. YFP is visualized in red and CFP in green. Co-localization of  $\alpha$ - and  $\beta$ -subunits is visualized in yellow. - barttin = without barttin co-expression, + barttin = with barttin co-expression. Scale bars = 10  $\mu$ m. K1 = rClC-K1, B\_K1\_K1 (+ B) = barttin\_rClC-K1\_rClC-K1 (+ barttin).

Because for barttin\_hClC-Ka\_hClC-Ka currents could be recorded despite a minimum surface membrane expression, electrophysiology was also performed for the respective rClC-K1 construct. Unexpectedly, recordings displayed robust rClC-K1 currents. Figure 26A shows representative currents of barttin\_rClC-K1\_rClC-K1 without and with co-expression of further barttin. Currents were smaller without co-expression of barttin. However, the hyperpolarization-induced block was prominent for both conditions (Fig.26B). The mean current amplitude of this concatamer at +105 mV was  $3.6 \pm 0.9$  nA without barttin excess and  $6.1 \pm 1.4$  nA with barttin excess (Fig.26C). After normalization to expression levels the

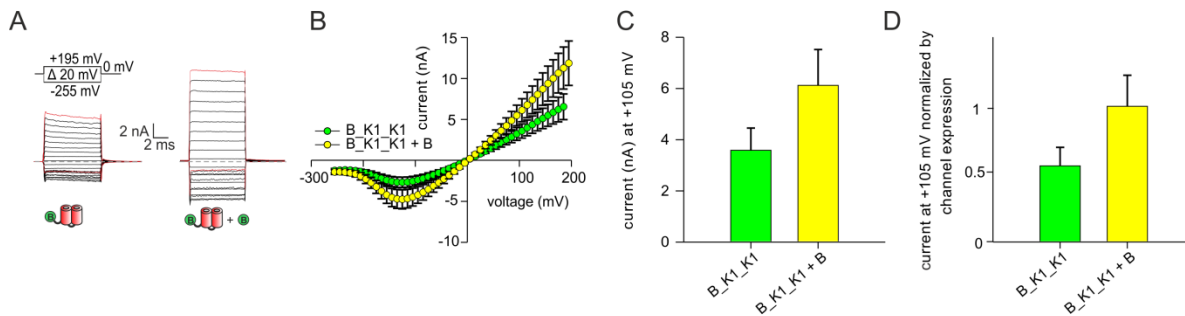
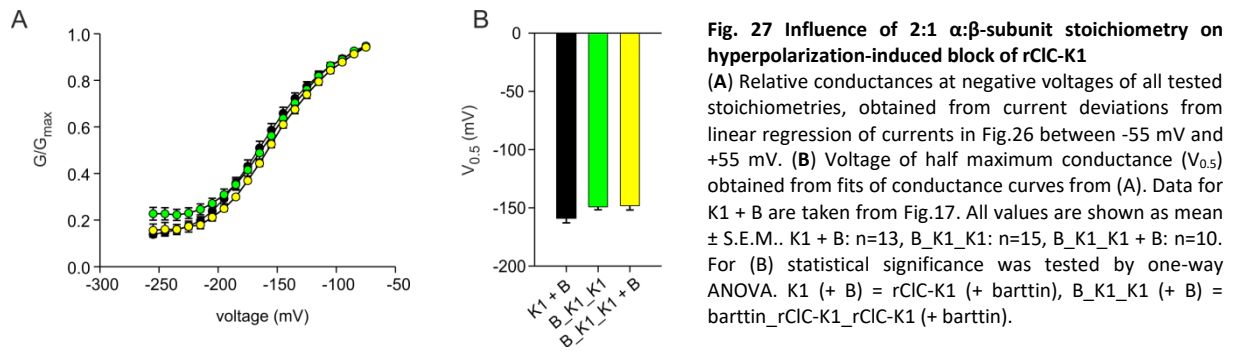


**Fig. 26 Currents of barttin\_rClC-K1\_rClC-K1 in absence and presence of additional barttin**

(A) Representative current traces of B\_K1\_K1 in absence and presence of co-expressed barttin under application of voltages between -255 mV and +195 mV. Red colored current traces represent currents at voltages of -255 mV and +195 mV. Dashed line represents 0 nA. (B) IV-plot of B\_K1\_K1, measured immediately after initial capacitive peak. All values are shown as mean  $\pm$  S.E.M.. (C) Mean current at +105 mV. All data are shown as mean values  $\pm$  S.E.M.. (D) Mean current at +105 mV normalized to channel expression as shown in Fig.25A. All data are shown as mean values  $\pm$  S.E.M. Statistical significance was tested using Student's t-test. B-D: B\_K1\_K1: n=15, B\_K1\_K1 + B: n=10. B\_K1\_K1 (+ B) = barttin\_rClC-K1\_rClC-K1 (+ barttin).

difference between the two conditions was not significant (Fig.26D). Robust current amplitudes of both conditions are in disaccord with results of expression analysis and confocal microscopy, which indicated poor concatamer expression and poor plasma membrane presence. Possible explanations for this finding will be debated in the 'discussion' chapter.

As for other rClC-K1/barttin concatamers the impact of barttin availability on hyperpolarization-induced block was analyzed. Relative channel conductances were determined from IV-plots as described above for other rClC-K1 concatamers and plotted against the applied voltage in figure 27A. Relative conductances for barttin\_rClC-K1\_rClC-K1 without and with barttin co-expression were similar for a wide range of voltages. Values at negative voltages around -250 mV for the concatamer barttin\_rClC-K1\_rClC-K1 with about 23% (Fig.27A, green dots) was only marginally higher than for conditions with barttin excess (Fig.27A, black/yellow dots). This would indicate that one barttin per two  $\alpha$ -subunits is enough for a robust hyperpolarization-induced block. Further, it might suggest that the block is more pronounced in a 2:1 than in a 2:2  $\alpha$ : $\beta$ -subunit stoichiometry because the relative conductance of 23% was lower than under the condition that one barttin was linked to one  $\alpha$ -subunit (33%, Fig.17C, red bar). This is contradictory to results from other characterized concatamers and suggests an inverse correlation. In the 'discussion' chapter this critical finding is debated in more detail. By fitting Boltzmann functions to data points the voltage of half maximum channel conductance ( $V_{0.5}$ ) was determined. The values did not differ between barttin\_rClC-K1\_rClC-K1 in absence and presence of barttin excess and rClC-K1 plus barttin, meaning that the curve was not shifted according to altered rClC-K1:barttin stoichiometry (Fig.27B).



Besides the hyperpolarization-induced block, which is potentiated by barttin, time-dependent gating of barttin\_rClC-K1\_rClC-K1 was addressed, too. Figure 28A shows representative current traces for the concatamer without and with additional barttin expression. Voltages from -155 mV to +145 mV were applied for 300 ms followed by a test step to +105 mV. The ratio of steady state current  $I_{ss}$  at +105 mV and the corresponding instantaneous current  $I_{ins}$  was used to categorize cells into classes of time-dependent gating as described above (Fig.28B). Cells with values below 0.6 were classified having a strong, between 0.6 and 0.8 a medium and above 0.8 a weak time-dependent fast gating. Cells expressing barttin\_rClC-K1\_rClC-K1 featured 21% strong, 43% medium and 36% weak time-dependent fast gating (Fig.28B, green dots). This was a higher tendency towards weak time-dependent fast gating than for barttin\_rClC-K1, which had a higher barttin:rClC-K1 ratio (see Fig.20). A further barttin excess in parallel to barttin\_rClC-K1\_rClC-K1 caused a shift to 10% of cells featuring medium and 90% of cells featuring weak time-dependent fast gating (Fig.28B, yellow dots). This finding validates that one  $\beta$ -subunit per two  $\alpha$ -subunits is not sufficient to obtain the full barttin effect. Figure 28C summarizes voltage-dependence of relative fast gate open probabilities of the concatamer in absence (green dots) and presence of barttin excess (yellow dots). For comparison, values for rClC-K1 without (grey line) and with barttin surplus (grey dashed line) as well as for barttin\_rClC-K1 without (dark red line) and with barttin surplus (dark red dashed line) from figure 20 were additionally integrated. The concatamer barttin\_rClC-K1\_rClC-K1 exhibits the typical voltage-dependence of the rClC-K1 fast gate with lowest values at positive voltages. Barttin within the 2:1 rClC-K1:barttin stoichiometry (green dots) had a stronger impact on the channel than for the 2:2 stoichiometry per dimer (dark red line) because fast gate open probability was higher than for the latter condition. If there was a further barttin excess, minimum open probabilities were shifted up to above 90% for the concatamers and the homodimer.



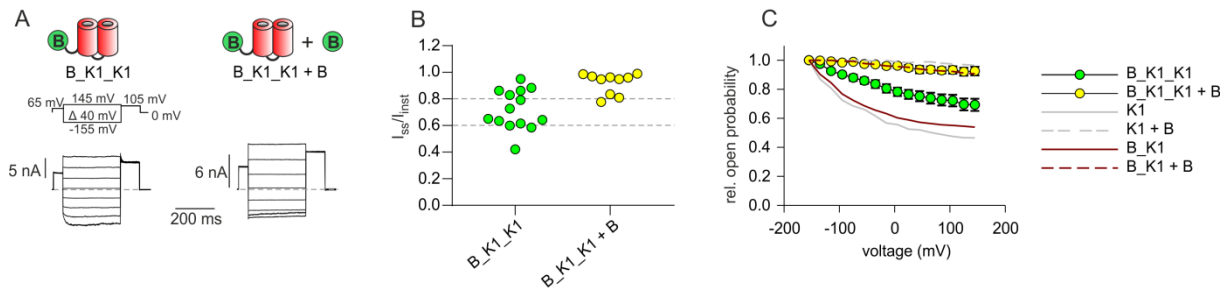


**Fig. 28 Time-dependent fast gating of barttin\_rCIC-K1\_rCIC-K1**

(A) Representative current traces of B\_K1\_K1 in absence and presence of additional barttin. Voltages from -155 mV to +145 mV were applied for 300 ms. Dashed grey line represents 0 nA. (B) Scatter plot of measured cells expressing either B\_K1\_K1 in absence (green dots) or presence of barttin excess (yellow dots) according to their  $I_{ss}/I_{inst}$  values. Cells were sorted as strong time-dependent, when after the voltage step from -155 mV to +105 mV steady state current amplitude ( $I_{ss}$ ) was lower than 60% of instantaneous current amplitude ( $I_{inst}$ ), as medium time-dependent, when  $I_{ss}/I_{inst}$  was between 60% and 80% and as weak time-dependent, when  $I_{ss}/I_{inst}$  was higher than 80%. Each dot is one measured cell. Dashed lines represent thresholds for categorization. (C) Relative fast gate open probabilities under different barttin availabilities, determined by plotting instantaneous current amplitudes during test pulse *versus* voltages of the pre-pulse. Data for B\_K1\_K1 (+ B) are shown as mean values  $\pm$  S.E.M.. B\_K1\_K1: n=14, B\_K1\_K1 + B: n=10. As references mean relative fast gate open probabilities of K1 (+ B) and B\_K1 (+ B) from Fig.20 were included (grey/red lines). K1 (+ B) = rCIC-K1 (+ barttin), B\_K1 (+ B) = barttin\_rCIC-K1 (+ barttin), B\_K1\_K1 (+B) = barttin\_rCIC-K1\_rCIC-K1 (+ barttin).

### 3.2 CIC-K/barttin concatamers of different stoichiometries containing non-palmitoylated barttin

By covalent linkage of different numbers of barttin to CIC-K subunits it became apparent that two barttin molecules per CIC-K channel subunit are necessary to obtain the maximum effect of  $\beta$ -subunits on  $\alpha$ -subunits by opening of the channel's fast and slow gate. Furthermore, it was found that only one  $\beta$ - per  $\alpha$ -subunit is sufficient for proper subcellular trafficking but not for constitutive opening of the fast gate. This differential functional stoichiometry of  $\alpha$ - and  $\beta$ -subunits offered the opportunity to use the here applied  $\alpha$ : $\beta$ -subunit concatamers as a tool for the functional characterization of barttin mutations known to be involved in induction of Bartter syndrome. Using the knowledge about barttin's effect on CIC-K channels for different stoichiometries made it possible to directly deduce functional consequences of these barttin mutations for example on trafficking or fast gating. As previously shown, a post-translational modification of barttin is essential for its function (Steinke et al., 2015). Proper activation of hCIC-Ka is only possible, if palmitic acid is covalently linked to two cysteines at positions 54 and 56 of barttin. A replacement of both cysteines by serines caused a complete inactivity of hCIC-Ka without affecting subcellular localization of the whole channel complex (Steinke et al., 2015). Moreover, it was demonstrated that the disease-causing barttin mutations R8L, R8W and G47R exhibit a reduced level of palmitoylation compared to WT barttin (Gorinski et al., 2020; Steinke et al., 2015), raising the assumption that lack of palmitoylation might play a key role for disturbed channel function and disease development.



In a further approach of this study, we aimed to get more insights into the mechanistic function of barttin palmitoylation and thus mutated both palmitoylation sites of barttin to serines. This non-palmitoylated barttin is named 'barttin<sub>MUT</sub>' in the following. Analyzing the mutated concatamers should disclose which barttin effects are preserved or abolished by non-palmitoylation and whether the abolished functions could be recovered, if co-expressed WT barttin competes with mutant barttin for the binding sites.

### 3.2.1 Non-palmitoylated barttin does not influence relative expression and subcellular localization of hClC-Ka/barttin concatamers

Prior to electrophysiological investigation, expression of non-palmitoylated hClC-Ka/barttin concatamers in HEK293T cells was investigated. After lysis of cells expressing concatamers in absence and presence of additional WT barttin whole cell lysates were subjected to SDS-PAGE. Figure 29A shows a fluorescence scan of a representative SDS-PAGE gel as well as expression analysis (n=3; hClC-Ka\_mYFP in red, barttin\_mCFP in green). Concatamers were expressed with the identical molecular weight as non-mutant concatamers and with comparable relative expression levels (see also Fig.12). hClC-Ka exhibited highest expression and was set as reference for all other conditions. For the concatamers with one or two linked barttins the expression decreased with the length of the protein. Additional barttin expression generally lowers the expression of all  $\alpha$ -subunits.

Next, subcellular localization of non-palmitoylated hClC-Ka concatamers was investigated to clarify potential trafficking defects caused by palmitoylation deficiency. For this, MDCKII cells expressing barttin<sub>MUT</sub>\_hClC-Ka and barttin<sub>MUT</sub>\_barttin<sub>MUT</sub>\_hClC-Ka in absence and presence of WT barttin was imaged using confocal microscopy (Fig.29B). YFP fluorescence of concatamers is depicted in red and CFP fluorescence of WT barttin in green. Overall expression of concatamers was very weak and only detectable within particular cells. One and two non-palmitoylated barttins per  $\alpha$ -subunit led to clear surface membrane staining, comparable to the palmitoylated form (a and c, see also Fig.12). This indicates that non-palmitoylation of barttin does not prevent plasma membrane transport in general, which supports previous findings obtained on hClC-Ka and co-expressed non-palmitoylated barttin (Steinke et al., 2015). Co-expression of WT barttin and non-palmitoylated concatamers led to co-localization of both components near plasma membrane as well, visualized by the yellowish staining (b and d).

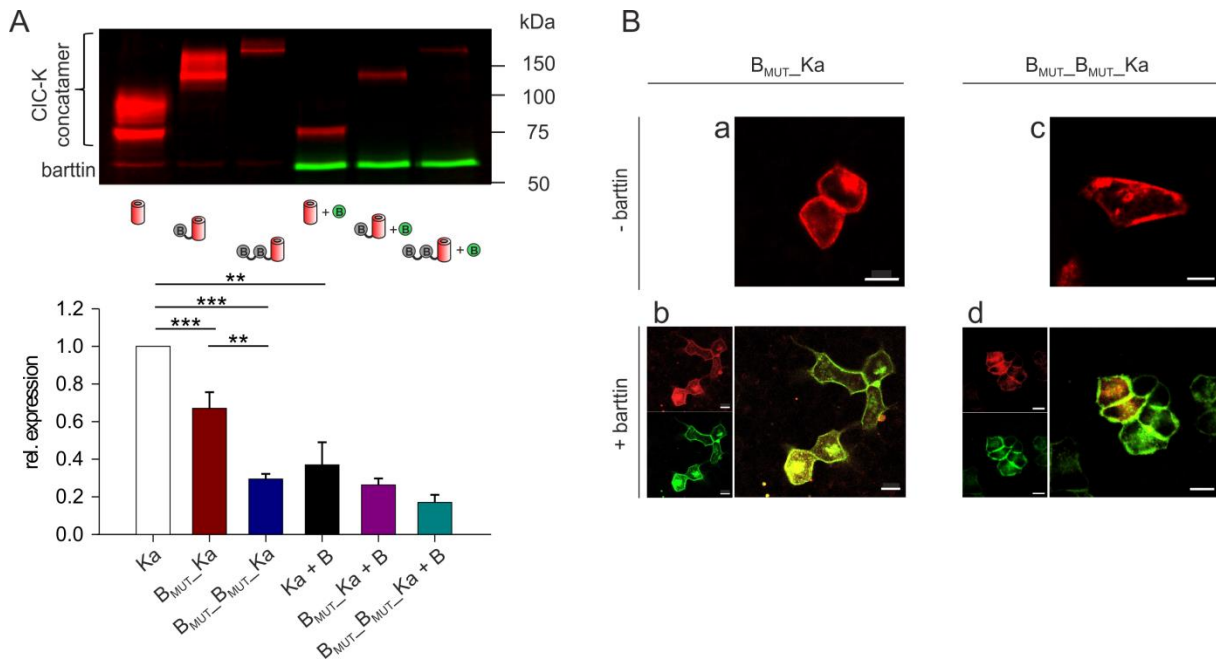


**Fig. 29 Expression and plasma membrane insertion of hClC-Ka/barttin<sub>MUT</sub> concatamers**  
**(A)** Fluorescence scan of SDS-PAGE gel with protein lysates from HEK293T cells expressing hClC-Ka\_mYFP concatamers (red), which harbored non-palmitoylated barttin molecules, without or with WT barttin\_mCFP co-expression (green). The faint red bands below the Ka monomer and the concatamers at around 60 kDa are degradation products of the channel and not barttin molecules. The quantitative expression analysis is shown in a bar chart below. Relative expression levels were normalized to the expression of the hClC-Ka monomer (white bar). All data show mean values  $\pm$  S.E.M.. Student's t-test was performed to test for significance ( $n \geq 3$ , \*\*  $p < 0.01$ , \*\*\*  $p < 0.001$ ). **(B)** Confocal microscopy images of MDCKII cells, expressing B<sub>MUT</sub>-Ka\_mYFP (a,b) and B<sub>MUT</sub>-B<sub>MUT</sub>-Ka\_mYFP (c,d) in absence (a,c) and presence (b,d) of additional WT barttin\_mCFP. YFP is visualized in red and CFP in green. Colocalization of  $\alpha$ - and  $\beta$ -subunits is visualized in yellow. – barttin = without WT barttin co-expression, + barttin = with WT barttin co-expression. Scale bars = 10  $\mu$ m. Ka (+ B) = hClC-Ka (+ WT barttin), B<sub>MUT</sub>-Ka (+ B) = barttin<sub>MUT</sub>-hClC-Ka (+ WT barttin), B<sub>MUT</sub>-B<sub>MUT</sub>-Ka (+ B) = barttin<sub>MUT</sub>-barttin<sub>MUT</sub>-hClC-Ka (+ WT barttin).

### 3.2.2 Currents of hClC-Ka/barttin<sub>MUT</sub> concatamers recover by the co-expression of WT barttin

Whole cell patch clamp analysis was performed using HEK293T cells expressing hClC-Ka concatamers harboring non-palmitoylated barttins. Figure 30A shows representative current recordings using voltages from -255 mV to 195 mV. Mean IV-plots are presented in figure 30B. As already shown, hClC-Ka did not conduct currents in absence of barttin (white dots). The channel was also not conductive in presence of non-palmitoylated barttin. This holds true, when one (dark red dots) or two non-palmitoylated barttin molecules (dark blue dots) were linked to one  $\alpha$ -subunit, and also, if non-palmitoylated barttin was co-expressed (grey dots). This observation is conform to published data (Steinke et al., 2015). If WT barttin was co-expressed to barttin<sub>MUT</sub>-hClC-Ka, channels became conductive again (violet dots) and exhibited the typical hyperpolarization-induced block. This result might be interpreted as binding of WT barttin to the second predicted binding site, which was not occupied by non-palmitoylated barttin. There was a similar effect for barttin<sub>MUT</sub>-barttin<sub>MUT</sub>-hClC-Ka in presence of WT barttin (cyan dots). Actually, for this concatamer both hypothetical barttin binding sites were meant to be occupied by non-palmitoylated barttin leading to an inactive

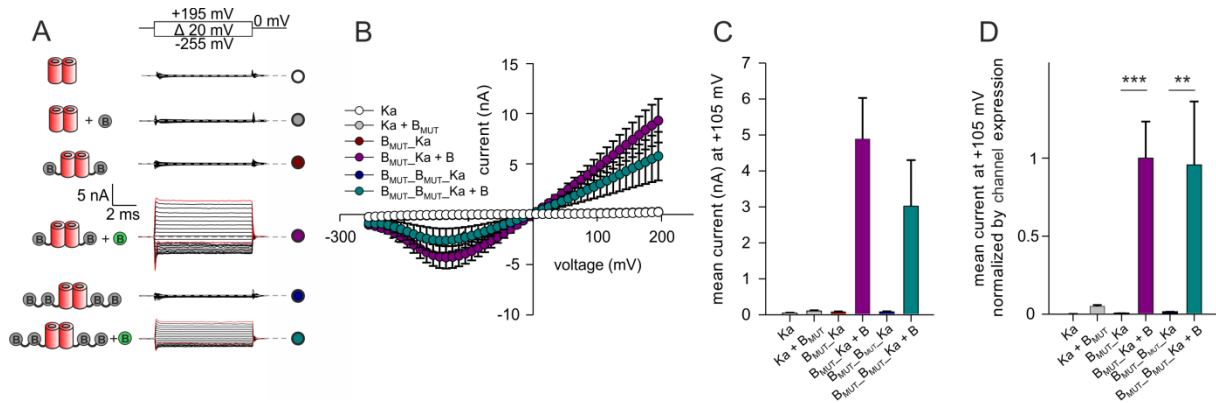


**Fig. 30 Currents of hClC-Ka concatamers, containing non-palmitoylated barttin, in absence and presence of additional WT barttin**  
**(A)** Representative current traces of hClC-Ka concatamers, harboring non-palmitoylated barttin molecules, in absence and presence of additional WT barttin under application of voltages between -255 mV and +195 mV. Red colored current traces represent currents at voltages of -255 mV and +195 mV. Dashed line represents 0 nA. **(B)** IV-plot of hClC-Ka concatamers, showing a hook-shaped IV-relationship at negative voltages, when channels were conductive. All values are shown as mean  $\pm$  S.E.M.. **(C)** Mean currents at +105 mV. All data are shown as mean  $\pm$  S.E.M.. **(D)** Mean currents at +105 mV normalized to channel expression as shown in Fig.29A. All data are shown as mean  $\pm$  S.E.M.. Data for hClC-Ka in (A)-(D) is taken from Fig.13. Statistical significance was tested using Student's t-test. (B)-(D): Ka: n=9, Ka + B<sub>MUT</sub>: n=11, B<sub>MUT</sub>\_Ka: n=10, B<sub>MUT</sub>\_Ka + B: n=11 (+6 not included cells without current), B<sub>MUT</sub>\_B<sub>MUT</sub>\_Ka: n=13, B<sub>MUT</sub>\_B<sub>MUT</sub>\_Ka + B: n=7 (+7 not included cells without current), \*\* p < 0.01, \*\*\* p < 0.001. Ka (+ B<sub>MUT</sub>) = hClC-Ka (+ barttin<sub>MUT</sub>), B<sub>MUT</sub>\_Ka (+ B) = barttin<sub>MUT</sub>\_hClC-Ka (+ WT barttin), B<sub>MUT</sub>\_B<sub>MUT</sub>\_Ka (+ B) = barttin<sub>MUT</sub>\_barttin<sub>MUT</sub>\_hClC-Ka (+ WT barttin).

channel. One possible explanation might be that non-palmitoylated barttin is pushed out of the binding site and replaced by WT barttin. Figure 30C shows mean current amplitudes at +105 mV. Conditions, where hClC-Ka is expressed without or only with non-palmitoylated barttin, offered current amplitudes at +105 mV far below 1 nA. In contrast, WT barttin co-expression increased mean currents to  $4.9 \pm 1.1$  nA for barttin<sub>MUT</sub>\_hClC-Ka and  $3.0 \pm 1.3$  nA for barttin<sub>MUT</sub>\_barttin<sub>MUT</sub>\_hClC-Ka. Currents were normalized to channel expression in figure 30D. We obtained almost no current increase for hClC-Ka with barttin<sub>MUT</sub> co-expression compared to hClC-Ka alone. Both concatamers showed a highly significant difference between with and without WT barttin co-expression, highly supporting the re-activating effect of palmitoylated barttin on hClC-Ka concatamers partially occupied by non-palmitoylated barttins.

### 3.2.3 Single pore parameters of hClC-Ka/barttin<sub>MUT</sub> concatamers recover by co-expression of WT barttin

To investigate the effect of barttin palmitoylation on single pore parameters, stationary noise analysis was performed for concatamers, containing non-palmitoylated barttin molecules. Because noise analysis was only applicable, if channels generate robust currents, single pore parameters could only be determined for conditions, where WT barttin was co-expressed. Representative noise analyses of barttin<sub>MUT</sub>\_hClC-Ka and barttin<sub>MUT</sub>\_barttin<sub>MUT</sub>\_hClC-Ka in presence of WT barttin were visualized in figure 31A,B. As described above, voltages from -5 mV to -255 mV were applied. The macroscopic current variance normalized to the product of

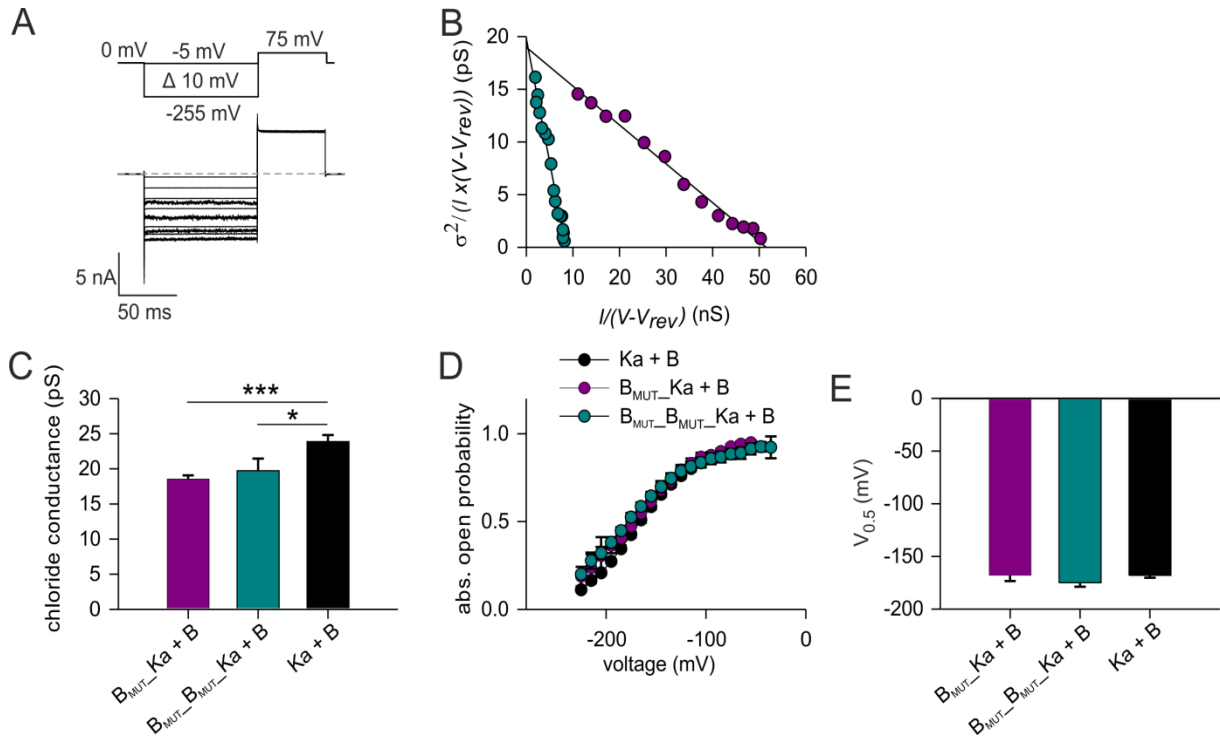


**Fig. 31 Stationary noise analysis of hClC-Ka concatamers, containing non-palmitoylated barttin, in presence of additional WT barttin**  
 (A) Representative current trace of  $B_{MUT\_Ka + B}$  used for stationary noise analysis. Voltages from -5 mV to -255 mV were applied for 100 ms followed by +75 mV for 50 ms. For more negative voltages current decreases with increasing noise. Dashed line represents 0 nA. (B) Representative stationary noise analyses for hClC-Ka/barttin<sub>MUT</sub> concatamers in presence of additional WT barttin. Data points were fitted by linear regression. (C) Mean chloride conductance of tested conditions, obtained by y-axis intercepts of linear regressions as in (B). All data are shown as mean  $\pm$  S.E.M.. Statistical significance was tested by one-way ANOVA and Holm–Sidak post hoc test *versus* Ka + B:  $F_{(2, 23)} = 9.5$  and  $p < 0.001$ , Ka + B:  $n=12$ ,  $B_{MUT\_Ka + B}$ :  $n=9$ ,  $B_{MUT\_B_{MUT\_Ka + B}}$ :  $n=5$ . (D) Absolute open probabilities of tested conditions at negative voltages, determined from (B). (E) Voltage of half maximum activation ( $V_{0.5}$ ) obtained from fits of activation curves from (D). Values for hClC-Ka + B in (C)–(E) are taken from Fig.14. All data in (D) and (E) are shown as mean  $\pm$  S.E.M.. Statistical significance in (E) was tested using one-way ANOVA. For (D) and (E): Ka + B:  $n=11$ ,  $B_{MUT\_Ka + B}$ :  $n=8$ ,  $B_{MUT\_B_{MUT\_Ka + B}}$ :  $n=4$ . Ka + B = hClC-Ka + WT barttin,  $B_{MUT\_Ka + B}$  = barttin<sub>MUT</sub>\_hClC-Ka (+ WT barttin),  $B_{MUT\_B_{MUT\_Ka + B}}$  = barttin<sub>MUT</sub>\_barttin<sub>MUT</sub>\_hClC-Ka (+ WT barttin).

the mean current amplitude and the electrical driving force was plotted against the macroscopic conductance. Linear regression of data distribution yielded a mean chloride conductance of 18.5 pS for one  $\alpha$ -subunit connected to one non-palmitoylated barttin (violet dots/bars) and 19.7 pS for one  $\alpha$ -subunit connected to two non-palmitoylated barttins (cyan dots/bars), which is represented by the y-axis intercept of linear regression lines (Fig.31B,C). Here it should be kept in mind, that WT barttin was co-expressed. Both conductances were slightly below chloride conductance of hClC-Ka with co-expressed WT barttin and in absence of non-palmitoylated barttin. This finding indicates that the presence of one or two non-palmitoylated barttins per  $\alpha$ -subunit might prevent maximum conductance level but facilitate a higher conductance than for the condition, if only one WT barttin was linked to an  $\alpha$ -subunit (see Fig.14C). Figure 31D illustrates the voltage-dependence of absolute open probabilities, which were determined as the quotient of the conductance at certain voltages and the maximum macroscopic conductance represented as x-axis intercept. Open probabilities were

fitted by Boltzmann functions. Voltage of half maximum activation ( $V_{0.5}$ ) was comparable for concatamers and hCIC-Ka plus WT barttin (Fig.31E). This indicates that non-palmitoylated barttins linked to hCIC-Ka do not change voltage-dependence of channel activation.

### 3.2.4 Non-palmitoylated barttin does not influence relative expression and subcellular localization of rCIC-K1/barttin concatamers

Up to now, the impact of non-palmitoylated barttin on WT rCIC-K1 is fairly unknown; especially the effect on fast and slow gating has not been reported. Therefore, also exchange of cysteines by serines at positions 54 and 56 of barttin within rCIC-K1 concatamers was conducted to characterize these mutants electrophysiologically.

Expression of concatamers was checked prior to patch clamp analysis. Figure 32A shows a fluorescence scan of a representative SDS-PAGE gel after separation of whole cell lysates from HEK293T cells, expressing concatamers in absence and presence of additional WT barttin. YFP fluorescence of rCIC-K1 monomers/concatamers is stained in red while CFP fluorescence of

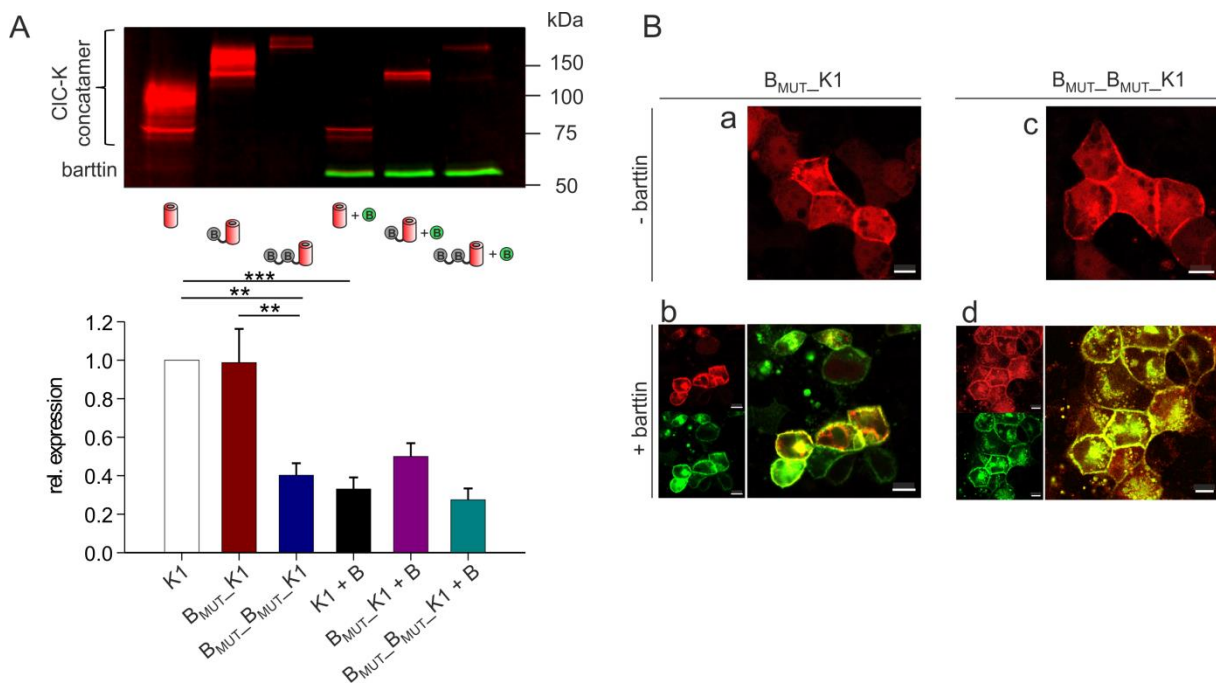


**Fig. 32 Expression and plasma membrane insertion of rCIC-K1/barttin<sub>MUT</sub> concatamers**

(A) Fluorescence scan of a SDS-PAGE gel with protein lysates from HEK293T cells expressing rCIC-K1<sub>mYFP</sub> concatamers (red), which harbored non-palmitoylated barttin molecules, without or with WT barttin<sub>mCFP</sub> co-expression (green) together with quantitative expression analysis shown in a bar chart below. Relative expression levels were normalized to the expression of the rCIC-K1 monomer (white bar). All data show mean values  $\pm$  S.E.M.. Student's t-test was performed to test for significance ( $n \geq 3$ , \*\*  $p < 0.01$ , \*\*\*  $p < 0.001$ ). (B) Confocal microscopy images of MDCKII cells, expressing B<sub>MUT</sub>-K1<sub>mYFP</sub> and B<sub>MUT</sub>-B<sub>MUT</sub>-K1<sub>mYFP</sub> in presence or absence of additional WT barttin<sub>mCFP</sub>. YFP is visualized in red and CFP in green. Colocalization of  $\alpha$ - and  $\beta$ -subunits is visualized in yellow. - barttin = without WT barttin co-expression, + barttin = with WT barttin co-expression. Scale bars = 10  $\mu$ m. K1 (+ B) = rCIC-K1 (+ WT barttin), B<sub>MUT</sub>-K1 (+ B) = barttin<sub>MUT</sub>-rCIC-K1 (+ WT barttin), B<sub>MUT</sub>-B<sub>MUT</sub>-K1 (+ B) = barttin<sub>MUT</sub>-barttin<sub>MUT</sub>-rCIC-K1 (+ WT barttin).

WT barttin is illustrated green. All monomers were expressed with their expected molecular weight as for previously described constructs. Statistical analysis of relative concatamer expression is shown under the representative gel ( $n \geq 3$  experiments). Expression of rClC-K1 monomers was taken as reference and set to 1. As for other investigated constructs expression decreased with higher molecular weight. However, the concatamer barttin<sub>MUT</sub>\_rClC-K1 exhibited a higher expression level than other comparable concatamers. It was similar to the expression of rClC-K1 monomers (dark red bar). If barttin was co-expressed, barttin<sub>MUT</sub>\_rClC-K1 expression even exceeds expression of rClC-K1 monomers. Still, general  $\alpha$ -subunit expression was lower in presence of extra barttin.

Subcellular localization was investigated using confocal imaging of transfected MDCKII cells. YFP fluorescence of concatamers is shown in red and CFP fluorescence of WT barttin in green (Fig.32B). YFP fluorescence of barttin<sub>MUT</sub>\_rClC-K1 was in major parts located near the plasma membrane (a). Besides, a faint and even YFP staining covered the inner space of the cell. This was probably attributed to C-terminal concatamer cleavage, which has been previously observed for other rClC-K1/WT barttin concatamers as well (see Fig.15, Fig.47). Barttin co-expression led to a co-localization of both barttin and the concatamer visualized by the yellow color (b). A similar distribution of YFP fluorescence was given for barttin<sub>MUT</sub>\_barttin<sub>MUT</sub>\_rClC-K1. This concatamer located close to the surface membrane while degraded YFP stained the cytosol (c). In presence of barttin both YFP and CFP were also found near the surface membrane (d).

### 3.2.5 Non-palmitoylated barttin does not influence the macroscopic current amplitude of rClC-K1 channels

Whole cell patch clamp analysis was performed with HEK293T cells expressing non-palmitoylated rClC-K1/barttin<sub>MUT</sub> concatamers. Representative current recordings for voltages between -255 mV and +195 mV are visualized in figure 33A. Mean IV-relationships were plotted in figure 33B. As for rClC-K1 in absence of barttin (solid line) currents featured a clearly visible time-dependence. A less pronounced hyperpolarization-induced 'block' was found for conditions, where one (dark red dots) or two non-palmitoylated barttins (dark blue dots) were linked to an  $\alpha$ -subunit or if non-palmitoylated barttin was co-expressed with rClC-K1 monomers (grey dots). In contrast, current traces of rClC-K1 in presence of co-expressed WT barttin were hardly time-dependent and had a distinct hyperpolarization-induced block

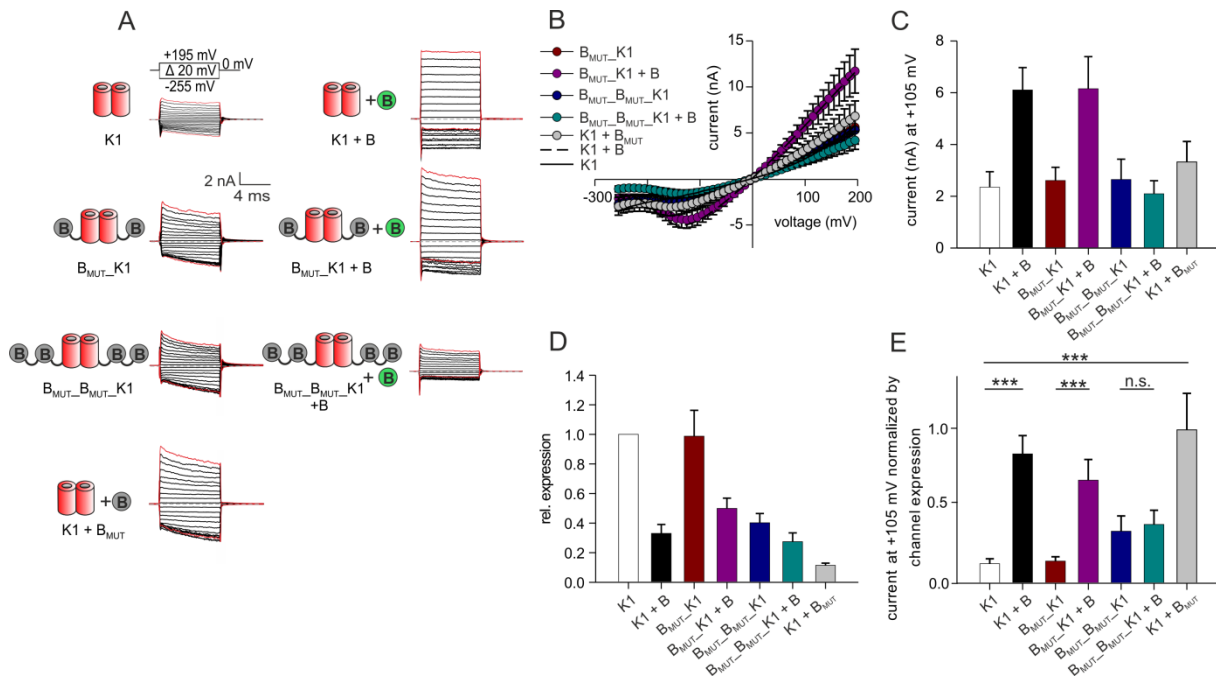


**Fig. 33 Currents of rClC-K1 concatamers, containing non-palmitoylated barttin, in absence and presence of additional WT barttin**  
 (A) Representative current traces of rClC-K1 concatamers, containing non-palmitoylated barttin, in absence and presence of additional WT barttin after application of voltages between -255 mV and +195 mV. Red colored current traces represent currents at voltages of -255 mV and +195 mV. Dashed lines represent 0 nA. (B) IV-plots of all tested rClC-K1 stoichiometries, measured immediately after initial capacitive peak. All values are shown as mean  $\pm$  S.E.M.. Mean values for K1 and K1 + B are shown as solid/dashed lines. (C) Mean currents at +105 mV. All data are shown as mean  $\pm$  S.E.M.. (D) Relative expression levels of rClC-K1 monomers/concatamers in absence and presence of additional WT barttin as shown in Fig.32A. (E) Mean current at +105 mV normalized to channel expression as shown in (D). Values for rClC-K1 and rClC-K1 + B in (B), (C) and (E) are taken from Fig.16. All data are shown as mean values  $\pm$  S.E.M.. Statistical significance was tested using Student's t-test. (B),(C),(E): K1: n=11, K1 + B: n=13, B<sub>MUT</sub>\_K1: n=13, B<sub>MUT</sub>\_K1 + B: n=9, B<sub>MUT</sub>\_B<sub>MUT</sub>\_K1: n=11, B<sub>MUT</sub>\_B<sub>MUT</sub>\_Ka + B: n=13, K1 + B<sub>MUT</sub>: n=9, \*\*\* p < 0.001, n.s. = not significant. K1 (+ B) = rClC-K1 (+ WT barttin), B<sub>MUT</sub>\_K1 (+ B) = barttin<sub>MUT</sub>\_rClC-K1 (+ WT barttin), B<sub>MUT</sub>\_B<sub>MUT</sub>\_K1 (+ B) = barttin<sub>MUT</sub>\_barttin<sub>MUT</sub>\_rClC-K1 (+ WT barttin), K1 + B<sub>MUT</sub> = rClC-K1 + barttin<sub>MUT</sub>.

(see also Fig.16). The co-expression of WT barttin with barttin<sub>MUT</sub>\_rClC-K1 and barttin<sub>MUT</sub>\_barttin<sub>MUT</sub>\_rClC-K1 seemed to promote hyperpolarization-induced block and to extenuate time-dependent gating, which is analyzed below. Figure 33C compares mean instantaneous current amplitudes at +105 mV. rClC-K1 and barttin<sub>MUT</sub>\_rClC-K1 in presence of WT barttin excess documented the highest current amplitudes with more than 6 nA. Conditions without or only with non-palmitoylated barttin expression were lower currents with 2 to 4 nA. Interestingly, barttin<sub>MUT</sub>\_barttin<sub>MUT</sub>\_rClC-K1 in presence of WT barttin also generated mean currents of only 2 nA (cyan bar), which is similar to conditions without WT barttin. Possibly, for this concatamer all binding sites were already occupied by non-palmitoylated barttin leading to no further activation by WT barttin. This would confirm the existence of only two functional binding sites of ClC-K for barttin. However, this would imply that the replacement of non-palmitoylated barttin by palmitoylated barttin does not lead to a significant current increase for rClC-K1 as for former analyzed hClC-Ka concatamers. Normalization of current amplitudes to channel expression (Fig.33D) made clear that WT barttin is not able to increase current amplitudes, if two non-palmitoylated barttins are

already linked to an  $\alpha$ -subunit (Fig.33E). Moreover, rClC-K1 plus barttin<sub>MUT</sub> generated mean currents (grey bar), which are comparable to WT barttin expression (black bar). This confirms that barttin palmitoylation rather has a minor influence on rClC-K1 current amplitudes, in contrast to hClC-Ka. Still, as rClC-K1 is also conductive in presence of non-palmitoylated barttin, this result may just prove the preserved trafficking ability of non-palmitoylated barttin, already shown above by confocal images. This could explain that equal current amplitudes for rClC-K1 in presence of non-palmitoylated barttin and palmitoylated barttin were observed here.

### 3.2.6 Non-palmitoylated barttin facilitates hyperpolarization-induced block for rClC-K1 less intense as palmitoylated barttin

To characterize the hyperpolarization-induced block for rClC-K1 in presence of non-palmitoylated barttin in more detail, mean IV-plots were normalized to the current amplitude at +105 mV (Fig.34A). Relative channel conductances at negative voltages were determined as described above for other rClC-K1 concatamers. Figure 34B summarizes all conductance curves, which decreased, as expected, for more negative voltages. The barttin effect was quantified using relative conductance at -255 mV (Fig.34C). This value was highest, if rClC-K1 was expressed in complete absence of barttin (0.88, white bar), and lowest, if rClC-K1 and WT barttin were co-expressed (0.14, black bar). One or two non-palmitoylated barttins linked to rClC-K1 in presence of further WT barttin featured relatively low  $G_{-255\text{mV}}/G_{\text{max}}$  values of 0.19 (violet bar) and 0.27 (cyan bar), indicating that WT barttin promotes the block for both concatamers and, thus, binds to both. This result might be interpreted as competition between WT and mutated barttin for binding to the  $\alpha$ -subunit.  $G_{-255\text{mV}}/G_{\text{max}}$  ratio of 0.43 for rClC-K1 plus barttin<sub>MUT</sub> was higher than with WT barttin but lower than without any barttin (grey bar). Concatamers with one and two non-palmitoylated barttins per  $\alpha$ -subunit exposed higher  $G_{-255\text{mV}}/G_{\text{max}}$  values of 0.62 (dark red bar) and 0.57 (dark blue bar), respectively. Thus, the block was not as pronounced as for rClC-K1 plus barttin<sub>MUT</sub> excess. Possibly, either one or two non-palmitoylated barttins were not as effective as co-expression of barttin<sub>MUT</sub>, or binding of barttin<sub>MUT</sub> to the  $\alpha$ -subunit was incomplete within concatamers due to sterical issues. A shift in conductance curves was checked by comparing voltages of half maximum conductance ( $V_{0.5}$ , Fig.34D). There were only slight differences between concatamers without and with WT barttin co-expression.



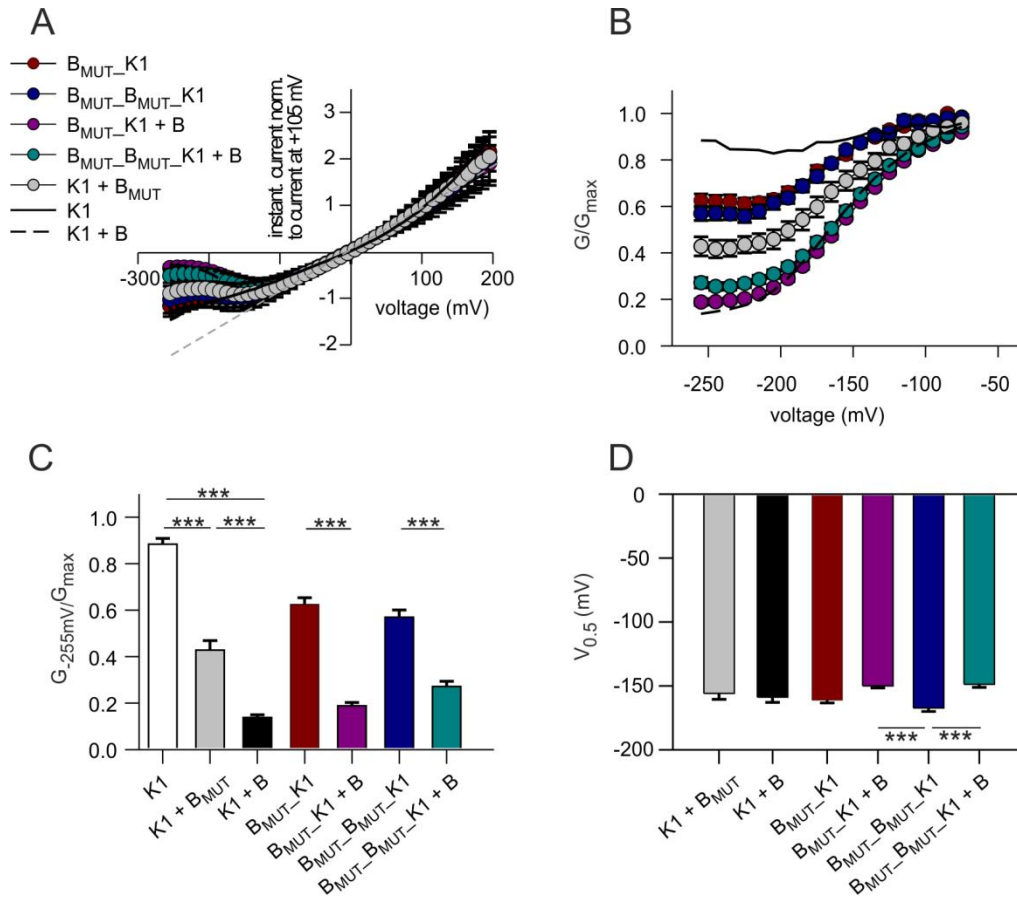


**Fig. 34 Influence of barttin palmitoylation on hyperpolarization-induced block of rClC-K1**

(A) IV-plot of instantaneous rClC-K1 currents normalized to currents at +105 mV, obtained from currents as shown in Fig.33A. All data are shown as mean values  $\pm$  S.E.M.. Dashed line represents linear regression of currents between -55 mV and +55 mV. (B) Relative conductances at negative voltages of all tested stoichiometries, obtained from current deviations from linear regression in (A). Mean values for K1 and K1 + B are shown as solid/dashed lines. (C) Relative conductances at -255 mV for all tested conditions. (D) Voltage of half maximum conductance ( $V_{0.5}$ ) obtained from fits of conductance curves from (B). Values for rClC-K1 and rClC-K1 + B in (A)-(D) are taken from Fig.17. (B)-(D): all values are shown as mean  $\pm$  S.E.M.. K1: n=13, K1 + B: n=13, B<sub>MUT</sub>\_K1: n=13, B<sub>MUT</sub>\_K1 + B: n=9, B<sub>MUT</sub>\_B<sub>MUT</sub>\_K1: n=11, B<sub>MUT</sub>\_B<sub>MUT</sub>\_K1 + B: n=13, K1 + B<sub>MUT</sub>: n=9. For (C) and (D) statistical significance was tested by one-way ANOVA with subsequent Holm-Sidak post hoc test: for (C):  $F_{(10, 107)} = 87.4$  and  $p < 0.001$ ; for (D):  $F_{(10, 104)} = 204.7$  and  $p < 0.001$ . K1 (+ B) = rClC-K1 (+ WT barttin), B<sub>MUT</sub>\_K1 (+ B) = barttin<sub>MUT</sub>\_rClC-K1 (+ WT barttin), B<sub>MUT</sub>\_B<sub>MUT</sub>\_K1 (+ B) = barttin<sub>MUT</sub>\_barttin<sub>MUT</sub>\_rClC-K1 (+ WT barttin), K1 + B<sub>MUT</sub> = rClC-K1 + barttin<sub>MUT</sub>.

### 3.2.7 Barttin palmitoylation is necessary for rClC-K1 fast gate modulation but not for slow gate modulation

In the following approach time-dependent fast gating was analyzed for rClC-K1 in presence of non-palmitoylated barttin. For this, we applied voltage steps between -155 and 145 mV over a longer time period of 300 ms followed by a test pulse to + 105 mV for 100 ms. Figure 35 compares representative measurements of rClC-K1 in co-expression of WT barttin (left) and barttin<sub>MUT</sub> (right). For WT barttin no time-dependent fast gating was observed at all. In contrast, non-palmitoylated barttin caused a fast increase in current at negative and a decrease at positive voltages.

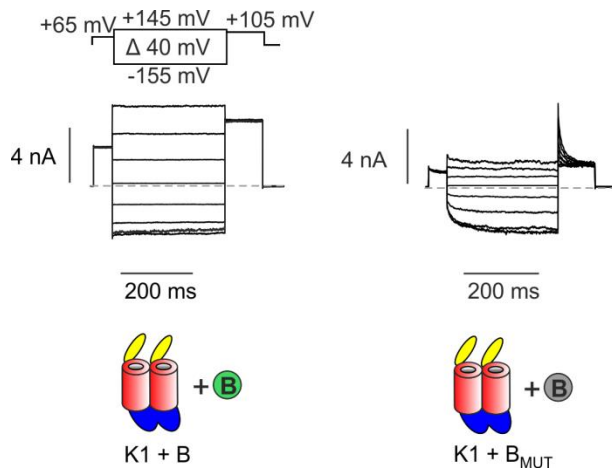


**Fig. 35 Time-dependent gating of rClC-K1 in co-expression of WT barttin or non-palmitoylated barttin**

Representative current traces of rClC-K1 in presence of WT barttin (left) or in presence of non-palmitoylated barttin (right) under application of voltages between -155 mV and +145 mV. Dashed lines represent 0 nA.

To quantify the effect of non-palmitoylated barttin on time-dependent fast gating for all concatamers steady state currents at a test pulse of +105 mV ( $I_{ss}$ ), normalized to the instantaneous current ( $I_{inst}$ ), were plotted for single cells and categorized into three different classes of time-dependent fast gating according to figure 20. As reference, data of rClC-K1 without any barttin co-expression and with WT barttin co-expression was included from figure 20D. As already visible in figure 20D,  $I_{ss}/I_{inst}$  values for rClC-K1 resided below 0.6, while WT barttin shifted values close to 1 (Fig.36A white/black dots). In contrast, non-palmitoylated barttin in any stoichiometry to the  $\alpha$ -subunit did not increase  $I_{ss}/I_{inst}$  but even lowered values below 0.4 (dark red, dark blue, grey dots). Thus, non-palmitoylated barttin did not reduce but even promoted time-dependent fast gating. The presence of further WT barttin molecules shifted values up again (pink, cyan dots). However, this effect for two linked  $\beta$ -subunits to one  $\alpha$ -subunit was not as intense as if there was only one barttin linked to one  $\alpha$ -subunit. Maybe, both  $\beta$ -subunits hindered WT barttin to bind to the channel. Values for single cells were categorized into groups to visualize changes in time-dependent fast gating. Below a value of 0.6 currents were sorted as 'strong time-dependent gating', between 0.6 and 0.8 as 'medium time-dependent gating' and above 0.8 as 'weak time-dependent gating'. Pie charts of categorization for each condition are given in figure 36B. Without barttin and with only non-palmitoylated barttin all currents were sorted exclusively as 'strong time-dependent'. WT barttin shifted currents to 'medium' or even to 'weak time-dependent gating'. This shift was more pronounced the lower the number of non-palmitoylated barttins was, which was linked to one  $\alpha$ -subunit. It demonstrates again that palmitoylated and non-palmitoylated barttin molecules compete for binding to the  $\alpha$ -subunit. For the  $\alpha$ -subunit homodimer without linkage currents were exclusively 'weak time-dependent', when WT barttin was co-expressed.

Representative current recordings for all tested conditions and categories are given in supplemental figure 2.

Relative fast gate open probabilities for all conditions were determined as for the palmitoylated concatamers, which was described above, and summarized in figure 36C. In co-expression with WT barttin the rClC-K1 fast gate was constitutively open and thus not voltage-dependent (black dots), whereas the other conditions exhibited data with highest values at -155 mV and lowest at +145 mV. As shown in figure 20, linkage of WT barttin increases the minimum fast gate open probability of rClC-K1. Mutant barttin, however, decreased the fast gate open probability (compare red, blue and grey symbols with white symbols for rClC-K1 in absence of barttin). Co-expression of WT barttin reversed this effect. Notably, this evaluation relies on relative open probabilities. (For absolute values, noise analyses or single channel recordings might help.)

A short inter-pulse to -180 mV (20 ms) was applied between pre- and test pulses that opens the fast gate without affecting the slow gate. Current amplitudes at the beginning of the test pulse were, thus, directly proportional to relative slow gate open probabilities for voltages of pre-pulses. A representative recording used for determination of relative rClC-K1 slow gate open probabilities in presence of barttin is given in supplemental figure 3. For conditions with two or even more barttin molecules available per  $\alpha$ -subunit slow gate was open (Fig.36D grey, pink, dark blue, cyan dots). If only one non-palmitoylated barttin was available per  $\alpha$ -subunit relative slow gate open probabilities decreased slightly to around 80% at negative voltages (dark red dots). However, in comparison to the respective concatamer containing one palmitoylated barttin molecule (red dots) relative slow gate open probabilities were only marginally different. If two palmitoylated barttin molecules were linked to one  $\alpha$ -subunit, slow gate is highly expected to be open because it was already so for the respective condition with non-palmitoylated barttin (dark blue dots). This demonstrates that modulation of rClC-K1 slow gate open probabilities is rather independent of barttin palmitoylation as even non-palmitoylated barttin can open the slow gate constitutively like palmitoylated barttin. Furthermore, results show that one barttin molecule per  $\alpha$ -subunit is able to highly increase relative slow gate open probabilities compared to rClC-K1 in absence of barttin (white dots), although, two barttins per  $\alpha$ -subunit seem to be necessary to fully transfer rClC-K1 slow gate into an open state.

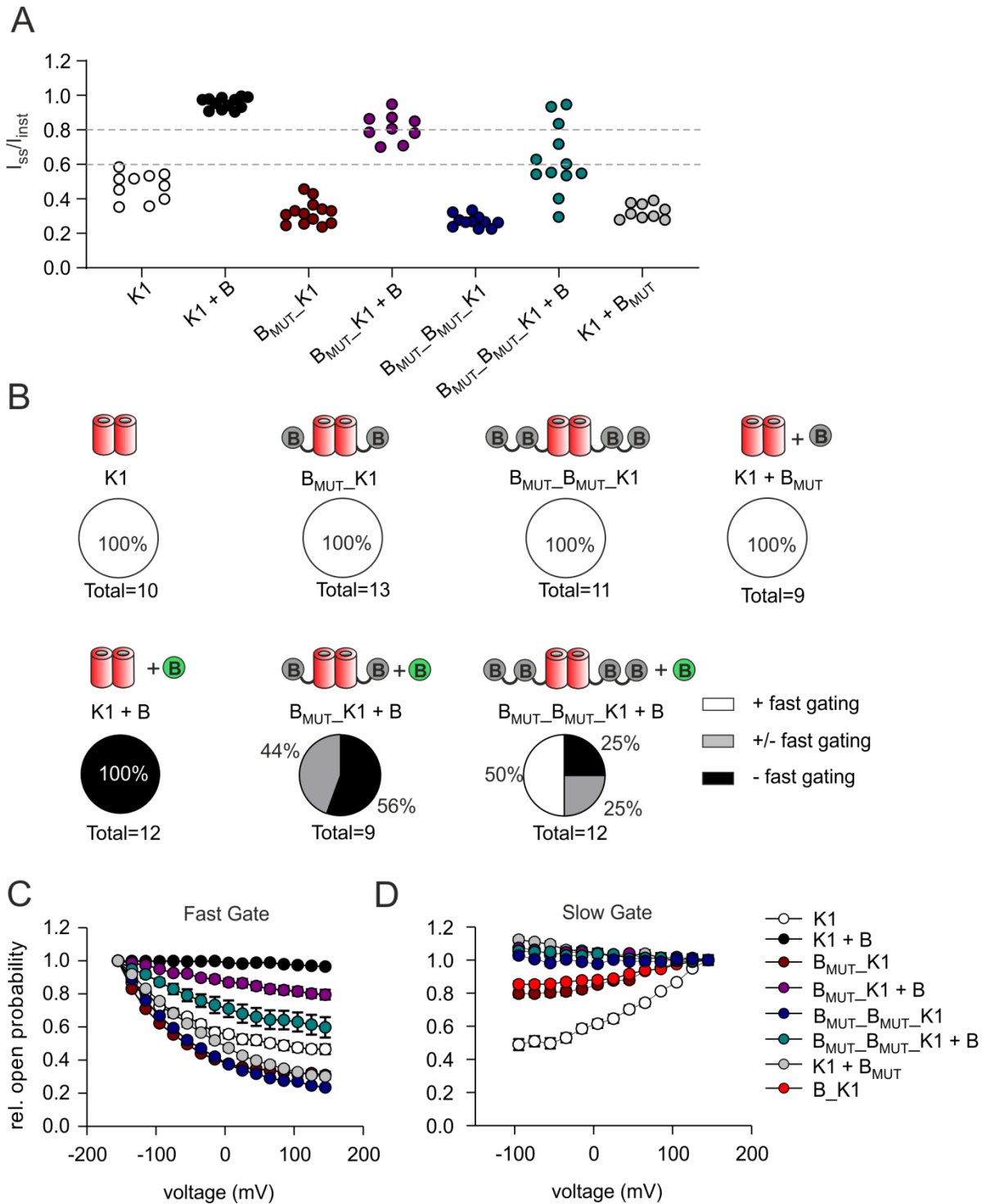


**Fig. 36 Time-dependent fast gating of rCIC-K1/barttin concatamers, containing non-palmitoylated barttin**

(A) Scatter plot of cells measured under different  $\alpha:\beta$ -subunit stoichiometries according to their  $I_{ss}/I_{inst}$  values. Cells were sorted according to Fig.20 as strong time-dependent, when after the voltage step from -155 mV to +105 mV steady state current amplitude ( $I_{ss}$ ) was lower than 60% of instantaneous current amplitude ( $I_{inst}$ ), as medium time-dependent, when  $I_{ss}/I_{inst}$  was between 60% and 80% and as weak time-dependent, when  $I_{ss}/I_{inst}$  was higher than 80%. Each dot is one measured cell. Dashed lines represent thresholds for categorization. (B) Distribution of cells under different barttin availabilities after categorization into the three classes as in (A) visualized as pie charts. (C) Relative fast gate open probabilities under different barttin availabilities, determined by plotting instantaneous current amplitudes during the test pulse versus voltages of the pre-pulse. For K1  $\pm$  B in (A)-(C), values were taken from Fig.20. (D) Relative slow gate open probabilities under different barttin availabilities and for different voltages. Data in (C) and (D) are shown as mean values  $\pm$  S.E.M.. K1: n=10, K1 + B: n=12,  $B_{MUT\_K1}$ : n=13,  $B_{MUT\_K1} + B$ : n=9,  $B_{MUT\_B_{MUT\_K1}}$ : n=11,  $B_{MUT\_B_{MUT\_K1}} + B$ : n=12, K1 +  $B_{MUT}$ : n=9,  $B_{MUT\_K1}$ : n=13. K1 (+ B) = rCIC-K1 (+ WT barttin),  $B_{MUT\_K1} (+ B)$  = barttin<sub>MUT</sub>\_rCIC-K1 (+ WT barttin),  $B_{MUT\_B_{MUT\_K1}} (+ B)$  = barttin<sub>MUT</sub>\_barttin<sub>MUT</sub>\_rCIC-K1 (+ WT barttin), K1 +  $B_{MUT}$  = rCIC-K1 + barttin<sub>MUT</sub>,  $B_{MUT\_K1}$  = barttin\_rCIC-K1.

Furthermore, the influence of barttin palmitoylation on slow gate kinetics should be investigated. For concatamers owning WT barttin it was already shown that barttin increases time constants of slow gating in a way that makes it difficult to determine them with pulses of only 300 ms. Therefore, voltage steps were extended four-fold to 1.2 s (Fig.37). Time constants were obtained by fitting mono-exponential functions to the slow gating process at negative voltages (Fig.37A, blue lines). Representative current traces show that slow gating decelerates with higher availability of non-palmitoylated barttin molecules, too. Time constants of rClC-K1 in absence of barttin, which were taken as reference from figure 21E, were around 100 ms (Fig.37A,E, white dots) and increase to around 300 ms for barttin<sub>MUT</sub>\_rClC-K1 (Fig.37B,E, dark red dots). Two barttins increased constants to around 1 s (Fig.37C,E, dark blue dots) similar to barttin<sub>MUT</sub> excess (> 1 s, Fig.37D,E, grey dots). This closely resembles respective conditions for WT barttin (see Fig.21E). Comparing slow gating time constants exemplarily at -115 mV between concatamers containing palmitoylated and non-palmitoylated barttin molecules indicates that there is no change in slow gating kinetics due to barttin's palmitoylation status (Suppl. Fig.4).

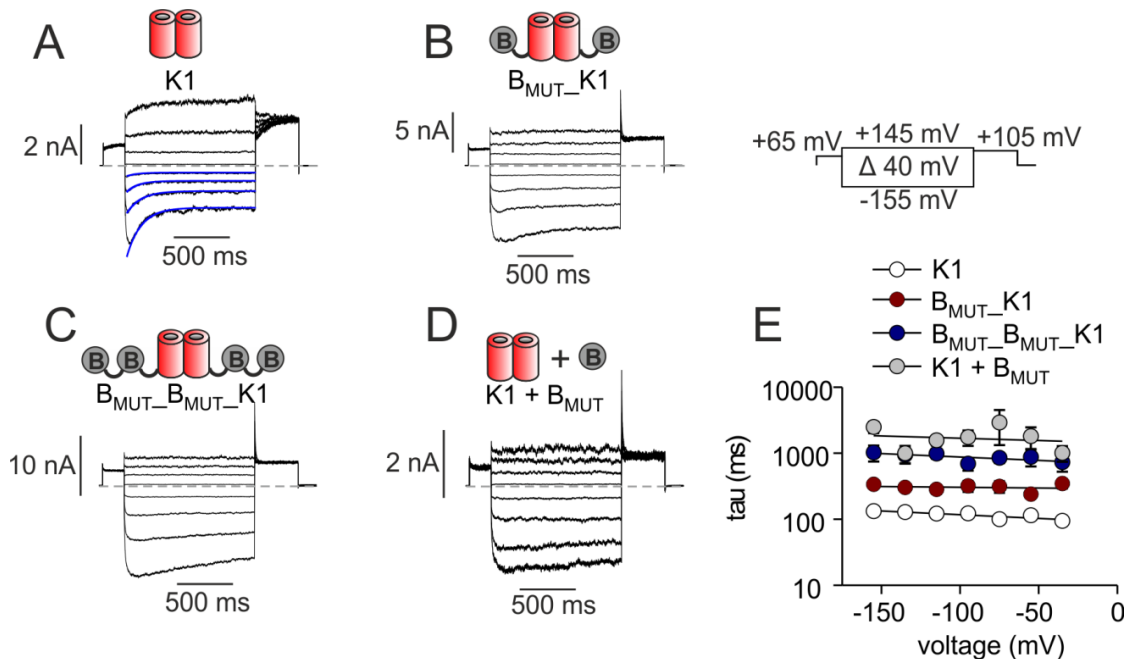


**Fig. 37 Impact of barttin palmitoylation under different  $\alpha$ : $\beta$ -subunit stoichiometries on rClC-K1 slow gate kinetics**

(A) Representative current traces of K1 used for determination of slow gating time constants. Blue lines demonstrate mono-exponential functions, fitted in slow current relaxation at negative voltages. Voltage steps, used for determination of time constants were 1.2 s long. (B) Representative current traces of B<sub>MUT</sub>\_K1. (C) Representative current traces of B<sub>MUT</sub>\_B<sub>MUT</sub>\_K1. (D) Representative current traces of K1 + B<sub>MUT</sub>. (A)-(D) dashed lines indicate 0 nA. (E) Slow time constants (tau) obtained from mono-exponential fits of currents as shown in (A)-(D) at negative voltages. Representative current trace and tau-values for rClC-K1 were taken from Fig.21. Values are given as mean  $\pm$  S.E.M.. K1: n=8, B<sub>MUT</sub>\_K1: n=13, B<sub>MUT</sub>\_B<sub>MUT</sub>\_K1: n=5, K1 + B<sub>MUT</sub>: n=4. Values were fitted by linear regressions. K1 (+ B<sub>MUT</sub>) = rClC-K1 (+ barttin<sub>MUT</sub>), B<sub>MUT</sub>\_K1 = barttin<sub>MUT</sub>\_rClC-K1, B<sub>MUT</sub>\_B<sub>MUT</sub>\_K1 = barttin<sub>MUT</sub>\_barttin<sub>MUT</sub>\_rClC-K1.

These results demonstrated that barttin palmitoylation is important for voltage-dependent rClC-K1 fast gating but not for slow gating.

### 3.2.8 Co-expression of WT barttin influences barttin<sub>MUT</sub>\_rClC-K1\_rClC-K1

For rClC-K1 the concatamer with one WT barttin connected to two linked  $\alpha$ -subunits a considerable hyperpolarization-induced block together with rather weak time-dependent fast gating was observed, which was unexpected as this was usually seen for conditions with high barttin availability per  $\alpha$ -subunit. So, also the respective concatamer with non-palmitoylated barttin was analyzed to check whether there was still this enormous barttin influence. Figure 38A shows representative current recordings of barttin<sub>MUT</sub>\_rClC-K1\_rClC-K1 in absence and presence of WT barttin. Without WT barttin currents exhibited clear time-dependent gating and a rudimentary hyperpolarization-induced block. This changed under co-expression of WT barttin to diminished time-dependent gating and to a considerable hyperpolarization-induced block. Mean IV-plots of both conditions are shown in figure 38B. Current amplitudes at +105 mV were compared and revealed significantly higher values under WT barttin co-expression (Fig.38C). Mean currents have not been normalized to relative expression level of this concatamer because only few HEK293T cells within the cell pool showed YFP fluorescence, which were subjected to patch clamp measurements. Furthermore, no YFP fluorescence at the expected molecular weight was detectable for expression analysis. Either the great majority of cells did not express the concatamer or almost the complete amount of concatamer proteins were cleaved C-terminally, thereby losing the fluorescence tag.

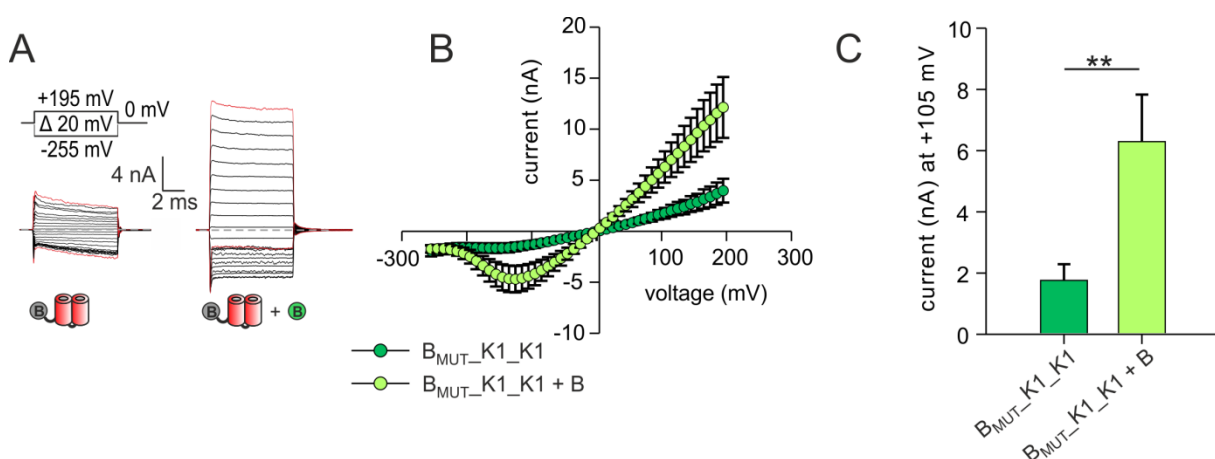


**Fig. 38 Currents of barttin<sub>MUT</sub>\_rClC-K1\_rClC-K1 in absence and presence of additional WT barttin**

(A) Representative current traces of  $B_{MUT\_K1\_K1}$  in absence or presence of co-expressed WT barttin under application of voltages between -255 mV and +195 mV. Red colored current traces represent currents at voltages of -255 mV and +195 mV. Dashed line represents 0 nA. (B) IV-plot of  $B_{MUT\_K1\_K1} \pm$  WT barttin, measured immediately after initial capacitive peak. All values are shown as mean  $\pm$  S.E.M.. (C) Mean current at +105 mV. All data are shown as mean  $\pm$  S.E.M.. Statistical significance was tested using Student's t-test (\*\* p < 0.01). (B)-(C):  $B_{MUT\_K1\_K1}$ : n=10,  $B_{MUT\_K1\_K1} + B$ : n=8.  $B_{MUT\_K1\_K1} (+ B)$  = barttin<sub>MUT</sub>\_rClC-K1\_rClC-K1 (+ WT barttin).

In both cases, concatamer expression measurement over many cells does not reflect expression levels at the single cell level.

To characterize the hyperpolarization-induced block of barttin<sub>MUT</sub>\_rClC-K1\_rClC-K1 mean IV-plots were normalized to the current amplitude at +105 mV and fitted by a regression line between -55 mV and +55 mV (Fig.39A). Deviations from linear slope revealed relative channel conductances for different voltages (Fig.39B). As reference the curve of rClC-K1 plus WT barttin was added from figure 17.  $G_{-255\text{mV}}/G_{\text{max}}$  values of conductance curves were compared to quantify the 'block' intensity (Fig.39C). Values were similar for rClC-K1 and concatamer with WT barttin co-expression with around 0.14. Without WT barttin concatamer had a higher  $G_{-255\text{mV}}/G_{\text{max}}$  value with 0.53. Here, effect of non-palmitoylated barttin on channel 'block' was much lower compared to the respective concatamer with WT barttin (see Fig.27). Conductance curves were fitted by Boltzmann functions to obtain the voltage of half maximum conductance ( $V_{0.5}$ ). There was no difference in  $V_{0.5}$  for the three conditions, indicating that there was no shift in conductance curve for barttin<sub>MUT</sub>\_rClC-K1\_rClC-K1 (Fig.39D).

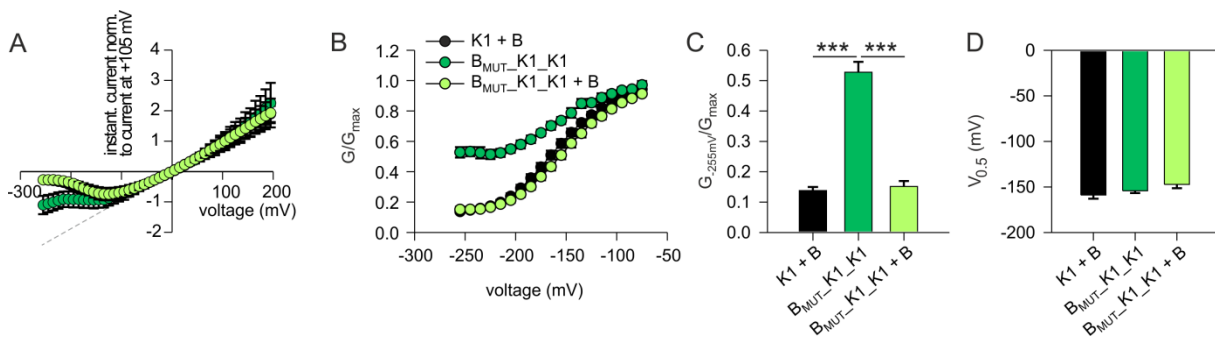


**Fig. 39 Influence of barttin palmitoylation on hyperpolarization-induced block of barttin\_rClC-K1\_rClC-K1**

(A) IV-plot of normalized instantaneous rClC-K1 currents, obtained from currents as shown in Fig.38A. All data are shown as mean values  $\pm$  S.E.M.. Dashed line represents linear regression of currents between -55 mV and +55 mV. (B) Relative conductances at negative voltages of all tested stoichiometries, obtained from current deviations from linear regression in (A). (C) Relative conductances at -255 mV for tested conditions. (D) Voltage of half maximum conductance ( $V_{0.5}$ ) obtained from fits of conductance curves from (B). (A)-(D): values for rClC-K1 + barttin were taken from Fig.17 as reference. All values are shown as mean  $\pm$  S.E.M.. K1 + B: n=13, B<sub>MUT</sub>\_K1\_K1: n=10, B<sub>MUT</sub>\_K1\_K1 + B: n=8. For (C) and (D) statistical significance was tested by one-way ANOVA with subsequent Holm-Sidak post hoc test for (C):  $F_{(10, 107)} = 87.4$  and  $p < 0.001$ . K1 + B = rClC-K1 + WT barttin, B<sub>MUT</sub>\_K1\_K1 (+ B) = barttin<sub>MUT</sub>\_rClC-K1\_rClC-K1 (+ WT barttin).

Characterizing the time-dependent gating behavior of barttin<sub>MUT</sub>\_rClC-K1\_rClC-K1 pre-pulses of -155 mV up to +145 mV were applied for 300 ms followed by a test pulse of +105 mV (Fig.40A). Steady state currents during the test pulse of +105 mV ( $I_{ss}$ ) were normalized to the instantaneous current ( $I_{inst}$ ) and plotted for each cell in figure 40B. Besides the concatamer in absence and presence of WT barttin also values for rClC-K1 in absence and presence of WT barttin were included as reference from figure 20. Measurements of the concatamer without



WT barttin presence (dark green dots) revealed exclusively strong time-dependent gating. This result is in great accordance to results of all other rCIC-K1/barttin<sub>MUT</sub> concatamers, which were sorted as exclusively strong time-dependent gating as well (see Fig.36). It gives further evidence for the important role of barttin palmitoylation for constitutive fast gate opening, since time-dependent fast gating was much less pronounced for barttin<sub>rCIC-K1\_rCIC-K1</sub> (see Fig.28).  $I_{ss}/I_{inst}$  values for barttin<sub>MUT\_rCIC-K1\_rCIC-K1</sub> in presence of WT barttin were predominantly shifted up to weak time-dependent gating (75%). This fraction was higher compared to respective values for barttin<sub>MUT\_rCIC-K1</sub> (56%) and barttin<sub>MUT\_barttinMUT\_rCIC-K1</sub> (25%, see Fig.36B). A feasible explanation might be that a 2:1  $\alpha:\beta$ -subunit stoichiometry offers more free binding sites for WT barttin than other concatamers with a higher barttin<sub>MUT</sub> fraction. Relative fast gate open probabilities revealed strong voltage-dependence for barttin<sub>MUT\_rCIC-K1\_rCIC-K1</sub> comparable to other rCIC-K1 concatamers with non-palmitoylated barttin (Fig.40C, dark green dots).

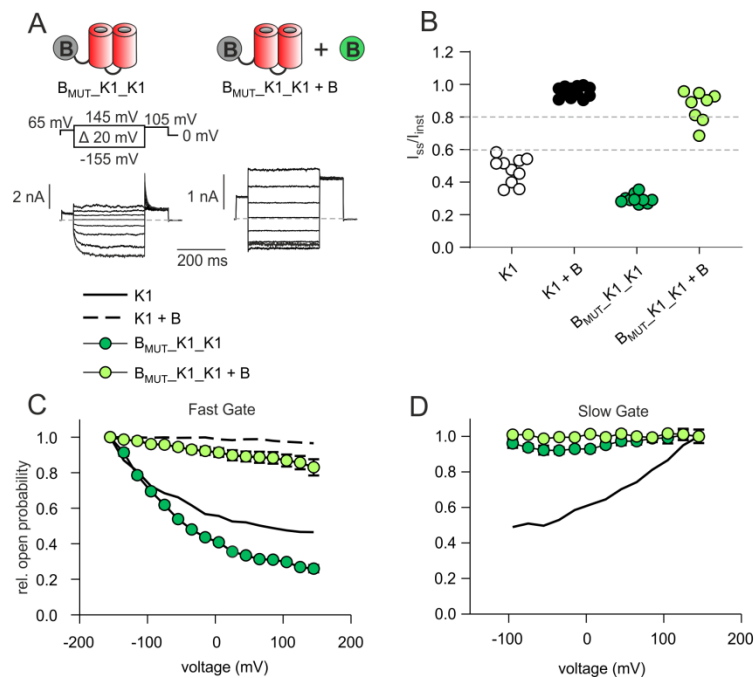


**Fig. 40 Time-dependent fast gating of barttin<sub>MUT\_rCIC-K1\_rCIC-K1</sub>**

(A) Representative current traces of  $B_{MUT\_K1\_K1}$  in absence and presence of additional WT barttin. Voltages from -155 mV to +145 mV were applied for 300 ms. Dashed lines indicate 0 nA. (B) Scatter plot of measured cells expressing either  $B_{MUT\_K1\_K1}$  in absence (dark green dots) or presence of WT barttin excess (light green dots) according to their  $I_{ss}/I_{inst}$  values. Cells were sorted as strong time-dependent, when after a voltage step from -155 mV to +105 mV steady state current amplitude ( $I_{ss}$ ) was lower than 60% of instantaneous current amplitude ( $I_{inst}$ ), as medium time-dependent, when  $I_{ss}/I_{inst}$  was between 60% and 80% and as weak time-dependent, when  $I_{ss}/I_{inst}$  was higher than 80%. Each dot is one measured cell. Dashed lines represent thresholds for categorization. (C) Relative fast gate open probabilities under different barttin availabilities, determined by plotting instantaneous current amplitudes during the test pulse versus voltages of the pre-pulse. (D) Relative slow gate open probabilities under different barttin availabilities and for different voltages. For (C) and (D) data for  $B_{MUT\_K1\_K1}$  (+ B) are shown as mean values  $\pm$  S.E.M..  $B_{MUT\_K1\_K1}$ : n=9,  $B_{MUT\_K1\_K1} + B$ : n=8 (fast gate), n=2 (slow gate). As reference mean values for K1 and K1 + B from Fig.20 are shown as solid/dashed lines in (C) and (D). K1 (+ B) = rCIC-K1 (+ barttin),  $B_{MUT\_K1\_K1} (+B)$  = barttin<sub>MUT\_rCIC-K1\_rCIC-K1</sub> (+ WT barttin).



WT barttin co-expression caused a shift towards almost voltage-independence (light green dots). Both in absence and in presence of WT barttin relative slow gate open probabilities for barttin<sub>MUT</sub>\_rClC-K1\_rClC-K1 were rather voltage-independent (Fig.40D).

### 3.3 Single channel measurements of ClC-K/barttin concatamers

#### 3.3.1 Niflumic acid blocks ClC-K channels in HEK293T cells

For hClC-Ka/barttin concatamers stationary noise analysis indicated modification of single pore parameters dependent on different  $\alpha:\beta$ -subunit stoichiometries. Using single channel measurements, in which pore characteristics can be deduced directly by opening and closing events, the mechanistic origin of noise results should be illuminated in more detail. On top of that, single channel measurements represent a further method to confirm results obtained from whole cell patch clamp measurements. Due to endogenous channels of HEK293T cells, however, single channel recordings of the desired channel were often not clearly distinguishable from others. Therefore, we used the ClC-K channel modulator niflumic acid (NFA) to prove, that obtained single channel currents were caused by ClC-K channels. Niflumic acid is a nonsteroidal anti-inflammatory fenamate, which also acts inhibitory on ClC-K channels in HEK cells. It was shown previously that an extracellularly applied concentration of 1 mM niflumic acid is sufficient to block almost all ClC-K induced currents (Imbrici et al., 2014). Therefore, we also tested the effect of 1 mM NFA on ClC-K channels in whole cell configuration before application on single channels. Figure 41A-C shows NFA treatment of cells expressing hClC-Ka plus WT barttin, figure 41D-F cells expressing rClC-K1 in absence of barttin and figure 41G-I cells expressing rClC-K1 in presence of WT barttin. Before perfusion with 1 mM NFA, currents were robust and exhibited the hyperpolarization-induced block, if barttin was present (Fig.41A,D,G, -NFA). Under NFA application currents decreased (+NFA). A special characteristic is found for hClC-Ka plus barttin, where currents seemed to be blocked preferentially at positive voltages by NFA. NFA block was reversible, since subsequent perfusion with bath solution recovered channel conductance (wash out). Comparison of IV-plots in presence and absence of NFA demonstrates inhibition over the whole voltage range (Fig.41B,E,H). Comparing currents at +105 mV revealed a highly significant current reduction of about 90% caused by NFA (Fig.41C,F,I).

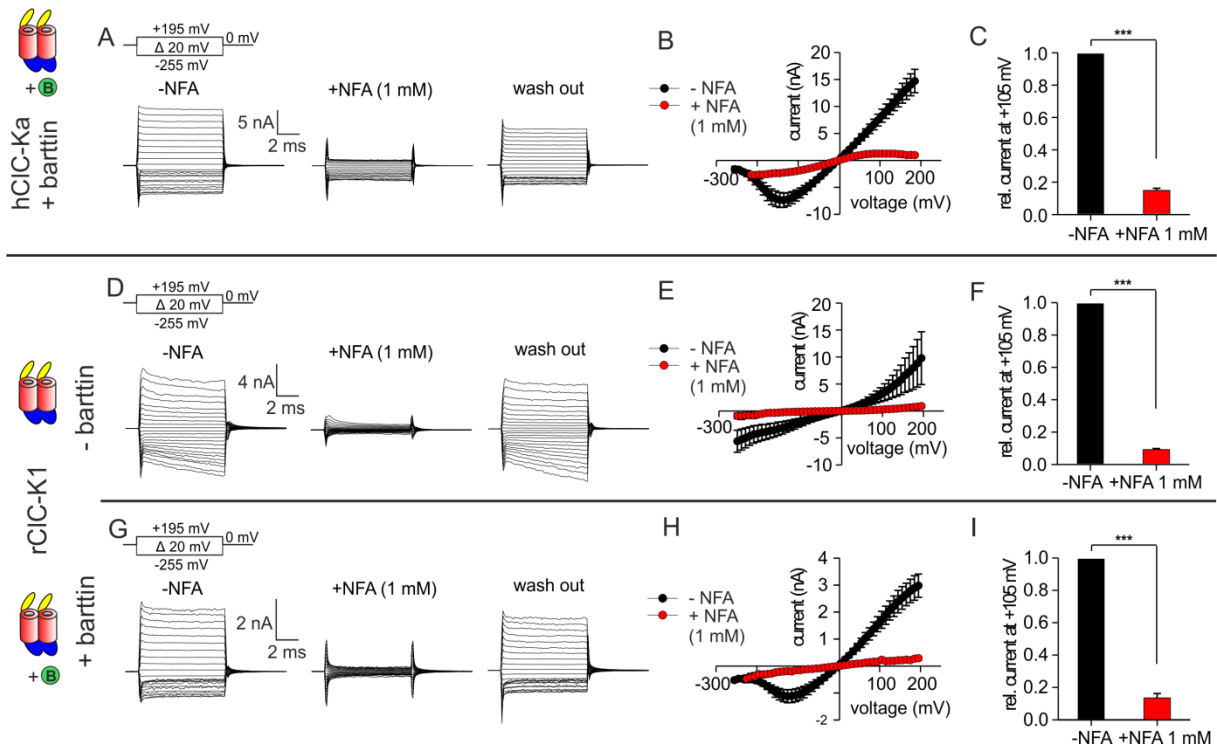


**Fig. 41 Inhibition of ClC-K channels by 1 mM NFA in whole cell configuration**

(A) Representative currents of hClC-Ka plus barttin without NFA perfusion, during NFA perfusion and after NFA washout for voltages between -255 mV and +195 mV. (B) IV-plots of hClC-Ka plus barttin without NFA perfusion (- NFA, black dots) or with NFA perfusion (+ NFA, red dots). (C) Relative mean currents at +105 mV for conditions with (red bar) and without (black bar) NFA perfusion after normalization on mean current without NFA perfusion. Data in (B) and (C) are mean values  $\pm$  S.E.M.. (-NFA: n=3, +NFA: n=3). (D) Representative currents of rClC-K1 without NFA perfusion, during NFA perfusion and after NFA washout for voltages between -255 mV and +195 mV. (E) IV-plots of rClC-K1 without NFA perfusion (- NFA, black dots) or with NFA perfusion (+ NFA, red dots). (F) Relative mean currents at +105 mV for conditions with (red bar) and without (black bar) NFA perfusion after normalization on mean current without NFA perfusion. Data in (E) and (F) are mean values  $\pm$  S.E.M.. (-NFA: n=3, +NFA: n=3). (G) Representative currents of rClC-K1 plus barttin without NFA perfusion, during NFA perfusion and after NFA washout for voltages between -255 mV and +195 mV. (H) IV-plots of rClC-K1 plus barttin without NFA perfusion (- NFA, black dots) or with NFA perfusion (+ NFA, red dots). (I) Relative mean currents at +105 mV for conditions with (red bar) and without (black bar) NFA perfusion after normalization on mean current without NFA perfusion. Data in (H) and (I) are mean values  $\pm$  S.E.M.. (-NFA: n=3, +NFA: n=3). Statistical significance in (C), (F) and (I) was tested using Student's t-test (\*\*\*)  $p < 0.001$ . NFA = niflumic acid.

### 3.3.2 High availability of barttin molecules per hClC-Ka $\alpha$ -subunit stabilizes single pore

#### opening and closing events

As reference, single channel recordings were obtained from hClC-Ka homodimers with co-expression of WT barttin (Fig.42). Measurements were performed in cell-attached configuration for most of measured patches to avoid channel rundown, which was previously observed for excised inside-out patches (Fischer et al., 2010). Figure 42 shows representative single channel measurement in cell attached configuration for hClC-Ka plus barttin at positive (Fig.42A,B) and negative voltages (Fig.42C,D). Channels exhibited three distinct and equidistant conductance states, which could be assigned to the closed state (C) or the states of one (O1) or two open pores (O2). This was expected for ClC-K channels as they harbor two separate conductance pathways. Amplitude histograms of current traces at +50 mV revealed single pore amplitudes of 1.1 pA (Fig.42A), which corresponds to a single

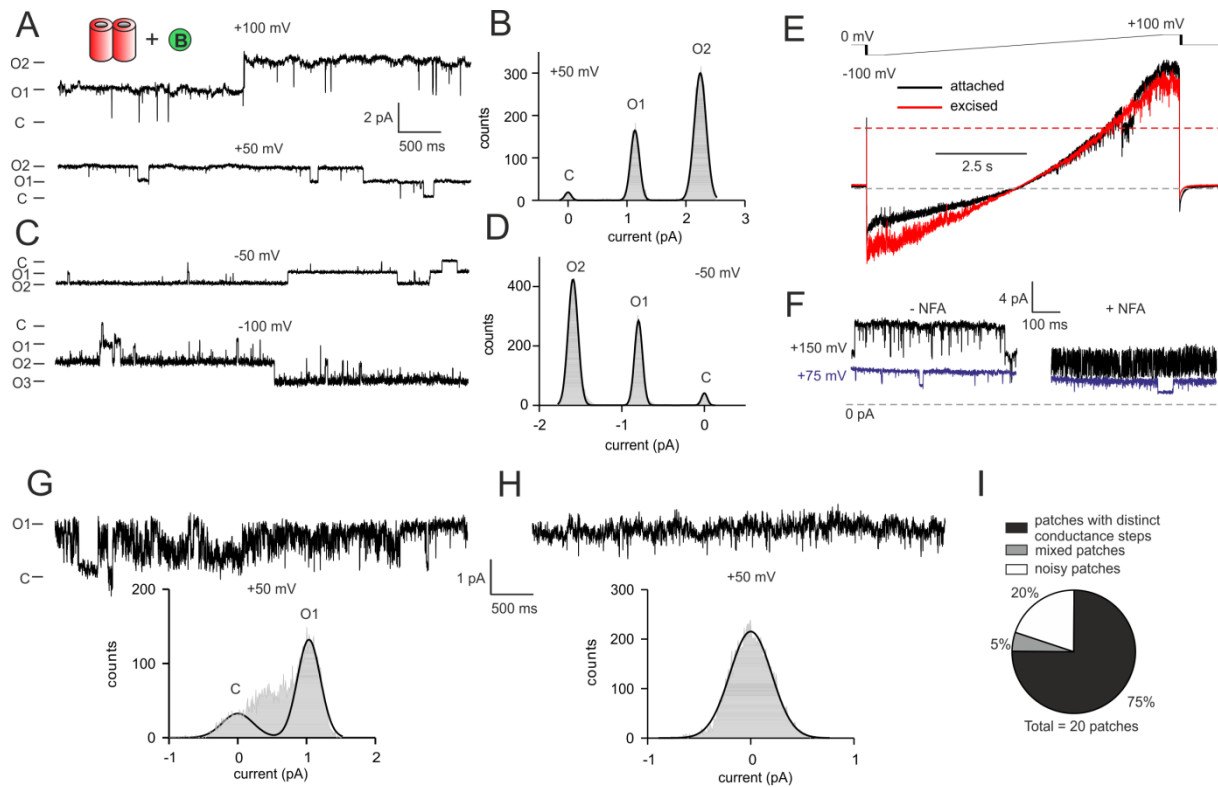


**Fig. 42 Single channel recordings of hClC-Ka with barttin co-expression**

(A) Representative single channel recordings in cell attached configuration at voltages of +100 mV and +50 mV. (B) Amplitude histogram from registration shown in (A) at +50 mV and fits with the sum of three equidistant Gaussian distributions. (C) Representative single channel recordings in cell attached configuration at voltages of -50 mV and -100 mV. (D) Amplitude histogram from registration shown in (C) at -50 mV and fits with the sum of three equidistant Gaussian distributions. (E) Current registration for voltage ramp from -100 mV to +100 mV in cell attached (black) or excised patch configuration (red). Red dashed line represents current amplitude to which both registrations were normalized. Grey dashed line represents 0 pA. (F) Representative single channel recordings in cell attached configuration without (-NFA) and with 1 mM NFA perfusion (+ NFA). Registrations are shown for +75 mV (blue traces) and for +150 mV (black traces). Dashed lines represent 0 pA. (G) Single channel recording in cell attached mode, exhibiting noisy periods and periods of distinct conductance levels. Amplitude histogram from this registration is shown below together with fits with the sum of two Gaussian distributions. Flickering in between could not be fitted. (H) Single channel recording in cell attached mode, exhibiting exclusively high frequent channel flickering. Amplitude histogram from this registration is shown below together with a mono-Gaussian fit. (I) Distribution of measured patches according to channel behavior as patches featuring distinct conductance states (black), as patches exclusively exhibiting rapid channel flickering (white) or as patches, possessing both phases with clear conductance states and phases with channel flickering, interchangeably (grey). C = closed state, O1-3 = open states 1-3, NFA = niflumic acid.

pore conductance of 22 pS, a value also obtained by stationary noise analysis (see Fig.14). Furthermore, single pore amplitudes at -50 mV with around -0.8 pA in (C) and (D) were smaller than those at +50 mV. To test whether this difference is caused by the cell attached mode, voltage ramps were applied on single channel measurements in excised patch and cell attached patch mode for the same patch (Fig.42E). For cell attached mode currents were reduced at negative voltages compared to positive (black trace). In contrast, in excised patch mode current/voltage relationship became linear (red trace). Negative currents correspond to a chloride flux out of the cell into the pipette. As in this study measurements were usually conducted in the cell attached mode, it is possible that chloride ions within the cell were not as high as chloride ion concentration in the bath or in the pipette solution, reducing all

outward directed currents. This indicates that in cell attached mode outward currents were rather unreliable due to the intracellular ion concentration, which could not be controlled exactly. Calculated on basis of Gaussian function areas, open probability of one pore at +50 mV were high (84% at +50 mV (Fig.42B), 78% at -50 mV (Fig.42D)). As the open probabilities were calculated only about the here shown, short time periods, which were selected subjectively, the open probabilities cannot be seen as representative for hClC-Ka plus barttin. Besides the here shown traces, exhibiting high pore open probability at positive and negative voltages, recordings frequently also showed periods, in which individual pores were closed over a longer time. Actually, almost permanently open pores were expected as stationary noise analyses gave absolute open probabilities near 100% at least for positive potentials (see Fig.14). To verify that currents were conducted by hClC-Ka, patches were perfused with 1 mM NFA. Figure 42F shows single channel measurements at +75 mV (blue traces) and +150 mV (black traces) with or without NFA perfusion. Currents increased for higher voltages without NFA application. In presence of NFA, however, currents did not increase for higher voltages but channels produced tremendous noise. This is in great accordance with whole cell measurements which demonstrate a current 'block' especially for positive voltages (see Fig.41). Thus, measured currents were conducted by hClC-Ka channels. Measurements depicted in 42A and C show clear and distinct channel opening or closing events. Notably, a minor fraction of patches displayed noisy recordings even in absence of NFA. However, such recordings displayed less regular current fluctuations. Figure 42G illustrates one registration containing the transition from clear channel events to rapid flickering. Plotting current amplitudes in a histogram gave a distribution, which aggravated fitting by Gaussian functions. The closed and the open state of that pore might be determined by fitting two Gaussian functions to counts of lowest and highest current values. However, in between about 28% of all counts could not be fitted, representing the occurring flickering of the channel. There were also few patches permanently showing unstable opening events, which could not be segregated into distinct conductance levels at all (Fig.42H). Here, the amplitude histogram only gave one large Gaussian-like distribution. In total, only 20% of all patches had this noisy behavior and 5% were patches with alternating clear and noisy channel events (Fig.42I). Most of all patches (75%), though, had channels with clear and distinct opening or closing events. The distribution of patches with noisy and/or stable opening events is of importance as single channel measurements of hClC-Ka/barttin concatamers, which are described in the following

part, indicate that a change in this distribution might be induced by different  $\alpha:\beta$ -subunit stoichiometries.

Analogous to hCIC-Ka plus barttin single channel measurements were performed for hCIC-Ka/barttin concatamers to investigate potential changes in single pore parameters. Representative single channel recordings for the concatamer barttin\_barttin\_hCIC-Ka at different voltages in the cell attached patch mode are shown in figure 43A. As for hCIC-Ka plus barttin co-expression there were three different, equidistant conducting states distinguishable, which were expected as one closed (C) and two open states (O1, O2) of a CIC-K channel with two pores. Single pore current amplitudes in cell attached mode was higher for positive voltages (1.1 pA at +50 mV, Fig.43B) than for negative voltages (-0.6 pA at -50 mV, Fig.43C). For the here presented current traces the open probability of one pore was high with 92% at +50 mV and 59% at -50 mV. In excised patch mode channel could adopt three different conducting states, too (Fig.43D). In contrast to the cell attached mode, single pore amplitudes were comparable for negative and positive voltages in the excised patch mode (Figs.43E,F). Furthermore, pore open probability was high with 94% at +50 mV and 98% at -50 mV for the here shown current traces. Again, as the open probabilities were calculated only about the here shown, short time periods, which were selected subjectively, the open probabilities obtained in cell attached and excised patch mode cannot be seen as representative for this concatamer. Both for cell attached and excised patch mode frequently also pores were observed with lower open probabilities. Plotting the single pore current amplitudes at voltages from -100 mV to +100 mV of the here shown current traces, confirms that currents were lower at negative than at positive voltages in cell attached mode (Fig.43G, black dots). In excised patch mode, now controlling both internal and external solutions, single pore IV-plot became linear (red dots). Identity of CIC-K channel was again validated by perfusion with 1 mM NFA at voltages of +50 mV (blue traces) and +150 mV (black traces, Fig.43H). If NFA was not perfused (-NFA), currents increased with higher voltage. Instead, currents did not increase but exhibited an intense flickering in presence of NFA (+NFA), proving the identity of CIC-K channels like for hCIC-Ka plus barttin. Also for this condition there were patches, which switched between a noisy flickering and distinct conductance states (Fig.43I). Thus, besides of the open and closed state, 27% of amplitude histogram area could not be fitted by Gaussian functions. Moreover, many patches contained channels not keeping distant conductance levels at all but exclusively high frequent flickering (Fig.43J).

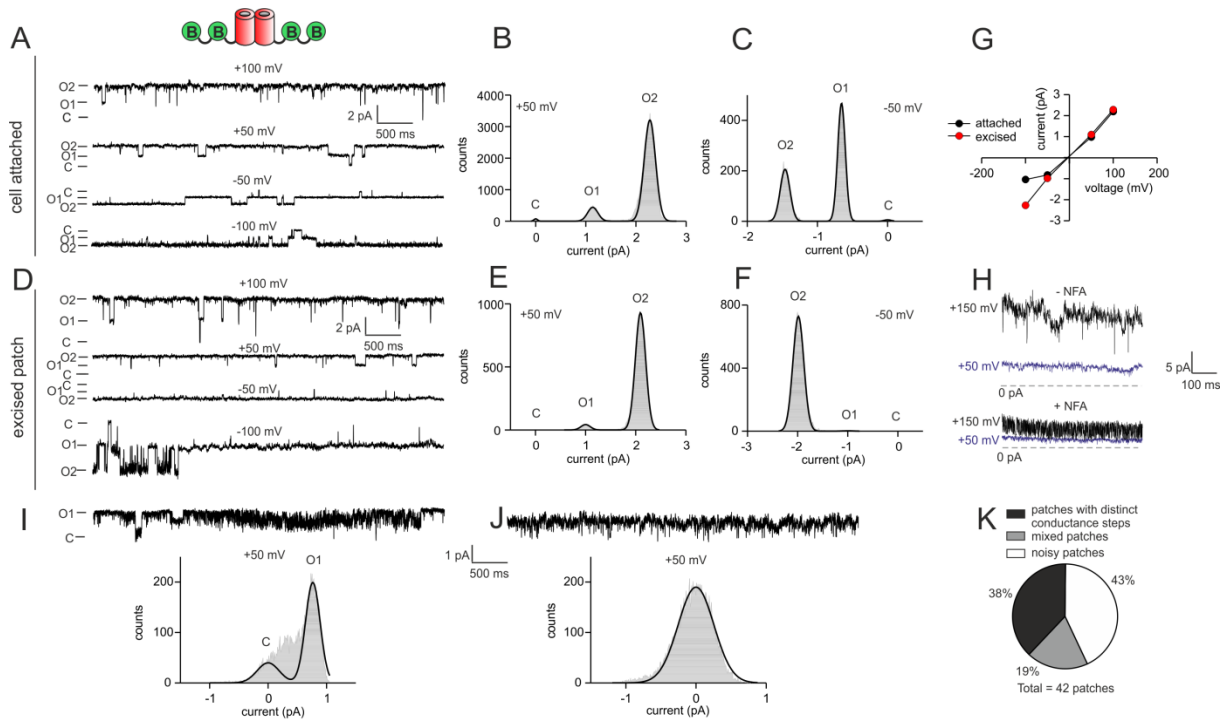


**Fig. 43 Single channel recordings of barttin\_barttin\_hClC-Ka**

(A) Representative single channel recordings in cell attached configuration at voltages of +100 mV, +50 mV, -50 mV and -100 mV. (B) Amplitude histogram from registration shown in (A) at +50 mV and fits with the sum of three equidistant Gaussian distributions. (C) Amplitude histogram from registration shown in (A) at -50 mV and fits with the sum of three equidistant Gaussian distributions. (D) Representative single channel recordings in excised patch configuration at voltages of +100 mV, +50 mV, -50 mV and -100 mV. (E) Amplitude histogram from registration shown in (D) at +50 mV and fits with the sum of three equidistant Gaussian distributions. (F) Amplitude histogram from registration shown in (D) at -50 mV and fits with the sum of three equidistant Gaussian distributions. (G) IV-plot of single pore current amplitudes for cell attached (black dots) and excised patch configuration (red dots). Values were obtained from representative single channel recordings shown in (A) and (D). (H) Representative single channel recordings in cell attached configuration without (-NFA) and with 1 mM NFA perfusion (+ NFA). Registrations are shown for +50 mV (blue traces) and for +150 mV (black traces). Dashed lines represent 0 pA. (I) Single channel recording in cell attached mode, exhibiting noisy periods and periods of distinct conductance levels. Amplitude histogram from this registration is shown below together with fits with the sum of two Gaussian distributions. Flickering in between could not be fitted. (J) Single channel recording in cell attached mode, exhibiting exclusively high frequent channel flickering. Amplitude histogram from this registration is shown below together with a mono-Gaussian fit. (K) Distribution of measured patches according to channel behavior as patches featuring distinct conductance states (black), as patches exclusively exhibiting rapid channel flickering (white) or as patches, possessing both phases with clear conductance states and phases with channel flickering, interchangeably (grey). C = closed state, O1-2 = open states 1-2, NFA = niflumic acid.

This flickering resulted in a distribution of current amplitudes, which could be fitted only by one Gaussian function. In total for the condition, where two barttins were available per hClC-Ka  $\alpha$ -subunit, patches with channels showing distant conductance levels had similar properties regarding single pore current amplitude and open probability as for hClC-Ka with barttin excess. However, the fractions of patches with distinct conductance states and patches with channel flickering changed (Fig.43K). For this condition the fraction of noisy patches increased to 43% and fraction of distinct conductance states decreased to 38%. From whole cell measurements it is known that two barttin molecules are sufficient to reach full hClC-Ka activation. Thus, for this condition a similar distribution of patches would be expected as for hClC-Ka with barttin co-expression. It could be speculated that barttin molecules linked within

a concatamer cannot bind to the  $\alpha$ -subunit as stably as co-expressed barttin. Thus, a greater fraction of patches might display unstable opening events.

Stationary noise analysis revealed smallest single pore conductance for hCIC-Ka/barttin concatamers composed of only one  $\beta$ -subunit linked to one  $\alpha$ -subunit (12 pS, see Fig.14C). Performing single channel measurements for this condition should illuminate whether this value arose really from reduced single pore current amplitudes. Figure 44A shows representative single channel measurements at different voltages in cell attached mode. For all traces three equidistant conducting states were observable, typical for channels with two pores. Single pore current amplitude of 0.9 pA at +50 mV was higher than -0.7 pA at -50 mV (Fig.44B-C), consistent with results of other conditions, as shown above. Furthermore, single pore current amplitude was rather not or only minimally reduced compared to conditions with higher barttin availability. Also, single pore open probability was high (53% at -50 mV, 92% at +50 mV). In excised patch mode single pore open probabilities with 98% at -50 mV and 88% at +50 mV were also comparably high as values in cell attached mode (Fig.44D-F). As the open probabilities were calculated only about the here shown, short time periods, which were selected subjectively, the open probabilities obtained in cell attached and excised patch mode cannot be seen as representative for barttin\_hCIC-Ka. Single pore current amplitudes at positive voltages were comparable between cell attached and excised patch mode, while current amplitudes at -100 mV were smaller in cell attached mode (black dots) than in excised patch mode (red dots, Fig.44G). Identity of CIC-K channels was tested by perfusion with 1 mM NFA leading to an increasing channel flickering or, in this case, even to a complete deactivation of CIC-K channels at +150 mV (Fig.44H), while, in contrast, the absence of NFA led to a current increase at +150 mV. Channel block by NFA proves that measured channels are CIC-K channels. The great majority of 76% of all measured patches, however, did not show clear opening or closing events in contrast to (A) and (D). Instead, channel activity was characterized by a high and noisy flickering with a single Gaussian distribution of current amplitudes (Fig.44I,K). Similar behavior was already observed for conditions with higher barttin availability but with a much lower prevalence than for this condition. Comparing all three conditions it seems likely that a higher barttin availability per  $\alpha$ -subunit opens the hCIC-Ka and stabilized opening or closing events. If only one barttin was present per  $\alpha$ -subunit, the channel was opened but rather unstably, leading to a high frequent channel flickering. In cell attached mode a reduced single pore current amplitude was not observed for this stoichiometry although indicated

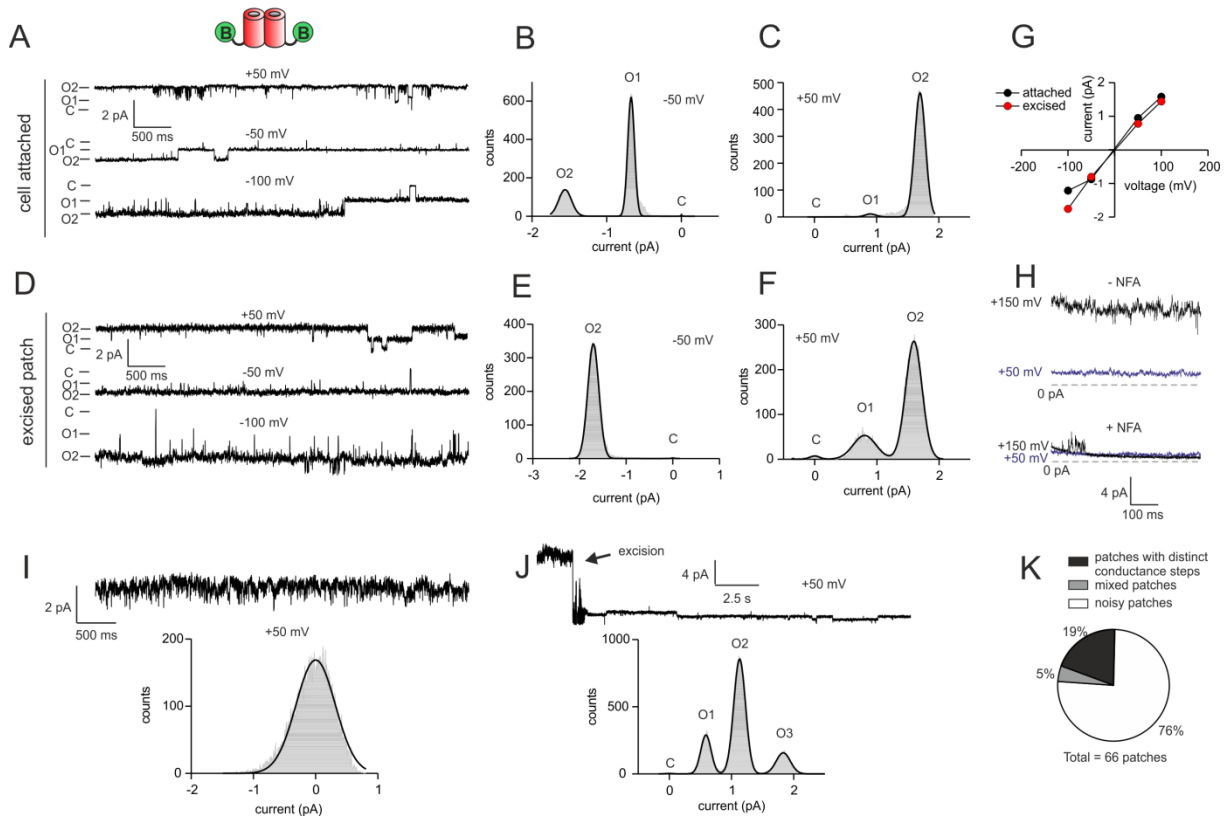


**Fig. 44 Single channel recordings of barttin\_hCIC-Ka**

(A) Representative single channel recordings in cell attached configuration at voltages of +50 mV, -50 mV and -100 mV. (B) Amplitude histogram from registration shown in (A) at -50 mV and fits with the sum of three equidistant Gaussian distributions. (C) Amplitude histogram from registration shown in (A) at +50 mV and fits with the sum of three equidistant Gaussian distributions. (D) Representative single channel recordings in excised patch configuration at voltages of +50 mV, -50 mV and -100 mV. (E) Amplitude histogram from registration shown in (D) at -50 mV and fits with the sum of two Gaussian distributions. (F) Amplitude histogram from registration shown in (D) at +50 mV and fits with the sum of three equidistant Gaussian distributions. (G) IV-plot of single pore current amplitudes for cell attached (black dots) and excised patch configuration (red dots). Values were obtained from representative single channel recordings shown in (A) and (D). (H) Representative single channel recordings in cell attached configuration without (-NFA) and with 1 mM NFA perfusion (+ NFA). Registrations are shown for +50 mV (blue traces) and for +150 mV (black traces). Dashed lines represent 0 pA. (I) Single channel recording in cell attached mode, exhibiting exclusively high frequent channel flickering. Amplitude histogram from this registration is shown below together with a mono-Gaussian fit. (J) Representative single channel recording of one patch showing channel behavior before and after patch excision (arrow). While channel exhibits flickering and high open probability before patch excision, many channels close after excision and show distinct conducting states after patch excision. Below registration amplitude histogram of currents after patch excision discloses fits of four equidistant Gaussian-like distributions. (K) Distribution of measured patches according to channel behavior as patches featuring distinct conductance states (black), as patches exclusively exhibiting rapid channel flickering (white) or as patches, possessing both phases with clear conductance states and phases with channel flickering, interchangeable (grey). C = closed state, O1-3 = open states 1-3, NFA = niflumic acid.

by stationary noise analysis. Still, a remarkable change in channel behavior was seen after patch excision (Fig.44J). While before excision channels flickered and possessed a high open probability, many channels closed after excision. This might be induced by a channel rundown, also previously seen for CIC-K channels after patch excision (Fischer et al., 2010). More interestingly, channels now exhibited clear and stable opening and closing events. Amplitude histogram for the period after patch excision revealed a single pore current amplitude of 0.6 pA at +50 mV, which was reduced compared to other measurements shown before. The calculated single pore conductance of this example (12 pS) is in high accordance with the



conductance, given by stationary noise analysis for this stoichiometry (see Fig.14C). Still, it could not be proved whether the remaining current arose from ClC-K channel action or from others. Nevertheless, this remarkable observation was seen for three independent patches and displays a characteristic at least for this stoichiometry.

In the 'discussion' part of this thesis the potential impact of rapid channel flickering on the outcome of stationary noise analysis is commented. It might be an explanation for noise analysis results, which could not be fully confirmed by single channel measurements. Thus, this discussion might indicate special circumstances, in which noise analysis results do not reflect channel properties correctly.

### 3.3.3 Barttin availability does not affect single pore conductance of rClC-K1

As for hClC-Ka concatamers the effect of different barttin availabilities per  $\alpha$ -subunit should be examined also for rClC-K1 concatamers on single channel level. As demonstrated in figure 18, stationary noise analysis revealed a single pore conductance of around 17 pS for rClC-K1 in presence of barttin. This was lower than the value of 34 pS, which was postulated before as unitary conductance for rClC-K1 (Fischer et al., 2010). However, at the time point of that publication it was unclear whether this value reflects single or double pore conductance. Because stationary noise analysis for hClC-Ka/barttin concatamers revealed for some conditions single pore conductances, which potentially did not reflect real circumstances, obtained conductance for rClC-K1 should be also verified by single channel measurements. As in this study only few single channel measurements were conducted for particular rClC-K1/barttin stoichiometries, the example registrations, which are shown in the following, might not be representative for every parameter and for the respective conditions. Especially with respect to open probabilities the given values are not comparable between tested conditions as amplitude histograms, used for determination of open probabilities, refer to registrations of different time scales. Moreover, registrations were conducted at different voltages. However, obtained parameters were consulted to substantiate former findings regarding rClC-K1 single pore conductance.

As reference, single channel measurements were also conducted for rClC-K1 with barttin co-expression (Fig.45A). For the shown registration three conducting states can be identified that can be assigned either to two closed pores (C) and one (O1) or two open pores (O2). As

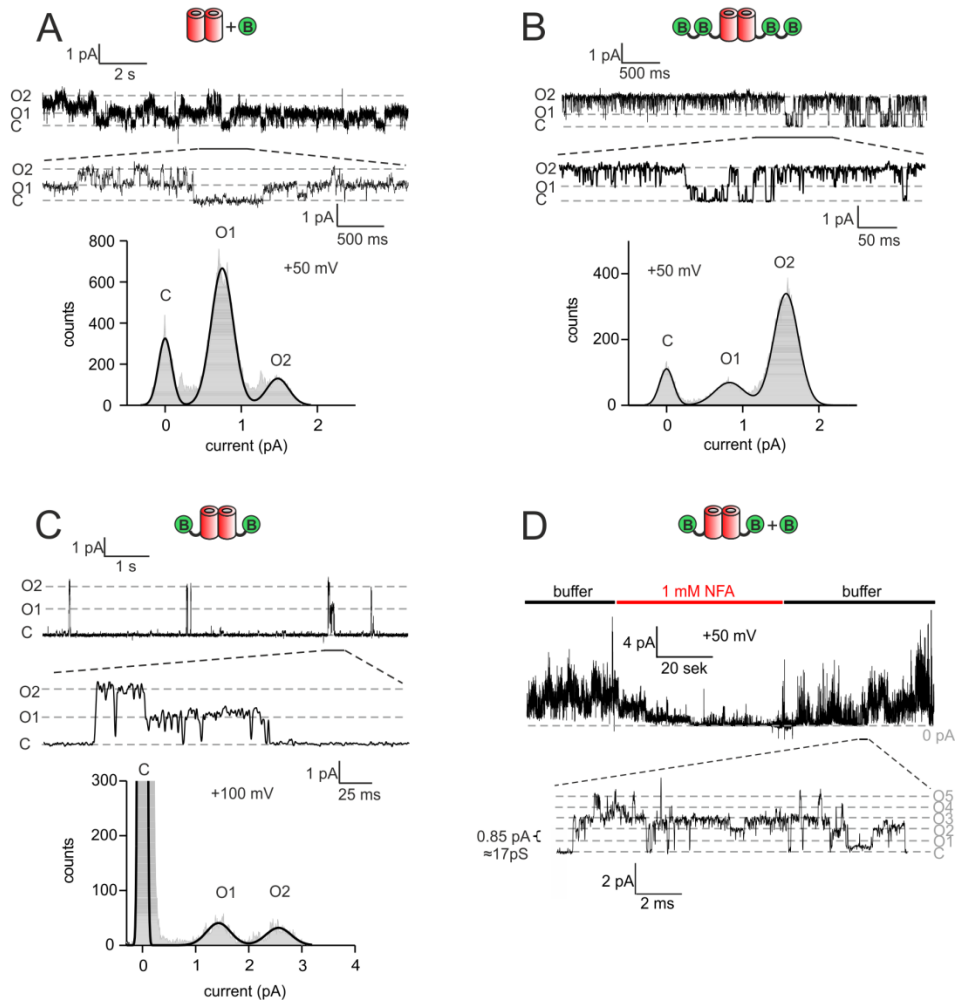


**Fig. 45 Single channel recordings of rClC-K1 under different  $\alpha:\beta$ -subunit stoichiometries**

(A) Representative single channel recording of rClC-K1 with barttin co-expression in cell attached mode at +50 mV. A magnification of one section of the upper trace (indicated by a bar) is depicted below. Amplitude histogram from this registration is shown at the bottom with the sum of three equidistant Gaussian distributions. (B) Representative single channel recording of rClC-K1 in a 2:4  $\alpha:\beta$ -subunit stoichiometry for a ClC-K homodimer in cell attached mode at +50 mV. A magnification of one section of the upper trace (indicated by a bar) is depicted below. Amplitude histogram from this registration is shown at the bottom with the sum of three equidistant Gaussian distributions. (C) Representative single channel recording of rClC-K1 in a 2:2  $\alpha:\beta$ -subunit stoichiometry for a ClC-K homodimer in cell attached mode at +100 mV. A magnification of one section of the upper trace (indicated by a bar) is depicted below. Amplitude histogram from this registration is shown at the bottom with the sum of three equidistant Gaussian distributions. (D) Representative single channel recording of barttin\_rClC-K1 concatamers with additional barttin co-expression in cell attached mode at +50 mV. Under perfusion with bath solution (buffer, black colored sections) channels exhibit a high open probability, while channels almost completely close under perfusion with 1 mM NFA (red colored section). A magnification of one section of the upper trace (indicated by a bar) is depicted below. C = closed state, O1-5 = open states 1-5, NFA = niflumic acid.

it is visible in the amplitude histogram, conducting states were equidistant and correspond to a single pore conductance of around 15 pS. This is close to the value determined by stationary noise analysis.

If two barttin molecules were linked to one  $\alpha$ -subunit of rClC-K1, open probability was quite high for the subjectively selected registration excerpt (82%, Fig.45B). Channel mostly switched between states, where one or two pores were open. Still, in several moments, both pores

were closed (C). A single pore conductance of 16 pS was obtained, highly consistent with results of stationary noise analysis.

Recording of the concatamer barttin\_rClC-K1 conveyed quite rare events of channel openings, which indicate a rather low open probability of one pore for the here presented recording section (11%, Fig.45C). However, when the channel became active, two conducting states were distinguishable (O1/O2). As it gets apparent by the amplitude histogram pore conductance was around 14 pS (O1) and 13 pS (O2), respectively. Co-expression of barttin with barttin\_rClC-K1 increased channel open probability with more channels switching into an open state (Fig.45D). Perfusion with 1 mM NFA induced a channel block (red bar phase), verifying the identity of rClC-K1 channels. NFA perfusion was stopped after around one minute and wash out with buffer solution started. rClC-K1 channels recovered from inhibition. Zooming into a region of high channel open probability demonstrates that the patch contained many channels. Despite high fluctuation between closed and open states distinct current states were identifiable with an amplitude of 0.85 pA at +50 mV, which corresponds to a pore conductance of 17 pA as determined by noise analysis.

Although it could not be completely excluded that there was a slightly lower pore conductance for rClC-K1 bound to only one barttin than for rClC-K1 with higher barttin availability, rClC-K1 pore conductance was not presumably changed by different  $\alpha:\beta$ -subunit ratios and was around 17 pS.

## 4 Discussion

ClC-K channels together with their  $\beta$ -subunit barttin are vitally important for physiological processes in the stria vascularis of the inner ear and in the Henle's loop of the kidney by the passive transepithelial transport of chloride ions. A deficiency of ClC-K channel complexes may lead to severe symptoms like deafness or salt-wasting polyuria, summarized as Bartter syndrome (Bartter et al., 1962). Understanding and analysis of determinants important for channel functionality might give the possibility to develop drugs targeting this disease. Since a concomitant symptom of Bartter syndrome is a distinct hypotension, studying functional determinants of ClC-K channels might support further approaches for the development of antihypertensive drugs.

Since barttin influences stability, trafficking and gating of ClC-K/barttin complexes (Fischer et al., 2010; Janssen et al., 2009; Scholl et al., 2006; Waldegger et al., 2002) one key requirement for proper channel activity is supposed to be the correct binding of the  $\beta$ -subunit barttin to the  $\alpha$ -subunit of the ClC-K channel. Up to now it has been only shown that the B- and J-helices of the  $\alpha$ -subunit are sufficient for barttin binding (Tajima et al., 2007). Because both helices are located at the opposite side of the channel a binding stoichiometry of at least two  $\beta$ -subunits per one  $\alpha$ -subunit is rational. However, it is still unknown what the stoichiometry is, which necessary is for channel modulation. As binding of barttin to the B- and J-helices has been only demonstrated by immunoprecipitation of very short channel segments, it remains to be shown that binding at these positions is also possible within the whole channel protein, as binding sites for barttin at both helices might be not accessible under physiological conditions. In addition, there might also exist further barttin binding sites within the whole channel  $\alpha$ -subunit, which have not been identified, yet. To investigate the functional stoichiometry between barttin and ClC-K channels in a first approach, we covalently linked either one or two  $\beta$ -subunits to one  $\alpha$ -subunit or one  $\beta$ - to two connected  $\alpha$ -subunits and analyzed expression level, subcellular transport and electrophysiological parameters like current amplitudes, open probabilities, time constants of current relaxations and single pore current amplitudes. Investigation was performed both for the human hClC-Ka and for the rodent rClC-K1. In a second approach we used these concatamers of different  $\alpha$ : $\beta$ -subunit stoichiometries as a tool to investigate the role of barttin palmitoylation for stability, trafficking and gating of ClC-K/barttin complexes. Previous studies indicate that lack of barttin

palmitoylation, induced by point mutations within barttin, might be involved in development of Bartter syndrome (Gorinski et al., 2020; Steinke et al., 2015).

An overview about the putative effects of  $\alpha$ : $\beta$ -subunit stoichiometries and barttin palmitoylation on ClC-K fast and slow gates is given in figure 46.

In brief, the first approach of this study shows that at least one barttin available per  $\alpha$ -subunit is able to transport the ClC-K complex to the plasma membrane. Furthermore, one barttin per  $\alpha$ -subunit activates hClC-Ka channels and opens the slow gate. For the rodent rClC-K1 it was observed in similar way that one barttin per protopore can open the common slow gate, while voltage-dependent gating of fast gate was marginally affected. However, with two barttins per  $\alpha$ -subunit also the fast gate was opened at physiological voltages for rClC-K1. The fast gate of the human orthologous channel hClC-Ka was found to be stabilized at physiological voltages by the second barttin per one  $\alpha$ -subunit.

Results of the second approach support the previous finding that barttin palmitoylation is not necessary for plasma membrane trafficking of hClC-Ka and rClC-K1. In exclusive presence of non-palmitoylated barttin the hClC-Ka channel is not conducting. This changes upon co-expression of palmitoylated barttin, proving that non-palmitoylated barttin can be replaced by palmitoylated barttin within the barttin binding site of the  $\alpha$ -subunit. For the rodent rClC-K1 we demonstrated that one non-palmitoylated barttin per  $\alpha$ -subunit is sufficient to open the slow gate in similar way as palmitoylated barttin. Instead, fast gate could not be opened constitutively by non-palmitoylated barttin for a 1:2  $\alpha$ : $\beta$ -subunit stoichiometry or even for higher mutant barttin availabilities. Consequently, barttin palmitoylation is important for fast gate modulation but not for slow gate modulation. It can be hypothesized that barttin palmitoylation is relevant for opening of the hClC-Ka fast gate, too. Thus, inactive hClC-Ka channels in presence of non-palmitoylated barttin could be explained by closed fast gates.

The results of this study, which substantiate the effects of the ClC-K/barttin stoichiometry as depicted in figure 46, are interpreted and debated in more detail in the following section.

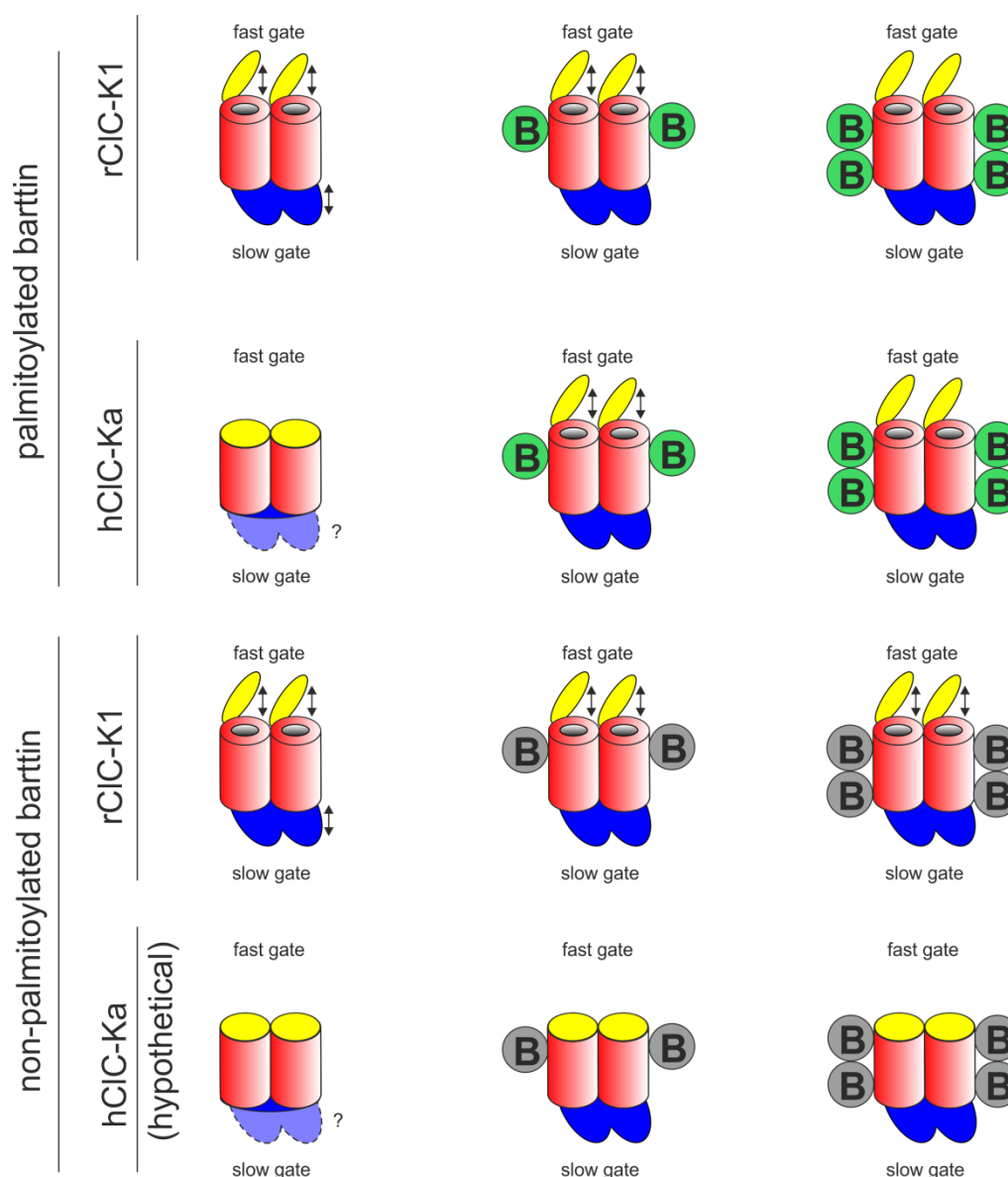


**Fig. 46 Overview about putative effects of palmitoylated and non-palmitoylated barttin on CIC-K channel gating**

'B' in green circle represents palmitoylated and 'B' in grey circles non-palmitoylated barttin. Double-arrows visualize flexible movement of fast or slow gates. Gates without arrows are proposed to stay mainly in the open or closed position.

#### 4.1 All CIC-K/barttin concatamers were successfully expressed in used cell lines

As a basic requirement of this study we found that concatamers of CIC-K  $\alpha$ -subunits and barttin  $\beta$ -subunits were successfully expressed at every tested stoichiometry. Expression analyses confirmed this finding both in the HEK293T and MDCKII cell lines. However, expression level of concatamers was lower than for the  $\alpha$ -subunit monomers (Figs.12,15). Furthermore, expression level decreased with the molecular weight of the concatamer. Possibly, mRNA or protein sequence of longer concatamers was more unstable or was degraded faster than shorter concatamers. In presence of additional barttin, expression level

of  $\alpha$ -subunit proteins decreased even more compared to the absence of additional barttin. At first glance, it seems to disagree with published data, demonstrating that barttin increased ClC-K expression (Janssen, 2008; Janssen et al., 2009). However, in the previous study both  $\alpha$ - and  $\beta$ -subunits were expressed by vectors, containing the CMV promotor for protein expression. Thus, the basic expression levels of both proteins are meant to be similar. However, in this study barttin was expressed by the pcDNA3.1 vector, which expressed encoded proteins very effectively, while ClC-K proteins were expressed by the pSVL vector exhibiting a lower expression effectivity. This might result in a competition between expression of both components for the cellular protein production machinery, which was clearly dominated by the pcDNA3.1 vector. A further study supports this assumption as it demonstrates that the co-expression of  $\alpha$ - and  $\beta$ -subunits in HEK293T cells might compete for expression, meaning that high expression of the  $\alpha$ -subunit repressed expression of the  $\beta$ -subunit and *vice versa* (Wojciechowski, 2013). Indeed in the present study, a clear barttin overexpression was required to guarantee the occupation of all potential barttin-binding sites per  $\alpha$ -subunit. Different expression levels of the tested conditions (different  $\alpha$ : $\beta$ -stoichiometries) have to be considered for interpretation of whole cell current amplitudes as they depend on the expression level of channels. By biotinylation experiments in HEK293T cells we demonstrated that the relative fraction of channels/concatamers within the plasma membrane, which is relevant for current generation, is similar between tested conditions in comparison to the whole cell expression level (Figs.12,15). This means that relative expression levels of all conditions could be directly used to normalize whole cell current amplitudes, which was also done in this study (Figs.13,16,23,30,33).

Confocal images of MDCKII cells, expressing concatamers composed of rClC-K1, frequently exhibited a faint YFP veil within the whole cytosol (Figs.15,25,32). This was actually not expected, since YFP was covalently bound to the concatamers and should stay membrane-associated. On basis of this finding it might be possible that degradation of rClC-K1/barttin concatamers falsifies subsequent electrophysiological analyses with normalization of current amplitudes to expression analyses. Therefore, we firstly investigated, on which factors degradation is dependent.

SDS-PAGE gels of HEK293T and MDCKII cell lysates indicate that parts of the constructs near the C-terminus, where the YFP tag was located, were cleaved off and spread freely in the cytosol, causing staining of the entire cytosol with YFP fluorescence. Such degradation was

especially seen by use of the pSVL vector but not of the pcDNA3.1 vector as vehicle for the rClC-K1 cDNA (Fig.47A,B). Moreover, constructs including hClC-Ka did neither show such intense degradation (Fig.47C,D). In the case of hClC-Ka/barttin concatamers, not only one but at least two additional distinct degradation bands appeared. This suggests that the C-terminus of hClC-Ka is processed differently from the C-terminus of rClC-K1 and harbors at least two cleaving sites for endogenous proteases. Comparing hClC-Ka and rClC-K1, the impact of protein degradation on the quantification of relative expression levels for hClC-Ka concatamers is thought to be smaller.

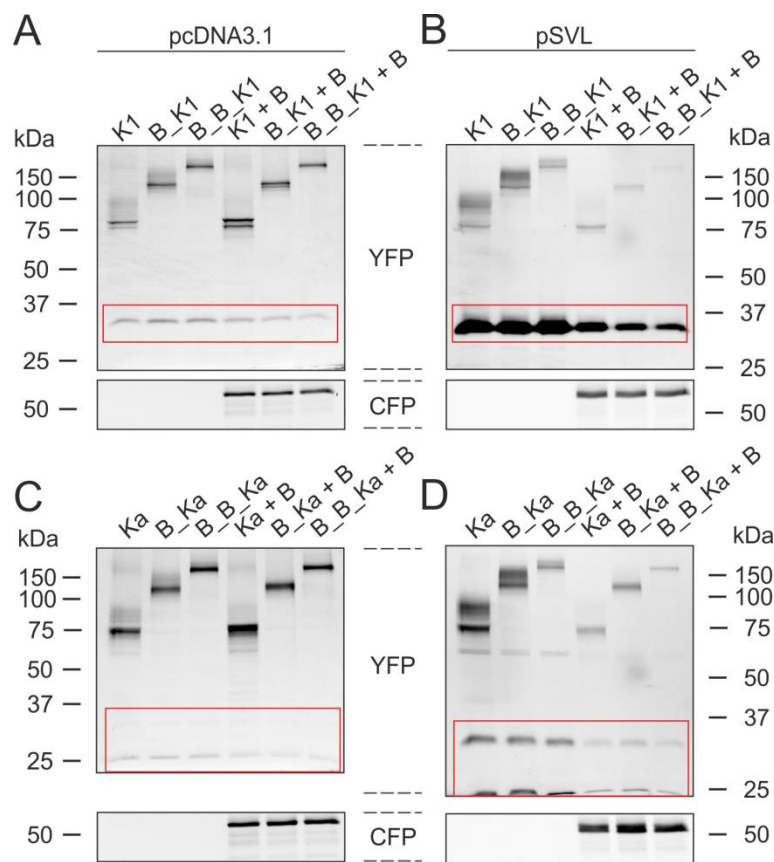


**Fig. 47 Fluorescent expression products of rClC-K1/hClC-Ka concatamers in HEK293T cells**

(A), (B) Fluorescence scan of a total SDS-PAGE gel with protein lysates from HEK293T cells, expressing rClC-K1 monomers/concatamers in presence or absence of additional barttin. YFP-tagged  $\alpha$ -subunits are shown in the upper picture and CFP-tagged barttin in the lower picture. (C), (D) Fluorescence scan of a total SDS-PAGE gel with protein lysates from HEK293T cells, expressing hClC-Ka monomers/concatamers in presence and absence of additional barttin. YFP-tagged  $\alpha$ -subunits are shown in the upper picture and CFP-tagged barttin in the lower picture. Both  $\alpha$ - and  $\beta$ -subunits in (A) and (C) were expressed *via* the pcDNA3.1 vector for one day.  $\alpha$ -subunits in (B) and (D) were expressed *via* the pSVL vector for two days. Degradation products of  $\alpha$ -subunits in (A) – (D) are always highlighted by a red box. K1 (+ B) = rClC-K1 (+ barttin), B\_K1 (+ B) = barttin\_rClC-K1 (+ barttin), B\_B\_K1 (+ B) = barttin\_barttin\_rClC-K1 (+ barttin), Ka (+ B) = hClC-Ka (+ barttin), B\_Ka (+ B) = barttin\_hClC-Ka (+ barttin), B\_B\_Ka (+ B) = barttin\_barttin\_hClC-Ka (+ barttin).

SDS-PAGE gels show, that the amount of concatamer degradation depends on the expression vector and on the  $\alpha$ -subunit isoform within the concatamers. In the next step we want to give



reasons for these degradation products. Furthermore, the relevance of these degradation products for validity of expression analyses should be pointed out.

One explanation for the intense cleavage product of rCIC-K1 constructs could be that the entire channel was degraded and a cleavage product at around 35 kDa remained. In this case, there should be no consequences for the expression analysis, since only the bands with the expected molecular weight would be relevant for analysis.

Expression profiles could imply that the amount of functional channels depended on their synthesis and degradation. For pcDNA3.1 expression, synthesis might be faster than degradation. The intact channels could be already clearly expressed after one day and accumulated in plasma membrane and endoplasmic reticulum. The short 35 kDa product as a sign of degradation could be left behind and is not relevant. For pSVL expression, synthesis might be so slow that degradation reduces the amount of functional channels. Also for this case there would be no falsification of results from expression analysis as only bands with expected molecular weight are relevant for analysis.

On the other hand, a further possible reason for degradation products could be that intracellular proteases cleaved off its C-terminus for physiological maturation of the channel. If in this case invisible/non-tagged proteins were still present, expression analyses could be biased. Since expression analyses were performed exclusively on rCIC-K1 concatamers when expressed *via* the pSVL vector - and in this case the degradation bands were particularly intense - a high proportion of invisible channel proteins would be expected. As, using the pSVL vector, the proteins were expressed for two days (instead of one day for pcDNA3.1 vector), this could be the reason why the degradation bands were so intense. The degradation products would have had more time to accumulate than with shorter expression time. Therefore, we also checked whether the degradation products were formed after one day of expression time. The proteins with expected molecular weight were still barely expressed after one day, while the degradation products were already clearly visible (Fig.48A). This means that regardless of the expression time, more of the degradation product was formed than the intact protein. In addition, the fluorescence intensity of the degradation product decreased the longer the expected protein was and also when barttin was co-expressed (Fig.48B,C). This observation is consistent with the results of expression analysis for the intact proteins, showing that the expression of the degradation products correlates with that of the intact proteins. This also means that even if invisible channels arose as a result of cleavage,

the total amount of functional channels would be proportional to the amount of channels still visible in the gel. Even if the absolute expression level of all channel proteins is not determinable due to partial degradation, relative channel/concatamer expression levels between different conditions correlate to absolute values. Accordingly, the fluorescence intensities of the intact proteins would reflect the actual expression of intact channels. It means that degradation products would be irrelevant for subsequent normalization steps using relative expression levels.

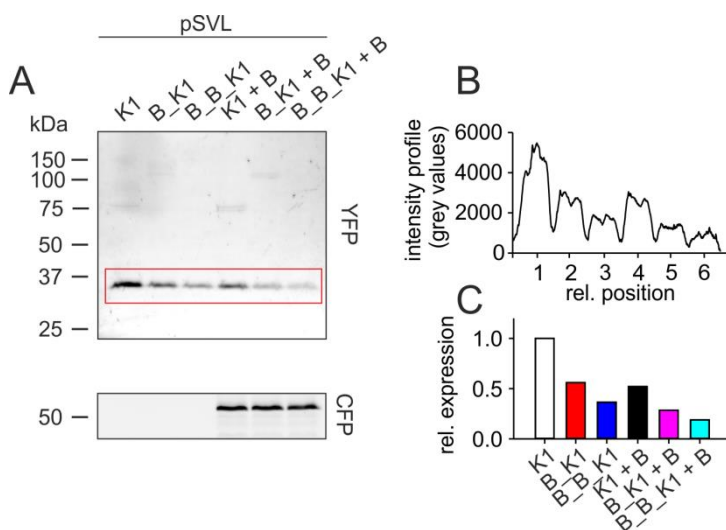


**Fig. 48 Amount of rClC-K1 concatamer degradation product after one expression day correlates with concatamer expression level after two days**

(A) Fluorescence scan of a SDS-PAGE gel with protein lysates from HEK293T cells, expressing rClC-K1 concatamers *via* the pSVL vector for one day. YFP-tagged  $\alpha$ -subunits are shown in the upper picture and CFP-tagged barttin in the lower picture. Degradation products of  $\alpha$ -subunits are highlighted by a red box. (B) Fluorescence intensity profile in grey values of rClC-K1 degradation products of (A) surrounded by a red box. (C) Relative expression levels of rClC-K1 concatamer degradation products determined from YFP fluorescence intensity profile in (B). Expression levels were normalized to expression of the rClC-K1 monomer (white bar). K1 (+ B) = rClC-K1 (+ barttin), B\_K1 (+ B) = barttin\_rClC-K1 (+ barttin), B\_B\_K1 (+ B) = barttin\_barttin\_rClC-K1 (+ barttin).

#### 4.1.1 The concatamer barttin\_rClC-K1\_rClC-K1 represents an expressional and functional exception among tested concatamers

Interestingly, the concatamer barttin\_rClC-K1\_rClC-K1 generated robust currents but was almost not expressed with the expected molecular weight (Figs.25,26).

As one explanation for the discrepancy between expression levels and current amplitudes, it might be conceivable that, unlike for other concatamers, the expression of the concatamer within the entire cell layer might not correlate with the expression of the single cells used for patch clamp experiments and confocal images. The mean expression of the concatamer within a cell layer might be very weak and only single cells fluoresced (strongly), which presumably had inserted many channels in the plasma membrane. These cells might have been subjectively selected for patch clamp experiments and presumably exhibited larger currents than expected for the average of cells. Similarly, areas within the MDCKII cell layer that exhibited particularly high numbers of YFP-fluorescent cells were specifically selected for

confocal imaging. This should not obscure the fact that the majority of all cells did not exhibit fluorescence.

To test whether the concatamer barttin\_rClC-K1\_rClC-K1 induces differences in fluorescence between expressing cells, which is higher than for other tested conditions, fluorescence measurements were carried for rClC-K1 and barttin\_rClC-K1\_rClC-K1 out by the use of a plate reader (Fig.49A,B). Using this method the fluorescence intensities of hundreds of individual cells per cover slip could be recorded automatically. The advantage is that the variance in fluorescence between cells can be compared between both channel constructs, which would be not possible by biochemical approaches. Mean fluorescence intensity over more than thousand cells appeared similar for both conditions, which is caused by great fractions of YFP-tagged degradation product freely floating within the cytosol. Therefore, it is not correlated to expression levels of intact channel proteins as shown in figure 25. The standard deviation of fluorescence intensity for all YFP-positive cells was compared between both constructs and revealed nearly identical values (Fig.49C). Thus, it seems unlikely that an altered fluorescence distribution within the cell layer caused the discordance between expression levels and measured whole cell current amplitudes.

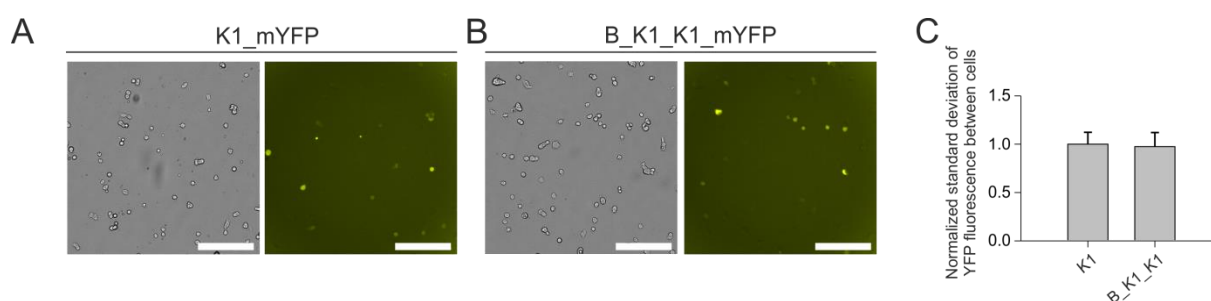


**Fig. 49 Analysis of YFP fluorescence distribution between HEK293T cells expressing rClC-K1 or barttin\_rClC-K1\_rClC-K1**  
(A) Singularized HEK293T cells expressing K1\_mYFP. Representative bright field image is shown left and YFP fluorescence on the right. YFP-positive cells are visible as yellow dots. (B) Singularized HEK293T cells expressing B\_K1\_K1\_mYFP. Representative bright field image is shown on the left and YFP fluorescence on the right. YFP-positive cells are visible as yellow dots. (C) Standard deviation of fluorescence of YFP-positive cells for conditions in (A) and (B). Data show mean values of four different wells of a six well plate for each condition  $\pm$  standard deviation. In total, fluorescence of 1782 cells was measured for K1 and of 1577 cells for B\_K1\_K1. Student's t-test was performed to test for significance. Scale bars in (A) and (B) = 200  $\mu$ m.

Within this study it has not been clarified up to now, why there is such a remarkable discrepancy between measured expression level and whole cell current deviation amplitudes for the concatamer barttin\_rClC-K1\_rClC-K1. The consequence is that expression analysis of this concatamer is not reliable for normalization of current amplitudes as values may not correspond to real expression.

Excluding the data of the concatamer barttin\_rClC-K1\_rClC-K1 from the overall evaluation is also justifiable due to electrophysiological results.

For the rClC-K1 concatamers with one, two or even more  $\beta$ -subunits per  $\alpha$ -subunit the influence of barttin on the channel increased the more barttin subunits were available per one  $\alpha$ -subunit. However, the concatamer barttin\_rClC-K1\_rClC-K1, exhibiting one  $\beta$ - per two  $\alpha$ -subunits, represented an exception. The time-dependent fast gating was more decreased and the hyperpolarization-induced block was more pronounced for this construct in comparison to the concatamer barttin\_rClC-K1 with one  $\beta$ - per one  $\alpha$ -subunit (Figs.17,20,27,28). This is surprising, since for these two stoichiometries an inverse correlation would have been expected for gating characteristics. One great difference between this concatamer and others is that here also two  $\alpha$ -subunits were covalently linked by a 22 amino acid long linker sequence. Although such linker sequences of comparable length have been successfully used in previous studies on ClC-K channels (Fahlke et al., 1997; Stölting et al., 2014), it might be possible that the linker induced a conformational change in both  $\alpha$ -subunits and the  $\beta$ -subunit, which led to an altered gating behavior. Potentially, one additional function of barttin is the correct orientation of both  $\alpha$ -subunits or the enhancement of binding affinity for both  $\alpha$ -subunits within a homodimer. The linker might adopt this part of barttin's function and orientate both  $\alpha$ -subunits in a way that mimics a higher barttin availability.

Remarkably, the altered gating behavior observed for this stoichiometry compared to other concatamers was only restricted to the concatamer with two rClC-K1  $\alpha$ -subunits. The respective concatamer with hClC-Ka did not exhibit conflicting results. Macroscopic current amplitudes were remarkably lowered compared to hClC-Ka in co-expression of barttin, which is in accordance with results for other hClC-Ka concatamers. Moreover, whole cell expression level of barttin\_hClC-Ka\_hClC-Ka was only around 33% of hClC-Ka monomer expression level (Fig.22), which is in high agreement with low whole cell current amplitudes for this construct (Fig.23). Therefore, we assume the hClC-Ka/barttin concatamer in 2:1 stoichiometry as valid for data interpretation.

To summarize expressional studies of this thesis, it is obvious that the concatamer barttin\_rClC-K1\_rClC-K1 represents an exception within all tested concatamers because it exhibits an expression level and gating behavior which is - at this time - not explainable and in disaccord to other rClC-K1/barttin concatamers. Still, for all other tested concatamers we found a successful protein expression, which could be taken for normalization of whole cell

current amplitudes and to extract information about the impact of different  $\alpha:\beta$ -subunit stoichiometries on whole cell currents.

#### **4.2 One barttin per one $\alpha$ -subunit is sufficient to promote plasma membrane insertion**

For the function of ClC-K/barttin channel complexes it is of high importance that trafficking to the plasma membrane is facilitated. Thus, it was tested which  $\alpha:\beta$ -subunit stoichiometry is sufficient for proper surface membrane transport.

Confocal microscopy images demonstrate that ClC-K monomers in absence of barttin predominantly stayed in intracellular compartments of MDCKII cells. An excessive overexpression of barttin led to a change in ClC-K distribution towards the plasma membrane together with barttin (Figs.12,15). This is consistent with published data, underlining barttin's function to promote plasma membrane trafficking of ClC-K channel complexes to the surface membrane (Scholl et al., 2006). Investigating concatamers of different  $\alpha:\beta$ -subunit stoichiometries it was found that at least one barttin available per  $\alpha$ -subunit is able to transport the ClC-K complex to the plasma membrane. This was demonstrated by confocal images of transfected MDCKII cells. YFP fluorescence of tagged channel proteins was located near the plasma membrane and rather not in intracellular compartments for ClC-K concatamers.

To prove not only transport but also plasma membrane insertion, biotinylation assays were performed, which enabled the extraction of proteins incorporated in the surface membrane. All concatamers and also ClC-K monomers were found in the surface membrane in comparable fractions for HEK293T and MDCKII cells (Figs.12,15). Still, previous results showed increased surface membrane expression for ClC-K channels in presence of barttin (Janssen, 2008; Janssen et al., 2009). However, in the previous studies complete cell biotinylation assays were performed on non-confluently grown MDCKII cells, exhibiting no clear cell polarization under this condition. In this study MDCKII cells were grown to confluency at day of biotinylation assay, which leads to clear cell polarization with development of tight junctions. The effect is that only the apical side of the cells was exposed to biotin. In a further approach of Janssen et al. (2009) using confluent grown, polarized MDCKII cells, it was found that the presence of barttin sorts ClC-K channels predominantly to the basolateral side of MDCKII cells. For MDCKII cells within a confluent cell layer the basolateral side is separated by tight junctions from the

apical side. Thus, biotin at the apical side is not able to reach the basolateral side where most of the ClC-K channels in presence of barttin are supposed to be. This circumstance could explain the difference between biotinylation results of this study and previous studies. Nevertheless, in this study biotinylation experiments were also performed with HEK293T cells that are not polarized and have not been used for biotinylation experiments of ClC-K channels in previous studies, yet. Thus, subcellular channel distribution and results of biotinylation experiments could completely differ from studies in which different cell lines were used. As non-polarized cells were not supposed to build tight junctions, biotin should be able to reach most parts of the plasma membrane. Relative surface membrane expression of channels in HEK293T cells, shown here, are therefore valid for the total plasma membrane. The fact that no difference between the different barttin availabilities were found for channel expression in the surface membrane constrains that normalization of macroscopic currents only by total cell expression level is sufficient without further normalization on plasma membrane expression. Confocal microscopy images as well as biotinylation experiments prove that transport and plasma membrane insertion is conducted in HEK293T as well as MDCKII cells, if there is at least one barttin bound to one  $\alpha$ -subunit.

One further aim was to investigate whether even one barttin molecule bound to two  $\alpha$ -subunits (2:1  $\alpha$ : $\beta$ -subunit stoichiometry) is sufficient to guarantee proper trafficking of the channel complex. Still, hClC-Ka/barttin concatamers of this stoichiometry have not been found to be in the plasma membrane by biotinylation assay (Fig.22C). However, this result might be caused by the low expression level of these concatamers. Considering confocal microscopy images it is hard to interpret subcellular localization of this concatamer, maybe again due to the low expression level (Fig.22B). Most of the concatamers seem to stay in intracellular compartments. However, electrophysiological whole cell currents refer to conductive hClC-Ka channels and show that channel complexes reach the surface membrane even at a 2:1  $\alpha$ : $\beta$ -subunit stoichiometry (Fig.23). As ClC-K channels reach the plasma membrane even without barttin at least to a certain extent, it remains questionable whether one barttin per two  $\alpha$ -subunits promotes plasma membrane trafficking or whether measured whole cell currents are just a concomitant phenomenon of overexpression in HEK293T cells.

#### **4.3 One barttin per one ClC-K $\alpha$ -subunit opens the common slow gate**

Barttin has been shown to activate ClC-K channels by modifying fast and slow gating (Fischer et al., 2010; Scholl et al., 2006; Wojciechowski et al., 2015). We here show for the human hClC-Ka that one  $\beta$ - per  $\alpha$ -subunit is sufficient to open the channel. Although highly reduced, there is a chloride conductance for respective concatamer (Fig.13). Corresponding results of single channel recordings for this condition suggest that activated hClC-Ka subunits by one barttin possess an open slow gate. Rapid channel flickering, which is mostly observed for this condition, premises that it is conducted by the fast gate, which regulates protopores individually (Fig.44). The unitary conductance within flickering, though hard to determine, does not exceed 20 pS which is the conductance of one hClC-Ka pore. If the flickering would have been mediated by the slow gate, the amplitude of flickering would be twice as high because the slow gate regulates both protopores together. To observe a flickering of the fast gate in single channel recordings an open slow gate is the precondition.

Similarly, for the rodent isoform rClC-K1, linked to one  $\beta$ -subunit, barttin seems to affect predominantly the slow gate. Slow gate seems constitutively open in presence of one barttin per pore (Figs.20,36), as interpreted from shorter pulse length around 300 ms in previous reports (Fischer et al., 2010). However, in this study we found that one barttin per pore decelerates time course of slow gating by increasing time constants in comparison to rClC-K1 in absence of barttin (Fig.21). Two barttins per  $\alpha$ -subunit increase time constants of this slow gating process even more indicating that slow gate opening is even more promoted in presence of a second barttin molecule per one  $\alpha$ -subunit.

In contrast, relative fast gate open probabilities were rather not increased by one barttin per rClC-K1 subunit and were comparable to values for rClC-K1 in absence of barttin (Fig.20).

These results demonstrate that one barttin linked to one  $\alpha$ -subunit of ClC-K channels opens the common slow gate, while fast gate is less affected.

#### **4.4 Two barttin molecules per one ClC-K $\alpha$ -subunit open the protopore fast gate**

For the human hClC-Ka, it was found that two barttins bound to one  $\alpha$ -subunit remarkably increase whole cell current amplitudes (Fig.13). After normalization on concatamer expression whole cell current amplitudes were comparable to conditions with barttin co-expression in

excess. This indicates that two  $\beta$ -subunits per one  $\alpha$ -subunit are sufficient to fully activate hClC-Ka. For single channel measurements of hClC-Ka/barttin concatamers it was observed that a second barttin per  $\alpha$ -subunit increased the fraction of patches, which did not exhibit high channel flickering but rather stable opening or closing events (Figs.42,43,44). Both channel flickering and stable open states represent two valid functional modes, as for both modes channels could be blocked by niflumic acid, demonstrating the identity of ClC-K channels. Since it could be assumed that high channel flickering was caused by a flickering fast gate, the second barttin stabilizes hClC-Ka fast gate at physiological voltages leading to longer dwell times in open or closed states. It is not sure whether open probabilities were well acquired within single channel recordings, since we found both stable open and closed states. Even channel rundown processes were described for single channel measurements of ClC-K channels (Fischer et al., 2010). However, consulting results from stationary noise analysis, the absolute open probability of the hClC-Ka channel at physiological voltages is meant to be near 100% (Fig.14). Thus, the fast gate should be constitutively open.

For the rodent isoform it was observed that one barttin per one  $\alpha$ -subunit does not appreciably increase fast gate open probabilities. This changed by linking two  $\beta$ -subunits to an rClC-K1 subunit. In this case the relative fast gate open probabilities increased for physiological potentials so that channel minimized time-dependent gating (Fig.20). Thus, two barttins per one rClC-K1 subunit open the fast gate at physiological voltages. This result was confirmed by stationary noise analysis, revealing absolute open probabilities of around 100% for rClC-K1 in co-expression with barttin (Fig.18). Accordingly, rClC-K1 fast gate has to be opened under this condition.

Previous studies already demonstrated that strong barttin overexpression influences fast gating, too. For V166E rClC-K1, a mutant with an artificial reconstitution of the gating glutamate, it could be shown that in presence of barttin minimum relative fast gate open probabilities were reduced, either caused by increase of maximum absolute open probability or by decrease of minimum absolute open probability (Fischer et al., 2010). Moreover, barttin was shown to shift V166E rClC-K1 fast gate activation curve to more negative potentials (Wojciechowski et al., 2015). Since the V166E mutation inverts the voltage-dependence of rClC-K1 fast and slow gate, this shift corresponds to a general increase in fast gate open probabilities. This is in great accordance to data, shown in this study for WT rClC-K1 indicating an increased fast gate open probability by two barttin molecules per one  $\alpha$ -subunit.



#### *4.4.1 The fast gate as origin of time-dependent fast gating and hyperpolarization-induced block*

Still, in this study the impact of the second barttin per  $\alpha$ -subunit on the fast gate was not uniform between cells. Electrophysiologically, rClC-K1 concatamers with defined  $\alpha$ - to  $\beta$ -subunit ratios comprised a high variability for time-dependent gating of the fast gate even for the same stoichiometry (Fig.20). This is unexpected at a first glance, since the same concatamer, expressed in different cells should actually feature the same  $\alpha$ : $\beta$ -subunit stoichiometry and an identical gating behavior. However, this variability could be explained at least by two possible reasons:

I) Firstly, although cells used for patch clamp experiments originate from the same cell line and were cultured under highly similar conditions, they might differ from each other in expression of unknown subunits or co-factors, which are potentially involved in ClC-K regulation. Waldegger et al. (2002) hypothesized about barttin acting as scaffolding protein, which recruits other endogenous ClC-K modulators to the cell membrane. In addition, other studies demonstrate that identical ClC-K channels expressed in HEK293T cells and oocytes exhibit highly different gating behavior as well as different responses to pharmacological treatment dependent on the used cell line (Gradogna et al., 2010; Imbrici et al., 2014; Riazuddin et al., 2009). Thus, besides barttin, the residual biochemical environment of a cell, including many other potential accessory subunits or modulation factors, seem to have an enormous effect on ClC-K channels. However, no further interaction partner for ClC-K channels has been identified so far.

II) Secondly, the covalent linkage of  $\beta$ - to  $\beta$ - and  $\beta$ - to  $\alpha$ -subunits might cause a reduced binding affinity of both subunits potentially due to sterical interference. Especially one barttin, which is inserted between a further barttin and an  $\alpha$ -subunit, might be susceptible for functional deficiencies because its N-terminus is linked to the C-terminus of the second barttin. The functional relevance of an intact barttin N-terminus on ClC-K channel activity was demonstrated recently with a nearly abolishment of barttin effect, if the short N-terminus was deleted (Wojciechowski et al., 2018b). A sterical disorder of barttin's N-terminus induced by the other barttin's C-terminus or the linker sequence could prevent the functionality of this barttin. Therefore, all the concatamers have been constructed with barttin's N-terminus at the N-terminus of the whole concatamer. In case of barttin\_barttin\_ClC-K a linker sequence of 12 amino acids separated both  $\beta$ -subunits, which was used successfully in similar way for

previous studies linking two ClC-K  $\alpha$ -subunits (Fahlke et al., 1997; Stölting et al., 2014). Furthermore, the C-terminus of the N-terminal barttin comprising a C-terminus length of 260 amino acids is meant to be sufficient to guarantee flexibility of the linked barttin N-terminus. Still, even if functional stoichiometry for one concatamer would be inhomogeneous due to reduced barttin binding affinity, one would assume that this effect would be similar for all cells, each exhibiting averaged currents of up to several thousands of channels in the plasma membrane.

Having mentioned several hypotheses, the true reason for variability in time-dependent gating of rClC-K1 still needs to be resolved by future experimental approaches.

Besides the reduction of time-dependent fast gating by opening of the rClC-K1 protopore gate, the second barttin also intensified the hyperpolarization-induced block of rClC-K1 (Fig.17). In this study this block was described the first time for rClC-K1, which was in former studies assigned as characteristic only for hClC-Ka. Other studies demonstrated that rClC-K1 in presence of barttin featured time-dependent fast gating, while barttin abolished slow gating by constitutive slow gate opening (Fischer et al., 2010). Instead, time-dependent gating of rClC-K1 under barttin overexpression vanished completely in this study. Because the only difference between this and the former study is the intense overexpression of barttin in this study, it is likely that hyperpolarization-induced block and reduction of time-dependent fast gating are only visible when all binding sites for barttin are occupied. Up to now the functional and structural determinant of the hyperpolarization-induced block is unknown for rClC-K1 as well as for hClC-Ka. Since this block was conducted in an extremely fast process ( $< 1$  ms), the fast gate might be involved. As coincidence with intensified hyperpolarization-induced block for increased barttin availability, the time-dependent opening of the fast gate vanished. The correlation between hyperpolarization-induced block ( $G_{-255\text{mV}}/G_{\text{max}}$ ) and time-dependent fast gating (rel. open probability at +105 mV) is visualized in figure 50. When relative fast gate open probability at +105 mV is high as for rClC-K1 in co-expression of WT barttin,  $G_{-255\text{mV}}/G_{\text{max}}$  values are low, while it is *vice versa* for lower barttin availability (Fig.50A). Same correlation was found for respective constructs with non-palmitoylated barttins available for ClC-K (Fig.50B). If the fast gate is responsible for both gating processes, it is possible that hyperpolarization-induced block is conducted in presence of two barttins per one  $\alpha$ -subunit, which lock fast gate in a mode with low open probability and fast flickering.

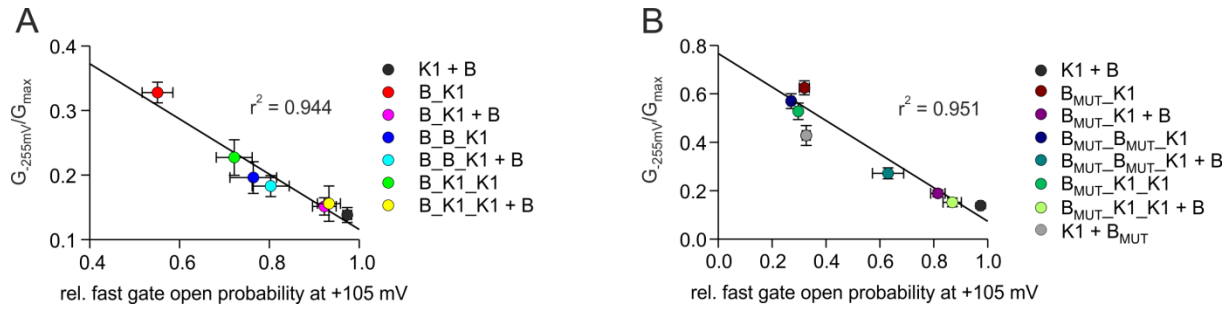


**Fig. 50 Correlation between relative conductance at -255 mV and relative fast gate open probability at +105 mV for rClC-K1 under different  $\alpha$ : $\beta$ -subunit stoichiometries**

(A) Correlation between relative conductance at -255 mV and relative fast gate open probability at +105 mV for rClC-K1/barttin concatamers, possessing palmitoylated barttin. Values were fitted by linear regression. Mean values are given  $\pm$  S.E.M.. Values are combined from Figs.17,20,27,28.  $G_{-255mV}/G_{max}$  / rel. fast gate open probability at +105 mV: K1 + B: n= 13/12, B\_K1: n=21/21, B\_K1 + B: n=14/12, B\_B\_K1: n=10/12, B\_B\_K1 + B: n= 9/9, B\_K1\_K1: n=15/15, B\_K1\_K1 + B: n=10/10. (B) Correlation between relative conductance at -255 mV and relative fast gate open probability at +105 mV for rClC-K1/barttin concatamers, possessing non-palmitoylated barttin. Values were fitted by linear regression. Mean values are given  $\pm$  S.E.M.. Values are combined from Figs.17,20,34,36,39,40.  $G_{-255mV}/G_{max}$  / rel. fast gate open probability at +105 mV: K1 + B: n= 13/12, B<sub>MUT</sub>\_K1: n=13/13, B<sub>MUT</sub>\_K1 + B: n=9/9, B<sub>MUT</sub>\_B<sub>MUT</sub>\_K1: n=11/11, B<sub>MUT</sub>\_B<sub>MUT</sub>\_K1 + B: n= 13/12, B<sub>MUT</sub>\_K1\_K1: n=10/9, B<sub>MUT</sub>\_K1\_K1 + B: n=8/8, K1 + B<sub>MUT</sub>: n= 9/9. K1 (+ B) = rClC-K1 (+ barttin), B\_K1 (+ B) = barttin\_rClC-K1 (+ barttin), B\_B\_K1 (+ B) = barttin\_barttin\_rClC-K1 (+ barttin), B\_K1\_K1 (+ B) = barttin\_rClC-K1\_rClC-K1 (+ barttin), B = palmitoylated barttin, B<sub>MUT</sub> = non-palmitoylated barttin.

Such rapid flickering of the fast gate at negative voltage (-100 mV) has already been proved by single channel measurements for hClC-Ka in co-expression with barttin (Riazuddin et al., 2009). The availability of less barttin molecules per  $\alpha$ -subunit might enable the rClC-K1 fast gate to leave this mode of high flickering and to increase its open probability. This might be represented by the fast current increase at negative voltages especially observed for conditions, in which no or only one barttin molecule was bound to one  $\alpha$ -subunit (Fig.20, Suppl. Fig.1). Accordingly, the hyperpolarization-induced block is less pronounced for these conditions. Moreover, releasing the fast gate from flickering at negative potentials also allows relaxation of the fast gate from the open position at positive potentials, if less than two barttins are bound to one pore-forming subunit. This might be represented by the fast current decrease at positive voltages.

Combining results of time-dependent rClC-K1 fast gating and results of hyperpolarization-induced block provides new insights into the regulation of the rClC-K1 fast gate at different voltages and for different  $\alpha$ : $\beta$ -subunit stoichiometries.

#### 4.5 Dwell times of single pore events affect the outcome of noise analyses

Having debated the influence of  $\alpha:\beta$ -subunit stoichiometry on properties of fast and slow gating, stoichiometry's impact on single pore conductance should be focused in the following part.

By stationary noise analysis the single pore conductance for different hClC-Ka/barttin concatamers were determined. A single pore conductance of 24 pS was found for hClC-Ka in co-expression with barttin, which is in high accordance with single channel measurements (Figs.14,42). For barttin\_hClC-Ka stationary noise analysis gave a reduced single pore conductance (13 pS) compared to hClC-Ka with barttin co-expression (Fig.14). Single channel measurements were consulted to validate this finding. However, due to the rapid channel flickering in most single channel measurements of barttin\_hClC-Ka, this result could not be confirmed faithfully for this channel mode exhibiting rapid flickering. If distinct pore events occurred, they exhibited single pore amplitudes similar to conditions with higher barttin availability (18 pS, Fig.44). Accordingly, we asked whether fast flickering events are reliably captured by stationary noise analyses. Measurements for noise analyses were filtered by a low pass Bessel filter of 10 kHz. If the flickering frequency of the channel exceeded the filter frequency, single pore current amplitudes might have been cut off. Figure 51 compares the influence of filter frequency on single channel recordings and noise analysis for different dwell times of channel openings. In figure 51A an example single channel recording is depicted, which exhibits rather stable opening and closing events. Filtering with a 1 kHz low pass Bessel filter gave a higher background noise than with a filter frequency of 100 Hz. Very short channel closures occur rarely and are reduced in amplitude or are hardly visible with lower filter frequency. Nevertheless, the amplitude histogram revealed Gaussian functions with equal current levels for both filtering conditions, since most dwell times are long. For 100 Hz filter frequency the width of Gaussian functions was smaller than for 1 kHz filtering. If pore events were not so stable and featured a high frequency of flickering without longer open states the impact of filtering was more severe (Fig.51B). Short open states were not exactly displayed by cutting off the peak of such events. In the amplitude histogram this effect became visible as the Gaussian function of the opening state (O1) was shifted towards lower values. Gaussian function of the closed state (C) was rather not shifted because the channel prevailed for a longer time period in the closed state, supporting the correct registration of this state.

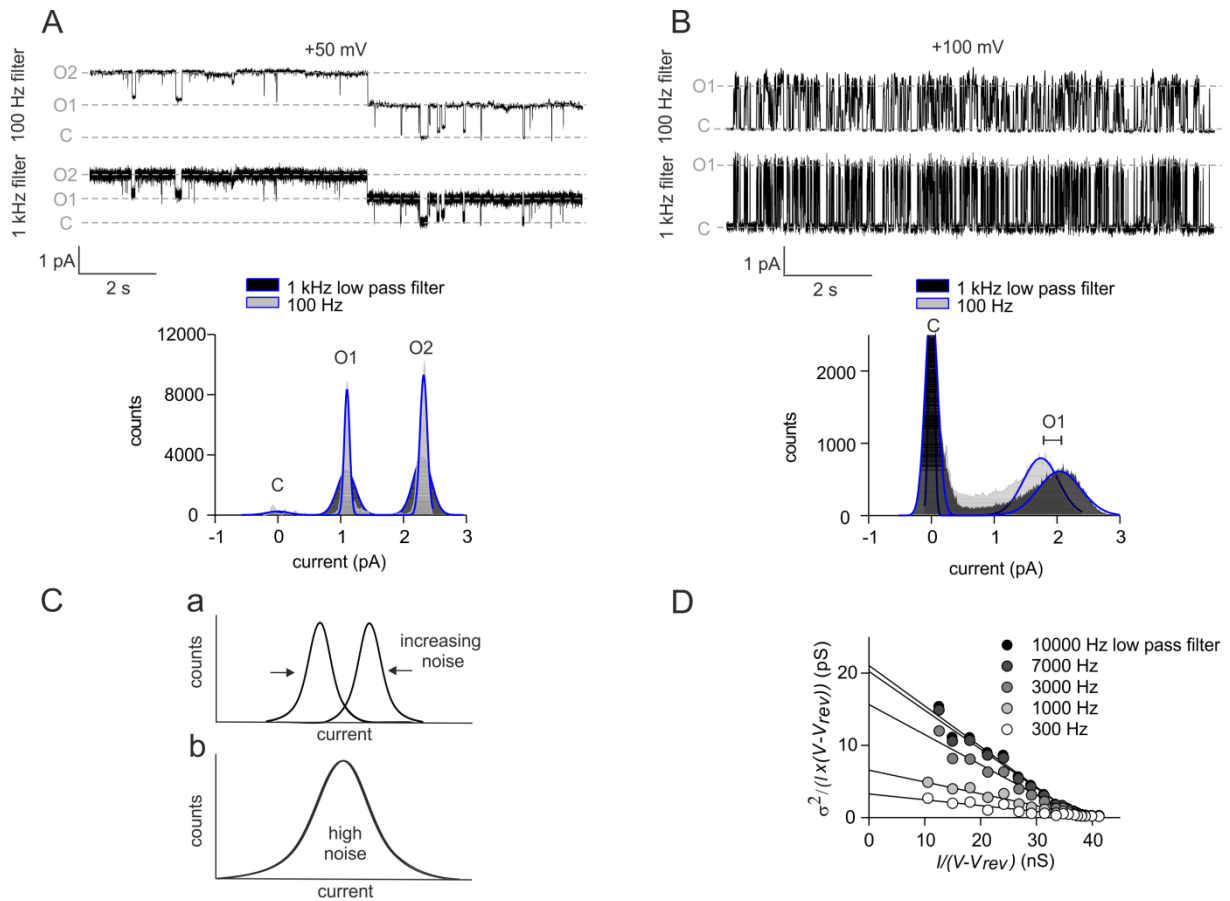


**Fig. 51 Influence of filter frequency on single pore current amplitudes in single channel recordings and on single pore conductance obtained by stationary noise analysis**

(A) Example single channel recording at +50 mV, showing distinct and stable opening and closing phases of pores. Recordings were either filtered by 100 Hz low pass Bessel filter (upper trace) or by a 1 kHz low pass Bessel filter (lower trace). Below, amplitude histograms of upper registration for both filter frequencies are shown with the sum of three Gaussian fits, each. (B) Example single channel recording at +100 mV, showing unstable opening and closing phases of pores with a rapid pore flickering. Recordings were either filtered by 100 Hz low pass Bessel filter (upper trace) or by a 1 kHz low pass Bessel filter (lower trace). Below, amplitude histograms of upper registration for both filter frequencies are shown with the sum of two Gaussian fits, each. (C) Hypothetical model for reaction of Gaussian distributions in amplitude histograms in the case of increasing channel flickering (a) and in the case of extreme rapid channel flickering (b), where different Gaussian distributions fuse to a large one. (D) Example stationary noise analysis of the same current recording but after subsequent filtering with different low pass Bessel filter frequencies. Values for each filter frequency were fitted by a linear regression. C = closed state, O1-2 = open states 1-2.

The effect of filtering on conductance levels for different flickering frequencies is illustrated in figure 51C. If dwell times in open and closed states are long (low flickering frequency), Gaussian functions of conductance states are well separated (a). When the flickering between states increases and dwell times become short, both Gaussian functions converge for the same filter frequency. In the case of extreme flickering, neither open states nor closed states are correctly recorded and both Gaussian functions may fuse together as one (b). Potentially, this was the case for noisy patches commonly measured when only one barttin was linked to one hClC-Ka  $\alpha$ -subunit (Fig.44). The gating frequency might be too high for proper registration of conductance states at the filter frequency of 1 kHz, as used for single channel measurements.

Next, it will be clarified how this high frequency flickering might impact the results of stationary noise analysis, where a reduced single pore conductance was observed for the condition that only one barttin was linked to one  $\alpha$ -subunit. Effect of different filter frequencies on the outcome of stationary noise analysis was tested by analyzing the same current traces after subsequent filtering with different filter frequencies (Fig.51D). Traces were recorded at a 10 kHz filter frequency representing the maximum limit. At this frequency the single pore conductance of hCIC-Ka was about 21 pS represented as the y-axis intercept. Applying lower filter frequencies the y-axis intercept or the single pore conductance respectively, decreased. There was only a slight conductance reduction for the frequency of 7000 Hz but a dramatically higher reduction for filter frequencies of 3000 Hz or lower. This means that a channel flickering above 10 kHz causes a reduced value for single pore conductance in noise analysis because real single pore amplitudes would have been cut off by the amplifier due to the rapid channel flickering. Results of stationary noise analysis could be explained by this effect. Besides the concatamer barttin\_hCIC-Ka also concatamers with barttin co-expression exhibited reduced single pore conductances compared to hCIC-Ka in co-expression with barttin (Fig.14). Regarding the possible impact of filtering on noise analysis, single pore conductance is likely not reduced for these cases but at least a certain fraction of measured channels seem to be in a mode, which exhibits extremely rapid channel flickering. Single channel measurements prove that even for a 1:2 hCIC-Ka/barttin stoichiometry a greater fraction of channel exhibited higher flickering than hCIC-Ka in co-expression with barttin (Figs.42,43). A feasible explanation for this finding might be that functional binding of barttin to the  $\alpha$ -subunit within concatamers is slightly less effective than to an  $\alpha$ -subunit, which is not part of a concatamer.

#### **4.6 Barttin palmitoylation is responsible for rCIC-K1 fast gate opening**

The second part of this study dealt with the role of barttin palmitoylation for distinct barttin functions. For this, expression level, subcellular localization and electrophysiological channel parameters were obtained for the CIC-K/barttin concatamers, lacking barttin palmitoylation. Biochemical analysis of these concatamers revealed expression of expected molecular weight for almost all concatamers in comparable amounts to concatamers possessing barttin palmitoylation (Figs.29,32). This is expected as palmitoylation deficiency of barttin did not

significantly reduce overall barttin and ClC-K expression levels (Gorinski et al., 2020; Steinke et al., 2015).

Furthermore, confocal microscopy images proved that even with one non-palmitoylated barttin per  $\alpha$ -subunit ClC-K channels were transported to the surface membrane, which is similar to the respective condition with palmitoylated barttin (Figs.29,32). This is consistent with previous studies demonstrating that barttin's property to promote plasma membrane insertion of ClC-K channels is not affected by palmitoylation deficiency (Steinke et al., 2015). Thus, barttin palmitoylation is not a trafficking signal for ClC-K channels.

Electrophysiologically, we found that exclusive presence of non-palmitoylated barttin caused a complete inactivity of hClC-Ka for any stoichiometry (Fig.30), which is in accordance with previous data (Steinke et al., 2015).

Still, co-expressed WT barttin was able to open hClC-Ka even linked to two non-palmitoylated barttins (Fig.30). This result implies that co-expressed WT  $\beta$ -subunits competed with the mutant, covalently linked  $\beta$ -subunits for binding to the  $\alpha$ -subunit. Accordingly, mutant barttin was frequently replaced but most likely not every mutant barttin. Relative whole cell current amplitudes of hClC-Ka/barttin<sub>MUT</sub> concatamers in co-expression with WT barttin were only 60% as high as relative current amplitudes of hClC-Ka plus WT barttin excess (values not shown in 'results' chapter). This difference indicates that a fraction of non-palmitoylated barttin molecules were still bound to the  $\alpha$ -subunit, which diminishes hClC-Ka current amplitude. So far, it is not clear whether the binding affinity of non-palmitoylated barttin and palmitoylated barttin is comparable. If the affinity of mutant barttin was lower, WT barttin would easily replace mutant barttin, but not *vice versa*. This hypothesis could be tested by co-expression of non-palmitoylated barttin and hClC-Ka concatamers linked to palmitoylated barttins. This condition would presumably not lead to a lower current level, since palmitoylated barttin would stay bound.

For concatamers with hClC-Ka channels linked to non-palmitoylated barttins no conductivity was observed according to previous studies. As subcellular trafficking is not affected by barttin palmitoylation all channels are meant to stay inactive in the plasma membrane. However, the co-expression of WT barttin was able to re-activate the channels with generation of robust macroscopic currents (Fig.30). Stationary noise analysis of hClC-Ka linked to non-palmitoylated barttin with additional WT barttin co-expression demonstrated that channel's activation curve was not shifted in presence of non-palmitoylated barttin (Fig.31). This accords

to published data, proving that lack of palmitoylation at only one of both barttin palmitoylation sites does not change activation curves, too (Steinke et al., 2015). Chloride conductance in presence of both palmitoylated and non-palmitoylated barttin was lower than exclusive WT barttin co-expression but higher than for the condition with one WT barttin linked to one  $\alpha$ -subunit (Figs.14,31). It might be possible that measured conductances were averaged by hundreds of channel pores with varying barttin composition. On the one hand, there could be pores to which one WT barttin and one barttin<sub>MUT</sub> were bound leading to a reduced conductance comparable to a 1:1  $\alpha$ : $\beta$ <sub>WT</sub>-stoichiometry with rapid fast gate flickering. On the other hand, there could be pores, at which WT barttin replaced all non-palmitoylated barttin molecules. These pores would exhibit a higher conductance of about 20 pS as expected for a 1:2  $\alpha$ : $\beta$ <sub>WT</sub>-stoichiometry with stabilized fast gate. A combination of both subunit compositions could lead to the measured conductance of around 18/19 pS, as obtained for hClC-Ka/barttin<sub>MUT</sub> concatamers with WT barttin co-expression (Fig.31).

For rClC-K1 linked to non-palmitoylated barttin we found that time-dependent fast gating and relative fast gate open probabilities were not affected by different barttin<sub>MUT</sub> availabilities (Figs.36,40). On the contrary, fast gate of respective concatamers with palmitoylated barttin was constitutively opened, if two or more barttins were available per one  $\alpha$ -subunit (Fig.20). Though, relative slow gate open probabilities and time constants were highly similar between concatamers containing palmitoylated and non-palmitoylated barttin (Figs.21,36,37). Obviously, barttin palmitoylation seems to be highly important for voltage independent opening of rClC-K1 fast gate, while the slow gate is rather not influenced. On basis of this finding, it is rational that barttin palmitoylation might also be responsible for fast gate regulation of the orthologous channel hClC-Ka. Thus, hClC-Ka inactivity in exclusive presence of non-palmitoylated barttin might be caused by a closed fast gate, which does not open voltage- and time-dependently. Unfortunately, hClC-Ka does not exhibit distinguishable voltage and time-dependency of fast and slow gate and is, furthermore, closed in absence of barttin palmitoylation, which makes it difficult to investigate the impact of barttin palmitoylation on both gates. Nevertheless, this presumption might indicate an evolutionary adaptation of the channel together with its  $\beta$ -subunit barttin. While the rodent rClC-K1 fast and slow gates are highly voltage-dependent, conductive even in absence of barttin and only modulated by the  $\beta$ -subunit, the human hClC-Ka fast and slow gates are rather not voltage-dependent and channel is not conductive in absence of barttin. ClC-K channels are closely



related to ClC-1, which needs voltage-dependence to regulate muscle excitation. Due to the close relationship this voltage-dependence might be still preserved for the rodent rClC-K1. As voltage-dependence is not needed for channel function in the kidney and the inner ear the human hClC-Ka may have already lost this voltage-dependence but the importance of barttin for this channel increased. Within this theory, barttin palmitoylation plays a key role for correct interaction of barttin and the ClC-K channel. The molecular changes in protein conformation induced by palmitoylation are still not known. It is possible that the hydrophobic palmitate residue induces a direct hydrophobic interface between barttin and the phospholipid bilayer, orientates barttin within the membrane and facilitates specific interaction and conformational changes within the ClC-K channel itself, presumably within its B- and J-helices. Furthermore, through direct interaction with the membrane lipids, the palmitate residues of barttin might change the lipid membrane environment near the ClC-K channel and/or create membrane dipoles, which in turn influence the functional activity of the ClC-K/barttin channels (Gorinski et al., 2020).

The barttin mutations R8W, R8L and G47R, which are known to cause Bartter syndrome type IV (Birkenhäger et al., 2001; Miyamura et al., 2003), have been shown to exhibit a reduced palmitoylation level in comparison to WT barttin (Gorinski et al., 2020; Steinke et al., 2015). Introduction of these barttin mutations into the here applied concatamers could be helpful to clarify the mechanistic origin of function deficiency. If concatamers with barttins, which contain these mutations, show similar behavior as concatamers possessing non-palmitoylated barttins, as used in this study, it is rational that function deficiency is caused by a lack of barttin palmitoylation.

#### **4.7 Summary**

In conclusion, this study gives deep insights into the ClC-K regulation by different barttin availabilities and barttin palmitoylation.

Comparing results of hClC-Ka and rClC-K1 indicates that the same  $\alpha:\beta$ -subunit stoichiometry affects the same functional determinant for both channels: One barttin per ClC-K subunit is sufficient for channel transport to the plasma membrane and for predominant modulation of the slow gate, while the second barttin primarily modulates the fast gate. This means that regulation of ClC-K channels by their  $\beta$ -subunit barttin is graduated as one or two barttins can

bind to one  $\alpha$ -subunit with distinct affects. This is physiologically relevant, because different  $\alpha$ : $\beta$ -subunit stoichiometries caused by different expression levels of both components might be a tool for cells in the kidney or inner ear to adapt precisely to changing requirements. Combination of noise analysis with single channel measurements indicate that single pore properties like absolute open probabilities of hCIC-Ka and conductances of hCIC-Ka and rCIC-K1 are not changed by different  $\alpha$ : $\beta$ -subunit stoichiometries.

Barttin palmitoylation is not relevant for expression and plasma membrane transport of CIC-K/barttin complexes. However, barttin palmitoylation is necessary to open the fast gate of rCIC-K1 but potentially also of hCIC-Ka. Moreover, the data show that non-palmitoylated barttin molecules can be replaced by palmitoylated barttin at the barttin binding site of the CIC-K  $\alpha$ -subunit. Thus, a dynamic exchange of barttin molecules within the plasma membrane can be supposed.

#### **4.8 Outlook**

This study indicates that the functional stoichiometry between CIC-K  $\alpha$ -subunits and barttin can be regulated variably, while a 1:2  $\alpha$ : $\beta$ -subunit stoichiometry appeared as functionally sufficient. By subsequent approaches clarifying also the structural stoichiometry between both subunits, the electrophysiological findings in this study might be confirmed.

One possibility to determine structural stoichiometry is the application of FRET (Förster resonance energy transfer). By FRET assay the energy of an excited donor dye is transferred non-radiatively to a second acceptor dye when both dyes are in close proximity of only few nanometers to each other. The decrease in donor emission and the increase in acceptor emission induced by FRET can be measured. As these dyes can be linked to proteins, the interaction between proteins can be proved. In this study the CIC-K subunits and barttin were already linked to the fluorophores YFP and CFP, which both represent a donor-acceptor pair well suited to conduct FRET. The prerequisite for FRET is that emission spectrum of the donor overlaps with the excitation spectrum of the acceptor, which is given by YFP and CFP. Using this method not only the interaction between both proteins can be demonstrated but also the binding stoichiometry between both subunits. The FRET efficiencies obtained from donor quenching and increased acceptor emission differ from each other, if the stoichiometry between two subunits is not 1:1 (Ben-Johny et al., 2016). If more than one donor molecule is

bound to one acceptor, FRET efficiency, obtained from increased acceptor emission, would be higher than FRET efficiency, obtained from donor quenching, by the factor of the stoichiometry ratio and *vice versa*. In previous studies protein interactions and binding stoichiometries could already be determined by FRET for other protein interaction partners like myosin domains and calmodulin or calcium channel domains and calmodulin (Ben-Johny et al., 2016; Butz et al., 2016). Thus, this method might be easily adopted to determine structural stoichiometry between CIC-K channels and barttin. Some FRET measurements have already been conducted for CIC-K channels and barttin during establishing of this thesis. Up to now, data indicate that more than one barttin molecule can bind to one CIC-K  $\alpha$ -subunit but stoichiometry seems to be variable. However, these findings have to be substantiated by further FRET approaches and have not been included in this thesis. Furthermore, FRET assay could be combined with patch clamp measurements for the same cells. The advantage of this approach would be that electrophysiological parameters of one cell could be directly correlated to the respective FRET efficiencies and, thus, potentially to different  $\alpha$ : $\beta$ -subunit stoichiometries. The general benefit of FRET assay is that protein interaction and function could be measured in real time, with a resolution in millisecond scale, within the physiological environment and within whole protein complexes. This might be an improvement compared to previous immunoprecipitation assays, which only showed interactions of short protein sequences, not supposed to be within their physiological arrangement.

One further method to determine structural stoichiometry between CIC-K channels and barttin adopts TIRF (total internal reflection fluorescence) microscopy. This method enables observation and analysis of labeled particles within cells or within the plasma membrane of cells in direct proximity to a glass surface. From the other side of the glass light is directed to the glass surface with an angle that causes a total reflection. At the reflection site an evanescent electromagnetic field is generated, which only illuminates labeled proteins in a proximity of up to 200 nm to the glass coverslip. Fluorescently labeled protein complexes can be bleached by this light. As bleaching of a fluorophore is conducted in an all-or-nothing reaction, bleaching of several fluorescently labeled subunits within a complex causes a stepwise decay in fluorescence signal. The number of steps depends on the number of labeled subunits within a protein complex. This stepwise decay can be used to determine the number of labeled subunits within single fluorescent spots/complexes (Ulbrich & Isacoff, 2007). This method could be also applied to determine stoichiometry of CIC-K channels and barttin. Using

fluorescence tags for both subunits as they were used in this study (YFP, CFP), bleaching of labeled ClC-K/barttin complexes are also supposed to lead to a stepwise decay in fluorescence intensity, which could unravel binding stoichiometry of both subunits. In previous studies the fluorescence bleaching by TIRF microscopy has already been successfully applied to determine the channel composition of chloride channels as for CFTR (cystic fibrosis transmembrane conductance regulator) but also to determine stoichiometry between other ion channels and their accessory subunits as for hyperpolarization-activated cyclic nucleotide-gated (HCN) channels and voltage-gated potassium channels (Bankston et al., 2012; Haggie & Verkman, 2008; Nakajo et al., 2010).

Using a covalent linkage between  $\alpha$ - and  $\beta$ -subunit in different stoichiometries we precisely determined the function of barttin palmitoylation, potentially relevant for development of Bartter syndrome IV. This tool is not only restricted to analysis of this modification but also for characterization of any other known disease causing  $\alpha$ - or  $\beta$ -subunit alterations. Several mutations within the *BSND* gene, coding for barttin, are known to cause Bartter syndrome like the missense mutations R8L, R8W, G10S, I12T, V33L, G47R, and the nonsense mutations Q32X and E88X (Birkenhäger et al., 2001; García-Nieto et al., 2006; Kitanaka et al., 2006; Miyamura et al., 2003; Ozlu et al., 2006; Riazuddin et al., 2009; Shafique et al., 2014). These mutations could be introduced into concatamers of different  $\alpha$ : $\beta$ -subunit stoichiometries to investigate the loss of distinct functions. As mutations R8L, R8W and G10S disturb ClC-K function without affecting plasma membrane insertion (Janssen et al., 2009), it might be interesting to test whether trafficking function is preserved even for a 1:1  $\alpha$ : $\beta$ -subunit stoichiometry and how these mutations affect fast and slow gate. The mutant G47R has been shown to modulate ClC-K channels like WT barttin but has a lower binding affinity to the  $\alpha$ -subunit (Janssen et al., 2009). Using this mutation within concatamers could help to quantify the binding affinity for different stoichiometries. Furthermore, the barttin mutations R8L, R8W and G47R have been found to exhibit a reduced palmitoylation level in comparison to WT barttin (Gorinski et al., 2020; Steinke et al., 2015). Introduction of these mutations into here used concatamers could clarify whether the mechanistic origin for function deficiency is the lack of barttin palmitoylation, as results could be directly compared with results of concatamers containing non-palmitoylated barttin. The nonsense mutations Q32X and E88X exhibit sorting and trafficking disorders within cells (Janssen et al., 2009). Covalent linkage of these mutations to  $\alpha$ -subunits could clarify whether trafficking failure is caused by a low binding affinity, which

prevents binding of even one barttin to the pore-forming subunit, or by a different mechanism. Remarkably, the two barttin missense mutations I12T and V33L, which have been reported most recently, induce deafness without affecting renal function (Riazuddin et al., 2009; Shafique et al., 2014). By functional analysis of these mutations it became apparent that channel function was not altered by both barttin mutations but transport of the channel complexes to the plasma membrane was disturbed (Riazuddin et al., 2009; Tan et al., 2017). Consulting results of this thesis, it might be possible that the function of one barttin per one  $\alpha$ -subunit to facilitate plasma membrane insertion is abolished for these two barttin mutations. Integrating these mutations into the here described concatamers might help to clarify whether a stoichiometric disorder is the reason for transport deficiencies and whether this function of barttin could be recovered by the presence of a second (mutated) barttin molecule per  $\alpha$ -subunit.

As investigated concatamers also contained ClC-K  $\alpha$ -subunits, they can be used to characterize mutations within them. Mutations within the *ClCNKb* gene, coding for hClC-Kb, were found to cause Bartter syndrome type III. Integrating mutant ClC-Kb subunits into the concatamers could unravel deficiencies of distinct channel functions, caused by these mutations. As in this study also concatamers were characterized, which include two connected  $\alpha$ -subunits, the impact of mutations on functional interaction between two  $\alpha$ -subunits, forming the homodimer, might be elucidated, too.

One far way aim might be to develop compounds that bear on the interaction between ClC-K channels and their  $\beta$ -subunit. On the one hand, this treatment could address the therapy against Bartter syndrome IV by strengthening the interaction between  $\alpha$ - and  $\beta$ -subunit. On the other hand, this treatment could aim the weakening of this interaction causing an increased water and salt loss. This in turn would be advantageous to treat hypertension. In both cases, the here used defined stoichiometry between  $\alpha$ - and  $\beta$ -subunits would be a well suited tool to monitor the effects of potential drugs on distinct barttin functions.

Besides the interaction of ClC-K channels and their  $\beta$ -subunit barttin, concatamers of defined subunit ratios supposedly can be applied as a tool to stoichiometry analyses of any other channel or protein and their respective interaction partners.

## 5 References

- Accardi, A., & Pusch, M. (2000). Fast and slow gating relaxations in the muscle chloride channel CLC-1. *The Journal of General Physiology*, *116*(3), 433–444. PubMed. <https://doi.org/10.1085/jgp.116.3.433>
- Accardi, A., & Pusch, M. (2003). Conformational Changes in the Pore of CLC-0. *Journal of General Physiology*, *122*(3), 277–294. <https://doi.org/10.1085/jgp.200308834>
- Alekov, A. K., & Fahlke, C. (2009). Channel-like slippage modes in the human anion/proton exchanger CLC-4. *Journal of General Physiology*, *133*(5), 485–496. <https://doi.org/10.1085/jgp.200810155>
- Alvarez, O., Gonzalez, C., & Latorre, R. (2002). COUNTING CHANNELS: A TUTORIAL GUIDE ON ION CHANNEL FLUCTUATION ANALYSIS. *Advances in Physiology Education*, *26*(4), 327–341. <https://doi.org/10.1152/advan.00006.2002>
- Bankston, J. R., Camp, S. S., DiMaio, F., Lewis, A. S., Chetkovich, D. M., & Zagotta, W. N. (2012). Structure and stoichiometry of an accessory subunit TRIP8b interaction with hyperpolarization-activated cyclic nucleotide-gated channels. *Proceedings of the National Academy of Sciences*, *109*(20), 7899. <https://doi.org/10.1073/pnas.1201997109>
- Bartter, F. C., Pronove, P., Gill, J. R., & MacCardle, R. C. (1962). Hyperplasia of the juxtaglomerular complex with hyperaldosteronism and hypokalemic alkalosis: A new syndrome. *The American Journal of Medicine*, *33*(6), 811–828. [https://doi.org/10.1016/0002-9343\(62\)90214-0](https://doi.org/10.1016/0002-9343(62)90214-0)
- Ben-Johny, M., Yue, D. N., & Yue, D. T. (2016). Detecting stoichiometry of macromolecular complexes in live cells using FRET. *Nature Communications*, *7*(1), 13709. <https://doi.org/10.1038/ncomms13709>
- Bennetts, B., Rychkov, G. Y., Ng, H.-L., Morton, C. J., Stapleton, D., Parker, M. W., & Cromer, B. A. (2005). Cytoplasmic ATP-sensing Domains Regulate Gating of Skeletal Muscle CLC-1 Chloride Channels. *Journal of Biological Chemistry*, *280*(37), 32452–32458. <https://doi.org/10.1074/jbc.M502890200>
- Birkenhäger, R., Otto, E., Schürmann, M. J., Vollmer, M., Ruf, E.-M., Maier-Lutz, I., Beekmann, F., Fekete, A., Omran, H., Feldmann, D., Milford, D. V., Jeck, N., Konrad, M., Landau, D., Knoers, N. V. A. M., Antignac, C., Sudbrak, R., Kispert, A., & Hildebrandt, F. (2001). Mutation of BSND causes Bartter syndrome with sensorineural deafness and kidney failure. *Nature Genetics*, *29*(3), 310–314. <https://doi.org/10.1038/ng752>
- Bonifacino, J. S. (2004). The GGA proteins: Adaptors on the move. *Nature Reviews Molecular Cell Biology*, *5*(1), 23–32. <https://doi.org/10.1038/nrm1279>
- Bonifacino, J. S., & Traub, L. M. (2003). Signals for Sorting of Transmembrane Proteins to Endosomes and Lysosomes. *Annual Review of Biochemistry*, *72*(1), 395–447. <https://doi.org/10.1146/annurev.biochem.72.121801.161800>
- Bösl, M. R., Stein, V., Hübner, C., Zdebik, A. A., Jordt, S.-E., Mukhopadhyay, A. K., Davidoff, M. S., Holstein, A.-F., & Jentsch, T. J. (2001). Male germ cells and photoreceptors, both dependent on close cell–cell interactions, degenerate upon CLC-2 Cl<sup>-</sup> channel disruption. *The EMBO Journal*, *20*(6), 1289–1299. <https://doi.org/10.1093/emboj/20.6.1289>

- Braulke, T., & Bonifacino, J. S. (2009). Sorting of lysosomal proteins. *Biochimica et Biophysica Acta (BBA) - Molecular Cell Research*, 1793(4), 605–614. <https://doi.org/10.1016/j.bbamcr.2008.10.016>
- Butz, E. S., Ben-Johny, M., Shen, M., Yang, P. S., Sang, L., Biel, M., Yue, D. T., & Wahl-Schott, C. (2016). Quantifying macromolecular interactions in living cells using FRET two-hybrid assays. *Nature Protocols*, 11(12), 2470–2498. <https://doi.org/10.1038/nprot.2016.128>
- Bykova, E. A., Zhang, X.-D., Chen, T.-Y., & Zheng, J. (2006). Large movement in the C terminus of CLC-0 chloride channel during slow gating. *Nature Structural & Molecular Biology*, 13(12), 1115–1119. <https://doi.org/10.1038/nsmb1176>
- Cao, L., Zhang, X.-D., Liu, X., Chen, T.-Y., & Zhao, M. (2010). Chloride channels and transporters in human corneal epithelium. *Experimental Eye Research*, 90(6), 771–779. <https://doi.org/10.1016/j.exer.2010.03.013>
- Catalán, M., Niemeyer, M. I., Cid, L. P., & Sepúlveda, F. V. (2004). Basolateral CLC-2 chloride channels in surface colon epithelium: Regulation by a direct effect of intracellular chloride. *Gastroenterology*, 126(4), 1104–1114. <https://doi.org/10.1053/j.gastro.2004.01.010>
- Cuddapah, V. A., & Sontheimer, H. (2010). Molecular Interaction and Functional Regulation of CLC-3 by Ca<sup>2+</sup>/Calmodulin-dependent Protein Kinase II (CaMKII) in Human Malignant Glioma. *Journal of Biological Chemistry*, 285(15), 11188–11196. <https://doi.org/10.1074/jbc.M109.097675>
- Dutzler, R. (2004). Structural basis for ion conduction and gating in CLC chloride channels. *FEBS Letters*, 564(3), 229–233. [https://doi.org/10.1016/S0014-5793\(04\)00210-8](https://doi.org/10.1016/S0014-5793(04)00210-8)
- Dutzler, R., Campbell, E. B., Cadene, M., Chait, B. T., & MacKinnon, R. (2002). X-ray structure of a CLC chloride channel at 3.0 Å reveals the molecular basis of anion selectivity. *Nature*, 415(6869), 287–294. <https://doi.org/10.1038/415287a>
- Dutzler, R., Campbell, E. B., & MacKinnon, R. (2003). Gating the Selectivity Filter in CLC Chloride Channels. *Science*, 300(5616), 108. <https://doi.org/10.1126/science.1082708>
- Estévez, R., Boettger, T., Stein, V., Birkenhäger, R., Otto, E., Hildebrandt, F., & Jentsch, T. J. (2001). Barttin is a Cl<sup>-</sup> channel  $\beta$ -subunit crucial for renal Cl<sup>-</sup> reabsorption and inner ear K<sup>+</sup> secretion. *Nature*, 414(6863), 558–561. <https://doi.org/10.1038/35107099>
- Fahlke, C., & Fischer, M. (2010). Physiology and Pathophysiology of CLC-K/barttin Channels. *Frontiers in Physiology*, 1, 155. <https://doi.org/10.3389/fphys.2010.00155>
- Fahlke, C., Knittle, T., Gurnett, C. A., Campbell, K. P., & George, A. L. (1997). Subunit Stoichiometry of Human Muscle Chloride Channels. *Journal of General Physiology*, 109(1), 93–104. <https://doi.org/10.1085/jgp.109.1.93>
- Fahlke, C., Yu, H. T., Beck, C. L., Rhodes, T. H., & George, A. L. (1997). Pore-forming segments in voltage-gated chloride channels. *Nature*, 390(6659), 529–532. <https://doi.org/10.1038/37391>
- Farmer, L. M., Le, B. N., & Nelson, D. J. (2013). CLC-3 chloride channels moderate long-term potentiation at Schaffer collateral-CA1 synapses: CLC-3 moderates hippocampal long-term potentiation. *The Journal of Physiology*, 591(4), 1001–1015. <https://doi.org/10.1113/jphysiol.2012.243485>
- Feng, L., Campbell, E. B., Hsiung, Y., & MacKinnon, R. (2010). Structure of a Eukaryotic CLC Transporter Defines an Intermediate State in the Transport Cycle. *Science*, 330(6004), 635–641. <https://doi.org/10.1126/science.1195230>

- Fernandes-Rosa, F. L., Daniil, G., Orozco, I. J., Göppner, C., El Zein, R., Jain, V., Boulkroun, S., Jeunemaitre, X., Amar, L., Lefebvre, H., Schwarzmayr, T., Strom, T. M., Jentsch, T. J., & Zennaro, M.-C. (2018). A gain-of-function mutation in the CLCN2 chloride channel gene causes primary aldosteronism. *Nature Genetics*, *50*(3), 355–361. <https://doi.org/10.1038/s41588-018-0053-8>
- Fischer, M., Janssen, A. G. H., & Fahlke, C. (2010). Barttin Activates ClC-K Channel Function by Modulating Gating. *Journal of the American Society of Nephrology*, *21*(8), 1281–1289. <https://doi.org/10.1681/ASN.2009121274>
- Földy, C., Lee, S.-H., Morgan, R. J., & Soltesz, I. (2010). Regulation of fast-spiking basket cell synapses by the chloride channel ClC-2. *Nature Neuroscience*, *13*(9), 1047–1049. <https://doi.org/10.1038/nn.2609>
- Friedrich, T., Breiderhoff, T., & Jentsch, T. J. (1999). Mutational Analysis Demonstrates That ClC-4 and ClC-5 Directly Mediate Plasma Membrane Currents. *Journal of Biological Chemistry*, *274*(2), 896–902. <https://doi.org/10.1074/jbc.274.2.896>
- Fujita, N., Mori, H., Yura, T., & Ishihama, A. (1994). Systematic sequencing of the Escherichia coli genome: Analysis of the 2.4–4.1 min (110,917–193,643 bp) region. *Nucleic Acids Research*, *22*(9), 1637–1639. <https://doi.org/10.1093/nar/22.9.1637>
- García-Nieto, V., Flores, C., Luis-Yanes, M. I., Gallego, E., Villar, J., & Claverie-Martín, F. (2006). Mutation G47R in the BSND gene causes Bartter syndrome with deafness in two Spanish families. *Pediatric Nephrology*, *21*(5), 643–648. <https://doi.org/10.1007/s00467-006-0062-1>
- Gentzsch, M., Cui, L., Mengos, A., Chang, X., Chen, J.-H., & Riordan, J. R. (2003). The PDZ-binding Chloride Channel ClC-3B Localizes to the Golgi and Associates with Cystic Fibrosis Transmembrane Conductance Regulator-interacting PDZ Proteins. *Journal of Biological Chemistry*, *278*(8), 6440–6449. <https://doi.org/10.1074/jbc.M211050200>
- George, A. L., Crackower, M. A., Abdalla, J. A., Hudson, A. J., & Ebers, G. C. (1993). Molecular basis of Thomsen's disease (autosomal dominant myotonia congenita). *Nature Genetics*, *3*(4), 305–310. <https://doi.org/10.1038/ng0493-305>
- Gerbino, A., De Zio, R., Russo, D., Milella, L., Milano, S., Procino, G., Pusch, M., Svelto, M., & Carosino, M. (2020). Role of PKC in the Regulation of the Human Kidney Chloride Channel ClC-Ka. *Scientific Reports*, *10*(1), 10268. <https://doi.org/10.1038/s41598-020-67219-8>
- Gorinski, N., Wojciechowski, D., Guseva, D., Abdel Galil, D., Mueller, F. E., Wirth, A., Thiemann, S., Zeug, A., Schmidt, S., Zareba-Kozioł, M., Włodarczyk, J., Skryabin, B. V., Glage, S., Fischer, M., Al-Samir, S., Kerkenberg, N., Hohoff, C., Zhang, W., Endeward, V., & Ponimaskin, E. (2020). DHHC7-mediated palmitoylation of the accessory protein barttin critically regulates the functions of ClC-K chloride channels. *Journal of Biological Chemistry*, *295*(18), 5970–5983. <https://doi.org/10.1074/jbc.RA119.011049>
- Gradogna, A., Babini, E., Picollo, A., & Pusch, M. (2010). A regulatory calcium-binding site at the subunit interface of ClC-K kidney chloride channels. *Journal of General Physiology*, *136*(3), 311–323. <https://doi.org/10.1085/jgp.201010455>
- Gradogna, A., Fenollar-Ferrer, C., Forrest, L. R., & Pusch, M. (2012). Dissecting a regulatory calcium-binding site of ClC-K kidney chloride channels. *Journal of General Physiology*, *140*(6), 681–696. <https://doi.org/10.1085/jgp.201210878>
- Graham, F. L., & Eb, A. J. van der. (1973). A new technique for the assay of infectivity of human adenovirus 5 DNA. *Virology*, *52*(2), 456–467. [https://doi.org/10.1016/0042-6822\(73\)90341-3](https://doi.org/10.1016/0042-6822(73)90341-3)



- Grieschat, M., Guzman, R. E., Langschwager, K., Fahlke, C., & Alekov, A. K. (2020). Metabolic energy sensing by mammalian CLC anion/proton exchangers. *EMBO Reports*, 21(6). <https://doi.org/10.15252/embr.201947872>
- Gründer, S., Thiemann, A., Pusch, M., & Jentsch, T. J. (1992). Regions involved in the opening of ClC-2 chloride channel by voltage and cell volume. *Nature*, 360(6406), 759–762. <https://doi.org/10.1038/360759a0>
- Gunther, W., Luchow, A., Cluzeaud, F., Vandewalle, A., & Jentsch, T. J. (1998). ClC-5, the chloride channel mutated in Dent's disease, colocalizes with the proton pump in endocytotically active kidney cells. *Proceedings of the National Academy of Sciences*, 95(14), 8075–8080. <https://doi.org/10.1073/pnas.95.14.8075>
- Haggie, P. M., & Verkman, A. S. (2008). Monomeric CFTR in Plasma Membranes in Live Cells Revealed by Single Molecule Fluorescence Imaging\*. *Journal of Biological Chemistry*, 283(35), 23510–23513. <https://doi.org/10.1074/jbc.C800100200>
- Hebeisen, S., Biela, A., Giese, B., Müller-Newen, G., Hidalgo, P., & Fahlke, C. (2004). The Role of the Carboxyl Terminus in ClC Chloride Channel Function. *Journal of Biological Chemistry*, 279(13), 13140–13147. <https://doi.org/10.1074/jbc.M312649200>
- Hebeisen, S., & Fahlke, C. (2005). Carboxy-Terminal Truncations Modify the Outer Pore Vestibule of Muscle Chloride Channels. *Biophysical Journal*, 89(3), 1710–1720. <https://doi.org/10.1529/biophysj.104.056093>
- Hebert, S. C. (2003). Bartter syndrome. *Current Opinion in Nephrology and Hypertension*, 12(5). [https://journals.lww.com/co-nephrolhypertens/Fulltext/2003/09000/Bartter\\_syndrome.8.aspx](https://journals.lww.com/co-nephrolhypertens/Fulltext/2003/09000/Bartter_syndrome.8.aspx)
- Hoegg-Beiler, M. B., Sirisi, S., Orozco, I. J., Ferrer, I., Hohensee, S., Auberson, M., Gödde, K., Vilches, C., de Heredia, M. L., Nunes, V., Estévez, R., & Jentsch, T. J. (2014). Disrupting MLC1 and GlialCAM and ClC-2 interactions in leukodystrophy entails glial chloride channel dysfunction. *Nature Communications*, 5(1), 3475. <https://doi.org/10.1038/ncomms4475>
- Hu, H., Haas, S. A., Chelly, J., Van Esch, H., Raynaud, M., de Brouwer, A. P. M., Weinert, S., Froyen, G., Frints, S. G. M., Laumonnier, F., Zemojtel, T., Love, M. I., Richard, H., Emde, A.-K., Bienek, M., Jensen, C., Hambrock, M., Fischer, U., Langnick, C., ... Kalscheuer, V. M. (2016). X-exome sequencing of 405 unresolved families identifies seven novel intellectual disability genes. *Molecular Psychiatry*, 21(1), 133–148. <https://doi.org/10.1038/mp.2014.193>
- Huang, M.-E., Chuat, J.-C., & Galibert, F. (1994). A Voltage-gated Chloride Channel in the Yeast *Saccharomyces cerevisiae*. *Journal of Molecular Biology*, 242(4), 595–598. <https://doi.org/10.1006/jmbi.1994.1607>
- Imbrici, P., Liantonio, A., Gradogna, A., Pusch, M., & Camerino, D. C. (2014). Targeting kidney CLC-K channels: Pharmacological profile in a human cell line versus *Xenopus* oocytes. *Biochimica et Biophysica Acta (BBA) - Biomembranes*, 1838(10), 2484–2491. <https://doi.org/10.1016/j.bbamem.2014.05.017>
- Janssen, A. G. H. (2008). *Disease-causing dysfunctions of barttin, an accessory subunit of ClC-K chloride channels*. PhD thesis, created at the Institute for Neurophysiology, Hannover Medical School, and published at the Gottfried Wilhelm Leibniz University Hannover. <https://doi.org/10.15488/7059>
- Janssen, A. G. H., Scholl, U., Domeyer, C., Nothmann, D., Leinenweber, A., & Fahlke, C. (2009). Disease-Causing Dysfunctions of Barttin in Bartter Syndrome Type IV. *Journal of the American Society of Nephrology*, 20(1), 145–153. <https://doi.org/10.1681/ASN.2008010102>

- Jentsch, T. J. (2008). CLC Chloride Channels and Transporters: From Genes to Protein Structure, Pathology and Physiology. *Critical Reviews in Biochemistry and Molecular Biology*, 43(1), 3–36. <https://doi.org/10.1080/10409230701829110>
- Jentsch, T. J. (2015). Discovery of CLC transport proteins: Cloning, structure, function and pathophysiology. *The Journal of Physiology*, 593(18), 4091–4109. <https://doi.org/10.1113/JP270043>
- Jentsch, T. J., Stein, V., Weinreich, F., & Zdebik, A. A. (2002). Molecular Structure and Physiological Function of Chloride Channels. *Physiological Reviews*, 82(2), 503–568. <https://doi.org/10.1152/physrev.00029.2001>
- Jentsch, T. J., Steinmeyer, K., & Schwarz, G. (1990). Primary structure of *Torpedo marmorata* chloride channel isolated by expression cloning in *Xenopus* oocytes. *Nature*, 348(6301), 510–514. <https://doi.org/10.1038/348510a0>
- Jeworutzki, E., Lagostena, L., Elorza-Vidal, X., López-Hernández, T., Estévez, R., & Pusch, M. (2014). GlialCAM, a CLC-2 Cl<sup>-</sup> Channel Subunit, Activates the Slow Gate of CLC Chloride Channels. *Biophysical Journal*, 107(5), 1105–1116. <https://doi.org/10.1016/j.bpj.2014.07.040>
- Jeworutzki, E., López-Hernández, T., Capdevila-Nortes, X., Sirisi, S., Bengtsson, L., Montolio, M., Zifarelli, G., Arnedo, T., Müller, C. S., Schulte, U., Nunes, V., Martínez, A., Jentsch, T. J., Gasull, X., Pusch, M., & Estévez, R. (2012). GlialCAM, a protein defective in a leukodystrophy, serves as a CLC-2 Cl<sup>-</sup> channel auxiliary subunit. *Neuron*, 73(5), 951–961. PubMed. <https://doi.org/10.1016/j.neuron.2011.12.039>
- Jordt, S.-E., & Jentsch, T. J. (1997). Molecular dissection of gating in the CLC-2 chloride channel. *The EMBO Journal*, 16(7), 1582–1592. <https://doi.org/10.1093/emboj/16.7.1582>
- Kasper, D., Planells-Cases, R., Fuhrmann, J. C., Scheel, O., Zeitz, O., Ruether, K., Schmitt, A., Poët, M., Steinfeld, R., Schweizer, M., Kornak, U., & Jentsch, T. J. (2005). Loss of the chloride channel CLC-7 leads to lysosomal storage disease and neurodegeneration. *The EMBO Journal*, 24(5), 1079–1091. <https://doi.org/10.1038/sj.emboj.7600576>
- Kieferle, S., Fong, P., Bens, M., Vandewalle, A., & Jentsch, T. J. (1994). Two highly homologous members of the CLC chloride channel family in both rat and human kidney. *Proceedings of the National Academy of Sciences*, 91(15), 6943–6947. <https://doi.org/10.1073/pnas.91.15.6943>
- Kitanaka, S., Sato, U., Maruyama, K., & Igarashi, T. (2006). A compound heterozygous mutation in the BSND gene detected in Bartter syndrome type IV. *Pediatric Nephrology*, 21(2), 190–193. <https://doi.org/10.1007/s00467-005-2091-6>
- Kleefuß-Lie, A., Friedl, W., Cichon, S., Haug, K., Warnstedt, M., Alekov, A., Sander, T., Ramirez, A., Poser, B., Maljevic, S., Hebeisen, S., Kubisch, C., Rebstock, J., Horvath, S., Hallmann, K., Dullinger, J. S., Rau, B., Haverkamp, F., Beyenburg, S., ... Lerche, H. (2009). CLCN2 variants in idiopathic generalized epilepsy. *Nature Genetics*, 41(9), 954–955. <https://doi.org/10.1038/ng0909-954>
- Klocke, R., Steinmeyer, K., Jentsch, T. J., & Jockusch, H. (1994). Role of innervation, excitability, and myogenic factors in the expression of the muscular chloride channel CLC-1. A study on normal and myotonic muscle. *Journal of Biological Chemistry*, 269(44), 27635–27639. [https://doi.org/10.1016/S0021-9258\(18\)47032-9](https://doi.org/10.1016/S0021-9258(18)47032-9)
- Kobayashi, K. (2002). Human CLC-KB Gene Promoter Drives the EGFP Expression in the Specific Distal Nephron Segments and Inner Ear. *Journal of the American Society of Nephrology*, 13(8), 1992–1998. <https://doi.org/10.1097/01.ASN.0000023434.47132.3D>

- Koch, M., Steinmeyer, K., Lorenz, C., Ricker, K., Wolf, F., Otto, M., Zoll, B., Lehmann-Horn, F., Grzeschik, K., & Jentsch, T. (1992). The skeletal muscle chloride channel in dominant and recessive human myotonia. *Science*, *257*(5071), 797–800. <https://doi.org/10.1126/science.1379744>
- Kornak, U., Kasper, D., Bösl, M. R., Kaiser, E., Schweizer, M., Schulz, A., Friedrich, W., Delling, G., & Jentsch, T. J. (2001). Loss of the ClC-7 Chloride Channel Leads to Osteopetrosis in Mice and Man. *Cell*, *104*(2), 205–215. [https://doi.org/10.1016/S0092-8674\(01\)00206-9](https://doi.org/10.1016/S0092-8674(01)00206-9)
- Krämer, B. K., Bergler, T., Stoelcker, B., & Waldegger, S. (2008). Mechanisms of Disease: The kidney-specific chloride channels ClCKA and ClCKB, the Barttin subunit, and their clinical relevance. *Nature Clinical Practice Nephrology*, *4*(1), 38–46. <https://doi.org/10.1038/ncpneph0689>
- Lange, P. F., Wartosch, L., Jentsch, T. J., & Fuhrmann, J. C. (2006). ClC-7 requires Ostm1 as a  $\beta$ -subunit to support bone resorption and lysosomal function. *Nature*, *440*(7081), 220–223. <https://doi.org/10.1038/nature04535>
- Liman, E. R., Tytgat, J., & Hess, P. (1992). Subunit stoichiometry of a mammalian K<sup>+</sup> channel determined by construction of multimeric cDNAs. *Neuron*, *9*(5), 861–871. [https://doi.org/10.1016/0896-6273\(92\)90239-A](https://doi.org/10.1016/0896-6273(92)90239-A)
- Lísal, J., & Maduke, M. (2008). The ClC-0 chloride channel is a ‘broken’ Cl<sup>-</sup>/H<sup>+</sup> antiporter. *Nature Structural & Molecular Biology*, *15*(8), 805–810. <https://doi.org/10.1038/nsmb.1466>
- Lísal, J., & Maduke, M. (2009). Proton-coupled gating in chloride channels. *Philosophical Transactions of the Royal Society B: Biological Sciences*, *364*(1514), 181–187. <https://doi.org/10.1098/rstb.2008.0123>
- Ludewig, U., Pusch, M., & Jentsch, T. J. (1996). Two physically distinct pores in the dimeric ClC-0 chloride channel. *Nature*, *383*(6598), 340–343. <https://doi.org/10.1038/383340a0>
- Meindl, A., Hosenfeld, D., Bruckl, W., Schuffenhauer, S., Jenderny, J., Bacskulin, A., Oppermann, H. C., Swensson, O., Bouloux, P., & Meitinger, T. (1993). Analysis of a terminal Xp22.3 deletion in a patient with six monogenic disorders: Implications for the mapping of X linked ocular albinism. *Journal of Medical Genetics*, *30*(10), 838–842. <https://doi.org/10.1136/jmg.30.10.838>
- Meyer, S., Savaresi, S., Forster, I. C., & Dutzler, R. (2007). Nucleotide recognition by the cytoplasmic domain of the human chloride transporter ClC-5. *Nature Structural & Molecular Biology*, *14*(1), 60–67. <https://doi.org/10.1038/nsmb1188>
- Middleton, R. E., Pheasant, D. J., & Miller, C. (1996). Homodimeric architecture of a ClC-type chloride ion channel. *Nature*, *383*(6598), 337–340. <https://doi.org/10.1038/383337a0>
- Miller, C., Keynes, R. D., & Ellory, J. C. (1982). Open-state substructure of single chloride channels from *Torpedo* electroplax. *Philosophical Transactions of the Royal Society of London. B, Biological Sciences*, *299*(1097), 401–411. <https://doi.org/10.1098/rstb.1982.0140>
- Miyamura, N., Matsumoto, K., Taguchi, T., Tokunaga, H., Nishikawa, T., Nishida, K., Toyonaga, T., Sakakida, M., & Araki, E. (2003). Atypical Bartter Syndrome with Sensorineural Deafness with G47R Mutation of the  $\beta$ -Subunit for ClC-Ka and ClC-Kb Chloride Channels, Barttin. *The Journal of Clinical Endocrinology & Metabolism*, *88*(2), 781–786. <https://doi.org/10.1210/jc.2002-021398>

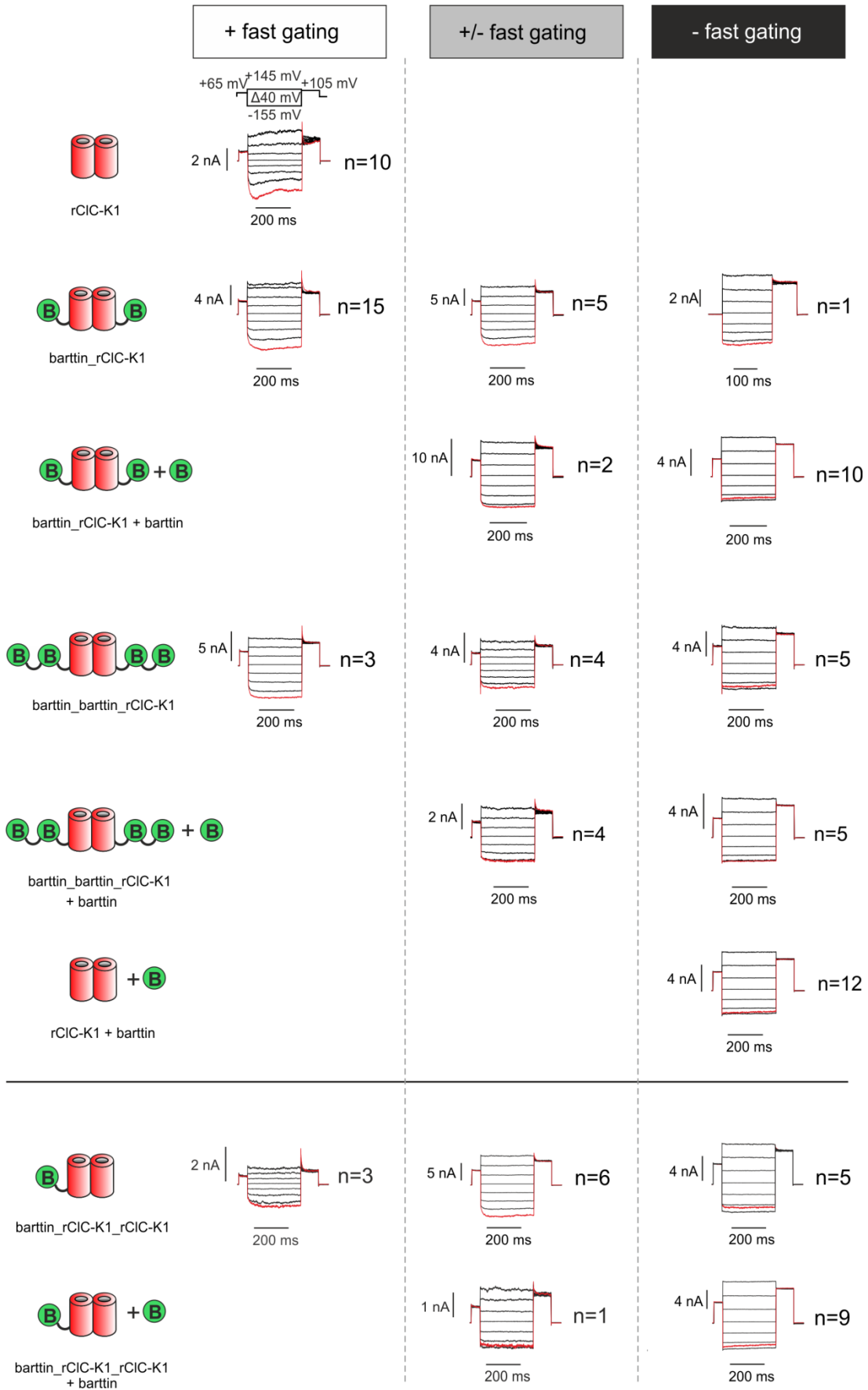
- Mohammad-Panah, R., Harrison, R., Dhani, S., Ackerley, C., Huan, L.-J., Wang, Y., & Bear, C. E. (2003). The Chloride Channel ClC-4 Contributes to Endosomal Acidification and Trafficking. *Journal of Biological Chemistry*, *278*(31), 29267–29277. <https://doi.org/10.1074/jbc.M304357200>
- Nakajo, K., Ulbrich, M. H., Kubo, Y., & Isacoff, E. Y. (2010). Stoichiometry of the KCNQ1—KCNE1 ion channel complex. *Proceedings of the National Academy of Sciences*, *107*(44), 18862. <https://doi.org/10.1073/pnas.1010354107>
- Niemeyer, M. I., Cid, L. P., Zúñiga, L., Catalán, M., & Sepúlveda, F. V. (2003). A Conserved Pore-Lining Glutamate as a Voltage- and Chloride-Dependent Gate in the ClC-2 Chloride Channel. *The Journal of Physiology*, *553*(3), 873–879. <https://doi.org/10.1113/jphysiol.2003.055988>
- Ozlu, F., Yapicioğlu, H., Satar, M., Narli, N., Ozcan, K., Buyukcelik, M., Konrad, M., & Demirhan, O. (2006). Barttin mutations in antenatal Bartter syndrome with sensorineural deafness. *Pediatric Nephrology*, *21*(7), 1056–1057. <https://doi.org/10.1007/s00467-006-0108-4>
- Park, E., Campbell, E. B., & MacKinnon, R. (2017). Structure of a ClC chloride ion channel by cryo-electron microscopy. *Nature*, *541*(7638), 500–505. <https://doi.org/10.1038/nature20812>
- Park, E., & MacKinnon, R. (2018). Structure of the ClC-1 chloride channel from *Homo sapiens*. *ELife*, *7*, e36629. <https://doi.org/10.7554/eLife.36629>
- Pear, W. S., Nolan, G. P., Scott, M. L., & Baltimore, D. (1993). Production of high-titer helper-free retroviruses by transient transfection. *Proceedings of the National Academy of Sciences*, *90*(18), 8392–8396. <https://doi.org/10.1073/pnas.90.18.8392>
- Pena-Munzenmayer, G. (2005). Basolateral localization of native ClC-2 chloride channels in absorptive intestinal epithelial cells and basolateral sorting encoded by a CBS-2 domain di-leucine motif. *Journal of Cell Science*, *118*(18), 4243–4252. <https://doi.org/10.1242/jcs.02525>
- Piwon, N., Günther, W., Schwake, M., Bösl, M. R., & Jentsch, T. J. (2000). ClC-5 Cl—Channel disruption impairs endocytosis in a mouse model for Dent’s disease. *Nature*, *408*(6810), 369–373. <https://doi.org/10.1038/35042597>
- Poët, M., Kornak, U., Schweizer, M., Zdebik, A. A., Scheel, O., Hoelter, S., Wurst, W., Schmitt, A., Fuhrmann, J. C., Planells-Cases, R., Mole, S. E., Hübner, C. A., & Jentsch, T. J. (2006). Lysosomal storage disease upon disruption of the neuronal chloride transport protein ClC-6. *Proceedings of the National Academy of Sciences*, *103*(37), 13854. <https://doi.org/10.1073/pnas.0606137103>
- Pusch, M., Jordt, S.-E., Stein, V., & Jentsch, T. J. (1999). Chloride dependence of hyperpolarization-activated chloride channel gates. *The Journal of Physiology*, *515*(2), 341–353. <https://doi.org/10.1111/j.1469-7793.1999.341ac.x>
- Pusch, M., Ludewig, U., Rehfeldt, A., & Jentsch, T. J. (1995). Gating of the voltage-dependent chloride channel ClC-0 by the permeant anion. *Nature*, *373*(6514), 527–531. <https://doi.org/10.1038/373527a0>
- Riazuddin, S., Anwar, S., Fischer, M., Ahmed, Z. M., Khan, S. Y., Janssen, A. G. H., Zafar, A. U., Scholl, U., Husnain, T., Belyantseva, I. A., Friedman, P. L., Riazuddin, S., Friedman, T. B., & Fahlke, C. (2009). Molecular Basis of DFNB73: Mutations of BSND Can Cause Nonsyndromic Deafness or Bartter Syndrome. *The American Journal of Human Genetics*, *85*(2), 273–280. <https://doi.org/10.1016/j.ajhg.2009.07.003>

- Rinke, I., Artmann, J., & Stein, V. (2010). ClC-2 Voltage-Gated Channels Constitute Part of the Background Conductance and Assist Chloride Extrusion. *Journal of Neuroscience*, *30*(13), 4776–4786. <https://doi.org/10.1523/JNEUROSCI.6299-09.2010>
- Saint-Martin, C., Gauvain, G., Teodorescu, G., Gourfinkel-An, I., Fedirko, E., Weber, Y. G., Maljevic, S., Ernst, J.-P., Garcia-Olivares, J., Fahlke, C., Nabbout, R., LeGuern, E., Lerche, H., Poncer, J. C., & Depienne, C. (2009). Two novel CLCN2 mutations accelerating chloride channel deactivation are associated with idiopathic generalized epilepsy. *Human Mutation*, *30*(3), 397–405. <https://doi.org/10.1002/humu.20876>
- Saviane, C., Conti, F., & Pusch, M. (1999). The Muscle Chloride Channel ClC-1 Has a Double-Barreled Appearance that Is Differentially Affected in Dominant and Recessive Myotonia. *The Journal of General Physiology*, *11*.
- Scholl, U., Hebeisen, S., Janssen, A. G. H., Muller-Newen, G., Alekov, A., & Fahlke, C. (2006). Barttin modulates trafficking and function of ClC-K channels. *Proceedings of the National Academy of Sciences*, *103*(30), 11411–11416. <https://doi.org/10.1073/pnas.0601631103>
- Scholl, U. I., Stölting, G., Schewe, J., Thiel, A., Tan, H., Nelson-Williams, C., Vichot, A. A., Jin, S. C., Loring, E., Untiet, V., Yoo, T., Choi, J., Xu, S., Wu, A., Kirchner, M., Mertins, P., Rump, L. C., Onder, A. M., Gamble, C., ... Lifton, R. P. (2018). CLCN2 chloride channel mutations in familial hyperaldosteronism type II. *Nature Genetics*, *50*(3), 349–354. <https://doi.org/10.1038/s41588-018-0048-5>
- Sesti, F., & Goldstein, S. A. N. (1998). Single-Channel Characteristics of Wild-Type IKs Channels and Channels formed with Two MinK Mutants that Cause Long QT Syndrome. *The Journal of General Physiology*, *112*(6), 651–663. <https://doi.org/10.1085/jgp.112.6.651>
- Seyberth, H. W. (2008). An improved terminology and classification of Bartter-like syndromes. *Nature Clinical Practice Nephrology*, *4*(10), 560–567. <https://doi.org/10.1038/ncpneph0912>
- Shafique, S., Siddiqi, S., Schraders, M., Oostrik, J., Ayub, H., Bilal, A., Ajmal, M., Seco, C. Z., Strom, T. M., Mansoor, A., Mazhar, K., Shah, S. T. A., Hussain, A., Azam, M., Kremer, H., & Qamar, R. (2014). Genetic Spectrum of Autosomal Recessive Non-Syndromic Hearing Loss in Pakistani Families. *PLOS ONE*, *9*(6), e100146. <https://doi.org/10.1371/journal.pone.0100146>
- Steinke, K. V., Gorinski, N., Wojciechowski, D., Todorov, V., Guseva, D., Ponimaskin, E., Fahlke, C., & Fischer, M. (2015). Human ClC-K Channels Require Palmitoylation of Their Accessory Subunit Barttin to Be Functional. *Journal of Biological Chemistry*, *290*(28), 11.
- Steinmeyer, K., Klocke, R., Ortland, C., Gronemeier, M., Jockusch, H., GrÜnder, S., & Jentsch, T. J. (1991). Inactivation of muscle chloride channel by transposon insertion in myotonic mice. *Nature*, *354*(6351), 304–308. <https://doi.org/10.1038/354304a0>
- Steinmeyer, K., Ortland, C., & Jentsch, T. J. (1991). Primary structure and functional expression of a developmentally regulated skeletal muscle chloride channel. *Nature*, *354*(6351), 301–304. <https://doi.org/10.1038/354301a0>
- Stobrawa, S. M., Breiderhoff, T., Takamori, S., Engel, D., Schweizer, M., Zdebik, A. A., Bösl, M. R., Ruether, K., Jahn, H., Draguhn, A., Jahn, R., & Jentsch, T. J. (2001). Disruption of ClC-3, a Chloride Channel Expressed on Synaptic Vesicles, Leads to a Loss of the Hippocampus. *Neuron*, *29*(1), 185–196. [https://doi.org/10.1016/S0896-6273\(01\)00189-1](https://doi.org/10.1016/S0896-6273(01)00189-1)

- Stölting, G., Fischer, M., & Fahlke, C. (2014). ClC-1 and ClC-2 form hetero-dimeric channels with novel protopore functions. *Pflügers Archiv - European Journal of Physiology*, 466(12), 2191–2204. <https://doi.org/10.1007/s00424-014-1490-6>
- Stölting, G., Teodorescu, G., Begemann, B., Schubert, J., Nabbout, R., Toliat, M. R., Sander, T., Nürnberg, P., Lerche, H., & Fahlke, C. (2013). Regulation of ClC-2 gating by intracellular ATP. *Pflügers Archiv - European Journal of Physiology*, 465(10), 1423–1437. <https://doi.org/10.1007/s00424-013-1286-0>
- Tajima, M., Hayama, A., Rai, T., Sasaki, S., & Uchida, S. (2007). Barttin binds to the outer lateral surface of the ClC-K2 chloride channel. *Biochemical and Biophysical Research Communications*, 362(4), 858–864. <https://doi.org/10.1016/j.bbrc.2007.08.097>
- Tan, H., Bungert-Plümke, S., Fahlke, C., & Stölting, G. (2017). Reduced Membrane Insertion of CLC-K by V33L Barttin Results in Loss of Hearing, but Leaves Kidney Function Intact. *Frontiers in Physiology*, 8, 269. <https://doi.org/10.3389/fphys.2017.00269>
- Tiemann, A., Gründer, S., Pusch, M., & Jentsch, T. J. (1992). A chloride channel widely expressed in epithelial and non-epithelial cells. *Nature*, 356(6364), 57–60. <https://doi.org/10.1038/356057a0>
- Uchida, S., Sasaki, S., Nitta, K., Uchida, K., Horita, S., Nihei, H., & Marumo, F. (1995). Localization and functional characterization of rat kidney-specific chloride channel, ClC-K1. *The Journal of Clinical Investigation*, 95(1), 104–113. <https://doi.org/10.1172/JCI117626>
- Ulbrich, M. H., & Isacoff, E. Y. (2007). Subunit counting in membrane-bound proteins. *Nature Methods*, 4(4), 319–321. <https://doi.org/10.1038/nmeth1024>
- Vandewalle, A., Cluzeaud, F., Peng, K.-C., Bens, M., Lüchow, A., Günther, W., & Jentsch, T. J. (2001). Tissue distribution and subcellular localization of the ClC-5 chloride channel in rat intestinal cells. *American Journal of Physiology-Cell Physiology*, 280(2), C373–C381. <https://doi.org/10.1152/ajpcell.2001.280.2.C373>
- Veeramah, K. R., Johnstone, L., Karafet, T. M., Wolf, D., Sprissler, R., Salogiannis, J., Barth-Maron, A., Greenberg, M. E., Stuhlmann, T., Weinert, S., Jentsch, T. J., Pazzi, M., Restifo, L. L., Talwar, D., Erickson, R. P., & Hammer, M. F. (2013). Exome sequencing reveals new causal mutations in children with epileptic encephalopathies. *Epilepsia*, 54(7), 1270–1281. <https://doi.org/10.1111/epi.12201>
- Waldegger, S., Jeck, N., Barth, P., Peters, M., Vitzthum, H., Wolf, K., Kurtz, A., Konrad, M., & Seyberth, H. W. (2002). Barttin increases surface expression and changes current properties of ClC-K channels. *Pflügers Archiv*, 444(3), 411–418. <https://doi.org/10.1007/s00424-002-0819-8>
- Waldegger, S., & Jentsch, T. J. (2000). Functional and Structural Analysis of ClC-K Chloride Channels Involved in Renal Disease. *Journal of Biological Chemistry*, 275(32), 24527–24533. <https://doi.org/10.1074/jbc.M001987200>
- Wang, K., Preisler, S. S., Zhang, L., Cui, Y., Missel, J. W., Grønberg, C., Gotfryd, K., Lindahl, E., Andersson, M., Calloe, K., Egea, P. F., Klaerke, D. A., Pusch, M., Pedersen, P. A., Zhou, Z. H., & Gourdon, P. (2019). Structure of the human ClC-1 chloride channel. *PLoS Biology*, 17(4), e3000218. <https://doi.org/10.1371/journal.pbio.3000218>
- Wang, S. S., Devuyst, O., Courtoy, P. J., Wang, X.-T., Wang, H., Wang, Y., Thakker, R. V., Guggino, S., & Guggino, W. B. (2000). Mice lacking renal chloride channel, CLC-5, are a model for Dent's disease, a nephrolithiasis disorder associated with defective receptor-mediated endocytosis. *Human Molecular Genetics*, 9(20), 2937–2945. <https://doi.org/10.1093/hmg/9.20.2937>

- Wang, X. Q., Deriy, L. V., Foss, S., Huang, P., Lamb, F. S., Kaetzel, M. A., Bindokas, V., Marks, J. D., & Nelson, D. J. (2006). CLC-3 Channels Modulate Excitatory Synaptic Transmission in Hippocampal Neurons. *Neuron*, *52*(2), 321–333. <https://doi.org/10.1016/j.neuron.2006.08.035>
- Weinert, S., Jabs, S., Hohensee, S., Chan, W. L., Kornak, U., & Jentsch, T. J. (2014). Transport activity and presence of CLC-7/Ostm1 complex account for different cellular functions. *EMBO Reports*, *15*(7), 784–791. <https://doi.org/10.15252/embr.201438553>
- Wojciechowski, D. (2013). *Tryptophan scanning of barttin identifies molecular determinants of its function on CLC-K chloride channels*. PhD thesis, created at the Institute for Neurophysiology, Hannover Medical School, and published at the Gottfried Wilhelm Leibniz University Hannover. <https://doi.org/10.15488/8202>
- Wojciechowski, D., Fischer, M., & Fahlke, C. (2015). Tryptophan Scanning Mutagenesis Identifies the Molecular Determinants of Distinct Barttin Functions. *Journal of Biological Chemistry*, *290*(30), 18732–18743. <https://doi.org/10.1074/jbc.M114.625376>
- Wojciechowski, D., Kovalchuk, E., Yu, L., Tan, H., Fahlke, C., Stölting, G., & Alekov, A. K. (2018). Barttin Regulates the Subcellular Localization and Posttranslational Modification of Human Cl<sup>-</sup>/H<sup>+</sup> Antiporter CLC-5. *Frontiers in Physiology*, *9*, 1490. <https://doi.org/10.3389/fphys.2018.01490>
- Wojciechowski, D., Thiemann, S., Schaal, C., Rahtz, A., de la Roche, J., Begemann, B., Becher, T., & Fischer, M. (2018). Activation of renal CLC-K chloride channels depends on an intact N terminus of their accessory subunit barttin. *Journal of Biological Chemistry*, *293*(22), 8626–8637. <https://doi.org/10.1074/jbc.RA117.000860>
- Yoshikawa, M., Uchida, S., Ezaki, J., Rai, T., Hayama, A., Kobayashi, K., Kida, Y., Noda, M., Koike, M., Uchiyama, Y., Marumo, F., Kominami, E., & Sasaki, S. (2002). CLC-3 deficiency leads to phenotypes similar to human neuronal ceroid lipofuscinosis. *Genes to Cells*, *7*(6), 597–605. <https://doi.org/10.1046/j.1365-2443.2002.00539.x>
- Zhang, S., Liu, Y., Zhang, B., Zhou, J., Li, T., Liu, Z., Li, Y., & Yang, M. (2020). Molecular insights into the human CLC-7/Ostm1 transporter. *Science Advances*, *6*(33), eabb4747. <https://doi.org/10.1126/sciadv.abb4747>

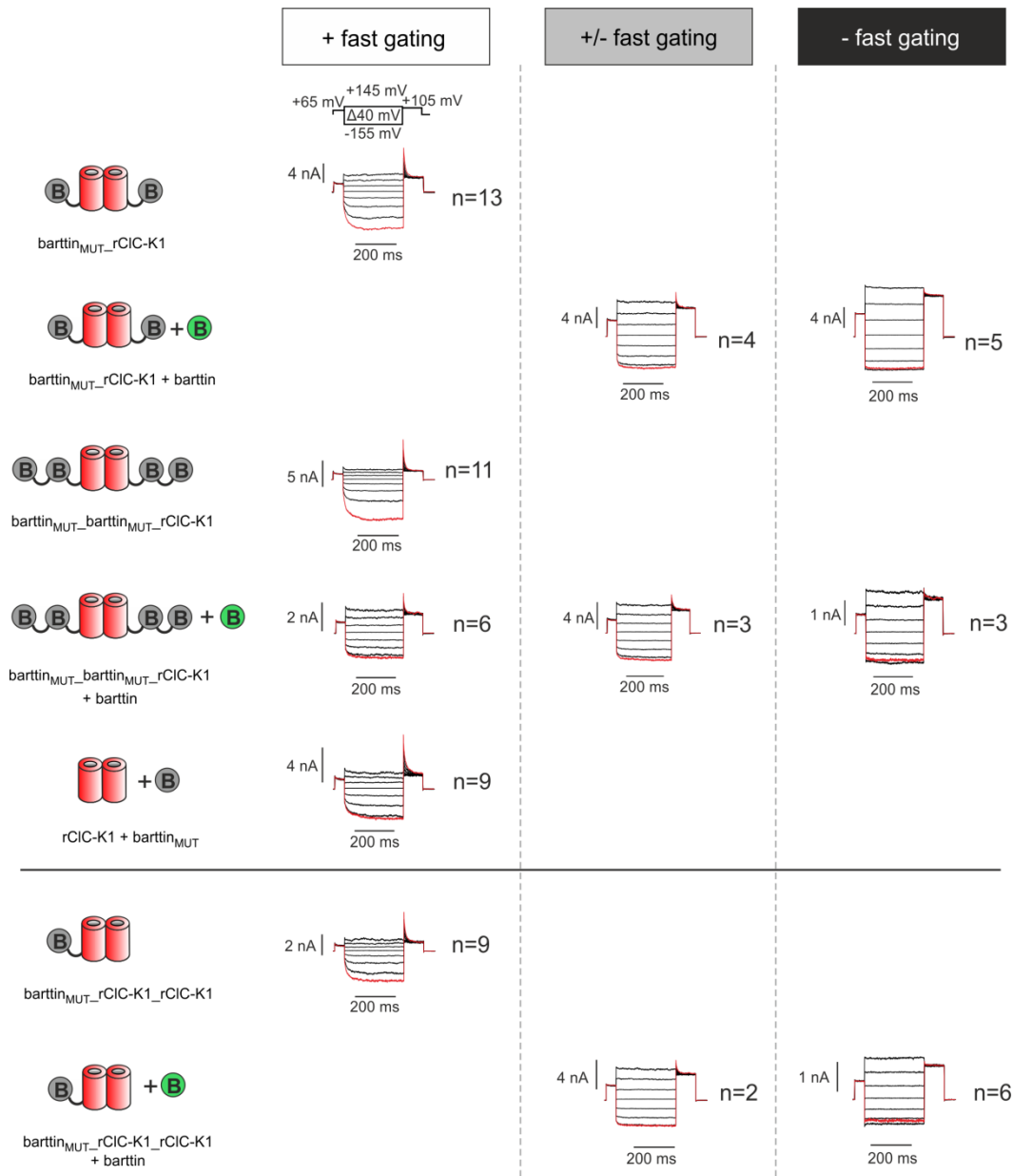
# 6 Supplement





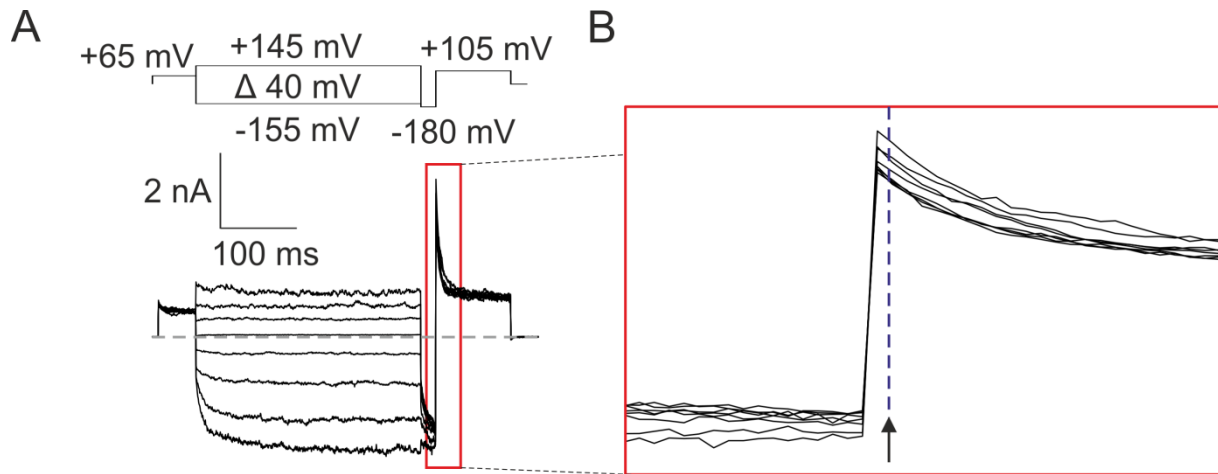
**Suppl. Fig. 1 Overview about representative current traces for each tested  $\alpha:\beta_{WT}$ -subunit stoichiometry categorized into three classes of time-dependent fast gating**

Cells were sorted as strong (+) time-dependent, when after the voltage step from -155 mV to +105 mV steady state current amplitude ( $I_{ss}$ ) was lower than 60% of instantaneous current amplitude ( $I_{inst}$ ), as medium (+/-) time-dependent, when  $I_{ss}/I_{inst}$  was between 60% and 80% and as weak (-) time-dependent, when  $I_{ss}/I_{inst}$  was higher than 80%. Red colored current traces represent relevant traces for categorization. For each tested condition and category, if available, the total number of cells (n) are given, which were sorted likewise with the representative registration. If for one condition and category no suitable registration was achieved, the space was left empty.



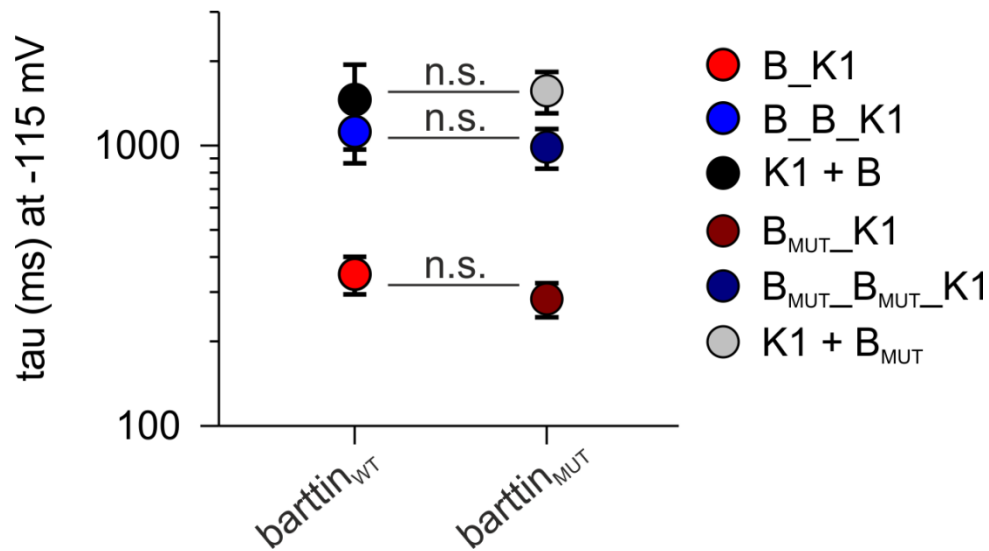
**Suppl. Fig. 2 Overview about representative current traces for each tested  $\alpha:\beta_{MUT}$ -subunit stoichiometry categorized into three classes of time-dependent fast gating**

Cells were sorted as strong (+) time-dependent, when after the voltage step from -155 mV to +105 mV steady state current amplitude ( $I_{ss}$ ) was lower than 60% of instantaneous current amplitude ( $I_{inst}$ ), as medium (+/-) time-dependent, when  $I_{ss}/I_{inst}$  was between 60% and 80% and as weak (-) time-dependent, when  $I_{ss}/I_{inst}$  was higher than 80%. Red colored current traces represent relevant traces for categorization. For each tested condition and category, if available, the total number of cells (n) are given, which were sorted likewise with the representative registration. If for one condition and category no suitable registration was achieved, the space was left empty.



**Suppl. Fig. 3 Representative current recording of rClC-K1 + barttin<sub>MUT</sub> used for determination of relative slow gate open probabilities**

(A) For determination of relative slow gate open probabilities for rClC-K1 in presence of barttin<sub>MUT</sub>, between the pre-pulses from -155 mV to +145 mV and the test pulse of +105 mV an inter-pulse of -180 mV for 20 ms was applied, which should open the fast gate without affecting the slow gate. Within the representative current recording of rClC-K1 + barttin<sub>MUT</sub> the relevant section for determination of slow gate open probabilities is surrounded by a red frame. Dashed line represents 0 nA. (B) Magnification of current section in (A), which is surrounded by a red frame and used for determination of relative slow gate open probabilities. Relative slow gate open probabilities were calculated by plotting the current amplitudes at the beginning of the test pulse (blue dashed line + arrow) against respective voltages of the pre-pulse.



**Suppl. Fig. 4 Comparison of slow gating time constants at -115 mV between rClC-K1/barttin<sub>WT</sub> and respective rClC-K1/barttin<sub>MUT</sub> concatamers**

Slow gating time constants ( $\tau$ ) at -115 mV taken from Figs.21E and 37E. Values are given as mean  $\pm$  S.E.M.. Student's t-tests were performed to test for significance between rClC-K1/barttin concatamers with and without barttin palmitoylation. n.s. = not significant. B\_K1: n=7, B\_B\_K1: n=9, K1 + B: n=5, B<sub>MUT</sub>\_K1: n=12, B<sub>MUT</sub>\_B<sub>MUT</sub>\_K1: n=11, K1 + B<sub>MUT</sub>: n=3. B\_K1 = barttin\_rClC-K1, B\_B\_K1 = barttin\_barttin\_rClC-K1, K1 + B, rClC-K1 + barttin, B<sub>MUT</sub>\_K1 = barttin<sub>MUT</sub>\_rClC-K1, B<sub>MUT</sub>\_B<sub>MUT</sub>\_K1 = barttin<sub>MUT</sub>\_ barttin<sub>MUT</sub>\_rClC-K1, K1 + B<sub>MUT</sub> = rClC-K1 + barttin<sub>MUT</sub>.

## 7 Acknowledgements

First of all, I would like to thank Prof. Dr. Christian Wahl-Schott, who gave me the opportunity to write my PhD thesis at the Institute for Neurophysiology at the Hannover Medical School and who examined my thesis as the first supervisor. For the helpful suggestions and the constructive criticism during writing of this thesis I am very thankful.

Furthermore, I would like to thank Prof. Dr. Thomas Scheper, Prof. Dr. Anaclet Ngezahayo, Prof. Dr. Christian Wahl-Schott and PD Dr. Martin Fischer for their time to read this manuscript and for being my referees and members of my graduation committee.

In particular, I would like to thank PD Dr. Martin Fischer, who provided me with excellent support in all matters as my direct supervisor. The time and effort he invested on my behalf were of an extraordinary value to me. The numerous and extensive discussions provided an inestimable input for conducting my experiments and for preparation of this thesis.

Many thanks also to Dr. Jeanne de la Roche for the frequent advices and for the professional support regarding experiments, data analysis, teaching and writing.

Of course, many thanks go to Birgit Begemann, Petra Kilian, Silke Schmidt, Toni Becher and to Ruth Thiemann, who gave enormous and ambitious technical support and advice regarding molecular biology, cell culture, biochemistry as well as regarding organizational and personnel matters.

Not forgotten should be the help of Dr. Michael Schänzler in every case involving advanced physical knowledge, the advices of Leon Sprenger and Ömer Kocdölü regarding scientific writing and software handling and the support of Martin Leibrock regarding measurements at the Cytation device. Of course I have to thank Dr. Hristo Varbanov for the kind atmosphere over the last months being my office mate, when I wrote this thesis.

In total, I want to thank all other members of the Institute for Neurophysiology I did not mention before for the pleasant and trustful collaboration over the last years. Their kindness and helpfulness made it very easy for me to work and to achieve research results.

Last but not least, huge thanks go to my family, who supported me beyond measure during this time in which I devoted myself intensively to my PhD thesis.

## 8 Curriculum vitae

### Personal information:

Stefan Thiemann

Born 06.07.1990 in Hameln, Germany

### Educational and Professional background:

- 2003-2010 Otto-Hahn-Gymnasium Springe  
Degree: Abitur
- 2010-2011 Student of human medicine at the Hannover Medical School
- 2011-2014 Student of biology at the Gottfried Wilhelm Leibniz University of Hannover  
Degree: Bachelor of Science
- 2014-2017 Student of biomedicine at the Hannover Medical School  
Degree: Master of Science
- 2017-present Scientific employee at the Institute for Neurophysiology  
Medical School Hannover
- 2018-present PhD studies at the Naturwissenschaftliche Fakultät  
Gottfried Wilhelm Leibniz University Hannover  
Conducted at the  
Institute for Neurophysiology  
Hannover Medical School  
Supervisor: Prof. Dr. Christian Wahl-Schott

## 9 List of publications

Daniel Wojciechowski, **Stefan Thiemann\***, Christina Schaal, Alina Rahtz, Jeanne de la Roche, Birgit Begemann, Toni Becher, Martin Fischer, 'Activation of renal ClC-K chloride channels depends on an intact N terminus of their accessory subunit barttin', *Journal of Biological Chemistry*, (2018) 293(22), 8626–8637 <doi: 10.1074/jbc.RA117.000860>

Jeanne de la Roche, Paweorn Angsutararux, Henning Kempf, Montira Janan, Emiliano Bolesani, **Stefan Thiemann**, Daniel Wojciechowski, Michelle Coffee, Annika Franke, Kristin Schwanke, Andreas Leffler, Sudjit Luanpitpong, Surapol Issaragrisil, Martin Fischer, Robert Zweigerdt, 'Comparing human iPSC-cardiomyocytes versus HEK293T cells unveils disease-causing effects of Brugada mutation A735V of Na<sub>v</sub> 1.5 sodium channels', *Scientific Reports*, (2019) 9(1), 11173 <doi: 10.1038/s41598-019-47632-4>

Lara-Antonia Beer, Helma Tatge, Carmen Schneider, Maximilian Ruschig, Michael Hust, Jessica Barton, **Stefan Thiemann**, Viola Fühner, Giulio Russo, Ralf Gerhard, 'The Binary Toxin CDT of *Clostridium difficile* as a Tool for Intracellular Delivery of Bacterial Glucosyltransferase Domains', *Toxins*, (2018) 10(6), 225 <doi 10.3390/toxins10060225>

Lika Draxhlis, Santoshi Biswanath, Clara-Milena Farr, Victoria Lupanow, Jana Teske, Katharina Ritzenhoff, Annika Franke, Felix Manstein, Emiliano Bolesani, Henning Kempf, Simone Liebscher, Katja Schenke-Layland, Jan Hegermann, Lena Nolte, Heiko Meyer, Jeanne de la Roche, **Stefan Thiemann**, Christian Wahl-Schott, Ulrich Martin, Robert Zweigerdt, 'Human heart-forming organoids recapitulate early heart and foregut development', *Nature Biotechnology* (2021) <https://doi.org/10.1038/s41587-021-00815-9>

Natalie Weber, Kathrin Kowalski, Tim Holler, Ante Radocaj, Martin Fischer, **Stefan Thiemann**, Jeanne de la Roche, Kristin Schwanke, Birgit Piep, Neele Peschel, Uwe Krumm, Alexander Lingk, Meike Wendland, Stephan Greten, Jan Dieter Schmitto, Issam Ismail, Gregor Warnecke, Urs Zywiets, Boris Chichkov, Joachim Meißner, Axel Haverich, Ulrich Martin, Bernhard Brenner, Robert Zweigerdt, Theresia Kraft, 'Advanced Single-Cell Mapping Reveals that in hESC Cardiomyocytes Contraction Kinetics and Action Potential Are Independent of Myosin Isoform', *Stem Cell Reports*, (2020) 14(5), 788-802 <https://doi.org/10.1016/j.stemcr.2020.03.015>

Nataliya Gorinski, Daniel Wojciechowski, Daria Guseva, Dalia Abdel Galil, Franziska E. Mueller, Alexander Wirth, **Stefan Thiemann**, Andre Zeug, Silke Schmidt, Monika Zareba-Kozioł, Jakub Włodarczyk, Boris V. Skryabin, Silke Glage, Martin Fischer, Samer Al-Samir, Nicole Kerkenberg, Christa Hohoff, Weiqi Zhang, Volker Endeward, Evgeni Ponimaskin, 'DHHC7-mediated palmitoylation of the accessory protein barttin critically regulates the functions of ClC-K chloride channels', *Journal of Biological Chemistry*, (2020) 295(18) 5970–5983 <doi: 10.1074/jbc.RA119.011049>

\* = co-first authorship